HAL open science

Statistics and dynamics of complex membranes

Anne-Florence Bitbol

To cite this version:

Anne-Florence Bitbol. Statistics and dynamics of complex membranes. Soft Condensed Matter [cond-mat.soft]. Université Paris-Diderot - Paris VII, 2012. English. NNT : . tel-00767943

HAL Id: tel-00767943

https://theses.hal.science/tel-00767943v1

Submitted on 20 Dec 2012

HAL is a multi-disciplinary open access archive for the deposit and dissemination of scientific research documents, whether they are published or not. The documents may come from teaching and research institutions in France or abroad, or from public or private research centers.

L'archive ouverte pluridisciplinaire **HAL**, est destinée au dépôt et à la diffusion de documents scientifiques de niveau recherche, publiés ou non, émanant des établissements d'enseignement et de recherche français ou étrangers, des laboratoires publics ou privés.

Université Paris Diderot – Paris 7
Paris Sorbonne Cité
École Doctorale Matière Condensée et Interfaces
Laboratoire Matière et Systèmes Complexes

Thèse de Doctorat
Discipline : Physique

Statistique et dynamique des membranes complexes

Anne-Florence BITBOL

Thèse dirigée par Jean-Baptiste FOURNIER

Soutenue le 21 juin 2012

Devant le jury composé de :

Mme	Miglena I. ANGELOVA	Membre
M.	Doru CONSTANTIN	Membre
M.	Ralf EVERAERS	Membre
M.	Jean-Baptiste FOURNIER	Directeur de thèse
M.	Andrea GAMBASSI	Rapporteur
M.	Chaouqi MISBAH	Rapporteur
M.	Jacques PROST	Membre
Mme	Annie VIALLAT	Présidente

University Paris Diderot – Paris 7
Paris Sorbonne Cité
Graduate School of Condensed Matter and Interfaces
Complex Matter and Complex Systems Laboratory

PhD Thesis
Subject: Physics

Statistics and dynamics of complex membranes

Anne-Florence BITBOL

Thesis advisor: Prof. Jean-Baptiste FOURNIER

Defended on June 21st, 2012

Examining committee:

Prof.	Miglena I. ANGELOVA	Member
Prof.	Doru CONSTANTIN	Member
Prof.	Ralf EVERAERS	Member
Prof.	Jean-Baptiste FOURNIER	Thesis advisor
Prof.	Andrea GAMBASSI	Referee
Prof.	Chaouqi MISBAH	Referee
Prof.	Jacques PROST	Member
Prof.	Annie VIALLAT	President

Remerciements

Mes premiers remerciements s'adressent à mon directeur de thèse, Jean-Baptiste Fournier. Son excellent cours de Master m'a convaincue de poursuivre en thèse avec lui, à un moment où je me posais des questions sur mon orientation scientifique. Je tiens à le remercier en particulier de m'avoir permis de travailler sur des projets variés, que j'ai trouvés extrêmement intéressants, et pour la confiance qu'il m'a accordée. J'ai beaucoup apprécié son enthousiasme scientifique et sa grande disponibilité. Jean-Baptiste a su me laisser de l'indépendance tout en m'encadrant quand j'en avais besoin.

Je remercie Andrea Gambassi et Chaouqi Misbah d'avoir accepté d'être rapporteurs de ma thèse, et Miglena Angelova, Doru Constantin, Ralf Everaers, Jacques Prost et Annie Viallat d'avoir accepté de participer au jury. J'adresse mes remerciements à tous les membres du jury pour m'avoir fait l'honneur d'évaluer mon travail.

J'ai beaucoup aimé travailler à la frontière entre théorie et expérience avec Miglena Angelova et Nicolas Puff. Je remercie aussi les membres de leur groupe avec lesquels j'ai travaillé. Cela a été un plaisir de regarder les expériences de microinjection, mais aussi de discuter du Japon, avec Yuka Sakuma. J'ai eu l'occasion d'apprendre à électroformer des vésicules unilamellaires géantes avec Nada Khalifat et Nicolas, ce qui m'a beaucoup intéressée. Je remercie par ailleurs Miglena de m'avoir conseillé d'aller à la conférence de la Biophysical Society : cela a été une expérience très enrichissante.

Mes remerciements vont également à Doru Constantin, avec qui il a été très agréable de collaborer sur l'élasticité membranaire à l'échelle nanométrique. J'ai particulièrement apprécié sa grande rigueur et ses connaissances encyclopédiques sur les membranes, les phases lamellaires, cubiques ou autres.

Je remercie aussi Paul Dommersnes et Luca Peliti, pour d'intéressantes discussions. J'ai beaucoup apprécié ma visite de l'Orwar Laboratory, et je remercie Paul, ainsi que Céline, de m'y avoir invitée.

J'adresse également des remerciements à Andrea Gambassi, avec qui j'ai eu l'occasion de discuter à plusieurs reprises des forces de Casimir : ces discussions ont réellement été stimulantes pour mon travail. Je le remercie aussi de m'avoir invitée au Workshop on Fluctuation-Induced Forces in Condensed Matter, qui a joué un grand rôle dans la partie de ma thèse consacrée à la définition de la force exercée par un fluide corrélé sur une inclusion. Je remercie aussi David Dean pour les discussions à ce sujet. Toujours dans le domaine des forces de Casimir, j'ai eu la chance de passer quelques jours dans le groupe du Prof. Dietrich : je lui adresse mes remerciements pour l'invitation, ainsi qu'à Thiago, pour l'accueil chaleureux.

Les enseignants-chercheurs avec lesquels j'ai travaillé ont contribué à faire de ma mission d'enseignement une expérience extrêmement enrichissante. Pour le module de physique statistique, j'exprime ma gratitude envers Paolo Galatola et Marc Durand, mais aussi envers mon prédécesseur Gérald Gurtner. Du côté de l'interface physique-biologie, je remercie les responsables du cours, Mathilde Badoual et Julien Heuvingh. Je souhaite aussi remercier mes étudiants physiciens de L3 et biologistes de L1 pour leur curiosité et leur vivacité, et Laurence Viennot pour m'avoir poussée à toujours plus d'exigence dans l'enseignement.

Je suis aussi très reconnaissante envers tous les chercheurs que j'ai interrogés lors de ma recherche de postdoctorat : ils m'ont bien aidée par leurs conseils avisés et m'ont permis d'envisager l'avenir de façon plus sereine.

J'ai réalisé ma thèse au laboratoire MSC, dont je remercie les directeurs successifs, Jean-Marc di Meglio et Loïc Auvray. J'ai bénéficié de l'environnement agréable de MSC pendant ma thèse, et je tiens à remercier l'ensemble des membres du laboratoire pour les discussions, les idées partagées et l'ambiance sympathique. Je remercie plus particulièrement les autres doctorants, tout d'abord ma "grande sœur" Camilla et mon "petit frère" Kévin pour les discussions sur les membranes et le reste, ainsi que Rémy, pour l'aide qu'il m'a apportée sur la programmation des plugins de traitement d'image, et pour les discussions partagées. Je remercie également mes "co-bureaux" de la pièce 768A, notamment Camilla, Gérald, Rémy, Luc, Baptiste et Hugo, pour l'atmosphère sympathique, ainsi que les occupants de la pièce 777A, notamment Stéphanie, Giuseppe, Julien et Alexis, pour la bonne ambiance et pour les déjeuners partagés, et, sans précision géographique, Camille, Delphine, Li, Amsha et Mathieu. Je remercie également Nadine, qui a su rendre agréables les formalités administratives.

Du côté de l'école doctorale Matières Condensée et Interfaces, mes remerciements s'adressent à Thomas Coudreau, ainsi qu'à Joëlle Taïeb.

À la fin de cette thèse, toute ma gratitude va à ceux qui m'ont permis d'arriver jusque là. Je remercie d'abord de tout mon cœur mes chers parents, qui m'ont toujours soutenue et encouragée, et qui m'ont énormément aidée et poussée pendant mes études. Ils se sont intéressés à ma thèse et ont même fait l'effort de la lire, avec peut-être un penchant pour les parties les moins denses en formules.

Mes professeurs du secondaire ont su me passionner pour les études, dans les matières scientifiques comme dans les domaines littéraires. En particulier, mon professeur de biologie-géologie du collège, M. Desloges, a beaucoup contribué à me donner le goût des disciplines scientifiques. En terminale, Mme Guilloux m'a encouragée à poursuivre dans le domaine des mathématiques et de la physique. Je remercie aussi tous les enseignants extrêmement impliqués et exigeants que j'ai eu la chance d'avoir en classes préparatoires, et qui m'ont énormément appris. À l'ENS de Lyon, puis en M2 de physique quantique, j'ai pu m'intéresser à des domaines très variés de la physique. Je remercie en particulier Nicolas Taberlet, grâce à qui j'ai fait un premier stage de recherche passionnant.

Mes amis m'ont permis de me changer les idées et de décompresser pendant ces trois ans, et ils ont aussi fait l'effort de s'intéresser à ce que je faisais. Les moments partagés avec mes amies de longue date, Raphaëlle, Emilie et Clémence, et avec mes amis rencontrés en classes préparatoires, Isabelle et Jérôme, sont précieux. Lorsque nos chemins se croisent, il est toujours très agréable de discuter avec Florian, et avec Jean-Nicolas, que je remercie aussi pour ses conseils. J'ai aussi partagé de bons moments avec les copains en thèse dans d'autres laboratoires, notamment Nawal, Juliette, Ziane, Joël, et le groupe à dominante chimique et (ex-)lyonnaise des dîners du mardi puis du X-di.

Enfin, mes derniers remerciements s'adressent à tous ceux que j'ai oublié de citer, et qui ont contribué à faire de cette thèse une très bonne expérience.

Résumé

Les bicouches lipidiques, qui constituent la base des membranes biologiques, sont des structures auto-assemblées appartenant au domaine de la matière molle. Leurs propriétés physiques sont extrêmement riches. Chacune des deux monocouches de la membrane est un fluide à deux dimensions. Par ailleurs, la membrane résiste à la flexion et à l'extension: elle est élastique. Les membranes biologiques sont composées de différents types de lipides et contiennent de nombreuses inclusions, en particulier des protéines membranaires. Ces inclusions interagissent non seulement avec la bicouche lipidique, mais aussi entre elles, à travers la bicouche lipidique. En outre, une membrane biologique est entourée d'un environnement hétérogène et en constante évolution, qui peut l'influencer et la perturber.

Cette thèse porte sur la statistique et la dynamique des membranes biologiques complexes. Nous nous intéressons à certains effets génériques de la présence d'une ou deux inclusions membranaires ou d'une modification chimique locale de l'environnement de la membrane.

Dans la partie I, nous étudions une interaction entre deux inclusions membranaires, qui est analogue à la force de Casimir: elle provient des contraintes que les inclusions imposent aux fluctuations thermiques de la forme de la membrane. Nous calculons les fluctuations de cette force entre deux inclusions ponctuelles, nous montrons leur importance quantitative et nous étudions leur dépendance en fonction de la distance entre les inclusions. Nous analysons ensuite les différences entre deux définitions de la force exercée par un fluide corrélé sur une inclusion, dans un micro-état du fluide. Cette force joue un rôle clé dans l'étude de la force de Casimir au-delà de sa valeur moyenne à l'équilibre. Enfin, nous étudions les interactions de Casimir entre des inclusions membranaires de forme allongée, pour différents types d'inclusions rigides, et pour des inclusions membranaires allongées comportant une rigidité finie à la flexion dans la direction orthogonale au plan de la membrane.

Dans la partie II, nous nous intéressons à l'élasticité membranaire à l'échelle nanométrique, qui est mise en jeu dans les déformations locales de l'épaisseur de la membrane à proximité de certaines protéines. Nous soulignons l'importance d'un terme énergétique qui a été négligé jusqu'à présent. Nous réanalysons des données numériques et expérimentales, ce qui nous permet d'obtenir des indices de la présence de ce terme.

Dans la partie III, nous présentons une description théorique, développée à partir de principes fondamentaux, de la dynamique d'une membrane soumise à une perturbation chimique locale de son environnement. Nous comparons nos prévisions théoriques à de nouveaux résultats expérimentaux portant sur la déformation dynamique d'une membrane biomimétique soumise à une augmentation locale de pH, et nous obtenons un bon accord entre théorie et expérience. Enfin, nous montrons que l'étude de la dynamique des perturbations locales donne accès à des informations sur la réponse de la membrane qui sont inaccessibles dans les études classiques, limitées aux perturbations statiques et globales de l'environnement de la membrane.

Abstract

Lipid bilayers, which form the basis of biological membranes, are self-assembled structures that belong to the field of soft matter. They feature very rich physical properties. While each of the two monolayers of the membrane is a two-dimensional fluid, the membrane resists bending and stretching: it is elastic. Biological membranes are composed of different lipid species and contain various inclusions, in particular membrane proteins. These inclusions interact with the lipid bilayer and with each other through the lipid bilayer. In addition, a biological membrane is surrounded by a heterogeneous and constantly changing environment, which can influence and perturb it.

This thesis deals with the statistics and dynamics of complex biological membranes. We focus on some generic effects of the presence of one or two membrane inclusions, or of a local chemical change of the environment of the membrane.

In Part I, we study the Casimir-like interaction between two membrane inclusions, which arises from the constraints imposed by the inclusions on the thermal fluctuations of the shape of the membrane. We calculate the fluctuations of the Casimir-like force between two point-like inclusions, showing the quantitative importance of these fluctuations, and studying their dependence on the distance between the inclusions. We then investigate the differences between two definitions of the force exerted by a correlated fluid on an inclusion, in a microstate of the fluid. This force plays a key part in studies of the Casimir-like force beyond its thermal equilibrium value. Finally, we study Casimir-like interactions between rod-shaped membrane inclusions, for different types of rigid rods, and for rods with finite out-of-plane bending rigidity.

In Part II, we examine membrane elasticity at the nanoscale, which is involved in local membrane thickness deformations in the vicinity of proteins. We put forward the importance of an energetic term that is neglected in existing models. We reanalyze numerical and experimental data, obtaining some clues for the presence of this term.

In Part III, we present a theoretical description of the dynamics of a membrane submitted to a local chemical perturbation of its environment, starting from first principles. We compare our theoretical predictions to new experimental results regarding the dynamical deformation of a biomimetic membrane submitted to a local pH increase, and we obtain good agreement between theory and experiments. Finally, we show that investigations of dynamical local perturbations provide more information on the response of the membrane than the standard studies that restrict to static and global perturbations of the membrane environment.

Contents

1 Introduction **1**
1.1 Cells and membranes . . . 1
1.2 The basic structure of biological membranes . . . 6
1.3 The physics of lipid bilayer membranes . . . 11
1.4 Brief outline of this thesis . . . 25

I Casimir-like interactions between two membrane inclusions **27**

2 Context: from the Casimir force to membrane-mediated interactions between inclusions **29**
2.1 Introduction . . . 30
2.2 The Casimir force in quantum electrodynamics . . . 30
2.3 Casimir-like forces in soft matter systems . . . 36
2.4 Casimir-like forces in membranes . . . 40
2.5 Membrane-mediated interactions due to the average deformation . . . 44
2.6 Outline of Part I . . . 49

3 Fluctuations of the Casimir-like force between two membrane inclusions **51**
3.1 Introduction . . . 52
3.2 Basics . . . 53
3.3 Approach based on the stress tensor . . . 58
3.4 Variance of the Casimir-like force . . . 62
3.5 Inclusions inducing a nonzero curvature . . . 71
3.6 Conclusion . . . 73
3.7 Appendix: Effect of varying the radius of the contour . . . 73

4 Forces exerted by a correlated fluid on embedded inclusions **75**
4.1 Introduction . . . 76
4.2 Embedded inclusion . . . 77
4.3 Non-embedded influencing object . . . 83
4.4 Casimir-like force . . . 87
4.5 A simple example of Casimir-like force . . . 90

4.6 Discussion . . . 96
4.7 Conclusion . . . 99
4.8 Appendix . . . 100

5 Casimir-like interactions between rods in fluid membranes 107
5.1 Introduction . . . 107
5.2 Model . . . 109
5.3 Simple rods with finite out-of-plane bending rigidity . . . 111
5.4 Other types of rods . . . 115
5.5 Discussion . . . 119
5.6 Conclusion . . . 122

II Inclusions and membrane thickness deformations 125

6 Context: Membrane thickness deformations close to proteins 127
6.1 Introduction . . . 127
6.2 Experimental studies on gramicidin . . . 129
6.3 Models for local membrane thickness deformations . . . 132
6.4 Insight from numerical simulations . . . 135
6.5 Brief outline of our contribution . . . 137

7 Bilayer elasticity at the nanoscale: the need for new terms 139
7.1 Introduction . . . 140
7.2 Membrane model . . . 140
7.3 Comparison with existing models . . . 146
7.4 Comparison with numerical results . . . 150
7.5 Comparison with experimental results . . . 155
7.6 Conclusion . . . 165
7.7 Appendix A: On our effective Hamiltonian . . . 166
7.8 Appendix B: Numerical fluctuation spectra . . . 168
7.9 Appendix C: Membrane containing a cylindrical mismatched protein . 171

III Dynamics of a membrane submitted to a local chemical modification 177

8 Context: Local modification of the environment of a membrane 179
8.1 Introduction . . . 179
8.2 Experimental studies . . . 180
8.3 Theory of local modifications of membranes . . . 184
8.4 Outline of Part III . . . 188

9 Theoretical description of the dynamics of a membrane submitted to a local chemical modification 191
9.1 Introduction . . . 192

9.2 Effective Hamiltonian of a monolayer 192
9.3 Force densities in the membrane 195
9.4 Membrane dynamics 199
9.5 Profile of the fraction of the chemically modified lipids 203
9.6 Resolution of the dynamical equations 205
9.7 Conclusion 206

10 Lipid membrane deformation in response to a local pH modification: theory and experiments 207
10.1 Introduction 207
10.2 Materials and methods 208
10.3 Experiments 210
10.4 Comparison between theory and experiments 213
10.5 Conclusion 219

11 Membrane properties revealed by spatiotemporal response to a local inhomogeneity 221
11.1 Introduction 221
11.2 Theoretical description 222
11.3 Extreme cases 225
11.4 General case 232
11.5 Conclusion 234

12 A tool: the membrane stress tensor in the presence of density and composition inhomogeneities 237
12.1 Introduction 238
12.2 Stress tensor formal derivation 238
12.3 Monolayer model 242
12.4 Projected stress tensor 247
12.5 Force density in a monolayer 250
12.6 Applications 254
12.7 Conclusion 258
12.8 Appendix A: Covariant calculation of the force density 259
12.9 Appendix B: Tangential stress tensor at second order 261

Conclusion 263

Publications 267

Bibliography 269

Chapter 1

Introduction

Contents

1.1 Cells and membranes 1

1.1.1 Biological overview 1

1.1.2 Short account of the discovery of cells and membranes . . 3

1.2 The basic structure of biological membranes 6

1.2.1 Lipids: the main constituents of biological membranes . . 6

1.2.2 Lipid bilayer membranes 8

1.2.3 Model lipid bilayer membranes 10

1.3 The physics of lipid bilayer membranes 11

1.3.1 Basic physical characteristics of lipid bilayers 11

1.3.2 The Helfrich model 15

1.3.3 The area-difference elasticity model 22

1.4 Brief outline of this thesis 25

1.1 Cells and membranes

1.1.1 Biological overview

Living organisms are composed of one or several cells. A whole cell can dynamically self-maintain, grow and multiply in vitro, contrary to the separate parts of this cell [1]. The crucial fact that the cell "dynamically self-maintains" means that it can use external molecules to continuously produce and replace its own constituents [2, 3]. These characteristics are often taken (either together or separately) as the basic definition of the living [1–3]. Cells are thus considered the basic units of life [1, 4].

In spite of the great diversity of living organisms, all known cells share universal features. First, they all store their hereditary information in a specific sequence of

the same polymer, DNA[1]. Moreover, the basic mechanisms by which this hereditary information is copied by the cell to be transmitted to daughter cells, and those by which it is used by the cell to produce its proteins, are common to all cells. Proteins, which are, like DNA, polymers with specific sequences, play crucial parts in all cells, by acting as enzymes to catalyze the reactions involved in various cellular chemical processes. Besides, since all cells produce DNA, RNA and proteins, they all use a similar collection of small molecules for their synthesis [4]. There is yet another universal feature of cells, which is less often cited: all cells are surrounded by a membrane, which acts as a barrier separating the inside and the outside of the cell [4, 5]. However, a cell is not a closed system, as it needs energy to maintain its organization: the membrane is a selective barrier, which enables the cell to incorporate nutrients and certain chemicals from its environment, and to excrete waste, while retaining the cell's own molecules inside it [4]. The basic structure of the membrane is the same among all living cells: it is essentially a lipid bilayer, with inclusions such as proteins.

The membrane plays a crucial part in the cell. Without it, the cell could not maintain its integrity as a coordinated chemical system [4]. The membrane also has a central role in the following fundamental definition of life[2]: what characterizes a living organism is that it self-maintains by constantly regenerating its own components via a chain of processes that takes place within its boundary [6]. This idea is called autopoiesis [3], a word with Greek roots meaning "to make itself". An important point in this framework is that the boundary, i.e., the membrane in the case of a cell, is itself produced by the living system. Whether a given system makes its own boundary or not can be taken as a fundamental criterion to determine if this system is autopoietic or not [6]. For instance, a virus is not an autopoietic system, as it does not produce its envelope, relying on the host cell for this.

Until now, we have focused on the membrane that encloses the cell. This cell membrane, or plasma membrane, is the only one present in prokaryotic cells, i.e., in bacteria and archaea. Conversely, the structurally more complex eukaryotic cells, which correspond to protists, fungi, plants, and animals, contain additional membranes, which enclose intracellular compartments called organelles [1]. Fig. 1.1 shows a sketch of a eukaryotic cell with its various organelles. It can be seen on this illustration that the membranes of organelles have various specific shapes, some of them being highly curved and densely packed. With all these organelles, eukaryotic cells contain a large amount of lipid bilayer membranes. It is estimated that in a human being, which is composed of about 10^{14} cells, the total surface of the

[1]This rule suffers a few exceptions. For instance, mammalian red blood cells do not have nuclei or DNA in their mature form: they are basically hemoglobin bags [4].

[2]A discussion of the question of the definition of life is (far) beyond the scope of the present work. Let us just mention that other definitions of life include the fact that a living being can grow and reproduce as being crucial, and that others yet are based on self-replication and Darwinian evolution of DNA and RNA. The autopoietic definition is somewhat different, because it aims at understanding the internal logic of minimal life. While growth and reproduction are not necessary ingredients of this definition, which is basically concerned with the homeostatic state, they come in as possible consequences of the fundamental self-regenerating process. Similarly, while DNA is not necessary ingredient of this definition either, it can be incorporated in the autopoietic scheme [6].

membranes is around 100 km^2 [5]. Each type of organelle has a specific role in the eukaryotic cell. For instance, the nucleus contains genetic information, while the mitochondria produce ATP, a molecule that is used as the cell's fuel. Like the cell membrane, the membranes of the various organelles are lipid bilayers containing inclusions such as membrane proteins. These lipid bilayer membranes are highly dynamical structures: they constantly deform during cell life, for instance to enable transport within the cell.

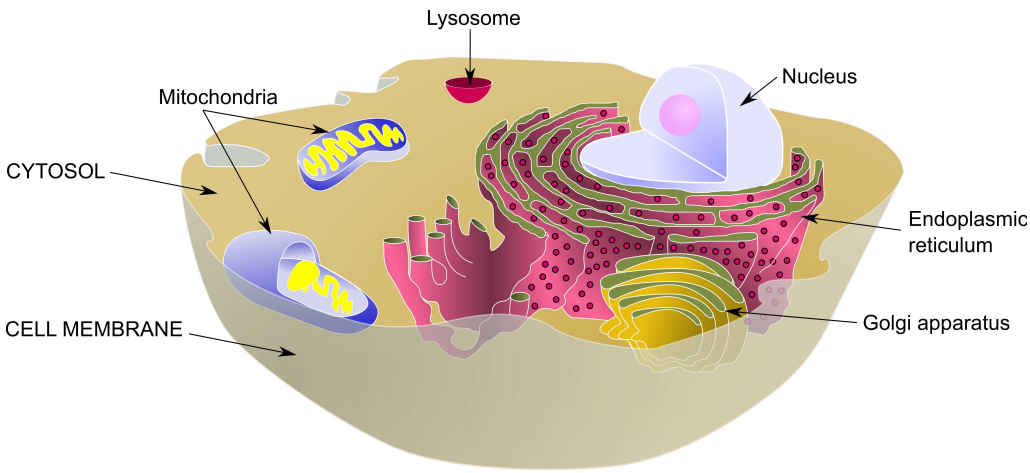

Figure 1.1: Sketch representing a cut of a eukaryotic cell (typical dimension: 10 to 100 μm). The various organelles, i.e., intracellular compartments surrounded by membranes, are indicated with a lower case legend. This cell corresponds to an animal cell. *Original illustration from Wikimedia Commons, adapted and modified.*

We have seen how lipid bilayer membranes compartmentalize living matter into cells and into subcellular structures. However, it has recently become clear that compartmentalization is far from being the only function of lipid bilayers. Membrane lipids are now known to play an active role in many biological processes that take place in the membrane or that are mediated by it: they can act as enzymes, receptors, drugs, regulators of neurotransmitter activity, messengers of signals, regulators of transcription factors that modulate the expression of genes, etc. [5]

1.1.2 Short account of the discovery of cells and membranes

a. Cells

The discovery of cells was strongly related to the invention and improvement of the optical microscope during the seventeenth century. Indeed, the typical dimension of a cell is 1 to 50 μm (10 to 50 μm for a eukaryotic cell, 1 to 10 μm for a prokaryotic cell). In 1665, Hooke observed a thin slice of cork under a microscope, and he noticed a porous structure that he compared to honeycomb. He coined the name "cells" to describe the pores in this structure, as they reminded him of the small rooms occupied by monks in a monastery. In fact, the structure he

was observing corresponds to the cell walls separating the plant cells of the cork. Thanks to the microscope too, Hooke's contemporary Leeuwenhoek observed a vast variety of microscopic moving "animalcules", which in fact correspond to unicellular organisms [1].

Most of the subsequent observations of cells were conducted on plant tissues, just like the one by Hooke, given that cell walls make the separations between cells easily visible in these tissues. In 1682, Grew compared the microscopic structure of plants to lace: he thought that the network corresponding to cell walls consisted of fibers woven together. The use of the word "tissue" in biology actually comes from this idea, even though it was soon abandoned in light of other observations. The network of cell walls then began to be viewed as a structure which was continuous throughout the whole plant. This structure was thought to be the essential constituent of the plant, while a nourishing fluid was thought to flow through its spaces, i.e., through the cells. In this framework, cells were thus regarded as connected to one another and forming a continuum. While this idea was widely supported until the beginning of the nineteenth century, it must be noted that contrary opinions had appeared early. For instance, Grew himself, in an early work of 1672, compared plant tissue to "a mass of bubbles", and in 1675, Malpighi observed rows of "utricles" (i.e., vesicles) flowing from a torn petal: these were actually cells [7].

In 1807, Link observed that adjacent cells could be filled with liquids of different colors, and that the presence of a damaged cell does not lead to flow from its neighbors. He thus questioned the idea that cells formed a continuum, and supported the idea that cells were separate, and that their walls were separate too. He then managed to separate some cells by boiling plant tissues. His view was supported by subsequent studies, and the idea that plant cells were separate finally prevailed around 1835 [7].

It was at this time that the fundamental importance of cells was realized. In 1838, Schleiden concluded that all the organs of a plant are constituted of cells, and that the plant embryo arises from a single cell. In 1839, Schwann extended this to animals and put forward the two first principles of cell theory: all organisms are constituted of one or several cells, and the cell is the structural unit of life. In 1855, Virchow's work was at the origin of the last principle of this theory: cells can only come from divisions of other cells. This rules out the idea of spontaneous generation of living organisms [1].

b. Membranes

Biological membranes are a few nanometer thick, which is below the resolution of optical microscopy. Thus, the discovery of the membrane occurred later than that of the cell, and it was first based on indirect evidence rather than on direct observation.

We have seen that the cell wall was long considered as a crucial part of cells, simply because it is the most easily visible structure. This was still the case in the time of Schwann's work on animal cells. As we now know that most animal cells have no cell wall, it seems strange that the unity between plant cells and animal cells could be established in this context. Actually, most early observations of animal

cells do mention the existence of a cell wall. In some cases, other structures could be mistaken with a cell wall. In other ones, we can blame these wrong observations on the low numerical aperture of microscopes in those times, which resulted into artifactual double lines around cells. It is also likely that the fact that scientists were expecting to observe a cell wall played a part in these wrong interpretations too [7].

This focus on the cell wall, which was often called "membrane", contributed to making the discovery of the actual membrane very tricky. In 1857, Leydig made the first clear claim that the cell wall was not a necessary part of the cell. The idea that primordial cells had no cell wall was supported by Schultze, who subsequently proposed the following definition: "a cell is a little lump of protoplasm, in the interior of which lies a nucleus". The protoplasm corresponds to the bulk of the cell (we would now say the interior of the cell). This concept of a cell without any envelope is very much at variance with the initial idea of a cell, and with the word "cell" itself. Despite an ongoing controversy about the essential or non-essential nature of the cell's envelope, the view according to which the simplest form of cell consisted of naked protoplasm with a nucleus prevailed for thirty years, until the end of the nineteenth century. It is interesting to note that several experiments on osmosis were conducted during this period, and that the observation of osmotic effects could have led to the idea that cells were surrounded by a semipermeable membrane. However, as all these studies were conducted on plant cells, the osmotic effects were attributed to the vacuole inside the plant cell, and not to the cell as a whole [7].

Overton studied in depth the osmotic properties of both plant and animal cells around 1895. He observed that plasmolysis, i.e., shrinking of protoplasm, occurred when exposing cells to certain substances, while other substances had no effect. He deduced that the former substances could not enter the cell easily, while the latter could. Moreover, he noticed that the substances soluble in organic solvents such as fatty oils could enter the cell more easily than those soluble in water. He was thus driven to the conclusion that the "outer layer" of the cell was composed of a substance with properties similar to those of fatty oils [7, 8]. This fundamental conclusion, which was published in 1899, is the basis of the concept of the lipid cell membrane [7, 9].

In 1925, Gorter and Grendel extracted the lipids from the membranes of red blood cells. Using the method developed by Langmuir in 1917 to control the spreading of oil on a water surface, they measured the area occupied by these lipids, which form a monolayer at the water surface. They found that this area was equal to twice that of the initial red blood cells. This led to the idea that cell membranes were lipid bilayers [8, 9]. In 1935, thanks to measurements of the surface tension of various cells, Danielli, Harvey and Davson showed that proteins were an important additional component of lipid membranes [8, 9].

The invention of electron microscopy and the subsequent improvement of its resolution finally enabled direct imaging of the membrane, whose thickness is of a few nanometers, in the 1950s. Once cell membranes had been observed, it was found that similar membranes also existed within some cells. In 1959, Robertson argued

that the envelope of all intracellular compartments has the same bilayer structure as the cell membrane [9]. Alternative membrane structures were still developed at this time: for instance, structures composed of discrete globular subunits were proposed in the 1960s as an alternative to the bilayer membrane [10]. A consensus on the lipid bilayer as the basic structure of cell membranes was finally reached in the 1970s [9].

1.2 The basic structure of biological membranes

In this Section, we will first review briefly the structure of lipid molecules and then explain how they self-assemble into bilayer membranes.

1.2.1 Lipids: the main constituents of biological membranes

Lipids regroup a vast and quite loosely defined class of organic molecules that do not easily dissolve in water. Most lipids are based on fatty acids, which are carboxylic acids with a long aliphatic (i.e., carbon-based and non-aromatic) chain. This chain is hydrophobic, which means it would not dissolve in water, while the carboxyl group, which is ionized in solution around neutral pH, is highly hydrophilic and chemically reactive. Thus, many lipids are derivatives of fatty acids in which the fatty acids are covalently linked to other molecules by the carboxyl group. In a cell, two main types of such derivatives can be found: triglycerids and phospholipids. The former are used by the cell as energy storage (and are the main component of fats and oils found in food), while the latter are the main constituents of membranes [1, 4, 5]. We will thus focus on phospholipids.

Phospholipids (more precisely, phosphoglycerids) are constituted of two fatty acids linked to a glycerol molecule via ester bonds, while the remaining hydroxyl group of the glycerol molecule is linked to a polar group, called headgroup, which includes phosphate [5]. The chemical structure of phospholipids is illustrated in Fig. 1.2, which shows two different fatty acids and a phospholipid deriving from them. Due to this structure, phospholipids are amphiphilic molecules, which means that they have a hydrophobic part and a hydrophilic part. The former corresponds to the aliphatic chains of the two fatty acids from which the phospholipid derives, while the latter corresponds to the headgroup. The amphiphilic nature of phospholipids plays a key role in the formation and stability of lipid bilayer membranes.

There is a large diversity of fatty acids, with various chain lengths and various numbers and positions of unsaturations, i.e., double bonds (see Fig. 1.2(a)): this leads to a great variety of the chains in phospholipids. Moreover, various headgroups exist too: the choline group of the lipid of Fig. 1.2(b) can be replaced by something else in other phospholipids. Some of these headgroups yield lipids that have zero net charge at neutral pH. For instance, phosphatidylcholine is zwitterionic, i.e., it contains both a negative charge and a positive charge, which makes it globally neutral (see Fig. 1.2(b)). Other headgroups result into lipids that have a nonzero net charge at neutral pH [1, 5]. Both globally neutral and negative phospholipids are found in membranes, but no globally positive ones [5].

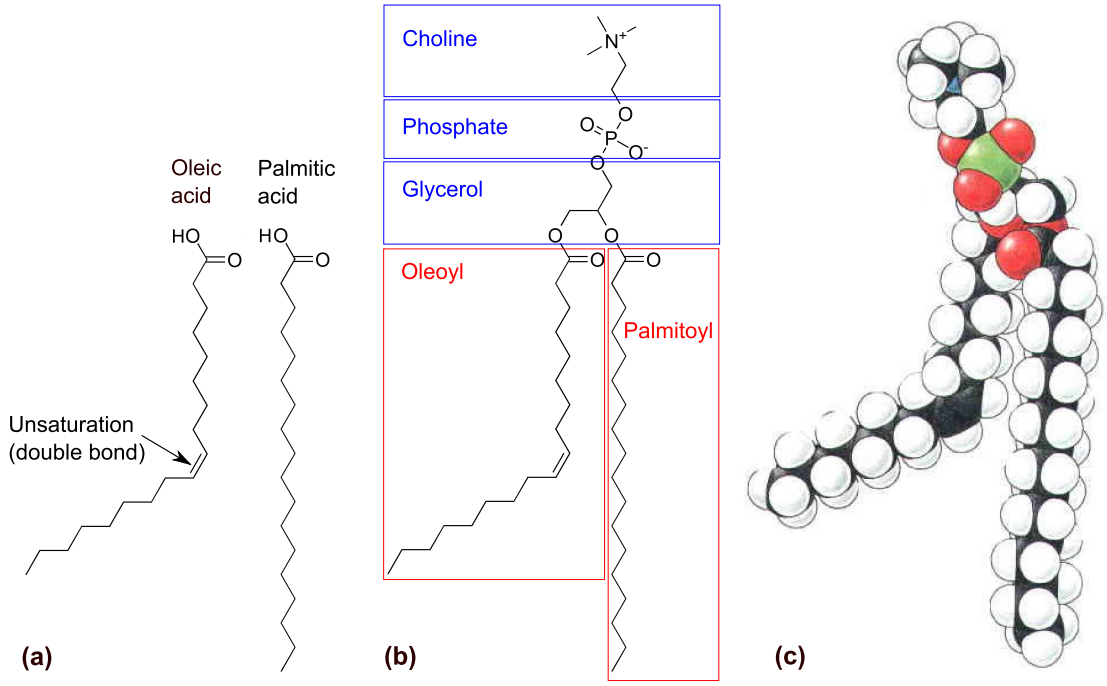

Figure 1.2: (a): Chemical formulas of two different fatty acids, a mono-unsaturated one (oleic acid) and a saturated one (palmitic acid). (b): Chemical formula of a phospholipid deriving from these two fatty acid: its full name is palmitoyl-oleyol-phosphatidylcholine, or POPC. The parts corresponding to the hydrophilic headgroup are indicated in blue, while the ones to the hydrophobic chains are indicated in red. (c): The same phospholipid, represented as a space-filling model. *Original illustrations from Wikimedia Commons (a-b) and from Ref. [4] (c), adapted and modified.*

While phospholipids are the main components of most biological membranes, other types of lipids can be involved too. For instance, some lipids arise from a fatty acid linked to sphingosine, which is a long-chain amine. This yields a structure similar to that of phospholipids, as it is composed of two hydrophobic chains and a hydrophilic head. These lipids are called sphingolipids [1]. Both phospholipids and sphingolipids can have their headgroups substituted by sugars, in which case they are called glycolipids [5]. Let us also mention cholesterol, which is very different from phospholipids and sphingolipids: it has a steroid structure involving cycles and a short hydrocarbon chain, and a simple hydroxyl group as its polar headgroup. Hence, cholesterol is a short lipid molecule with a bulky and stiff hydrophobic part and a small headgroup [5].

A vast variety of lipids can be found in the same membrane. There is also often an asymmetry between the composition of the two monolayers that constitute the bilayer membrane. Besides, in eukaryotic cells, there are important differences between the composition of the cell membrane and the composition of the membranes of the various organelles. Finally, there is a great variability in lipid membrane composition among different species [5].

1.2.2 Lipid bilayer membranes

The lipid bilayer, which is the basic structure of all biological membranes, is an assembly of billions of lipids that hold together without being covalently linked [5]. The formation and the stability of lipid bilayers in an aqueous environment is deeply related to the fact that lipids are amphiphilic. This crucial property arises from their molecular structure, as seen in the previous Section: the lipids that constitute biological membranes have hydrophobic chains and hydrophilic headgroups. Let us now present hydrophobicity in more detail, before moving on to the behavior of lipids in water.

a. The hydrophobic effect

The Greek roots of the word "hydrophobic" mean "which hates water". And indeed, until now, we have defined a hydrophobic molecule as one that does not dissolve in water. This "hatred" of water is in fact not at all intrinsic to the hydrophobic molecule. It is rather due to the fact that the presence of such a molecule in water destabilizes the structure of water.

Water is stabilized by hydrogen bonds, which occur when a hydrogen atom in a water molecule is attracted by a nonbonding pair of electrons belonging to the oxygen atom of another water molecule. Each water molecule can participate in up to four hydrogen bonds (see Fig. 1.3(a)). In ice, each water molecule has four static hydrogen bonds with its neighbors: this configuration is especially stable since all hydrogen atoms and all nonbonding pairs of electrons are engaged in a hydrogen bond. In liquid water, the network of hydrogen bonds is highly dynamical, with hydrogen bonds constantly forming and breaking under the action of thermal fluctuations. Due to the many different ways the hydrogen bond network can reorganize, it is strongly stabilized by entropy [5]. On average, each molecule has 3 to 3.5 hydrogen bonds in liquid water [11].

Let us consider molecules that cannot form hydrogen bonds, e.g., hydrocarbon chains. These molecules do not dissolve in water because their presence in water disrupts the network of hydrogen bonds, which destabilizes the system. The water molecules closest to our extraneous molecules are unable to form four hydrogen bonds (see Fig. 1.3(b)), and moreover, there is less freedom for them to reorganize their hydrogen bonds, which yields an important entropy loss [11, 12]. Hence, such extraneous molecules spontaneously cluster together in order to minimize the disruption of the dynamical hydrogen bond network of water: this is called the hydrophobic effect [5, 12]. The hydrophobic effect is an effective attractive interaction mediated by water [12], which is mostly of entropic origin [11].

On the contrary, polar or ionic compounds can form hydrogen bonds thanks to their charges: they dissolve easily in water.

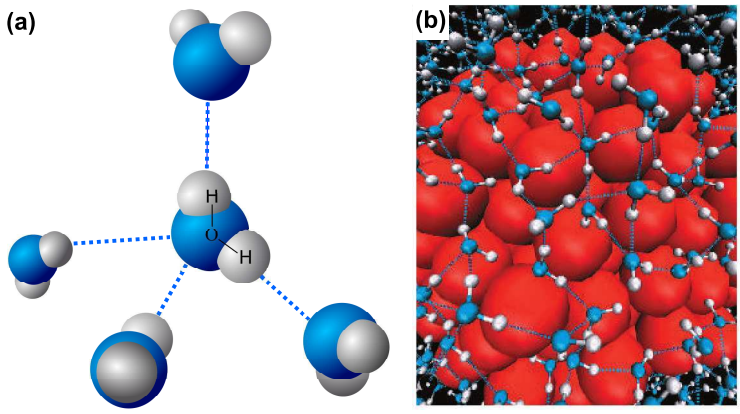

Figure 1.3: (a): In bulk water, each water molecule is able to participate in up to four hydrogen bonds. The blue and white spheres represent oxygen and hydrogen atoms, respectively, and the dotted blue lines indicate hydrogen bonds. (b): Configurations of water molecules near a hydrophobic cluster in a molecular dynamics simulation. The water molecules closest to the cluster have typically three or fewer hydrogen bonds, and are less able to rearrange them: the dynamical network of hydrogen bonds is disrupted. The red spheres represent hydrophobic objects, while other symbols are the same as in (a). *Original illustration (a) from Wikimedia Commons, adapted and modified. Illustration (b) reproduced from Ref. [12].*

b. Self-assembly of amphiphilic molecules in water

When amphiphilic molecules, such as lipids, are mixed with water, the hydrophobic effect acts in such a way that their hydrophobic parts tend to cluster together. However, since each amphiphilic molecule also has a hydrophilic part, this does not lead to bulk phase separation as when mixing a hydrocarbon with water. Instead, supramolecular aggregates spontaneously form, with a structure such that the hydrophilic parts are hydrated by water while the hydrophobic chains avoid contact with water [5]. The precise shapes of these aggregates are determined by the effective shapes of the amphiphilic molecules involved, as illustrated in Fig. 1.4.

In particular, most phospholipids spontaneously self-assemble into bilayers in water, with the hydrophilic headgroups pointing towards water in both monolayers (see Fig. 1.4(b)). Hence, lipid bilayer membranes spontaneously form when adequate lipids are mixed with water. Furthermore, in order not to have an unfavorable edge which would expose some hydrophobic chains to water, these bilayers spontaneously close to form quasi-spherical vesicles, also called liposomes (see Fig. 1.4(b)-(c)). It is interesting to stress that self-assembled aggregates such as lipid bilayers owe their existence to the peculiar properties of water: lipid bilayers do not exist without water as a solvent [5].

The fact that lipids can self-assemble to form bilayer membranes has led to speculate that this might have played a part in the origin of life. In this hypothesis, the first protocells appeared in a solution containing diverse molecules by self-assembly of lipid vesicles encapsulating hydrophilic solutes with catalytic activity [13].

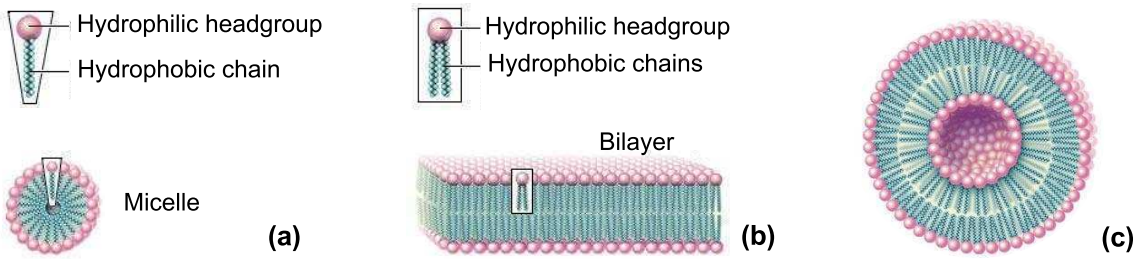

Figure 1.4: Simple examples of supramolecular structures formed by amphiphilic molecules in water. (a): Amphiphilic molecules that have an effective "conical shape", with a hydrophilic headgroup thicker than their hydrophobic chain(s), form micelles. This is typically the case for molecules with a single hydrophobic chain, such as fatty acids, but also surfactants and detergents. (b): Amphiphilic molecules that have an effective "cylindrical shape", with a hydrophilic headgroup roughly as thick as their hydrophobic chain(s), form bilayers. This is typically the case for phospholipids. (c): Bilayers spontaneously close to form vesicles. *Original illustrations from* Encyclopedia Britannica*, adapted and modified.*

1.2.3 Model lipid bilayer membranes

We have seen that the basic structure underlying a biological membrane is a lipid bilayer. Within a cell, this lipid bilayer can have a heterogeneous lipid composition, it contains many inclusions, in particular membrane proteins, and it is coupled to the cytoskeleton. Moreover, as living matter in general, cell membranes are out-of-equilibrium systems. For instance, they include active membrane proteins (e.g., ATP-consuming enzymes) [1]. This makes cell membranes highly complex systems.

Studying the physics of a simple lipid bilayer is an important step to gain understanding of biological membranes. Besides, lipid bilayer membranes are, on their own, an interesting system to study from a physical point of view: their self-assembled, highly structured and flexible nature gives them many original physical properties, as we will see in the following Section.

In order to study experimentally the properties of lipid bilayers, it is possible to work on liposomes, which are lipid bilayer vesicles formed by the self-assembly of lipids in water. Liposomes were first described by Bangham, Standish and Watkins in 1965, as they observed with an electron microscope shaken lipid solutions [14]. These authors noted that the "spherulites" they observed shared many properties with cell membranes, for instance a higher permeability to anions than to cations [14]. Since then, liposomes, which are composed of pure lipid bilayer membranes, have been widely used as model systems to investigate the basic properties of membranes.

Spontaneously formed vesicles tend to be multilamellar, i.e., to be composed of several bilayers nested within one another. It is however of particular interest to study giant unilamellar vesicles (GUVs), which are vesicles composed of a closed single lipid bilayer (see Fig. 1.4(c)), with dimension larger than 1 μm. These vesicles have dimensions similar to those of cells and are large enough to be studied using

optical microscopy. In order to produce them, it is necessary to control the self-assembly of the lipids.

Currently, three main protocols are widely used to prepare GUVs [15, 16]. Lipid film hydration, introduced by Reeves and Dowben in 1969 [17], consists in controlled hydration of a thin dry film of lipids: the lipid film progressively swells, which leads to the formation of GUVs. This method requires a few percent of negatively charged lipids [15]. Electroformation, introduced by Angelova and Dimitrov in 1986 [18], involves applying an electric field to electrodes on which a dried lipid film has been deposited and that are immersed in water. The electric field facilitates the formation of GUVs on the electrodes. This procedure has a high reproducibility, but it cannot be used if the proportion of charged lipids is too high, or at high ionic strength [15]. Finally, in the water-oil emulsion method introduced by Pautot and coworkers in 2003 [19], some water is introduced in a denser water-oil emulsion stabilized by lipids, which leads to GUV formation as the lipid-coated water droplets migrate through the lipid-saturated oil-water interface of the emulsion. A disadvantage of this method is that there can be some oil remaining in the membrane, which can affect the physical properties of the bilayer [15].

We are now going to focus on the physical description of pure lipid bilayer membranes. The models we will describe have been tested quantitatively using experiments on GUVs.

1.3 The physics of lipid bilayer membranes

1.3.1 Basic physical characteristics of lipid bilayers

We have seen that there are no covalent bonds between lipids in membranes and that lipids form membranes by self-assembly processes. This structure gives many original physical properties to lipid bilayer membranes.

a. Softness

Lipid bilayer membranes are pieces of soft matter, which means that they deform easily under the action of thermal fluctuations at ambient temperature (see Fig. 1.5). Other examples of soft matter objects include polymers and liquid crystals, which are structured, complex and flexible objects, like lipid bilayer membranes [5, 20]. The study of soft matter was pioneered by de Gennes, starting in the late 1960s [20].

The softness of lipid bilayer membranes comes from the fact that lipid bilayers are made of molecules with substantial conformational complexity, and from the fact that these molecules self-assemble due to entropic effects, as seen in Sec. 1.2.2. Lipids have a large conformational complexity because their hydrophobic chains are flexible [5]. Indeed, each single carbon-carbon bond in a hydrophobic chain can rotate about its axis, which yields a large space of possible conformations for the chain. This rotation degree of freedom is excited at ambient temperature, as the energy barrier between two different rotational states in a hydrocarbon chain is of

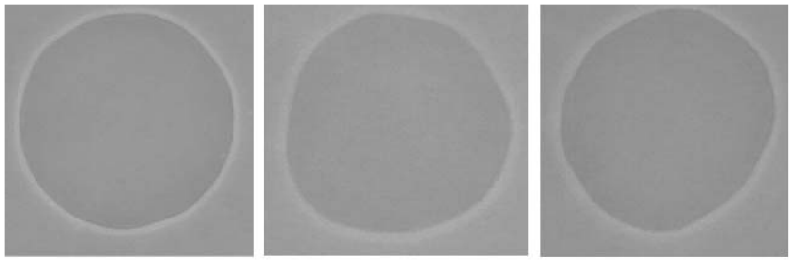

Figure 1.5: Snapshots of a giant unilamellar vesicle (i.e., a closed bilayer formed by self-assembly of lipids in water, see Fig. 1.4(c)) of diameter 50 μm observed under the microscope at different times. The vesicle constantly deforms under the effect of thermal fluctuations. *Illustration reproduced from Ref. [5].*

order $k_{\mathrm{B}}T$, where k_{B} is Boltzmann's constant and T denotes temperature. This is illustrated in Fig. 1.6.

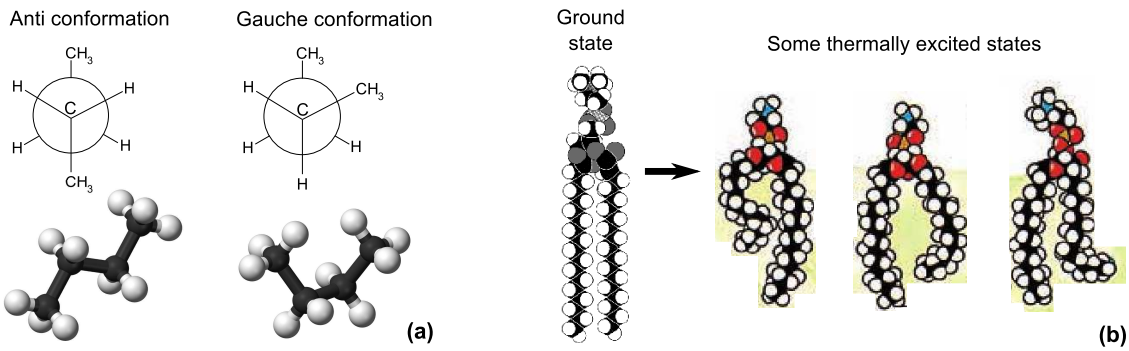

Figure 1.6: (a): Anti and gauche conformations of butane: the anti conformation has a lower energy than the gauche one (black spheres: carbon atoms; white spheres: hydrogen atoms). The energy barrier between these two conformations can be overcome by thermal fluctuations at ambient temperature. (b): Ground state and some thermally excited states of a phospholipid with two saturated chains. In the ground state, all the carbon-carbon bonds in the hydrophobic chains are in the anti conformation. Due to thermal fluctuations, these bonds can rotate towards the gauche conformation, which induces dynamical kinks in the chains. *Original illustrations from Wikimedia Commons (a) and from Refs. [5] and [1] (b), adapted and modified.*

In spite of their softness, lipid bilayer membranes are robust since they arise from self-assembly: for instance, if a small pore forms accidentally, the membrane can often self-heal thanks to the hydrophobic effect. From a biological point of view, the fact that membranes can be deformed easily while being robust is very important, since deformations of membranes are involved in many processes, such as endo- and exocytosis, transport in the cell, communication between cells, etc. In practice, membranes keep deforming dynamically during cell life [1, 5].

b. Fluidity

In 1970, Frye and Edidin fused together a mouse cell and a human cell, whose membranes contained differently fluorescently labelled antibodies. They found that the human antibodies and the mouse antibodies, which were initially located in different halves of the membrane, were homogeneously dispersed over the whole membrane forty minutes after the fusion [21]. This was the first direct evidence showing that molecules can diffuse within the cell membrane, and thus that the membrane is fluid at physiological temperature. The fluidity of membranes is deeply related to the conformational degrees of freedom of lipids, which are excited at ambient temperature, as seen in the previous Section.

In fact, each monolayer of the membrane forms a two-dimensional fluid [5]. Note that rearrangement between the two monolayers is more difficult than within a monolayer, since the hydrophilic headgroups then have to cross the hydrophobic region. This phenomenon, called flip-flop, does occur, but rarely.

Note that gel phases also exist in lipid bilayer membranes, at lower temperatures than the physiological one (see Fig. 1.7). The transition temperature from the gel phase to the fluid phase in a given membrane depends on the precise type(s) of lipid(s) involved. For instance, with the same headgroup, a phospholipid with unsaturated chains will have a lower transition temperature than one with saturated chains. Indeed, unsaturations create kinks in the chains (see Fig. 1.2), which allows for more disorder in the membrane, thus favoring the liquid phase. A similar effect exists in the more familiar case of the triglycerids we find in food: butter contains more saturated fat than olive oil, for instance.

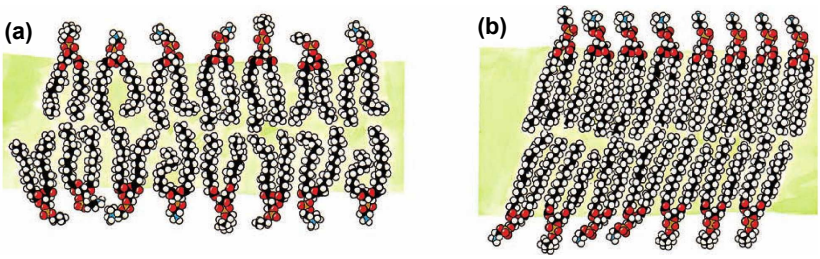

Figure 1.7: Sketches of a lipid bilayer membrane composed of saturated phospholipids. (a): Liquid phase. (b): Gel phase. *Illustration reproduced from Ref. [1].*

c. Intrinsic surface tension (or the lack thereof)

Lipid bilayers are a few nanometers thick, while the typical sizes of cells range from 1 to 100 μm. Hence, on a large scale, lipid bilayer membranes can be viewed as fluid surfaces. Usual fluid surfaces, for instance liquid-vapor interfaces, are characterized by a surface tension

$$\gamma = \left.\frac{\partial F}{\partial A}\right|_{V,N,T} , \tag{1.1}$$

where F denotes the free energy of the liquid (which is in equilibrium with its vapor), A its area (i.e., the area of the liquid-vapor interface), V its volume, N the number of molecules in it, while T denotes temperature. Here, γ arises from the fact that the liquid molecules at the interface have fewer neighbors than the ones in bulk liquid, which is unfavorable because it means fewer attractive interactions. Hence, increasing the area of the interface has an energetic cost that is proportional to the area increase, which yields γ. For a liquid-vapor interface, the value of γ is an intrinsic characteristic of the substance considered.

In the case of lipid bilayer membranes, things are different. Indeed, within the self-assembled membrane, each lipid molecule adopts an equilibrium area a_0 (we assume that all the lipids are identical for the sake of simplicity). Hence, if we consider a membrane with constant number N of molecules, the total area of the membrane is equal to its equilibrium value $A_0 = Na_0$ in the absence of external actions. As a consequence, Eq. (1.1) yields $\gamma = 0$ [5]. Qualitatively, this difference with other fluid interfaces can be understood through the fact that lipid bilayers form spontaneously, while other interfaces, such as liquid-vapor interfaces, are less favorable than the bulk and cost some energy with respect to it.

d. Elasticity

As lipid bilayer membranes have no intrinsic surface tension, their response to deformation is an elastic one. Membranes being fluid, they do not resist shearing. Hence, we are left with two different deformation modes: stretching and bending. Note that, as the specific structure of lipid bilayers involves aligned long molecules, there is an additional relevant mode of deformation, which is lipid tilt. This is reminiscent of nematic liquid crystals. We will not deal with this degree of freedom here, but it can be included in membrane descriptions [22, 23].

A stretching deformation corresponds to deforming the membrane in such a way that its area A differs from its equilibrium area A_0. To lowest order, i.e., in the harmonic approximation, the associated variation of the free energy per unit area $f = F/A$ of the membrane reads:

$$\Delta f = \frac{K_a}{2} \left(\frac{A - A_0}{A_0} \right)^2 , \tag{1.2}$$

where the constant K_a is the stretching modulus of the bilayer membrane [5].

If we consider a membrane composed of two identical monolayers, symmetry implies that its equilibrium shape will be flat. The simplest bending deformation corresponds to deforming this membrane in such a way that it becomes a piece of cylinder with radius R, the initial radius in the plane shape being infinity. In the harmonic approximation, we then have:

$$\Delta f = \frac{\kappa}{2} c^2 , \tag{1.3}$$

where the constant κ is the bending modulus of the bilayer membrane. We have also introduced the curvature $c = 1/R$ of our cylinder. We will see in the next

Section that two distinct bending moduli are in fact necessary to describe a general deformation of the membrane. However, the one introduced here, κ, usually plays the most important part.

Let us now see in more detail how lipid bilayer membranes and their deformations can be described from a physical point of view. We will present the two main models used to describe the physics of lipid bilayer membranes. These models are continuum models, in which membranes are considered as mathematical surfaces: this means that membrane thickness is neglected. Hence, these coarse-grained models are only valid at length scales larger than the thickness of the membrane, which is a few nanometers. In spite of this restriction in their domain of validity, such models are very useful since the characteristic radius of cells and vesicles is much larger than the thickness of the membrane. Note that, in these coarse-grained descriptions, the fluctuations occurring at length scales smaller than the membrane thickness are already integrated over. This means that the effective Hamiltonians we will introduce do not strictly correspond to energy: they contain an entropic part.

1.3.2 The Helfrich model

a. The Helfrich Hamiltonian: curvature energy

The first comprehensive physical model of lipid bilayer membranes was elaborated by Helfrich in 1973 [24]. In the literature, it is either called the Helfrich model, or the Canham–Helfrich model[3], or the spontaneous curvature (SC) model. In this model, only bending deformations are accounted for. Helfrich's initial argument for neglecting stretching was that "a bilayer is capable of exchanging lipid molecules with its environment", so that stretching effects only last a limited time [24]. This argument can be questioned in general, given the very low solubility of lipids in water, but there are many relevant cases in which the system studied can exchange lipids with its environment. For instance, if we focus on a patch of membrane with fixed projected area, the rest of the vesicle will play the part of a lipid reservoir for this system. Conversely, if we work on a whole vesicle, which can be considered as a closed system with a fixed number of lipids, disregarding stretching corresponds to working at fixed area A, i.e., it amounts to restricting to vesicles shapes such that $A = A_0$. In his original work, Helfrich calculated the total curvature energy of a spherical vesicle using his model, and showed that such an energy would yield negligible stretching or tilting [24]. Let us follow Helfrich and focus on bending deformations, i.e., on membrane curvature.

The local curvature of a two-dimensional surface embedded in three-dimensional space can be described mathematically by a second-order tensor (hence, it can be represented by a 2×2 matrix). Let us denote by c_1 and c_2 the two eigenvalues of this tensor, which are called the principal curvatures (see Fig. 1.8). The trace $c = c_1 + c_2$ and the determinant $c_1 c_2$ of the curvature tensor are independent of the

[3] In 1970, Canham minimized the functional $\int_A dA \left(c_1^2 + c_2^2\right)$ to find the equilibrium shape of a red blood cell [25]. In the particular case of a homogeneous membrane with fixed topology and with two identical monolayers, this is equivalent to minimizing the Helfrich Hamiltonian Eq. (1.4).

frame: they are the two invariants of the curvature tensor [26, 27]. They are called the total curvature and the Gaussian curvature, respectively. Since the energy of the membrane must not depend on the frame chosen (in other words, it is a scalar), it can only depend on c and $c_1 c_2$.

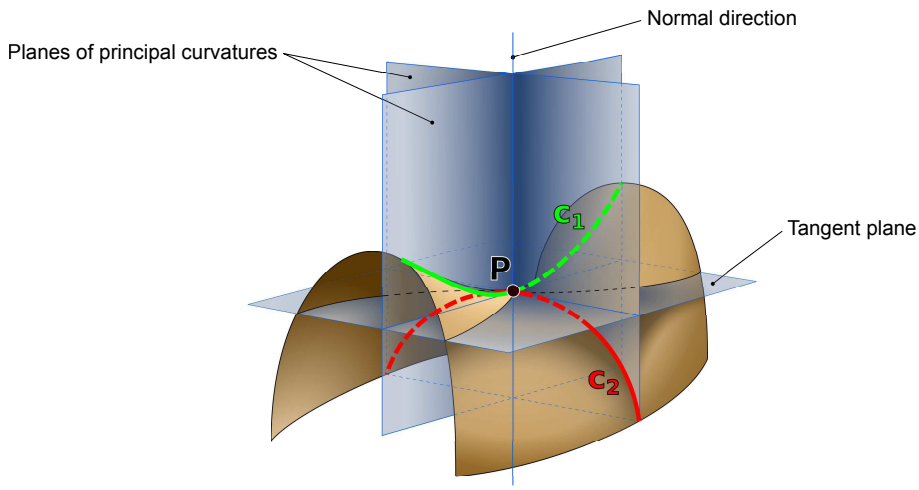

Figure 1.8: Sketch representing the principal curvatures c_1 and c_2 at a saddle point P on a surface. *Original illustration from Wikimedia Commons, adapted and modified.*

Helfrich wrote the effective Hamiltonian H of the membrane as:

$$H = \int_A dA \left[\frac{\kappa}{2} (c - c_0)^2 + \bar{\kappa}\, c_1 c_2 \right] , \tag{1.4}$$

where κ is the bending rigidity of the membrane, while $\bar{\kappa}$ is its Gaussian bending rigidity, and c_0 is called the "spontaneous curvature" of the membrane [24]. For a homogeneous membrane, κ, $\bar{\kappa}$ and c_0 are constants. Eq. (1.4) corresponds to the most general quadratic bending energy. Since stretching is disregarded in this model, the total area A of the membrane is fixed.

Remark on the "spontaneous curvature" c_0. The quantity c_0 characterizes the preferred curvature of the membrane, which depends on the differences between its two monolayers. For a symmetric bilayer, composed of two identical monolayers, c_0 vanishes. Let us see precisely in which respects c_0 is the spontaneous curvature of a membrane. The membrane being fluid, it is natural to assume isotropy within each monolayer. Hence, if we consider an isolated membrane with large fixed area A, it will assume the shape of one or several spheres[4] of radius R: in this case, $c_1 = c_2 = 1/R$. Minimizing the Helfrich Hamiltonian with respect to R for this system yields its preferred radius R_p or, equivalently, the corresponding preferred total curvature $c_p = 2/R_p$. There is a minimum at finite c_p only if $2\kappa + \bar{\kappa} >$

[4]Note that we restrict to shapes without free edges to avoid including line tension effects. Thus, we do not consider intermediate cases with a non-integer number of spheres. However, in the thermodynamic limit, the discreteness of the number of spheres is not a problem.

0: this is a stability condition for the membrane. In this case, we obtain $c_p = 2\kappa\, c_0/(2\kappa + \bar{\kappa})$. Owing to the traditional name "spontaneous curvature", we might have expected to obtain $c_p = c_0$. This is not exactly the case due to the contribution of Gaussian curvature: the traditional expression "spontaneous curvature" can thus be somewhat misleading, which is why we have put it between quotation marks until now. However, since c_p is proportional to c_0, the constant c_0 does characterize the preferred curvature of the system, even if it is not strictly equal to it. We will drop the quotation marks in the following to be consistent with standard denominations.

Remark on the contribution of the Gaussian curvature. In the case of a homogeneous membrane, $\bar{\kappa}$ is a constant, so that the contribution of the Gaussian curvature to the Helfrich Hamiltonian in Eq. (1.4) reads $\bar{\kappa} \int_A dA\, c_1 c_2$: it is proportional to the integral of the Gaussian curvature over A. The Gauss-Bonnet theorem states that the integral of the Gaussian curvature over a closed surface only depends on the topology of this surface, and that, for an open surface, this integral can be rewritten as a boundary term [28]. As a consequence, the Gaussian curvature term can often be disregarded because it remains constant. It is the case if one focuses on a closed vesicle which does not undergo any change of topology (i.e., roughly speaking, if no holes are formed). It is also the case if one studies a patch of membrane with fixed boundary conditions.

b. Small deformations with respect to the plane shape

In this thesis, we will often focus on the small deformations of a membrane with respect to the plane shape. It is then convenient to describe the membrane in the Monge gauge, i.e., by its height $z = h(x, y)$ with respect to a reference plane, x and y being Cartesian coordinates in the reference plane (see Fig. 1.9). The small deformations we consider are those such that $\partial_i h = \mathcal{O}(\epsilon)$ and $e\, \partial_i \partial_j h = \mathcal{O}(\epsilon)$ where $i, j \in \{x, y\}$, while ϵ is a small dimensionless quantity and e represents the thickness of the membrane.

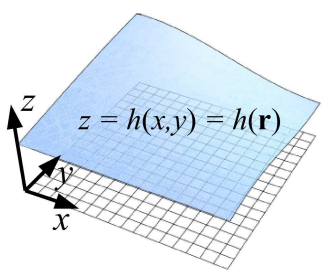

Figure 1.9: Monge gauge: the blue surface, representing the membrane, is characterized by its height $z = h(x, y)$ with respect to a reference plane. The squared zone corresponds to the projection of the blue membrane patch on the reference plane.

For such small deformations, the curvature tensor K of the membrane reads, to second order in ϵ [27]:

$$K = \begin{pmatrix} \partial_x^2 h & \partial_x \partial_y h \\ \partial_x \partial_y h & \partial_y^2 h \end{pmatrix} . \tag{1.5}$$

Hence, to second order in ϵ, the total curvature is $c = \operatorname{Tr} K = \nabla^2 h$, while the Gaussian curvature is $c_1 c_2 = \det K = \partial_x^2 h \partial_y^2 h - (\partial_x \partial_y h)^2$. The latter will be noted $c_1 c_2 = \det(\partial_i \partial_j h)$. The Helfrich Hamiltonian (see Eq. (1.4)) can thus be rewritten

$$H = \int_{A_p} dxdy \left[\frac{\kappa}{2} \left(\nabla^2 h - c_0 \right)^2 + \bar{\kappa} \det(\partial_i \partial_j h) \right] . \tag{1.6}$$

In this equation, the integral runs over the projected area A_p of the membrane, i.e., on the projection on the reference plane of the real area A of the membrane patch we consider (for instance, in Fig. 1.9, it corresponds to the area of the squared surface). While A is the real area of the membrane and includes dynamical undulations due to thermal fluctuations, its projection A_p does not include them. The effective Hamiltonian Eq. (1.6) is convenient to work at fixed projected area A_p, but not to work at fixed area A. It is thus necessary to be careful about A, especially since the Helfrich model disregards stretching.

We have seen that disregarding stretching can be interpreted in two distinct ways, depending on the system studied:
(i) If the system is in contact with a reservoir of lipids, stretching does not play any part.
(ii) If the system has a fixed number of molecules, neglecting stretching amounts to restricting to configurations such that $A = A_0$.
In case (i), the appropriate thermodynamic ensemble is the one where the number N of molecules is free to fluctuate while a chemical potential μ is imposed to the system. Hence, the appropriate effective Hamiltonian is $H' = H - \mu N = H + \sigma A$, where we have introduced the effective "tension" $\sigma = -\mu/a_0$ of the reservoir of lipids, a_0 being the area per lipid, which is constant here [29]. In addition, we work at fixed projected area A_p. At equilibrium, H' is minimal with respect to A, which yields the equilibrium area $A_{\text{eq}}(\sigma, A_p)$, through

$$\sigma = - \left. \frac{\partial H}{\partial A} \right|_{A_p} (A = A_{\text{eq}}) . \tag{1.7}$$

In case (ii), it is necessary to account explicitly for the constraint that $A = A_0$ when working with the Hamiltonian in Eq. (1.6). For this, we can introduce a Lagrange multiplier σ. Then, the function $H' = H + \sigma A$ can be minimized with respect to A, which yields Eq. (1.7). Here, this equation yields the value σ such that $A_{\text{eq}}(\sigma, A_p) = A_0$: this value of the Lagrange multiplier σ is the effective "tension" of the system for $A = A_0$. Another way of obtaining the value of σ as a function of A_0 and A_p, which is often easier to use in practice, is to write explicitly the constraint $A = A_0$ as a function of σ and A_p.

Hence, in both cases, the appropriate effective Hamiltonian is $H' = H - \sigma A$. To second order, and discarding the term $(\sigma - \kappa c_0^2/2) A_p$, which is constant since we

work at fixed A_p, H' can be expressed as

$$H' = \int_{A_p} dxdy \left[\frac{\sigma}{2}\left(\boldsymbol{\nabla} h\right)^2 + \frac{\kappa}{2}\left(\nabla^2 h\right)^2 - \kappa c_0 \nabla^2 h + \bar{\kappa}\,\det(\partial_i \partial_j h)\right] , \tag{1.8}$$

where we have used the relation

$$dA = dxdy\sqrt{1 + \left(\boldsymbol{\nabla} h\right)^2} = dxdy\left[1 + \frac{\left(\boldsymbol{\nabla} h\right)^2}{2} + \mathcal{O}(\epsilon^2)\right] . \tag{1.9}$$

The "tension" σ that appears in H' is not a surface tension intrinsic to the membrane [29]: we have seen in Sec. 1.3.1 that this quantity, γ, vanishes in the case of the membrane. Instead, σ is a parameter that depends on the precise conditions: in case (i), it depends on the chemical potential of the lipid reservoir which is in contact with the system, and in case (ii), it depends on the fixed area A_0 and on the projected area A_p.

Note that the effective Hamiltonian in Eq. (1.8) can also be obtained directly from field theoretical arguments. To second order in ϵ, it is indeed the most general scalar that depends locally on the field h and on its first and second-order derivatives, while complying with the symmetries of the system. Here, the symmetry that must be taken into account is a translational symmetry: the energy of the membrane must not change if h is replaced by $h + C$, where C is a constant [29].

c. Experiments and orders of magnitude

Several experimental methods have been used to test the Helfrich model and to evaluate experimentally the values of the membrane elastic constants κ, σ and K_a. These experiments are conducted on giant unilamellar vesicles (GUVs), i.e., model lipid bilayer membranes, rather than on cells, since they aim at testing a model of pure lipid bilayers.

Contour analysis experiments. In these experiments, introduced by Servuss, Harbich and Helfrich in 1976 [30], the contour of a lipid vesicle is monitored under the microscope during some time, and analyzed in order to obtain the fluctuation spectrum of this contour (see Fig. 1.10(a)). The spectrum of the thermal fluctuations of a lipid bilayer membrane can be predicted using the Helfrich model. Considering a symmetric bilayer, we have $c_0 = 0$. Besides, since the vesicle is closed and does not undergo any topological change, the Gaussian curvature contribution can be omitted (see above). It was shown in Ref. [31] that the fluctuation spectrum of a quasi-spherical vesicle can be approximated satisfactorily by that corresponding to a quasi-flat membrane. In the case of small fluctuations with respect to a flat shape, we can use the effective Hamiltonian Eq. (1.8) with $c_0 = 0$ and $\bar{\kappa} = 0$ to describe the fluctuations:

$$H' = \frac{1}{2}\int_{A_p} dxdy \left[\sigma\left(\boldsymbol{\nabla} h\right)^2 + \kappa\left(\nabla^2 h\right)^2\right] = \frac{1}{2}\sum_{\boldsymbol{q}} |\hat{h}(\boldsymbol{q})|^2 \left[\sigma q^2 + \kappa q^4\right] . \tag{1.10}$$

In this formula, the sum runs over the two-dimensional wave vectors $\boldsymbol{q} = (q_x, q_y) = 2\pi A_p^{-1/2}(n_x, n_y)$ where $(n_x, n_y) \in \mathbb{N}^2$. In addition, $\hat{h}(\boldsymbol{q}) = A_p^{-1/2} \int_{A_p} d\boldsymbol{r}\, h(\boldsymbol{r}) e^{-i\boldsymbol{q}\cdot\boldsymbol{r}}$, with $\boldsymbol{r} = (x, y)$, denotes the Fourier coefficient of h corresponding to the wave vector $\boldsymbol{q}$. Eq. (1.10) shows that each Fourier mode yields an independent quadratic degree of freedom in the energy. Hence, by virtue of the equipartition theorem, each of them yields a contribution $k_\mathrm{B}T/2$ to the average energy, where k_B is Boltzmann's constant and T denotes temperature. The fluctuation spectrum of the height h of the membrane is thus given by

$$\left\langle |\hat{h}(\boldsymbol{q})|^2 \right\rangle = \frac{k_\mathrm{B}T}{\sigma q^2 + \kappa q^4}\,, \tag{1.11}$$

where the brackets denote thermal average.

Given that only the fluctuations of the vesicle in the plane of its equator are experimentally accessible, what is measured is actually $< |u(q_x, y = 0)|^2 >$, where u denotes the Fourier transform of h with respect to x only. An example of the corresponding experimental spectrum, from Ref. [31], is shown in Fig. 1.10(b). By fitting this experimental spectrum to the theoretical formula derived from Eq. (1.11), one can measure the constants σ and κ involved in the Helfrich model (see Fig. 1.10(b)).

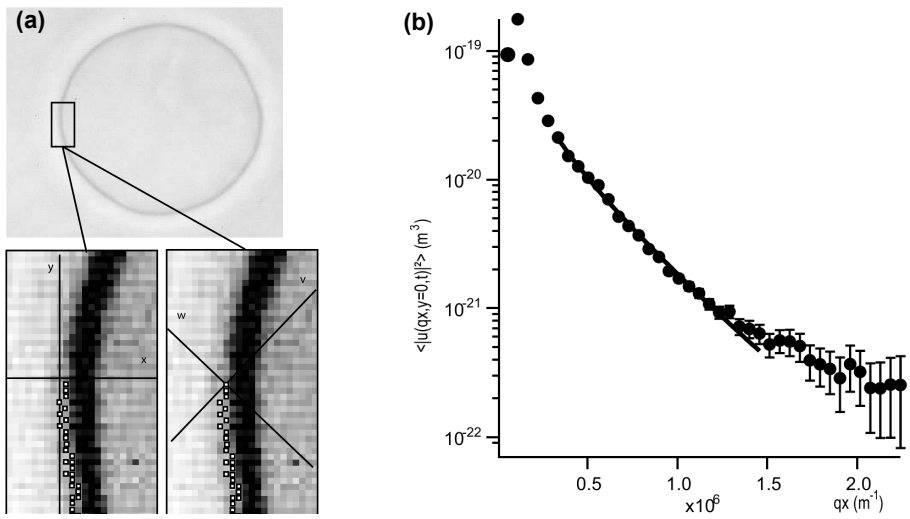

Figure 1.10: (a): High-resolution detection of the contour of a quasi-spherical GUV observed under the microscope. The shape of this contour fluctuates (see Fig. 1.5). (b): Spectrum of the shape fluctuations of a GUV, representing $< |u(q_x, y = 0)|^2 >$ versus q_x (for a SOPC vesicle). The solid line is a fit to the spectrum predicted by the Helfrich Hamiltonian. It yields a bending modulus $\kappa = 9.44 \times 10^{-20}$ J and a tension $\sigma = 1.74 \times 10^{-7}$ N/m [31]. *Illustrations reproduced from Ref. [31].*

It is important to note that microscope observations do not give access to the thermal undulations that are below optical resolution: these observations yield a coarse-grained vision of the membrane shape. As a consequence, the values

of κ and σ obtained using this method are in fact renormalized quantities, i.e., they correspond to the effective bending rigidity and the effective tension after integration over the fluctuation modes with wavelength below optical resolution. Renormalization calculations have been carried out for the bending rigidity, yielding a wavelength-dependent correction [32]: for usual vesicles, the difference between the Helfrich bending rigidity and its renormalized counterpart is of order 10% for the largest wavelengths involved, and smaller for other wavelengths. The question of the renormalization of tension is still discussed [33].

Micropipette experiments. In these experiments, introduced by Evans in the 1980s, a lipid vesicle is sucked by a micropipette. The suction pressure exerted through the micropipette can be related to the mechanical tension τ applied to the membrane through Laplace's law. When the suction (and thus τ) is increased, the apparent area of the vesicle increases too (see Fig. 1.11(a)-(b)). What we call "apparent area" is the area deduced from the vesicle contour observed under the microscope: it disregards all the thermal undulations that are below optical resolution, so it is different from the real area A of the membrane. It is similar to the projected area introduced above, so we will call it A_p.

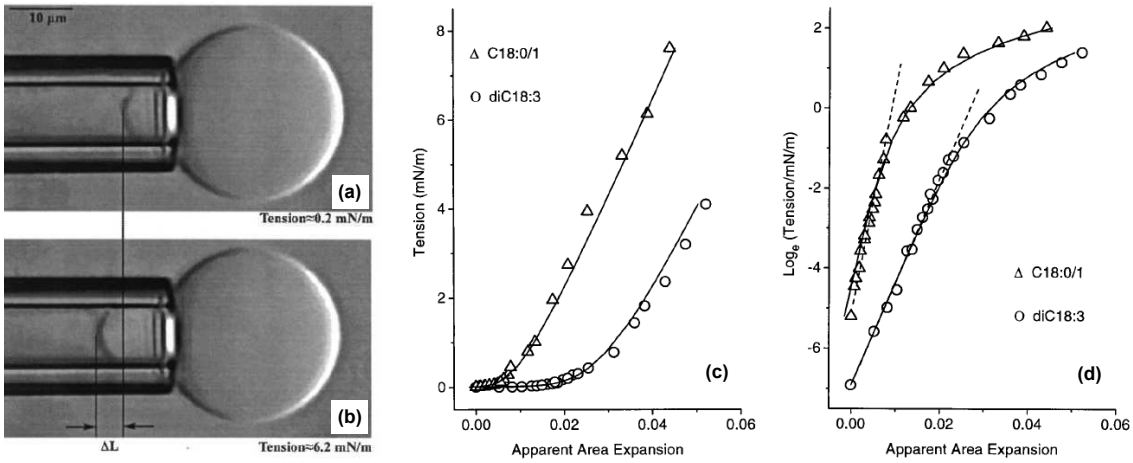

Figure 1.11: (a) and (b): Micrographs of a lipid vesicle during a micropipette experiment. The suction pressure is higher in (b) than in (a), resulting into a higher mechanical tension τ. The apparent area of the membrane increases as the vesicle is sucked inside the pipette, yielding ΔL. (c) and (d): Plots representing τ as a function of the apparent area expansion α during micropipette experiments conducted on vesicles made of two different phospholipids: "C18:0/1" contains one unsaturation in one chain while its second chain is saturated, and "diC18:3" contains three unsaturations in each chain. The slopes of the dashed lines on the semilogarithmic graph (d) yield the bending moduli: $\kappa = 9 \times 10^{-20}$ J for "C18:0/1" and $\kappa = 4 \times 10^{-20}$ J for "diC18:3". The plain lines are fits to the theory including both the Helfrich Hamiltonian and stretching. The values of K_a obtained are $K_a = 235$ mN/m for "C18:0/1" and $K_a = 244$ mN/m for "diC18:3" [34]. *Illustrations reproduced from Ref. [34].*

At small values of τ, the increase of A_p is due to the unfolding of thermal undulations, which can be related to κ using the Helfrich model for small deformations Eq. (1.8), assuming that $\tau = \sigma$. Indeed, since the area A of the vesicle is constant (noted A_0), a relation between σ, A_0 and A_p can be obtained by expressing the constraint $A = A_0$ explicitly. It can be shown to yield, in the regime of interest,

$$\frac{d\alpha}{d[\ln(\sigma)]} = \frac{k_\mathrm{B}T}{8\pi\kappa}\,, \tag{1.12}$$

where α is the relative expansion of A_p [29, 35]. At higher values of τ, the membrane gets stretched, so that K_a is involved. In the regime of high τ, where the effect of stretching is dominant, we have

$$\tau = K_a\alpha\,, \tag{1.13}$$

which corresponds to Hooke's law [5, 35]. In Fig. 1.11(c)-(d), these two asymptotic regimes can be observed: at low τ, α increases exponentially, while at high τ, it increases linearly. Hence, these experiments enable to measure κ and K_a, assuming that $\tau = \sigma$. Note however that τ is conjugate to A_p, while σ is conjugate to the area A, which implies that there are differences between these two "tensions". This subtle issue was recently investigated by Fournier and Barbetta (see Refs. [33, 36–38]).

Another interesting information obtained in micropipette experiments is the rupture tension of lipid bilayer membranes. Rupture is found to occur when τ reaches a few mN/m [34, 35].

Orders of magnitude. The experiments we have described are in good agreement with the predictions of the Helfrich model, and they give practical values for the elastic constants. We will often use the following orders of magnitude:

- $\kappa \simeq 10^{-19}$ J
- $K_a \simeq 0.1$ N/m
- $\sigma \in [10^{-8}, 10^{-3}]$ N/m

At ambient temperature $T = 300$ K, we have $\kappa \simeq 25\,k_\mathrm{B}T$: this is consistent with the fact that lipid bilayer membranes are quite soft and fluctuating, while having a definite shape (see Fig. 1.5). The value of σ can span numerous orders of magnitude, which reflects its non-intrinsic nature. In practice, spontaneously self-assembled vesicles have a tension $\sigma \in [10^{-8}, 10^{-6}]$ N/m, while higher tensions rather correspond to externally imposed tensions.

1.3.3 The area-difference elasticity model

While the Helfrich model gives a satisfactory description of many aspects of the physics of lipid bilayer membranes, it does not predict adequately the equilibrium shapes of vesicles. In experiments, vesicles prepared together assume various shapes, some tending to curve outwards and others tending to curve inwards. Such tendencies arise from an asymmetry between the two monolayers forming the membrane.

Within the Helfrich model, the only possible source of this asymmetry is the spontaneous curvature c_0, which is an intrinsic characteristic of the membrane, reflecting, e.g., a difference in the chemical composition of the two monolayers. Hence, within the Helfrich model, two vesicles prepared in the same way (i.e., formed from the same lipids, under the same external conditions) should have the same equilibrium shape [39].

An alternative model, called the bilayer-couple (BC) model, was used in the 1980s by Svetina, Žekš and co-workers to investigate the equilibrium shape of vesicles. In this model, shape is assumed to be determined by the difference $\Delta A = A^+ - A^-$ between the area A^+ of the external monolayer and the area A^- of the internal one. The area $A^\pm$ is defined on the neutral surface of monolayer $\pm$, which is the surface where the stretching and bending modes of this monolayer are decoupled [27]: since this neutral surface is at some distance from the interface between the two monolayers, ΔA can be nonzero while the membrane maintains its cohesion (i.e., no space appears beween the two monolayers). Qualitatively, a vesicle whose internal monolayer has a larger area than the external one will tend to curve inwards. The value of ΔA depends on the way the bilayer closed to form the vesicle during the self-assembly process. Hence, within a given preparation of vesicles, ΔA can vary among vesicles [5]. In the BC model, the effective Hamiltonian corresponds to Eq. (1.4) with $c_0 = 0$, and it is assumed that ΔA is fixed. This yields a constraint when minimizing the effective Hamiltonian in order to obtain the equilibrium shapes.

In reality, the asymmetry between the two monolayers of a membrane arises both from the composition of the membrane and the difference of area between the two monolayers. The model which succeeds best in predicting the equilibrium shapes of vesicles is a generalization of both the Helfrich model and the BC model, which is called the area-difference elasticity (ADE) model. The full effective Hamiltonian of the bilayer membrane can be written as:

$$H_{\mathrm{ADE}} = \int_A dA \left[\frac{\kappa}{2}\left(c - c_0\right)^2 + \bar{\kappa}\, c_1 c_2\right] + \frac{K_a}{2\,A_0}\left(A - A_0\right)^2 + \frac{K_d}{2\,A_0}\left(\Delta A - \Delta A_0\right)^2 . \quad (1.14)$$

In this expression, the first term corresponds to the Helfrich Hamiltonian Eq. (1.4), the second one to stretching (see Eq. (1.2)), while the last one literally corresponds to "area-difference elasticity", K_d being the associated elastic constant. Note that including a term quadratic in $A - A_0$ and another in $\Delta A - \Delta A_0$, as in Eq. (1.14), is equivalent to including a term quadratic in $A^+ - A_0^+$ and another in $A^- - A_0^-$. The Hamiltonian Eq. (1.14) was written in 1985 by Svetina, Brumen and Žekš in Ref. [40]. It was then fully developed and applied to the study of vesicle shapes in the 1990s by Miao, Seifert, Döbereiner and Wortis (see Refs. [39, 41]). In practice, the stretching term is generally disregarded, and the area A of the vesicle is assumed to be fixed, while variations of the area difference ΔA around ΔA_0 are accounted for [39, 41].

Qualitatively, each monolayer has a preferred area, which is fixed by the self-assembly process: the difference between them is ΔA_0. However, for this preferred area difference to be adopted, the vesicle would have to curve, which costs bending energy. The actual vesicle shape is thus determined by a compromise between

bending energy and area-difference elasticity energy.

It was shown in Ref. [39] that, within the ADE model, the equilibrium shape of a vesicle is determined by two dimensionless parameters. The first one is its reduced volume

$$v = 3\sqrt{4\pi}\ V A^{-\frac{3}{2}}\,, \tag{1.15}$$

where V is the volume of the vesicle, which is fixed by the osmotic conditions in experiments: as a consequence, the minimization of the effective Hamiltonian must be conducted at fixed V (recall that A is fixed too). Note that, for a sphere, $v = 1$. The second relevant dimensionless parameter is

$$\overline{\Delta a_0} = \Delta a_0 + \frac{g_0}{2\pi\alpha}\,, \tag{1.16}$$

with

$$\Delta a_0 = \sqrt{\pi}\,\frac{\Delta A_0}{D\sqrt{A}}\,, \quad g_0 = c_0\sqrt{\frac{A}{4\pi}}\,, \quad \alpha = \frac{1}{\pi}\,\frac{D^2 K_d}{\kappa}\,, \tag{1.17}$$

where D denotes the distance separating the neutral surfaces of the two monolayers (i.e., about half the bilayer thickness). This means that, at given v, the shape of the vesicle is determined by the combined quantity $\overline{\Delta a_0}$, which is a sum of a contribution from the preferred area difference and of a contribution from the spontaneous curvature of the vesicle. The two ingredients discussed separately in the Helfrich model and in the BC model thus contribute on the same footing to the equilibrium shape in the ADE model.

Detailed experimental study of vesicle shapes and of the characteristics of the transitions between them has shown good agreement with the phase diagram in the $\left(\overline{\Delta a_0}, v\right)$ plane predicted by the ADE model [42]. This phase diagram is shown in Fig. 1.12, together with examples of vesicle shapes.

The ADE model is currently considered the best model to describe lipid bilayer membranes [5, 43]. It is interesting to note that, while the Helfrich model considers the membrane as a mathematical surface, the refinement present in the ADE model corresponds to taking into account an effect of its bilayer structure, the area difference [44]. However, there are many cases where the Helfrich model is sufficient. For instance, if one focuses on a membrane in contact with a reservoir of lipids, the area-difference elasticity term can be disregarded. This is relevant to study a patch of membrane within a vesicle, as the rest of the vesicle plays the part of a reservoir for the patch. Hence, the Helfrich model is still widely used.

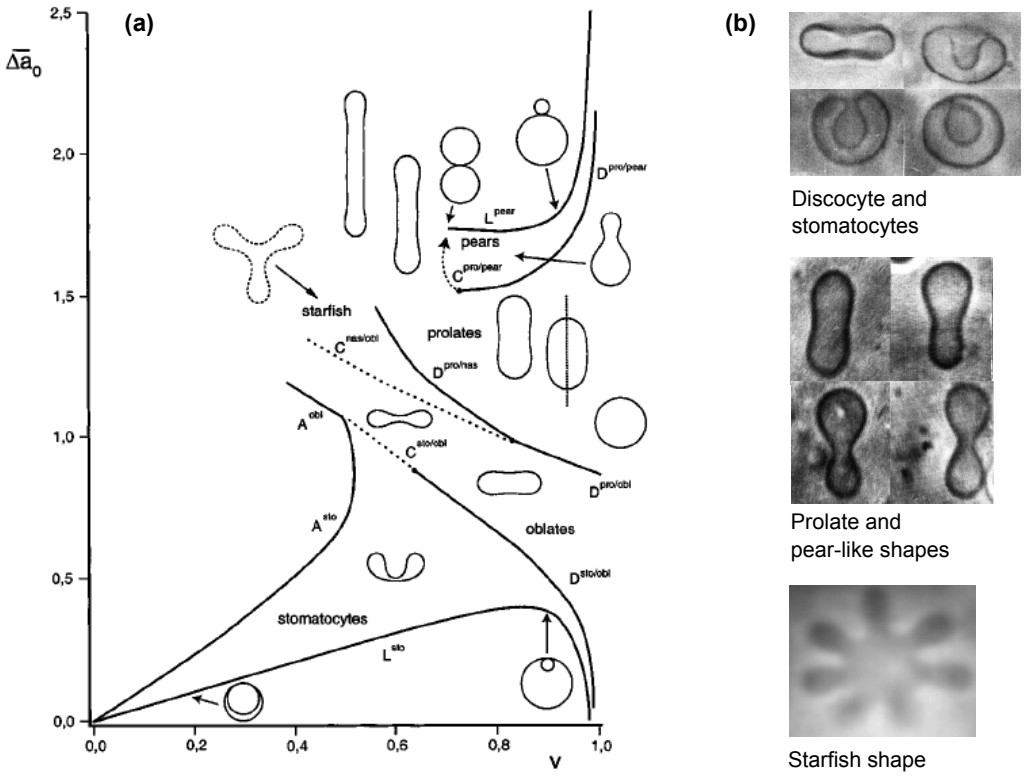

Figure 1.12: (a): Phase diagram of equilibrium vesicle shapes in the $\left(\overline{\Delta a_0}, v\right)$ plane, as predicted by the ADE model. (b): Some examples of vesicle shapes observed under the microscope. The typical dimension of the vesicles shown is of order 25 μm. *Illustrations reproduced from Ref. [43] (a) and Ref. [44] (b).*

1.4 Brief outline of this thesis

In the previous Section, we focused on the physical description of a pure homogeneous lipid bilayer membrane. However, as already stressed, within a cell, the membrane is a much more complex system. This thesis deals with some aspects of the statistics and dynamics of complex biological membranes. It starts from the physics of the pure bilayer membrane, i.e., the Helfrich model or the ADE model, to investigate some cases where a small amount of complexity is added.

Biological membranes contain many inclusions, in particular membrane proteins. These proteins deform the membrane and interact through it. In Part I, we present some contributions to the study of the Casimir-like interaction between membrane inclusions. This interaction is a generic, long-range, membrane-mediated force arising from the fact that inclusions constrain the thermal fluctuations of the shape of the membrane.

In Part II, we focus on models describing membrane elasticity at the nanoscale, which are useful to study the local deformations of the membrane in the vicinity of proteins. Studying such deformations is interesting to understand how the membrane and the proteins within it can influence each other.

Biological membranes are also submitted to an inhomogeneous and varying environment. In Part III, we present a theoretical description of an experiment where a model lipid bilayer membrane is submitted to a local pH variation, and a comparison with experimental data. Understanding the response of the membrane to local modifications of its environment, and of its pH in particular, is crucial because local pH heterogeneities are strongly related to many biological processes, such as cell motility or ATP synthesis in mitochondria.

The three parts address quite different subjects and can be read independently. While Part I is purely theoretical, Part II contains a comparison of our theoretical predictions with previously published numerical and experimental data. Finally, Part III is the result of a collaboration with the experimental group of Miglena I. Angelova and Nicolas Puff, and it contains experimental results together with a theoretical description.

The two first parts are united in that they deal with the effect of inclusions in membranes, and the two last ones in that they deal with inhomogeneities of the thickness or of the lipid density due to local perturbations.

Part I

Casimir-like interactions between two membrane inclusions

Chapter 2

Context: from the Casimir force to membrane-mediated interactions between inclusions

Contents

2.1 Introduction **30**

2.2 The Casimir force in quantum electrodynamics **30**

2.2.1 From van der Waals forces to the Casimir force 30

2.2.2 The Casimir force 33

2.3 Casimir-like forces in soft matter systems **36**

2.3.1 Casimir-like forces in critical binary mixtures 37

2.3.2 Universality of Casimir-like forces 38

2.4 Casimir-like forces in membranes **40**

2.4.1 First study 40

2.4.2 Point-like inclusions 41

2.4.3 Rod-shaped inclusions and polymers 43

2.4.4 Alternative methods to calculate Casimir-like interactions in membranes 44

2.5 Membrane-mediated interactions due to the average deformation **44**

2.5.1 First study 44

2.5.2 Further developments in the regime of small deformations 45

2.5.3 Large deformations 48

2.5.4 An experimental study 48

2.6 Outline of Part I **49**

2.1 Introduction

Biological membranes contain many inclusions, in particular membrane proteins, which have crucial biological roles. It is important to study how these inclusions interact with one another, in order to understand how they may aggregate and how they may move within the membrane. Many different interactions exist between membrane inclusions, including electrostatic interactions, steric interactions and specific chemical reactions.

A particular class of interactions is independent of the specific structure and chemistry of the inclusions. These universal interactions arise from the constraints imposed by the inclusions on the membrane shape. Indeed, because of these constraints, the free energy of the membrane containing two inclusions depends on the distance between them: an effective interaction exists between the two inclusions. This interaction is mediated by the membrane.

As inclusions are more rigid than the membrane, they impose constraints on its curvature. This is the most generic type of constraints for passive inclusions that do not impose forces or torques to the membrane (otherwise, they could impose the height or the slope of the membrane). Membrane-mediated interactions between inclusions can arise from the average deformation imposed by the inclusions to the membrane, but also from the constraints imposed by the inclusions on the fluctuations of the shape of the membrane. The latter fluctuation-induced forces are analogous to the Casimir force in quantum electrodynamics. In this introductory Chapter, we are first going to present the Casimir force. Then, we will show how analogous effects appear in soft matter systems, and finally we will focus on the case of membranes.

2.2 The Casimir force in quantum electrodynamics

2.2.1 From van der Waals forces to the Casimir force

The Casimir force is deeply linked to the van der Waals–London force. It is by studying the latter that Casimir discovered the force that now bears his name. Let us introduce briefly the Casimir force from a historical point of view, starting with van der Waals forces.

a. Van der Waals forces

In 1873, van der Waals elaborated an equation of state to account for deviations from the ideal gas law observed in the behavior of real gases. The van der Waals equation of state includes a term that corresponds to an attractive interaction between gas molecules. Experiments showed that this interaction existed in all kinds of gases. However, its origin was unknown.

In 1912, Keesom showed that an attractive interaction appears between two polar molecules or atoms separated by a distance r. Its potential is proportional to r^{-6}. This interaction arises from the electrostatic interaction between two electric dipoles, thermally averaged (with Boltzmann weights) over all relative orientations of the dipoles: the relative orientations that yield an attraction between the two dipoles are statistically favored. Keesom's result was then generalized by Debye to the case of a molecule with a permanent multipole interacting with a nonpolar molecule. Indeed, the nonpolar molecule can be polarized by the first one. However, these interactions were not general enough to explain the success of the van der Waals equation of state. Indeed, the origin of the attractive interaction in gases composed only of nonpolar atoms or molecules remained a mystery [45].

In 1930, London used quantum perturbation theory to prove the existence of an attractive interaction between two nonpolar, but polarizable, atoms [46, 47]. Its potential is proportional to r^{-6} too. This interaction is completely generic. London's result constituted one of the first major successes of quantum physics [45, 48].

In practice, these three forces are usually grouped under the name of "van der Waals forces", the van der Waals–London force being the most generic of them.

b. Casimir's study of the van der Waals–London force

Hamaker [49], Overbeek and Verwey [50, 51] explained the attractive interactions between two colloids from the van der Waals–London force between the constitutive atoms. However, their experimental results showed that the long-range decrease of this force was faster than predicted. They conjectured that it was due to the effect of retardation on the van der Waals–London force [50, 51]: since the two polarizable molecules interact electromagnetically, their interaction is not instantaneous and should involve the speed of light.

Their colleagues Casimir and Polder then studied the van der Waals–London interaction in the framework of quantum electrodynamics [52]. In 1948, they obtained a general form of the interaction between two polarizable atoms, which gives back that of London in the short-range limit, where retardation is negligible. Conversely, in the long-range limit, their result yields a potential that involves the speed of light, and that decreases in r^{-7} instead of r^{-6}. Here, "long-range" means that the distance r between the two atoms is much larger than the atomic transition wavelengths. They also studied the interaction between a polarizable atom and a perfectly conducting wall, which was simpler to calculate than the interaction between two polarizable atoms [52]. In this case too, they obtained a simple power law in the long-range, retarded regime.

c. Link with the quantum fluctuations of the electromagnetic vacuum

The simple long-range forms of the two interactions studied in Ref. [52] led Casimir to seek a fundamental explanation. Bohr suggested that there was a link with zero-point energy [45, 48]. Casimir calculated the shift in the (infinite) zero-point energy of a system constituted of a polarizable atom inside a cavity with perfectly

conducting walls, when the atom is approached to one of the walls of the cavity. Indeed, approaching the atom to the wall modifies the eigenfrequencies of the cavity, and consequently its zero-point energy. This calculation gave back the long-range limit of the interaction between an atom and a perfectly conducting wall. Casimir also recovered the long-range behavior of the interaction between two polarizable atoms from the zero-point energy shift induced by adding a second atom in the cavity [53].

This approach based on the zero-point energy was then used to recover the full interaction between two polarizable atoms at any range [54]. To do this, one considers the interaction energy between the induced dipole of the first atom and the electromagnetic field that induces this dipole. This electromagnetic field is due to vacuum fluctuations and to the radiation from the dipole of the second atom, which is itself induced by the electromagnetic vacuum fluctuations. The quantum average of this interaction in the vacuum state yields the full van der Waals–London interaction.

Hence, the van der Waals–London force is due to the correlations between the vacuum fluctuations of the electromagnetic field at the position where the first atom stands and those at the position where the second atom stands [45].

d. Quantum fluctuations and zero-point energy

Let us clarify what we mean by the quantum fluctuations of the electromagnetic vacuum and the zero-point energy [45]. The quantized electric field at position $\boldsymbol{r}$ and time t reads, for a single mode noted m (corresponding to a given wave vector $\boldsymbol{k}$ and to a given polarization):

$$\boldsymbol{E}_m(\boldsymbol{r},t) = \boldsymbol{C}_m \left[a_m e^{-i(\omega_k t - \boldsymbol{k}\cdot\boldsymbol{r})} + a_m^\dagger e^{i(\omega_k t - \boldsymbol{k}\cdot\boldsymbol{r})}\right] , \tag{2.1}$$

where we have introduced the annihilation operator a_m associated with the mode m and its hermitian conjugate the creation operator $a_m^\dagger$. Their commutator is $[a_m, a_m^\dagger] = 1$. Besides, $\omega_k = ck$, where c denotes the speed of light, and k is the norm of $\boldsymbol{k}$. The magnetic field $\boldsymbol{B}_m$ has the same form, with a different complex vectorial amplitude $\boldsymbol{C}'_m$. The Hamiltonian associated with mode m can be shown to read

$$H_m = \int_V d\boldsymbol{r} \left(\frac{\epsilon_0}{2}E_m^2 + \frac{1}{2\mu_0}B_m^2\right) = \hbar\omega_k \left(\frac{1}{2} + a_m^\dagger a_m\right) , \tag{2.2}$$

where V is the volume of the system, ϵ_0 is the vacuum permittivity, μ_0 is the vacuum permeability, and $\hbar$ is Planck's reduced constant. This is completely analogous to a one-dimensional quantum harmonic oscillator. It can be shown that the eigenvalues of $a_m^\dagger a_m$ are the natural integers, that they are nondegenerate, and that the corresponding eigenvectors, noted $|n_m\rangle$, with $n_m \in \mathbb{N}$, verify $a_m^\dagger|n_m\rangle = \sqrt{n_m+1}|n_m+1\rangle$ and $a_m|n_m\rangle = \sqrt{n_m}|n_m-1\rangle$. The number n_m corresponds to the number of energy quanta, or *photons*, in the mode m.

The state $|0\rangle$, where there is zero photon, is called the vacuum state. In this state, the energy of the mode m of the electromagnetic field reads $\mathcal{E}_{0,m} = \langle 0|H_m|0\rangle = \hbar\omega_k/2$: this energy is called the zero-point energy of mode m. The vacuum state

$|0\rangle$ is an eigenstate of the Hamiltonian of the field, but not of the field itself. It is easy to show from Eq. (2.1) that the quantum average of the electric field of mode m in the vacuum state is $\langle 0|\boldsymbol{E}_m|0\rangle = \mathbf{0}$, but that $\langle 0|E_m^2|0\rangle \neq 0$, so that the variance of the electric field of mode m is nonzero. These vacuum fluctuations are directly linked to the zero-point energy of the field. Indeed, Eq. (2.2) yields

$$\mathcal{E}_{0,m} = \int_V d\boldsymbol{r} \left(\frac{\epsilon_0}{2} \langle 0|E_m^2|0\rangle + \frac{1}{2\mu_0} \langle 0|B_m^2|0\rangle \right) . \tag{2.3}$$

All our discussion can be easily adapted to the general case with all the field modes. In the vacuum state, where there is no photon of any mode, the average value of the electromagnetic field is zero, but its fluctuations are nonzero.

2.2.2 The Casimir force

a. Casimir's prediction

Just after interpreting the interactions between two atoms and between an atom and a mirror in terms of zero-point energy shifts, Casimir calculated the zero-point energy shift between a large cavity and a cavity where two parallel walls are closer, assuming that the cavity walls were perfectly conducting. He predicted the existence of an attractive interaction between two perfectly conducting plates in vacuum [55].

This interaction, which is now named after Casimir, exists in the absence of any charge or any imposed electromagnetic field, and at zero temperature. It is a manifestation of the boundary conditions imposed by the plates on the fluctuating vacuum electromagnetic field. The difference between the interior and the exterior of the cavity arises from the difference between the field modes that can exist inside and outside the cavity. The boundary conditions imposed by the plates on the electromagnetic field constrain its quantum fluctuation modes in such a way that the zero-point energy of the system depends on the distance between the plates. An illustration of this effect is provided in Fig. 2.1, focusing on a component of the electromagnetic field that must vanish on the two perfectly conducting plates (e.g., the tangential component of the electric field).

In 1956, Lifshitz elaborated a macroscopic theory of the forces between two planar dielectrics, which gives back Casimir's result in the limit of perfect conductors [45, 56].

b. Derivation of the Casimir force

Let us present a simple derivation of the Casimir force between two perfectly conducting plates [45], in the spirit of the original paper Ref. [55]. The crucial point is to identify the field modes that can exist inside the cavity constituted by the two plates. As the two plates are perfect conductors, the tangential component of the electric field must vanish on the plates. Assuming that one plate is in the $x = 0$ plane and the second one in the $x = d$ plane, the wave vectors $\boldsymbol{k}$ allowed are such that $k_x = n\pi/d$, $n \in \mathbb{N}$ (see Fig. 2.1). In the other directions, we consider, for

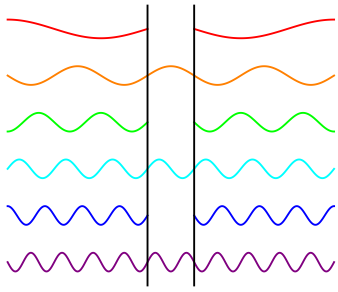

Figure 2.1: Qualitative view of the Casimir effect. Since the field must vanish on the two walls (represented by the black vertical lines in this two-dimension sketch), only certain field modes can exist inside the cavity, while no such restrictions apply outside the cavity. Hence, the zero-point energy of the system depends on the distance between the two walls.

instance, that there are perfectly conducting planar boundaries too, but that they are far enough to consider a continuum of modes. Let us call L the distance between these boundaries, which verifies $L \gg d$: the surface of our two interacting plates is then L^2. A sketch of this geometry is presented in Fig. 2.2.

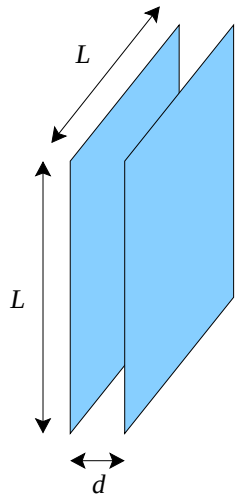

Figure 2.2: Geometry: two square plates of surface L^2, separated by a distance $d \ll L$.

As shown above, the zero-point energy of the mode with wave vector $\boldsymbol{k}$ and polarization p reads $\hbar\omega_k/2$, with $\omega_k = ck$. Hence, the zero-point energy $\mathcal{E}_0$ of the electromagnetic field inside the cavity reads:

$$\begin{aligned}\mathcal{E}_0(d) &= \sum_{\boldsymbol{k},p} \frac{\hbar c k}{2} = \frac{\hbar c\, L^2}{\pi^2} \sum_{n\in\mathbb{N}}{}' \int_0^{+\infty} dk_y \int_0^{+\infty} dk_z \sqrt{\frac{n^2\pi^2}{d^2} + k_y^2 + k_z^2} \\ &= \frac{\pi^2 \hbar c\, L^2}{4\, d^3} \sum_{n\in\mathbb{N}}{}' \int_0^{+\infty} du\, \sqrt{n^2 + u}\,, \end{aligned} \tag{2.4}$$

where the notation $\sum'$ means that the term corresponding to $n = 0$ in the sum has to be multiplied by $1/2$. Indeed, it can be shown that there are generally two

independent polarizations for each wave vector $\boldsymbol{k}$, but only one for the modes with vanishing n. In the last line, we have introduced $u = (k_y^2 + k_z^2)d^2/\pi^2$, and we have used the cylindrical symmetry of the system (which holds for $L \to \infty$).

The vacuum energy expressed in Eq. (2.4) is infinite. To make it finite, let us introduce a regularizing function f such that $f(k) = 1$ for $k \ll k_c$ and $f(k) = 0$ for $k \gg k_c$ where k_c plays the part of a cutoff. The regularized vacuum energy $\tilde{\mathcal{E}}_0$ reads

$$\tilde{\mathcal{E}}_0(d) = \frac{\pi^2 \hbar c\, L^2}{4\, d^3} \sum_{n\in\mathbb{N}}{}' F(n,d)\,, \tag{2.5}$$

where we have introduced

$$F(n,d) = \int_0^{+\infty} du\, f\left(\frac{\pi}{d}\sqrt{n^2+u}\right)\sqrt{n^2+u} = \int_{n^2}^{+\infty} du\, f\left(\frac{\pi}{d}\sqrt{u}\right)\sqrt{u}\,. \tag{2.6}$$

For real materials, it is in fact necessary to include such a function f, given that the assumption of perfect conduction breaks down at small wavelengths. For instance, if the conductor is described by the plasma model, $k_c \approx \omega_p/c$, where ω_p denotes the plasma frequency and c the speed of light. The Casimir interaction energy between the two plates is given by the difference

$$U(d) = \tilde{\mathcal{E}}_0(d) - \lim_{d\to\infty} \tilde{\mathcal{E}}_0(d)\,, \tag{2.7}$$

which corresponds to the energy needed to approach the plates from infinity to a separation d. For $d \to \infty$, the discrete values of k_x can be replaced by a continuum, as for k_x and k_y. Hence, we have

$$\lim_{d\to\infty} \tilde{\mathcal{E}}_0(d) = \frac{\pi^2 \hbar c\, L^2}{4\, d^3} \int_0^{+\infty} dn\, F(n,d)\,. \tag{2.8}$$

Combining Eqs. (2.5, 2.7, 2.8) yields

$$U(d) = \frac{\pi^2 \hbar c\, L^2}{4\, d^3}\left[\frac{1}{2}F(0,d) + \sum_{n=1}^{+\infty} F(n,d) - \int_0^{+\infty} dn\, F(n,d)\right]. \tag{2.9}$$

This expression can be simplified by using the Euler-Maclaurin sum formula, which gives

$$U(d) = \frac{\pi^2 \hbar c\, L^2}{4\, d^3}\left[-\frac{1}{12}\frac{\partial F}{\partial n}(0,d) + \frac{1}{720}\frac{\partial^3 F}{\partial n^3}(0,d) + \text{h.d.}\right], \tag{2.10}$$

where the shorthand "h.d." symbolizes a linear combination of higher order derivatives of F with respect to n, evaluated in $(0,d)$. Eqs. (2.6) yields $\partial F/\partial n\,(n,d) = -2n^2 f(\pi n/d)$. Recall that the regularizing function f is such that $f(k) = 1$ for $k \ll k_c$ and $f(k) = 0$ for $k \gg k_c$. Hence, assuming that f is sufficiently regular, it verifies $\partial^p f/\partial n^p\,(0,d) = 0$ for all $p \geq 1$, which entails $\partial^p F/\partial n^p\,(0,d) = 0$ for all $p \geq 4$, so that our "h.d." term vanishes. Finally, we obtain:

$$U(d) = -\frac{\pi^2 \hbar c\, L^2}{720\, d^3}\,. \tag{2.11}$$

This interaction potential is finite and independent of the regularization. Moreover, it does not depend on any specific property of the material of the plates, provided that this material can be considered a perfect conductor for sufficiently large wavelengths. This universal interaction potential involves the fundamental constants $\hbar$ and c, which testifies of its quantum electrodynamic origin.

The attractive force that derives from this potential is the Casimir force. It reads

$$f_C(d) = -\frac{\partial U}{\partial d}(d) = -\frac{\pi^2 \hbar c\, L^2}{240\, d^4}\,. \tag{2.12}$$

This force is proportional to the surface of the plates L^2. This comes from taking the large L limit, i.e., from neglecting the edges of the plates. Hence, it is convenient to introduce the "Casimir pressure" $|f_C|/L^2$. For this Casimir pressure to reach the atmospheric pressure, one needs to approach two plates at a distance $d \approx 10$ nm[1]. The Casimir force is a manifestation of the zero-point energy of the electromagnetic vacuum. As such, its very existence was first questioned. However, the Casimir force has been now measured experimentally with a very good precision (see, e.g., Refs. [58, 59]).

The Casimir force is particularly relevant at small length scales, and can for instance make small parts stick together in nano- and micro-electromechanical systems (NEMS and MEMS), a phenomenon called "stiction" [60, 61]. Apart from such applications, studying the Casimir effect could provide information of fundamental interest. Indeed, many theoretical models that attempt to unify the fundamental interactions predict the existence of new forces at the nanometer to micrometer range. Looking for experimental evidence of such effects involves accounting very precisely for the Casimir force, which is dominant at this scale [61].

2.3 Casimir-like forces in soft matter systems

We have seen that the Casimir force appears between two uncharged metallic plates because of the boundary conditions imposed by the plates on the quantum fluctuations of the vacuum electromagnetic field. This force is *long-range*, in so far as it decays as a power law with the distance d between the plates. In fact, the Casimir force constitutes the first historical example of a wide class of forces that arise between objects that impose constraints on a fluctuating field [62, 63]. Such forces, which we will call "Casimir-like forces", are especially relevant in soft matter systems, where thermal fluctuations play an important part. In this case, the thermal fluctuations of the medium play the part of the quantum fluctuations of the vacuum electromagnetic field in the Casimir force. If the fluctuating medium has long-range correlations, the Casimir-like forces are long-range too (i.e., in practice, they decay as power laws with the distance between the interacting objects). This is the case for critical systems.

[1] For distances smaller than 100 nm, corrections to Eq. (2.12) due to optical properties and surface roughness become non-negligible [57]. Our result is a mere order of magnitude.

2.3.1 Casimir-like forces in critical binary mixtures

Casimir-like forces driven by the thermal fluctuations of a fluid medium were first discussed by Fisher and de Gennes in the context of critical binary mixtures, in Ref. [64].

A binary mixture constituted of two components A and B can be characterized by the local mass fraction $c_A(\boldsymbol{r})$ of component A at each position $\boldsymbol{r}$ in the mixture. Depending on the spatial average $\bar{c}_A$ of c_A in the mixture, and on the temperature, the binary mixture can exist either in a mixed state, where the two components are homogeneously mixed, or in a demixed, inhomogeneous state, where a zone richer in A coexists with a zone poorer in A. The phase transition between the mixed phase and the demixed phase can be characterized by the order parameter $\phi(\boldsymbol{r}) = c_A(\boldsymbol{r}) - \bar{c}_A$. Indeed, the thermal average of this quantity vanishes in the mixed phase, whereas in the demixed phase, it takes different values in the zone richer in A and in the zone poorer in A. At the critical point, where the transition between the mixed phase and the demixed phase is a second-order phase transition, the correlation length ξ of the order parameter field ϕ becomes infinite [63].

Let us assume that a solid object, or *inclusion*, is immersed in the binary mixture. Generically, the material this inclusion is made of will interact differently with the constituents A and B of the binary mixture [63]. For instance, let us assume that the inclusion shows preferential adsorption of the A molecules. This means that some configurations of the thermally fluctuating field ϕ, which feature higher values of ϕ close to the inclusion, will be energetically favored, and have a larger statistical weight. If the preferential adsorption of A (or B) is very strong, it is possible to consider that the inclusion imposes a value of ϕ on its surface, which is reminiscent of the Casimir situation where each plate imposed boundary conditions to the electromagnetic field. Let us now consider two inclusions, e.g., for simplicity, two plates separated by a distance d, as in the original Casimir geometry. The free energy of the binary liquid including the two walls depends on d if the field ϕ has significant correlations over the distance d, i.e., if $d \lesssim \xi$. Indeed, the influence of one inclusion on the field ϕ is important up to a distance ξ away from this inclusion. Hence, an effective interaction appears between the two plates, and its range is of order ξ. Generally, ξ is of the order of the range of molecular interactions, so this effective interaction is very short-range. However, when approaching the critical point where ξ diverges, this interaction becomes long-range and universal [62–65].

In Ref. [64], Fisher and de Gennes used scaling law theory in the case of finite systems in order to predict the effective interaction between two plates immersed in a critical binary mixture. They obtained the following attractive interaction potential between two identical plates, in the geometry described by Fig. 2.2:

$$U(d) \sim -k_{\mathrm{B}} T \frac{L^2}{d^2}\,, \tag{2.13}$$

where k_{B} represents Boltzmann's constant, T the temperature and L^2 the area of the plates. The notation $\sim$ denotes a scaling law, i.e., a positive numerical prefactor is understood. This formula can be recovered qualitatively. Since we expect a universal

interaction arising from thermal fluctuations, the potential can only depend on $k_\mathrm{B}T$ and on the geometrical parameters L and d. In the limit of large plates, we expect a pressure independent of the size of the plates, and hence a force proportional to L^2. Then, the dependences in d and in $k_\mathrm{B}T$ follow from dimensional analysis.

This universal and long-range effective interaction between two inclusions in a critical binary mixture is due to the constraints imposed by the inclusions on the thermally fluctuating order parameter field ϕ, which has long-range correlations. In other words, it arises from the confinement of the fluctuations of a correlated field. It is thus analogous to the Casimir force, with ϕ playing the part of the electromagnetic field and thermal fluctuations playing the part of quantum ones [62, 63]. Hence, this interaction between inclusions, which is mediated by the fluid, is often called "critical Casimir effect", "thermal Casimir effect", or "Casimir-like effect". We will use the latter denomination.

The first direct measurement of thermal Casimir-like forces was achieved recently by Hertlein and co-workers between a colloid and a surface immersed in a critical binary mixture (see Ref. [66]).

2.3.2 Universality of Casimir-like forces

a. Critical systems

In the previous section, we have introduced Casimir-like forces in the context of critical binary mixture, which corresponds historically to the first thermal Casimir-like forces which were discussed. However, such long-range fluctuation-induced forces arise between any objects that impose boundary conditions on a fluctuating field with long-range correlations [62].

In particular, Casimir-like forces can appear in all sorts of media at critical points. These forces are determined by the large-scale behavior of the critical medium and not by its microscopic details. More precisely, it can be shown using finite-size scaling theory that they only depend on the bulk universality class of the confined medium, and on the surface universality classes of the confining surfaces, which are related to the boundary conditions imposed by the surfaces on the order parameter field [65, 67]. Thus, for instance, numerical results obtained in the case the three-dimensional Ising model [67] have been used to obtain a quantitative agreement with the experiments conducted on a binary mixture [66], as the binary mixture belongs to the three-dimensional Ising universality class.

b. Other correlated media

While systems at critical points are canonical examples of media featuring long-range correlations, other correlated media exist. Long-range Casimir-like forces have been predicted to occur in soft matter systems such as liquid crystals [68, 69], fluid membranes [70–74] and fluid interfaces [75], as well as in superfluids [76, 77]. All these fluid media can be described on a large scale by effective field theories which feature long-range correlations.

The presence of long-range correlations in such systems is linked to a global continuous symmetry of the system that is spontaneously broken in the ground state of the system. The energy cost of small fluctuations around this state, and hence the effective Hamiltonian of the system, must obey the global continuous symmetry. The fluctuation modes which result are massless Goldstone modes associated with the broken continuous symmetry [62, 78, 79], which feature long-range correlations. Let us explain this in more detail in each case.

In the case of a fluid interface (e.g., a liquid-vapor interface), if the effect of gravity is neglected, the effective Hamiltonian describing small deformations with respect to the flat shape reads

$$H[\phi] = \frac{\sigma}{2} \int d\boldsymbol{r} \, [\boldsymbol{\nabla}\phi(\boldsymbol{r})]^2 \, , \tag{2.14}$$

where the field ϕ is the height of the interface, and $\boldsymbol{r} \in \mathbb{R}^2$ denotes position, while σ represents surface tension. This Hamiltonian is invariant by any translation of the interface: it verifies $H[\phi'] = H[\phi]$, where $\phi'(\boldsymbol{r}) = \phi(\boldsymbol{r}) + C$ for all $\boldsymbol{r}$, with C being any real constant [79]. This continuous symmetry is broken in an actual state: as the interface has a definite height, it is not invariant by translation. In the absence of this symmetry, e.g., in the presence of gravity, the effective Hamiltonian of the interface would read

$$\tilde{H}[\phi] = \int d\boldsymbol{r} \left\{ \frac{\sigma}{2} [\boldsymbol{\nabla}\phi(\boldsymbol{r})]^2 + \frac{m}{2} [\phi(\boldsymbol{r})]^2 \right\} \, , \tag{2.15}$$

where m is a constant: for instance, in the case of gravity, $m = \rho g$ where ρ is the mass density of the liquid and g denotes gravity. Since this theory is Gaussian, it is easy to show that the length scale $\sqrt{\sigma/m}$ sets the correlation length of the thermal fluctuations of ϕ. Hence, for $m \neq 0$, the latter have a finite range. The term $m\phi^2/2$ in $\tilde{H}$ is often called a "mass term", in analogy with quantum field theory, where such terms represent the effect of the mass m of the particles associated with the field ϕ [79]. This is why the effective Hamiltonian H in Eq. (2.14) is said to be massless. Note that, owing to the vanishing mass of the photon, the Lagrangian of the free electromagnetic field is massless, which is related to the long-range character of the quantum electrodynamic Casimir force.

Let us now consider the case of fluid membranes. On a large scale, a symmetric membrane which undergoes small deformations with respect to the flat shape can be described by the Helfrich Hamiltonian presented in Sec. 1.3.2:

$$H_m[\phi] = \int d\boldsymbol{r} \left\{ \frac{\kappa}{2} \left[\nabla^2\phi(\boldsymbol{r})\right]^2 + \bar{\kappa} \, \det[\partial_i\partial_j\phi(\boldsymbol{r})] + \frac{\sigma}{2} [\boldsymbol{\nabla}\phi(\boldsymbol{r})]^2 \right\} \, , \tag{2.16}$$

where ϕ is the height of the membrane, with $\boldsymbol{r} = (x, y) \in \mathbb{R}^2$, while κ is the bending rigidity of the membrane, $\bar{\kappa}$ is its Gaussian bending rigidity and σ is its tension. It corresponds to Eq. (1.8) for $c_0 = 0$ (since the membrane is assumed to be symmetric). This Hamiltonian is massless, and it has the same translational symmetry as H in Eq. (2.14).

Let us move on to the case of a superfluid. In states in which the phase of the wavefunction varies slowly, the Landau-Ginzburg Hamiltonian of a superfluid can be simplified to yield the effective Hamiltonian H in Eq. (2.14) [79]. In this case, the field ϕ represents the phase of the wavefunction, $\boldsymbol{r} \in \mathbb{R}^3$, and σ is a stiffness related to the superfluid density [76]. The translational symmetry then means that the energy of the system is not affected by a global shift of the wavefunction phase [62, 79].

Finally, in the case of nematic liquid crystals, the relevant field is the director, a vector that represents the local orientation of the rod-shaped molecules [68]. The relevant continuous symmetry is the rotational symmetry, which is spontaneously broken in a state where the molecules align in one arbitrary direction [62].

As all these media are described by effective field theories featuring long-range correlations, long-range Casimir-like interactions arise between inclusions immersed in them.

2.4 Casimir-like forces in membranes

2.4.1 First study

Let us now focus on the case of biological membranes. The existence of long-range Casimir-like forces between inclusions in lipid membranes was first predicted in 1993 by Goulian, Bruinsma and Pincus in Ref. [70]. In this work, the membrane was described by the effective Hamiltonian

$$H[h] = \int d\boldsymbol{r} \left\{ \frac{\kappa}{2} \left[\nabla^2 h(\boldsymbol{r}) \right]^2 + \bar{\kappa} \det[\partial_i \partial_j h(\boldsymbol{r})] \right\} , \tag{2.17}$$

where $h(\boldsymbol{r})$ is the height of the membrane at position $\boldsymbol{r} = (x, y) \in \mathbb{R}^2$ with respect to a reference plane, while κ is the bending rigidity of the membrane and $\bar{\kappa}$ is its Gaussian bending rigidity. This corresponds to the Helfrich Hamiltonian for a symmetric membrane (see Eq. (2.16)) where the contribution of the membrane tension σ is discarded. Neglecting the effect of tension is appropriate below the length scale $\sqrt{\kappa/\sigma}$. As σ is in the range 10^{-6}–10^{-8} N/m for usual floppy membranes, while $\kappa \simeq 10^{-19}$ J, this length scale is of order 1 μm. Recall that the continuum description of the membrane is valid for distances larger than a few nanometers, while the diameter of a cell or of a GUV is of order 1–100 μm. Thus, there is a wide range of relevant distances, below the micron, to which the Hamiltonian in Eq. (2.17) is adapted.

The inclusions considered in Ref. [70] have both a bending rigidity and a Gaussian bending rigidity different from that of the membrane. A zone with a small perturbation of the two rigidities can represent a phase-separated domain, with a lipid composition different from the rest of the membrane, while a very rigid zone can represent a membrane protein. Both cases are discussed in Ref. [70], in the geometry of two identical circular domains of radius a such that $a \ll d$, where d is the distance between the two inclusions. In these two situations, an interaction potential proportional to $1/d^4$ is obtained. In the perturbative case, it depends on

the perturbations of κ and $\bar{\kappa}$ in the inclusions and on the value of κ in the membrane as well as on $k_{\mathrm{B}}T$, while in the case of rigid inclusions, it simply reads

$$U(d) = -6\, k_{\mathrm{B}}T\, \frac{a^4}{d^4}\,. \tag{2.18}$$

A multipole expansion, valid for $a \ll d$, is used to calculate this interaction. This long-range attractive interaction is due to the constraints imposed by the rigid inclusions on the thermal fluctuation modes of the membrane: it is a Casimir-like interaction. Note, however, that the geometry is quite different from the standard Casimir one involving infinite plates: for $a \ll d$, it is in fact much closer to the geometry of van der Waals–London interactions. A sketch of the fluctuating membrane with two rigid inclusions is presented in Fig. 2.3.

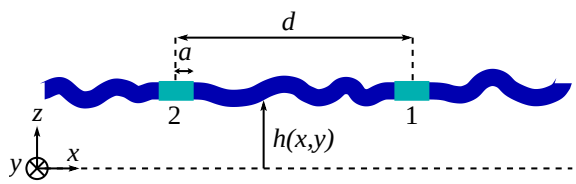

Figure 2.3: Longitudinal cut of a membrane with fluctuating shape, containing two rigid circular inclusions of radius a separated by a distance d.

While the modification of the Gaussian bending rigidity plays a crucial part in the Casimir-like interaction between perturbative inclusions [70], the Gaussian curvature term involved in the Helfrich Hamiltonian Eq. (2.17) does not contribute to membrane-mediated interactions between very rigid inclusions. Indeed, such inclusions can be treated as objects extraneous to the membrane, which impose boundary conditions to the membrane on their edge. The contribution of the Gaussian curvature term in the membrane (where $\bar{\kappa}$ is constant) depends only on the topology of the membrane and on the contact angle imposed by the inclusions, which do not depend on the distance between inclusions [80]. For this reason, in most of the subsequent studies of the Casimir-like forces between rigid membrane inclusions, the Gaussian curvature term is discarded and the following effective Hamiltonian is used:

$$H[h] = \int d\boldsymbol{r}\, \frac{\kappa}{2} \left[\nabla^2 h(\boldsymbol{r})\right]^2 , \tag{2.19}$$

instead of Eq. (2.17).

2.4.2 Point-like inclusions

The results of Ref. [70] were reproduced using different inclusion-membrane coupling models, and they were extended to anisotropic inclusions, which have an elliptic cross-section instead of a circular one[2], by Park and Lubensky in Ref. [71]. The

[2]Here, we are only dealing with in-plane anisotropy. Inclusions that break the up-down symmetry of the membrane were also considered in Refs. [70, 71]. The up-down symmetry breaking does not affect the Casimir-like force, but another force appears in addition to it. This new interaction is an elastic effect due to the average deformation of the membrane. It will be discussed in Sec. 2.5.

Casimir-like interaction obtained has the same d-dependence as Eq. (2.18), but with an anisotropic amplitude depending on the relative orientation of the two inclusions. This illustrates the crucial importance of geometry in Casimir-like forces.

In Ref. [71], it is shown that in the geometry $d \gg a$, circular inclusions can be described as point-like, giving back the results of Ref. [70]. This simplifies the calculation of the Casimir-like force, as the multipole expansion is no longer needed. Considering the inclusions as point-like is justified in the case of proteins, since the typical radius of membrane proteins is comparable to the membrane thickness, which vanishes in the coarse-grained description where the membrane is considered as a thin surface. The effective radius a of the point-like inclusions is related to the ultraviolet cutoff of the theory Λ through $\Lambda = 2/a$ [71].

This formalism of point-like inclusions was further developed by Dommersnes and Fournier in Refs. [72, 73]. Rigid inclusions that can be considered point-like impose local constraints on the curvature of the membrane. This is the most generic type of constraints in the absence of external forces or torques (otherwise, inclusions could constrain the height or the slope of the membrane). It is the point-like equivalent of the inclusions that impose a contact angle in Ref. [70]. Inclusions that impose a nonzero contact angle or local curvature also yield a membrane-mediated elastic interaction due to the average membrane deformation they impose, in addition to the Casimir-like interaction [70–73]. We will say more about this interaction in Sec. 2.5.

The case of point-like inclusions subject to external torques was considered in Ref. [73]. This may be applied to magnetic particles adhering to the membrane submitted to torques induced by a magnetic field. In this case, the Casimir-like interaction potential has a logarithmic dependence in d: it is thus much stronger than in usual cases. Note that such a logarithmic interaction potential was also predicted by Ref. [81], where point-like inclusions that constrain the membrane height were considered. Constraining the membrane height implies the presence of an external force. We note that much stronger Casimir-like attractions are obtained with such external constraints, which impose drastic conditions on the fluctuation modes, than without them.

An interesting and biologically relevant question is whether the Casimir-like attraction between membrane proteins could play a part in protein aggregation. Eq. (2.18) shows that, while Casimir-like interactions between membrane inclusions are long-range, the interaction energy involved is quite small compared to $k_\mathrm{B}T$. For instance, if $d = 4a$, which is a small distance (recall that the calculations of Ref. [70], and all those involving point-like inclusions are relevant only for $d \gg a$), we find $U \approx 0.02\, k_\mathrm{B}T$. Hence, in this geometry, we expect that the effect of Casimir-like interactions should be weak. In Ref. [72], the aggregation of point-like inclusions imposing anisotropic local curvatures was investigated. The effect of the Casimir-like interaction was found to be negligible, compared to membrane-mediated elastic interactions. An experimental study of the aggregation of colloidal particles bound to biomimetic lipid membranes is presented in Ref. [82]. In this study, only the effect of a short-range force driving the aggregation is observed. However, in Ref. [83], aggregation induced by Casimir-like interactions was found to occur in Monte-Carlo

simulations, which shows that these interactions may be relevant for aggregation if the other interactions are not too strong.

2.4.3 Rod-shaped inclusions and polymers

The case of two very narrow rigid rods of length L, at a distance $d \gg L$ was investigated by Golestanian, Goulian and Kardar in Refs. [84, 85], yielding a Casimir-like interaction with the same d-dependence as Eq. (2.18), but with an anisotropic amplitude depending on the relative orientation of the two rods. This case is still close to the point-like case.

The more different case of semi-flexible polymers adsorbed on the membrane was studied by Golestanian in Ref. [86]. Very stiff parallel polymers correspond to rods in the limit $d \ll L$ (see Fig. 2.4), yielding a Casimir-like interaction potential $\sim -k_{\mathrm{B}}T\,L/d$ [76, 86]. Note that this geometry is the two-dimensional analogous of the standard Casimir geometry involving two plates. Two such rods tend to bend toward one another below a certain critical distance, and their interaction was found to be screened by out-of-plane fluctuations if the rigidity of the polymer is finite [86].

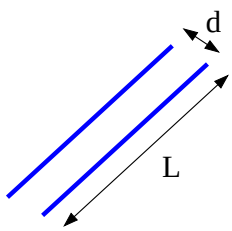

Figure 2.4: Two parallel rods of length L separated by a distance $d \ll L$.

Earlier, in Ref. [87], the effect of the reduction of the membrane fluctuations by the presence of a semiflexible (wormlike) polymer had been discussed. An effective nematic interaction was found in this work between different segments of the polymer chain orientational, and it was found that this interaction can yield an orientational ordering transition.

Recently, Ref. [88] discussed the entropic contribution to the elastic repulsion between two long cylinders adsorbed on a membrane (see next section for a discussion of such elastic interactions). Interestingly, it was found that this entropic contribution enhances the repulsion between the two cylinders, while we have seen that the usual Casimir-like interaction is attractive. The crucial difference between this situation and the ones usually studied is that here, the equilibrium shape of the membrane can be highly curved, as Ref. [88] does not restrict to small deformations.

Until now, we focused on the cases of point-like inclusions and rod-shaped inclusions that have a rigidity different from that of the membrane. The case where the membrane rigidity is heterogeneous because of heterogeneities in the composition of the membrane was investigated in Ref. [74]. The resulting fluctuation-induced interaction may be relevant to the formation of membrane domains.

2.4.4 Alternative methods to calculate Casimir-like interactions in membranes

In Ref. [89], Casimir-like interactions between membrane inclusions were studied by calculating directly the entropy of each fluctuation mode of the membrane. In this work, each possible shape of a membrane was viewed as a superposition of local mean curvature modes (in the domain of small deformations around the flat shape). A local curvature mode was represented by the configuration of a "hat" in a two-state hat model. The Casimir-like interaction Eq. (2.18) was recovered using this model.

Recently, in Ref. [90], Casimir-like interactions between circular inclusions such that $d \gg a$ were studied using a general effective field theory, both in the case of a membrane described by the Hamiltonian in Eq. (2.19), and in the case of a fluid interface described by the Hamiltonian in Eq. (2.14). This promising method yields in particular the three-body Casimir-like interactions. Note that non-pairwise additivity is a general feature of fluctuation-induced interactions, as the restriction imposed on the fluctuation modes by the presence of the different objects is complex. For instance, the existence of a three-body effect in the van der Waals–London interaction was demonstrated in Ref. [91]. In addition, the method of Ref. [90] enables to calculate systematically higher-order terms in the small variable a/d. Furthermore, it provides general scaling laws for the leading-order Casimir-like interaction in a/d between objects of arbitrary shape and internal flexibility.

Another recent work, Ref. [92], addressed the general calculation of the Casimir-like interaction in a membrane described by the Hamiltonian in Eq. (2.16), i.e., including the effect of its tension σ. The method developed in this work is an adaptation of the scattering-matrix approach developed in the context of the electrodynamic Casimir effect [93]. In particular, in the case of two circular inclusions such that $d \gg a$ similar to that of Ref. [70], the crossover between the bending-rigidity–dominated regime, where the Casimir interaction scales as $1/d^4$ (see Eq. (2.18)), and the tension-dominated regime, where it scales as $1/d^8$ [75], was investigated in Ref. [92]. Besides, by summing numerically multipolar terms, they found a result at short separations d that agrees with that obtained using the proximity force approximation [94] and the interaction between two long parallel rods [76]: the interaction potential then scales as $1/d^{1/2}$.

2.5 Membrane-mediated interactions due to the average deformation

2.5.1 First study

In addition to the Casimir-like interaction, Ref. [70] also discusses another type of membrane-mediated interaction, of elastic nature, which arises from the average deformation of a membrane due to inclusions with circular cross-sections that impose a contact angle to the membrane on their edges (see Fig. 2.5). This elastic interaction

reads

$$U'(d) = 4\pi\kappa(\alpha_1^2 + \alpha_2^2)\,\frac{a^4}{d^4}\,, \tag{2.20}$$

where α_1 and α_2 are the contact angles imposed by inclusion 1 and inclusion 2. This interaction has the same power-law behavior as the Casimir-like one in Eq. (2.18), but it is repulsive. Its different physical origin is emphasized by the absence of $k_\mathrm{B}T$: this interaction does not arise from constraints imposed on thermal fluctuations, but from the average deformation of the membrane due to the inclusions.

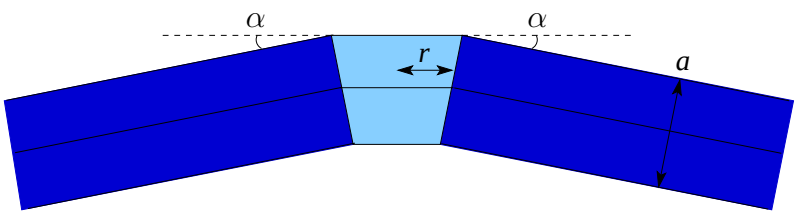

Figure 2.5: Cut of a membrane containing a conical inclusion of radius r imposing a contact angle α. This inclusion breaks the up-down symmetry of the membrane. The membrane thickness is denoted by a.

These membrane-mediated elastic interactions are very often studied together with the Casimir-like interactions. Indeed, as soon as the inclusions break the up-down symmetry of the membrane, the two interactions coexist. For instance, calculating the derivative of the membrane free energy with respect to the distance between inclusions gives the sum of these two interactions.

It is interesting to compare the strength of the elastic interactions and of the Casimir-like interactions. For two identical inclusions imposing the same contact angle α, comparing Eq. (2.18) and Eq. (2.20) shows that the two interactions have the same absolute value if

$$|\alpha| = \sqrt{\frac{3}{4\,\pi}\,\frac{k_\mathrm{B}T}{\kappa}}\,. \tag{2.21}$$

Using the typical value $\kappa \approx 25\,k_\mathrm{B}T$, we obtain $|\alpha| \approx 6°$. Beyond this quite small contact angle, the elastic repulsion overwhelms the Casimir-like attraction. Hence, the former is usually dominant over the latter in the case of inclusions that break the up-down symmetry of the membrane.

2.5.2 Further developments in the regime of small deformations

Inclusions that break the up-down symmetry of the membrane were considered in Ref. [71]. In the case of circular cross-sections (i.e., conical inclusions as in Fig. 2.5), the result Eq. (2.20) of Ref. [70] was recovered, while in the case of elliptic cross-sections, an anisotropic interaction with a potential scaling as $1/d^2$ was obtained. In Ref. [71], the case of non-transmembrane proteins was also considered: such inclusions break the up-down symmetry of the membrane. The three-body and four-body interactions were calculated in this case.

Anisotropic[3] point-like inclusions that locally constrain the curvature of the membrane by setting a preferred curvature tensor were considered in Ref. [72]. The $1/d^2$ behavior of the elastic interaction potential of Ref. [71] was recovered, and the three-body interactions were also calculated explicitly. In addition, Monte-Carlo simulations were presented in Ref. [72], showing aggregation of the anisotropic point-like inclusions induced by the elastic force (see Fig. 2.6). The shape of the aggregates depends on the curvature tensor imposed by the inclusions, with a phase diagram including compact aggregates and linear polymer-like aggregates. This study was pursued in Ref. [95], where the full N-body elastic interaction was discussed analytically, and where anisotropic "saddle" inclusions were shown to self-assemble into an egg-carton structure in a Monte-Carlo simulation (see Fig. 2.6). This structure is reminiscent of some patterns observed in biological membranes. The influence of the long-range elastic repulsion between isotropic inclusions that break the up-down symmetry of the membrane (e.g., conical inclusions, as on Fig. 2.5) on their aggregation was also discussed in Ref. [96].

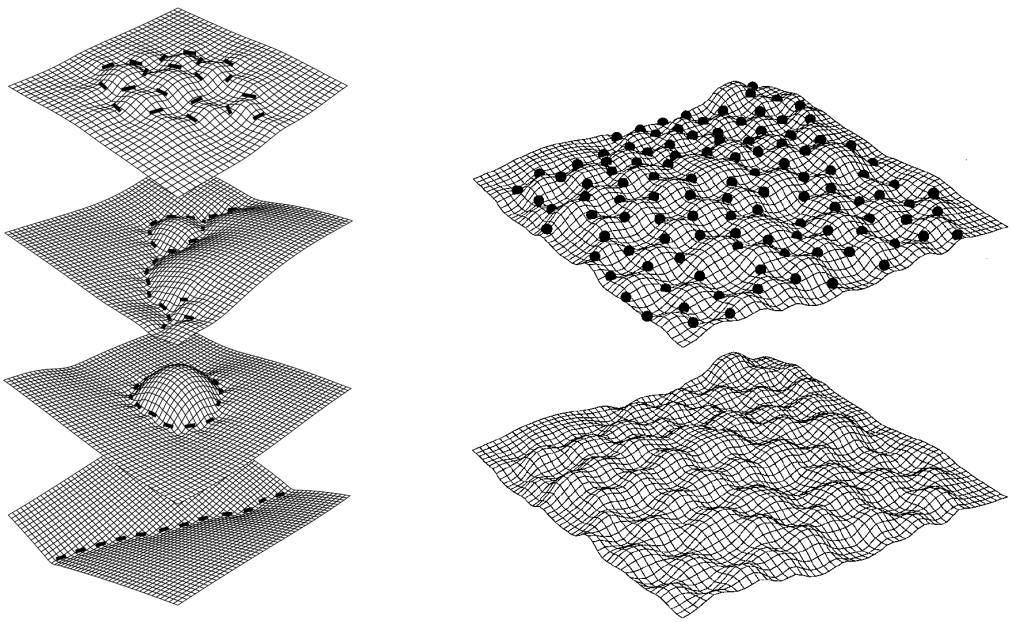

(a) Different aggregates obtained for different curvature tensors imposed by the anisotropic inclusions. Reproduced from Ref. [72].

(b) Egg-carton structure formed by anisotropic inclusions. Reproduced from Ref. [95].

Figure 2.6: Aggregation of anisotropic curvature-inducing inclusions on a membrane. Snapshots from the equilibrium configurations obtained via Monte-Carlo simulations.

The elastic interaction between rigid inclusions that set a contact angle to the membrane of a spherical vesicle was considered in Ref. [97]. The results obtained previously in the usual case of a quasi-flat membrane were recovered at separations

[3] In general, both in-plane anisotropy and up-down symmetry breaking are involved for point-like inclusions that locally impose a curvature tensor to the membrane.

small with respect to the radius of the vesicle, while the elastic interaction was found to be enhanced in the case where the spherical shape of the vesicle becomes relevant.

Ref. [73] focused on the effect of external torques on the elastic interaction between isotropic point-like inclusions that locally constrain the curvature of the membrane. As the Casimir-like interaction, the elastic interaction is enhanced in the presence of external torques that constrain the orientation of the inclusions.

The effect of membrane tension on the elastic interaction between inclusions imposing a contact angle to the membrane was investigated in Ref. [98]. In the presence of tension σ, the elastic interaction was found to be exponentially suppressed for large $d/\sqrt{\kappa/\sigma}$. Recall that, conversely, the Casimir-like interaction remains long-ranged (with a potential in $1/d^8$) in the presence of tension, even if it is weaker than in the bending-rigidity–dominated case (where the potential scales as $1/d^4$). Ref. [98] also shows that in the presence of tension, the elastic interaction depends on the orientations of the inclusions with respect to the membrane plane, which was not the case for vanishing tension (see Eq. (2.20), where only the absolute values of α_1 and α_2 are relevant). For oppositely oriented inclusions (i.e., when α_1 and α_2 have opposite signs), the interaction was found to change from repulsive to attractive as d increases, while the interaction between equally oriented inclusions was found to be repulsive at all distances. Conversely, in the absence of tension, the elastic interaction Eq. (2.20) is always repulsive.

A summary of the various interaction laws mentioned here is provided in Table 2.1, which includes both the Casimir-like interaction and the elastic one.

Geometry	Casimir-like interaction energy Attractive	Elastic interaction energy Repulsive – Vanishes in up-down symmetric cases
Point-like inclusions: $d \gg a$ Isotropic cross section	$\sim 1/d^4$ [70–72]	$\sim 1/d^4$ [70–72]
Point-like inclusions: $d \gg a$ Anisotropic cross section	$\sim 1/d^4$ [71, 72] Anisotropic	$\sim 1/d^2$ [71, 72] Anisotropic
Rods of length L $d \gg L$	$\sim 1/d^4$ [84, 85] Anisotropic	
Parallel rods of length L $d \ll L$	$\sim 1/d$ [85]	
Tension-dominated case Point-like inclusions: $d \gg a$ Isotropic cross-section	$\sim 1/d^8$ [75]	No long-range interaction
Tension-dominated case Parallel rods of length L $d \ll L$	$\sim 1/d$ [75]	

Table 2.1: Summary of the power laws obtained for the Casimir-like and the elastic interactions as a function of the separation d between the inclusions, in the regime of small deformations. All the results presented correspond to the bending-rigidity–dominated case, apart from the two last lines. Note that the elastic interaction vanishes for inclusions that respect the up-down symmetry of the membrane.

2.5.3 Large deformations

All the studies we mentioned until now focused on the domain of small deformations of the membrane, where the free energy of the membrane containing the inclusions can be calculated analytically. Different methods must be used to study membrane-mediated interactions in strongly deformed membranes. In Refs. [99, 100], it was shown formally that the membrane stress tensor in covariant formalism [101] can be used to study such problems. However, one still needs to find the equilibrium shape of the membrane in the presence of the inclusions to compute the exact elastic force between them, which is not easy in the case of large deformations. In Ref. [99], the elastic interaction between two cylinders adsorbed on a membrane was calculated in the regime of small deformations using this method. The result is in agreement with that of Ref. [102], obtained with the more standard method based on calculating the free energy of the system.

The coarse-grained membrane simulations of Ref. [103] showed that the elastic interaction between two isotropic curvature-inducing membrane inclusions can become attractive at short separations, while it is always repulsive in the regime of small deformations (see Eq. (2.20)). Hence, this elastic interaction can yield aggregation and vesiculation as soon as the inclusions deform the membrane strongly enough and are close enough. Such effects were observed in the simulations of Ref. [103] (see Fig. 2.7). In addition, the result of Ref. [103] was confirmed in Ref. [104] by a numerical minimization of the Helfrich Hamiltonian, showing that the attraction really arises from a curvature effect and not from an artifact that could be present in the simulations, which are more complex than a continuum Helfrich membrane. More precisely, this study showed that, for sufficiently large contact angles, the elastic interaction between two inclusions becomes attractive, while a good agreement with Eq. (2.20) was obtained for small deformations and large separations. To emphasize the interest of this result, let us quote Ref. [104]: "Mathematically, this flip of sign in the force law is every bit as striking as if Einstein had discovered that two masses will repel if they are really heavy."

2.5.4 An experimental study

Let us conclude this section by mentioning an experimental study related to this elastic interaction. Experimental observations of vesicles containing partially budded phase-separated lipid domains were presented recently in Ref. [105]. In this work, the interaction strength between the domains was deduced from the mean square displacement of one domain with respect to its neighbors. It was found to be consistent with the $1/d^4$ potential corresponding to the elastic membrane-mediated forces (see Eq. (2.20)).

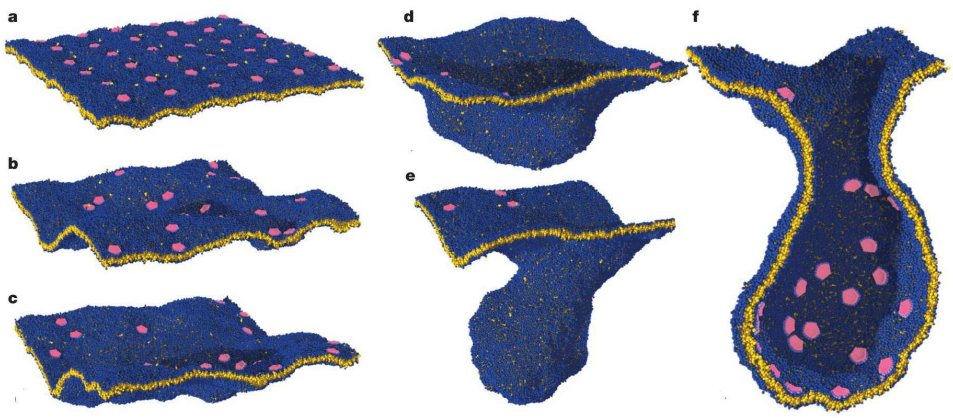

Figure 2.7: Successive snapshots of a coarse-grained simulation of a membrane with several curvature-inducing inclusions. A process of vesiculation is induced by the elastic interaction between inclusions, which becomes attractive at short separations. Reproduced from Ref. [103].

2.6 Outline of Part I

Chapters 3, 4 and 5 of this thesis deal with the Casimir-like force.

First, in Chapter 3, we study the fluctuations of the Casimir-like force between two point-like inclusions in a membrane. We show that this force is dominated by its fluctuations. Besides, we discuss the dependence of these fluctuations on the distance between the two inclusions. The case where the inclusions impose a specific nonvanishing local curvature to the membrane is treated, including the contribution of the elastic interaction.

Second, Chapter 4 deals with a more general issue, which is related to the study of the fluctuations of the Casimir-like force. In order to study the Casimir-like force beyond its thermal equilibrium value, for instance its fluctuations or its out-of-equilibrium behavior, it is necessary to define precisely the force exerted on an inclusion by the correlated fluid it is immersed in, in a microstate of this fluid. Two different definitions of this force are currently used in the literature. We have studied the respective origins of these definitions, their domains of application, and the differences they yield.

Third, Chapter 5 is devoted to the study of Casimir-like interactions between two long parallel rod-shaped membrane inclusions, which can model semiflexible polymers adsorbed on the membrane. In this geometry, the Casimir-like force is much stronger than in the case of point-like inclusions (see the power laws in Table 2.1), so it can be more relevant in practice. The prefactors of this force are calculated for four different types of rigid rods. The effect of a finite out-of-plane bending rigidity of the rods is also investigated. Besides, it is shown that a rod and a "ribbon" which impose completely antagonistic constraints repel each other. The conditions of validity of the description of polymers as rigid rods are also studied.

Chapter 3

Fluctuations of the Casimir-like force between two membrane inclusions

Contents

3.1 Introduction **52**

3.2 Basics **53**

3.2.1 Model 53

3.2.2 Partition function of the membrane containing the two inclusions 54

3.2.3 Traditional calculation of the Casimir-like force 57

3.3 Approach based on the stress tensor **58**

3.3.1 Membrane stress tensor 58

3.3.2 Average Casimir-like force 59

3.4 Variance of the Casimir-like force **62**

3.4.1 Formal expression 62

3.4.2 Calculation of each diagram 65

3.4.3 Interpretation of the result 67

3.4.4 Other components 70

3.5 Inclusions inducing a nonzero curvature **71**

3.5.1 Partition function and average force 71

3.5.2 Variance of the force 72

3.6 Conclusion **73**

3.7 Appendix: Effect of varying the radius of the contour . **73**

3.1 Introduction

Although the fluctuation-induced Casimir and Casimir-like forces are by essence inseparable from their fluctuations, the latter have been scarcely studied. When Casimir forces are discussed, one usually refers to their average value. In 1969, Brown and Maclay showed that the quantum electrodynamical Casimir force coincides with the average of the Maxwell stress tensor associated with the fluctuating electromagnetic field [106]. In 1991, Barton first characterized the fluctuations of the Casimir force by calculating the variance of this stress tensor [107]. There have been few studies since then [108–110]. The fluctuations of Casimir and Casimir-like forces are, however, of fundamental importance. Indeed, the measurements of these forces are always performed by probing a fluctuating quantity, either the force itself [58, 59] or the position of one of the interacting objects [66]. In addition, the distance dependence of the fluctuations of Casimir and Casimir-like forces is intriguing as it shares a common origin with the Casimir effect: the suppression of fluctuating degrees of freedom.

The study of the fluctuations of Casimir-like forces was initiated by Bartolo and coworkers, who considered the case of parallel plates imposing Dirichlet boundary conditions on a thermally fluctuating scalar field [111]. Although the case studied in Ref. [111] is quite generic, including, e.g., classical spin systems [112], it does not encompass all the soft matter systems that can give rise to a Casimir-like effect. In particular, membrane inclusions, which are small objects interacting with the membrane through a complicated stress tensor [101, 113], are left out.

In this Chapter, we present a study of the fluctuations of the membrane-mediated Casimir-like force acting between two inclusions, e.g., proteins, that locally constrain the curvature of the membrane. We use the membrane stress tensor to calculate these fluctuations. First, we show that the Casimir-like force, which is usually derived from the membrane free energy [70–73], can be obtained by integrating the average membrane stress tensor. Then we calculate the variance of this force. We show that the Casimir-like force is dominated by its fluctuations. Furthermore, when the distance d between the inclusions is decreased from infinity, the variance of the Casimir-like force decreases as $-1/d^2$. This distance dependence shares a common physical origin with the Casimir-like force itself. We also discuss the effect on the variance of the interplay between the Casimir-like force and the curvature-dependent force.

The main results presented in this Chapter have been published in: A.-F. Bitbol, P. G. Dommersnes and J.-B. Fournier, *Fluctuations of the Casimir-like force between two membrane inclusions*, Physical Review E 81, 050903(R) (2010), cited as Ref. [114] here.

3.2 Basics

3.2.1 Model

a. Description of the membrane

We consider a lipid bilayer membrane containing two rigid inclusions. We use the Helfrich model [24], presented in Section 1.3.2, to describe the membrane. We focus on small deformations of the membrane around the flat shape. Hence, it is convenient to parametrize the membrane in the Monge gauge, by its height relative to a fixed plane $h(\boldsymbol{r})$ where $\boldsymbol{r} \in \mathbb{R}^2$ (see Fig. 1.9). We assume that our membrane is symmetric, i.e., constituted of two identical monolayers. The effective Hamiltonian of the membrane then corresponds to Eq. (1.8) with $c_0 = 0$. In addition, as mentioned in Sec. 2.4.1, the contribution of Gaussian curvature can be discarded as it is constant [80].

Furthermore, following Refs. [70–73], we assume that the separation d between the two inclusions is sufficiently small to neglect the tension term with respect to the curvature term in the Helfrich Hamiltonian Eq. (1.8): we assume $d \ll \sqrt{\kappa/\sigma}$, where κ is the membrane bending rigidity, while σ is its tension (see Sec. 2.4.1). This hypothesis is not too restrictive since the Casimir-like interactions are important only at quite short distances. This leaves us with the following effective Hamiltonian:

$$H = \int d\boldsymbol{r}\, \frac{\kappa}{2} \left[\nabla^2 h(\boldsymbol{r})\right]^2 . \tag{3.1}$$

b. Description of the inclusions

We consider two inclusions embedded in the membrane in $\boldsymbol{r_1}$ and $\boldsymbol{r_2}$, with $d = |\boldsymbol{r_1} - \boldsymbol{r_2}|$. We model these inclusions as point-like objects [71–73]. This is justified since the typical radius of membrane proteins is comparable to the membrane thickness (see Fig. 3.1), which vanishes in our coarse-grained description: the Helfrich model considers the membrane as a mathematical surface with no thickness. This simplification makes the calculation of the force variance tractable. A disadvantage of this model, however, is that the size of the inclusions and the ultraviolet cutoff will not be independent from one another.

We consider inclusions that locally constrain the curvature of the membrane [72, 73]. This corresponds to the most generic case for inclusions not subject to external forces or torques. Particles such as proteins with Bin/amphiphysin/Rvs (BAR) domains [115] (see Fig. 3.1) and viral capsids [116] are good examples of inclusions producing local membrane curvature [103, 117, 118].

We start by considering the case of two inclusions imposing a vanishing curvature, since it gives the Casimir-like force without the elastic interaction arising from an average deformation of the membrane [70, 72, 73], which was described in Sec. 2.5. The case where the inclusions impose a nonzero curvature will be discussed in Sec. 3.5. The two inclusions thus impose the constraints $\partial_x^2 h = \partial_x \partial_y h = \partial_y^2 h = 0$ at their positions $\boldsymbol{r_1}$ and $\boldsymbol{r_2}$.

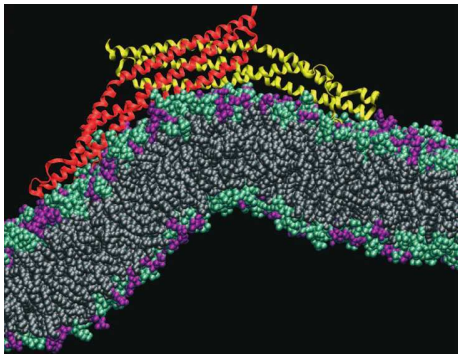

Figure 3.1: Atomistic molecular dynamics simulation of a BAR domain inducing a strong local curvature in a lipid membrane. *Illustration reproduced from Ref. [115].*

Introducing the vectors $\mathbb{D} = (\partial_x^2,\, \partial_x\partial_y,\, \partial_y^2,\, \partial_x^2,\, \partial_x\partial_y,\, \partial_y^2)$ and $\boldsymbol{R} = (\boldsymbol{r_1},\, \boldsymbol{r_1},\, \boldsymbol{r_1},\, \boldsymbol{r_2},\, \boldsymbol{r_2},\, \boldsymbol{r_2})$, these constraints can be expressed as:

$$\mathbb{D}_i h(\boldsymbol{R}_i) = 0\,, \tag{3.2}$$

for $i \in \{1, \ldots, 6\}$. Note that no summation over i is implied in this equation. The Einstein summation convention will not be used in this Chapter.

3.2.2 Partition function of the membrane containing the two inclusions

Let us start by reviewing the calculation of the partition function of the membrane containing the two point-like inclusions. This calculation relies on standard methods of statistical field theory (see, e.g., Refs. [79, 119]). In the case of membrane inclusions, such a calculation was first presented in Ref. [70] for circular inclusions, and it was subsequently adapted to point-like inclusions in Refs. [71–73].

a. Formal expression

The partition function can be written as a functional integral running over all the membrane shapes h that satisfy the constraint in Eq. (3.2):

$$Z[u] = \int \mathcal{D}h \left[\prod_{j=1}^{6} \delta\left(\mathbb{D}_j h(\boldsymbol{R}_j)\right)\right] \exp\left[-\beta H + \int d\boldsymbol{r}\; h(\boldsymbol{r}) u(\boldsymbol{r})\right], \tag{3.3}$$

where δ denotes the Dirac distribution, while $\beta = 1/k_{\mathrm{B}}T$, where k_{B} is Boltzmann's constant and T denotes temperature. We have formally introduced an external field u conjugate to h: it will be useful in order to compute the average and the correlation function of h.

We can rewrite the constraints involved in the functional integral Eq. (3.3) as:

$$\delta\left(\mathbb{D}_j h(\boldsymbol{R}_j)\right) = \int_{\mathbb{R}} \frac{dk_j}{2\pi} \exp\left[i\, k_j\, \mathbb{D}_j h(\boldsymbol{R}_j)\right] = \int_{\mathbb{R}} \frac{dk_j}{2\pi} \exp\left[i \int d\boldsymbol{r}\; h(\boldsymbol{r})\, k_j\, \mathbb{D}_j \delta(\boldsymbol{r} - \boldsymbol{R}_j)\right], \tag{3.4}$$

where we have used the Fourier representation of the Dirac distribution, and then two integrations by parts, assuming that the boundary terms do not contribute, which is the case with adequate boundary conditions. In addition, using integrations by parts, Eq. (3.1) can be transformed into

$$\beta H = \frac{1}{2} \int d\boldsymbol{r}\ h(\boldsymbol{r})\ \beta\kappa\, \nabla^4 h(\boldsymbol{r})\,, \tag{3.5}$$

where ∇^4 stands for the biharmonic operator $(\nabla^2)^2$: this notation will be used throughout.

Using Eqs. (3.4) and (3.5), the partition function in Eq. (3.3) can be expressed as

$$Z[u] = \int \left[\prod_{j=1}^{6} \frac{dk_j}{2\pi}\right] \int \mathcal{D}h\ \exp\left[-\frac{1}{2}\int d\boldsymbol{r}\ h(\boldsymbol{r})\ \beta\kappa\, \nabla^4 h(\boldsymbol{r}) + \int d\boldsymbol{r}\, h(\boldsymbol{r}) f(\boldsymbol{r})\right], \tag{3.6}$$

where we have introduced

$$f(\boldsymbol{r}) = u(\boldsymbol{r}) + i \sum_{j=1}^{6} k_j \mathbb{D}_j \delta(\boldsymbol{r} - \boldsymbol{R}_j)\,. \tag{3.7}$$

Performing the Gaussian functional integral over h, Eq. (3.6) becomes

$$Z[u] = Z_0 \int \left[\prod_{j=1}^{6} \frac{dk_j}{2\pi}\right] \exp\left[\frac{1}{2}\int d\boldsymbol{r} \int d\boldsymbol{r}'\ f(\boldsymbol{r})\, G(\boldsymbol{r} - \boldsymbol{r}')\, f(\boldsymbol{r}')\right], \tag{3.8}$$

where Z_0 is the partition function of a membrane with no inclusion and no external field, while G is a Green's function of the differential operator $\beta\kappa\,\nabla^4$: it verifies $\beta\kappa\,\nabla^4 G(\boldsymbol{r}) = \delta(\boldsymbol{r})$. Performing the Gaussian integral over the k_js finally yields

$$Z[u] = Z_0 \frac{(2\pi)^3}{\sqrt{\det M}}\ \exp\left[\frac{1}{2}\int d\boldsymbol{r}\, d\boldsymbol{r}'\, u(\boldsymbol{r})\, C(\boldsymbol{r}, \boldsymbol{r}')\, u(\boldsymbol{r}')\right], \tag{3.9}$$

where we have introduced the matrix M with elements

$$M_{ij} = \mathbb{D}_i \mathbb{D}_j G(\boldsymbol{R}_i - \boldsymbol{R}_j)\,, \tag{3.10}$$

for $i \in \{1, \ldots, 6\}$ and $j \in \{1, \ldots, 6\}$, and where C is defined by

$$C(\boldsymbol{r}, \boldsymbol{r}') = G(\boldsymbol{r} - \boldsymbol{r}') + G'(\boldsymbol{r}, \boldsymbol{r}')\,, \tag{3.11}$$

$$G'(\boldsymbol{r}, \boldsymbol{r}') = -\sum_{i,j=1}^{6} \left[\mathbb{D}_i G(\boldsymbol{r} - \boldsymbol{R}_i)\right] M_{ij}^{-1}\, \mathbb{D}_j G(\boldsymbol{r}' - \boldsymbol{R}_j)\,. \tag{3.12}$$

b. Average and correlation function of the height of the membrane

We can now express the average and the correlation function of the height of the membrane in the presence of the two inclusions. They are obtained by successive functional differentiations of $Z[u]$ in Eq. (3.9) with respect to the external field u conjugate to h (see Eq. (3.3)) [79, 119]. The average reads:

$$\langle h(\boldsymbol{r})\rangle = \frac{1}{Z[0]}\,\frac{\delta Z[u]}{\delta u(\boldsymbol{r})}\bigg|_{u=0} = 0\,, \tag{3.13}$$

which was expected given that our membrane is symmetric and that our inclusions impose a vanishing curvature.

The correlation function of the height of our membrane containing two inclusions reads:

$$\langle h(\boldsymbol{r})h(\boldsymbol{r}')\rangle = \frac{1}{Z[0]}\,\frac{\delta^2 Z[u]}{\delta u(\boldsymbol{r})\delta u(\boldsymbol{r}')}\bigg|_{u=0} = C(\boldsymbol{r},\boldsymbol{r}')\,, \tag{3.14}$$

where C is defined by Eqs. (3.11) and (3.12).

c. Green's function associated with the membrane Hamiltonian

We have expressed formally the partition function of the membrane with the two inclusions (see Eq. (3.9)), and its correlation function (see Eq. (3.14)). In order to obtain their explicit expressions, it is necessary to calculate the Green's function G of the differential operator $\beta\kappa\,\nabla^4$ associated with the effective Hamiltonian in Eq. (3.1). The equation $\beta\kappa\,\nabla^4 G(\boldsymbol{r}) = \delta(\boldsymbol{r})$ can be solved in Fourier space, yielding

$$G(\boldsymbol{r}) = \frac{k_{\mathrm{B}}T}{\kappa}\int_{1/\xi\le|\boldsymbol{q}|\le\Lambda}\frac{d\boldsymbol{q}}{(2\pi)^2}\,\frac{e^{i\boldsymbol{q}\cdot\boldsymbol{r}}}{q^4} = \int_{\boldsymbol{q}}\frac{e^{i\boldsymbol{q}\cdot\boldsymbol{r}}}{q^4}\,, \tag{3.15}$$

where Λ is the ultraviolet cutoff, comparable with the inverse membrane thickness, while ξ stands for the membrane size in the absence of tension, or the fluctuation correlation length $\xi \approx \sqrt{\kappa/\sigma}$ otherwise. We have introduced the shorthand

$$\int_{\boldsymbol{q}} \equiv \frac{k_{\mathrm{B}}T}{\kappa}\int_{1/\xi\le|\boldsymbol{q}|\le\Lambda}\frac{d\boldsymbol{q}}{(2\pi)^2}\,, \tag{3.16}$$

which will be used henceforth.

Introducing an ultraviolet cutoff Λ amounts to disregarding wavelengths smaller than about $1/\Lambda$. As the Helfrich model is a continuum theory that describes the membrane as a mathematical surface, it disregards everything that occurs at length scales smaller than the membrane thickness. There is thus a natural cutoff Λ in the theory, of order of the inverse of the membrane thickness.

d. Explicit expression of the matrix M

Thanks to the expression of G in Eq. (3.15), we can now obtain explicitly the matrix M defined by Eq. (3.10), which is involved in the correlation function C of the height of the membrane (see Eqs. (3.11) and (3.12)). For instance,

$$M_{11} = \partial_x^4 G(0) = \int_{\boldsymbol{q}} \frac{q_x^4}{q^4} = \frac{k_\mathrm{B}T}{(2\pi)^2\kappa} \int_0^{2/a} dq\, q \int_0^{2\pi} d\theta\ \cos^4\theta = \frac{k_\mathrm{B}T}{8\pi\,\kappa}\,\frac{3}{a^2}\,, \tag{3.17}$$

where we have introduced $a = 2/\Lambda$: this distance is of order of the membrane thickness. The interest[1] of introducing a is that it plays the part of the effective radius of our point-like inclusions (see Sec. 3.2.3).

Hence, M can finally be written as:

$$M = \frac{k_\mathrm{B}T}{8\pi\kappa} \left(\begin{array}{ccc|ccc} 3a^{-2} & 0 & a^{-2} & -2d^{-2} & 0 & -2d^{-2} \\ 0 & a^{-2} & 0 & 0 & -2d^{-2} & 0 \\ a^{-2} & 0 & 3a^{-2} & -2d^{-2} & 0 & 6d^{-2} \\ \hline -2d^{-2} & 0 & -2d^{-2} & 3a^{-2} & 0 & a^{-2} \\ 0 & -2d^{-2} & 0 & 0 & a^{-2} & 0 \\ -2d^{-2} & 0 & 6d^{-2} & a^{-2} & 0 & 3a^{-2} \end{array}\right), \tag{3.18}$$

where $d = |\boldsymbol{r}_1 - \boldsymbol{r}_2|$ denotes the distance between the two inclusions. We have emphasized the block structure of this matrix. The two diagonal blocks depend on a, i.e., on the ultraviolet cutoff Λ, since they involve derivatives of G evaluated in 0. The two off-diagonal blocks depend on d since they involve derivatives of G evaluated in d. Formally, the interaction between the inclusions will arise from this dependence on d.

3.2.3 Traditional calculation of the Casimir-like force

We now have at hand all the elements necessary to express explicitly the free energy of the membrane with the two inclusions. Setting to zero the field u conjugate to h (this field has no physical meaning, it is just a tool for computing correlation functions), Eq. (3.9) shows that the distance-dependent part $F_c(d)$ of the free energy $F = -k_\mathrm{B}T\ln(Z[0])$ of the membrane is:

$$F_c(d) = \frac{k_\mathrm{B}T}{2}\ln(\det M)\,. \tag{3.19}$$

The quantity $F_c(d)$ represents the Casimir-like interaction energy between the two inclusions. The presence of $k_\mathrm{B}T$ illustrates its deep relation to thermal fluctuations: the Casimir-like interaction comes from the fact that the two inclusions constrain the thermal fluctuations of the shape of the membrane. Formally, F_c stems from the curvature constraints introduced in the partition function.

[1] Alternatively, we can keep Λ throughout all our calculations and then note that $2/\Lambda$ plays the part of the effective radius of our point-like inclusions: this approach was chosen in Ref. [114].

We can now calculate the (average) Casimir-like force f_c using the traditional method, i.e., differentiating F_c with respect to d. Using Eqs. (3.18) and (3.19), we obtain:

$$f_c(d) = \frac{\partial F_c}{\partial d} = \frac{24\, k_\mathrm{B}T}{d} \frac{\epsilon^4\,(1-6\epsilon^4+4\epsilon^8)}{1-12\epsilon^4+36\epsilon^8-16\epsilon^{12}}\,, \tag{3.20}$$

where we have introduced the small dimensionless ratio $\epsilon = a/d$. Note that we have chosen a somewhat unusual sign convention in the definition of f_c, for attractive forces to be positive.

Since we have considered the inclusions point-like, our results are only relevant in the regime $d \gg a$. Recall that $a = 2/\Lambda$ is of order of the membrane thickness. Performing an expansion in the small parameter a/d yields

$$f_c(d) = 24\, k_\mathrm{B}T\, \frac{a^4}{d^5} + \frac{1}{a}\, \mathcal{O}\left(\frac{a^9}{d^9}\right)\,. \tag{3.21}$$

The leading order term corresponds to the Casimir-like force obtained in the literature [70–73]: this attractive force is the force deriving from the potential in Eq. (2.18). Note that subleading terms are quickly negligible: their contribution to the force falls below 1% as soon as $d > 5\,a$. The result Eq. (3.21), obtained for point-like inclusions, coincides with the Casimir-like force between two rigid disks of radius a [70]. Thus, $a = 2/\Lambda$ can be interpreted as the effective radius of our point-like inclusions [71–73].

3.3 Approach based on the stress tensor

Now that we have presented the calculation of the partition function of the membrane with the two point-like inclusions, and reviewed the traditional calculation of the Casimir-like force, let us introduce our own approach to the Casimir-like force. This approach is based on the stress tensor of the membrane.

3.3.1 Membrane stress tensor

The stress tensor associated with the Helfrich Hamiltonian was first derived in 2002 by Capovilla and Guven in covariant formalism, using Noether's theorem [101]. In 2007, Fournier recovered and extended their results using the principle of virtual work and expressing the stress tensor in the Monge gauge [113]. We will use the latter formulation.

In order to define the stress tensor of the membrane, let us consider an infinitesimal cut separating a region 1 from a region 2 in the membrane, and let us denote by $\boldsymbol{m}$ the normal to the projection of this cut on the (x, y) plane, directed toward region 1 (see Fig. 3.2). The stress tensor $\boldsymbol{\Sigma}$ relates linearly the force $d\boldsymbol{f}$ that region 1 exerts onto region 2 to the vectorial length $\boldsymbol{m}\, ds$ of the projected cut through

$$d\boldsymbol{f} = \boldsymbol{\Sigma}\, \boldsymbol{m}\, ds\,. \tag{3.22}$$

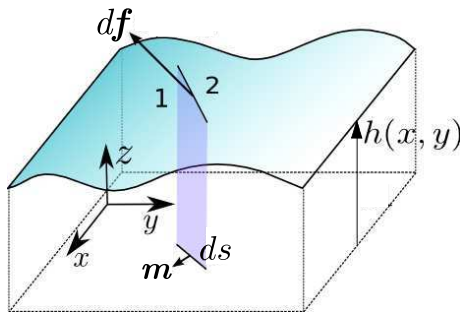

Figure 3.2: Sketch of a membrane in the Monge gauge, featuring an infinitesimal cut between separating a region 1 from a region 2. *Original illustration from Ref. [33], adapted and modified.*

This defines the six components of the projected stress tensor: Σ_{ij} and Σ_{zj}, where $i \in \{x, y\}$ and $j \in \{x, y\}$ [113].

The components of the stress tensor $\boldsymbol{\Sigma}$ associated with the effective Hamiltonian Eq. (3.1) are given by [113]:

$$\Sigma_{xx} = \frac{\kappa}{2}\left[\left(\partial_y^2 h\right)^2 - \left(\partial_x^2 h\right)^2\right] + \kappa\left(\partial_x h\right)\partial_x \nabla^2 h\,, \tag{3.23}$$

$$\Sigma_{xy} = \kappa\left[\left(\partial_x h\right)\partial_y \nabla^2 h - \left(\partial_x \partial_y h\right)\nabla^2 h\right], \tag{3.24}$$

$$\Sigma_{xz} = -\kappa\,\partial_x \nabla^2 h\,. \tag{3.25}$$

The three other components, Σ_{yx}, Σ_{yy} and Σ_{yz}, can be deduced by exchanging x and y.

Integrating the stress tensor over a closed contour gives the force exerted by the exterior of this contour on the interior of the contour, in any shape h of the membrane. Note that $\boldsymbol{\Sigma}$ is defined in such a way that the force exerted on a membrane domain delimited by a contour is obtained by integration over the *projection* of this contour onto the reference plane [113].

Note that, in Chapter 12, we will present a derivation of the membrane stress tensor in the presence of lipid density and composition inhomogeneities, i.e., for a more general Hamiltonian than the Helfrich one. In particular, in this work, we have obtained the stress tensor associated with the ADE model.

3.3.2 Average Casimir-like force

Let us now come back to our membrane with two point-like inclusions in $\boldsymbol{r_2} = (0, 0)$ and $\boldsymbol{r_1} = (d, 0)$. Let $\boldsymbol{f}$ be the force exerted by the rest of the membrane on a membrane patch whose projection on the reference plane is a disk of radius r centered on $\boldsymbol{r_2}$ (see Fig. 3.3). Let us take $r < d$, so that the contour surrounds inclusion 2 but not inclusion 1. The projection of $\boldsymbol{f}$ along the x axis joining the two inclusions is

$$f_x = \boldsymbol{e}_x \cdot \int_{\mathcal{C}} \boldsymbol{\Sigma}\,\boldsymbol{m}\,ds = r\int_0^{2\pi} d\theta\left[\Sigma_{xx}(\boldsymbol{r})\cos\theta + \Sigma_{xy}(\boldsymbol{r})\sin\theta\right], \tag{3.26}$$

where $\boldsymbol{e}_x$ is the unit vector along x, while $\mathcal{C}$ denotes the circle of radius r which is the projected contour of our membrane patch. We have introduced polar coordinates: $\boldsymbol{r} = r\,(\cos\theta, \sin\theta)$.

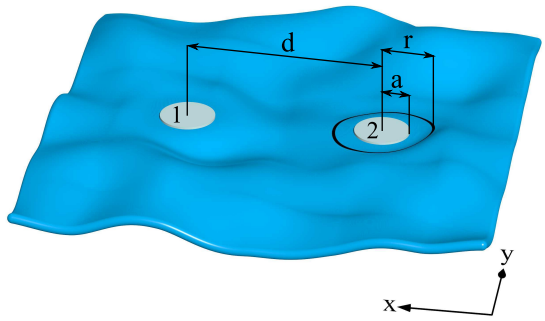

Figure 3.3: Two inclusions of radius a separated by a distance d in a fluctuating membrane. The inclusions impose a vanishing curvature to the membrane. The black line is a circular contour of radius r: its projection is used for the calculation of the Casimir-like force by integration of the stress tensor.

Let us calculate the thermal average of f_x. We focus exclusively on f_x because the symmetry of the system (see Fig. 3.3) shows that the other components of the force vanish on average. Starting from Eqs. (3.23) and (3.24), the thermal average of the stress tensor components can be expressed as linear combinations of the derivatives of the correlation function C of the height of the membrane (see Eq. (3.14)). Explicitly, we have:

$$\begin{aligned}\langle\Sigma_{xx}(\boldsymbol{r})\rangle &= \frac{\kappa}{2}\left[\langle[\partial_y^2 h(\boldsymbol{r})]^2\rangle - \langle[\partial_x^2 h(\boldsymbol{r})]^2\rangle\right] + \kappa\left[\langle\partial_x h(\boldsymbol{r})\,\partial_x^2 h(\boldsymbol{r})\rangle + \langle\partial_x h(\boldsymbol{r})\,\partial_y^2 h(\boldsymbol{r})\rangle\right] \\ &= \kappa\left[\frac{1}{2}\,\partial_y^2\partial_{y'}^2 C(\boldsymbol{r},\boldsymbol{r}') - \frac{1}{2}\,\partial_x^2\partial_{x'}^2 C(\boldsymbol{r},\boldsymbol{r}')\right. \\ &\qquad \left. + \partial_x\partial_{x'}^2 C(\boldsymbol{r},\boldsymbol{r}') + \partial_x\partial_{y'}^2 C(\boldsymbol{r},\boldsymbol{r}')\right]\Bigg|_{\boldsymbol{r}'=\boldsymbol{r}}, \end{aligned} \tag{3.27}$$

and a similar expression for $\langle\Sigma_{xy}(\boldsymbol{r})\rangle$.

We now have all the elements to calculate explicitly $\langle f_x\rangle$, since we have already expressed explicitly G (see Eq. (3.15)) and the matrix M in G' (see Eq. (3.18)), which are involved in C (see Eqs. (3.11) and (3.12)). Carrying out this calculation yields:

$$\langle f_x\rangle = \frac{24\,k_{\mathrm{B}}T}{d}\,\frac{\epsilon^4\,(1-6\epsilon^4+4\epsilon^8)}{1-12\epsilon^4+36\epsilon^8-16\epsilon^{12}}\,, \tag{3.28}$$

where $\epsilon = a/d$. This expression coincides with the exact expression of the Casimir-like force between two point-like membrane inclusions obtained in Eq. (3.20) by

differentiating the free energy. The leading order in a/d yields the usual expression

$$\langle f_x \rangle = 24\, k_{\mathrm{B}} T\, \frac{a^4}{d^5} + \frac{1}{a}\, \mathcal{O}\left(\frac{a^9}{d^9}\right) . \tag{3.29}$$

Remark: contour-independence. The result obtained for $\langle f_x \rangle$ is independent of the radius r of the integration contour, as long as $r < d$. In fact, this can be generalized beyond circular contours: as long as one inclusion is inside and the other one outside the contour, $\langle f_x \rangle$ is equal to the Casimir-like force between the two inclusions. If no inclusion is inside the contour, or if both are inside, $\langle f_x \rangle$ vanishes. Qualitatively, this is because the only average force in the system is the one exerted by one inclusion on the other, through the membrane.

Let us prove this contour-independence formally. First, let us prove an additivity property. We take a membrane patch $\mathcal{D}$, with projected contour $\mathcal{C}$, and we separate it into two patches $\mathcal{D}_1$ and $\mathcal{D}_2$ (with respective projected contours $\mathcal{C}_1$ and $\mathcal{C}_2$), such that $\mathcal{D} = \mathcal{D}_1 \cup \mathcal{D}_2$. The force exerted on $\mathcal{D}$ by the rest of the membrane reads:

$$\boldsymbol{f}_{\mathcal{D}} = \int_{\mathcal{C}} d\ell\, \boldsymbol{\Sigma}\, \boldsymbol{m} = \int_{\mathcal{C}_1} d\ell\, \boldsymbol{\Sigma}\, \boldsymbol{m_1} + \int_{\mathcal{C}_2} d\ell\, \boldsymbol{\Sigma}\, \boldsymbol{m_2} = \boldsymbol{f}_{\mathcal{D}_1} + \boldsymbol{f}_{\mathcal{D}_2} . \tag{3.30}$$

Indeed, the contributions of $\mathcal{C}_1 \cap \mathcal{C}_2$ in $\boldsymbol{f}_{\mathcal{D}_1}$ and in $\boldsymbol{f}_{\mathcal{D}_2}$ cancel each other (see Fig. 3.4).

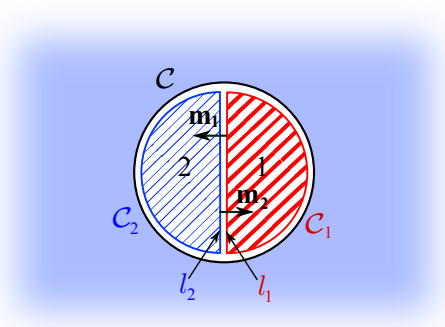

Figure 3.4: Additivity property illustrated on a disk. The white disk with contour $\mathcal{C}$ represents the projection of a membrane patch $\mathcal{D}$. It is separated into two half-disks 1 and 2 (shaded in blue and red, respectively) corresponding to the projections of $\mathcal{D}_1$ and $\mathcal{D}_2$. The contours of each of these patches are slightly separated for the sake of clarity. When calculating $\boldsymbol{f}_{\mathcal{D}_1} + \boldsymbol{f}_{\mathcal{D}_2}$, the integrals on l_1 and l_2, i.e., on $\mathcal{C}_1 \cap \mathcal{C}_2$, cancel each other because the exterior normals $\boldsymbol{m}_1$ and $\boldsymbol{m}_2$ have opposite directions.

Thanks to this additivity property, we now simply have to prove that the average of the force $\boldsymbol{f}_{\mathcal{M}}$ exerted on a patch $\mathcal{M}$ of inclusion-free membrane by the rest of the membrane containing the two inclusions vanishes. For this, we use Stokes' theorem

$$\boldsymbol{f}_{\mathcal{M}} = \int_{\mathcal{C}_{\mathcal{M}}} d\ell\, \boldsymbol{\Sigma}\, \boldsymbol{m} = \int_{\mathcal{M}} d\boldsymbol{r}\, \boldsymbol{\nabla} \cdot \boldsymbol{\Sigma} . \tag{3.31}$$

Eqs. (3.23) and (3.24) yield the following expression for the divergence of the stress tensor:

$$\boldsymbol{\nabla}\cdot\boldsymbol{\Sigma} = \big(\partial_x\Sigma_{xx}+\partial_y\Sigma_{xy},\ \partial_x\Sigma_{yx}+\partial_y\Sigma_{yy},\ \partial_x\Sigma_{zx}+\partial_y\Sigma_{zy}\big) = \kappa\nabla^4 h\ \big(\partial_x h,\ \partial_y h,\ -1\big), \tag{3.32}$$

and its thermal average thus reads

$$\langle\boldsymbol{\nabla}\cdot\boldsymbol{\Sigma}\ (\boldsymbol{r})\rangle = \kappa\left(\nabla^4_{\boldsymbol{r}}\partial_{x'}C(\boldsymbol{r},\boldsymbol{r}')\,,\ \nabla^4_{\boldsymbol{r}}\partial_{y'}C(\boldsymbol{r},\boldsymbol{r}')\,,\ -\nabla^4_{\boldsymbol{r}}\langle h(\boldsymbol{r})\rangle\right)\Big|_{\boldsymbol{r}'=\boldsymbol{r}}\,. \tag{3.33}$$

Using the definition of C in Eqs. (3.11) and (3.12), the expression of G in Eq. (3.15) and the matrix M in Eq. (3.18) to express G', we can show that the x and y-components of $\langle\boldsymbol{\nabla}\cdot\boldsymbol{\Sigma}\rangle$ vanish, apart from singularities at the positions $\boldsymbol{r_1}$ and $\boldsymbol{r_2}$ of the inclusions. In addition, the average shape of the membrane is flat (see Eq. (3.13)), so the z-component of $\langle\boldsymbol{\nabla}\cdot\boldsymbol{\Sigma}\rangle$ is equal to zero.

Hence, the average of the force $\boldsymbol{f}_{\mathcal{M}}$ exerted on a patch $\mathcal{M}$ of inclusion-free membrane by the rest of the membrane containing the two inclusions vanishes. Consequently, in our calculation of the average force exerted on an inclusion, the contour can be freely deformed as long as it surrounds exactly one inclusion.

3.4 Variance of the Casimir-like force

We have shown that the usual Casimir-like force can be recovered using the stress tensor. The interest of this method based on the stress tensor is that it enables to go beyond this average force. Indeed, the stress tensor provides the force exerted on inclusion 2 by the membrane including inclusion 1 in any shape of the membrane. This allows for studying the fluctuations of this force, which can be interpreted as the fluctuations of the Casimir-like force.

Until now, we have only discussed f_x, i.e., the projection along the x axis, which joins the two inclusions, of the force $\boldsymbol{f}$ exerted on inclusion 2 by the rest of the membrane containing inclusion 1 (see Fig. 3.3). Indeed, symmetry shows that the other components of the force vanish on average. This symmetry argument does not hold for the fluctuations of the force. However, the variance of f_x actually contains the main features of the variance of $\boldsymbol{f}$. As the calculations involved are quite lengthy, we will first present and discuss the variance of f_x, and then we will briefly mention the other components.

3.4.1 Formal expression

Starting from Eq. (3.26), the variance of f_x can be expressed as

$$\Delta f_x^2 = r^2\int_{\mathcal{D}} d\alpha d\theta\Big[V_{xx}(\boldsymbol{r},\boldsymbol{r}')\cos\theta\cos\alpha + 2V_{xy}(\boldsymbol{r},\boldsymbol{r}')\cos\theta\sin\alpha + V_{yy}(\boldsymbol{r},\boldsymbol{r}')\sin\theta\sin\alpha\Big], \tag{3.34}$$

where we have used polar coordinates: $\boldsymbol{r} = r\,(\cos\theta,\sin\theta)$ and $\boldsymbol{r}' = r\,(\cos\alpha,\sin\alpha)$, and we have introduced the notation $\mathcal{D} = [0,2\pi]\times[0,2\pi]$. In addition, we have

denoted by V_{ij} the correlation functions of the stress tensor components:

$$V_{ij}(\boldsymbol{r},\boldsymbol{r}') = \langle \Sigma_{xi}(\boldsymbol{r})\, \Sigma_{xj}(\boldsymbol{r}')\rangle - \langle \Sigma_{xi}(\boldsymbol{r})\rangle \langle \Sigma_{xj}(\boldsymbol{r}')\rangle \ , \tag{3.35}$$

where $i \in \{x, y\}$ and $j \in \{x, y\}$.

The stress tensor components in Eqs. (3.23) and (3.24) are linear combinations of terms that are quadratic in the derivatives of h. Hence, the correlation functions V_{ij} of these stress tensor components involve the thermal average of quantities that are quartic in the derivatives of h. Given that the field h has Gaussian statistics (see the partition function (3.9)) and that its average vanishes, we can use Wick's theorem [120] to express these average quartic quantities in terms of the correlation function C of the height of our membrane containing the two inclusions. Formally, if the h_is denote terms that are proportional to h or to one of its derivatives, Wick's theorem yields

$$\langle h_1 h_2 h_3 h_4\rangle = \langle h_1 h_2\rangle\langle h_3 h_4\rangle + \langle h_1 h_3\rangle\langle h_2 h_4\rangle + \langle h_1 h_4\rangle\langle h_2 h_3\rangle \, . \tag{3.36}$$

The idea behind this is that a Gaussian distribution is fully characterized by its first and second moments, so that the fourth moment, for instance, can be expressed in terms of them.

For instance, the term $v_{xx}(\boldsymbol{r},\boldsymbol{r}')$ in $V_{xx}(\boldsymbol{r},\boldsymbol{r}')$ that originates from the product of the first and second terms in Σ_{xx} (see Eq. (3.23)) can be expressed as

$$\begin{aligned} v_{xx}(\boldsymbol{r},\boldsymbol{r}') &= -\frac{\kappa^2}{4}\left[\left\langle \left[\partial_y^2 h(\boldsymbol{r})\right]^2 \left[\partial_{x'}^2 h(\boldsymbol{r}')\right]^2\right\rangle - \left\langle \left[\partial_y^2 h(\boldsymbol{r})\right]^2\right\rangle \left\langle \left[\partial_{x'}^2 h(\boldsymbol{r}')\right]^2\right\rangle\right] \\ &= -\frac{\kappa^2}{2}\left\langle \partial_y^2 h(\boldsymbol{r})\partial_{x'}^2 h(\boldsymbol{r}')\right\rangle^2 \\ &= -\frac{\kappa^2}{2}\left[\partial_y^2\partial_{x'}^2 C(\boldsymbol{r},\boldsymbol{r}')\right]^2 \ , \end{aligned} \tag{3.37}$$

and its contribution to Δf_x^2 (see Eq. (3.34)) thus reads

$$\begin{aligned} r^2\int_{\mathcal{D}} d\alpha\, d\theta\, v_{xx}(\boldsymbol{r},\boldsymbol{r}')\cos\theta\cos\alpha &= -\frac{\kappa^2}{2}\times r^2\int_{\mathcal{D}} d\alpha\, d\theta\, \left[\partial_y^2\partial_{x'}^2 C(\boldsymbol{r},\boldsymbol{r}')\right]^2 \cos\theta\cos\alpha \\ &= -\frac{\kappa^2}{2} \ . \end{aligned} \tag{3.38}$$

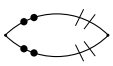

In the last line, we have introduced a diagrammatic notation (see, e.g., Refs. [119, 120]) that will help to simplify our expressions and our calculations. In this notation, inspired by Feynman diagrams, each line stands for the propagator $C(\boldsymbol{r},\boldsymbol{r}')$. Each dash on such a line symbolizes a differentiation with respect to x if it stands on the left of the diagram, or to x' if it stands on its right. Similarly, each dot symbolizes a differentiation with respect to y if it stands on the left of the diagram, or to y' if it stands on its right. The angular integrations with the appropriate projection factors (e.g., $\cos\theta\cos\alpha$ in Eq. (3.38)) are understood.

Using this diagrammatic notation, the contribution arising from V_{xx} in Δf_x^2 reads:

$$\frac{1}{\kappa^2}\int_{\mathcal{D}} d\alpha\, d\theta\, V_{xx}(\boldsymbol{r},\boldsymbol{r}')\cos\theta\cos\alpha =$$

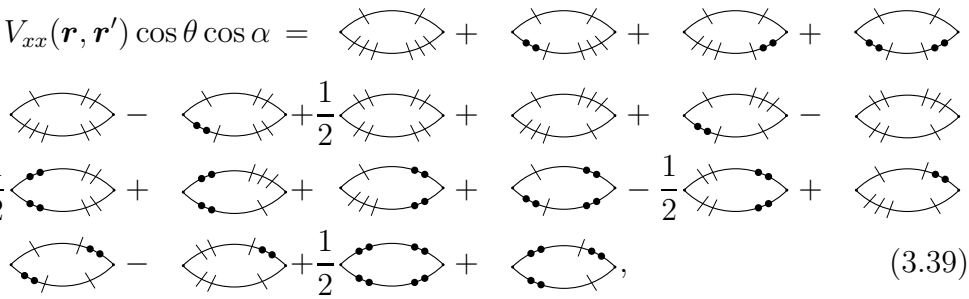

(3.39)

where the first diagram must be understood as

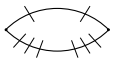

$$= r^2\int_{\mathcal{D}} d\alpha\, d\theta\, [\partial_x\partial_{x'}C(\boldsymbol{r},\boldsymbol{r}')]\left[\partial_x^3\partial_{x'}^3 C(\boldsymbol{r},\boldsymbol{r}')\right]\cos\theta\cos\alpha. \tag{3.40}$$

Similarly, the terms coming from V_{xy} are

$$\frac{1}{\kappa^2}\int_{\mathcal{D}} d\alpha\, d\theta\, V_{xy}(\boldsymbol{r},\boldsymbol{r}')\cos\theta\sin\alpha =$$

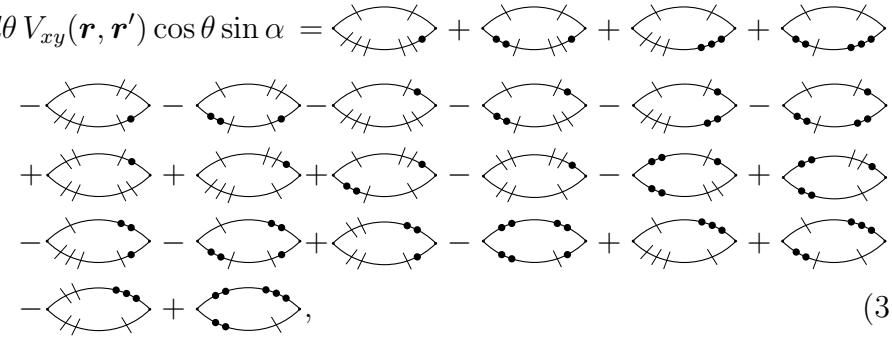

(3.41)

where the first diagram must be understood as

$$= r^2\int_{\mathcal{D}} d\alpha\, d\theta\, [\partial_x\partial_{x'}C(\boldsymbol{r},\boldsymbol{r}')]\left[\partial_x^3\partial_{x'}^2\partial_{y'} C(\boldsymbol{r},\boldsymbol{r}')\right]\cos\theta\sin\alpha. \tag{3.42}$$

Finally, the last terms in Δf_x^2, which come from V_{yy}, are given by

$$\frac{1}{\kappa^2}\int_{\mathcal{D}} d\alpha\, d\theta\, V_{yy}(\boldsymbol{r},\boldsymbol{r}')\sin\theta\sin\alpha =$$

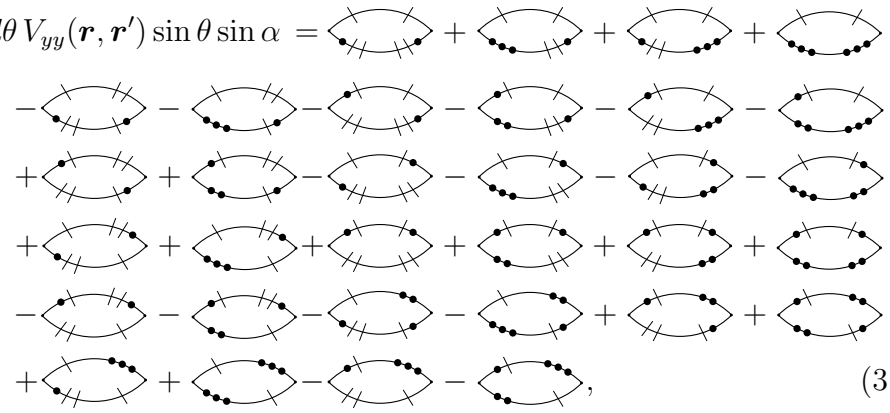

(3.43)

where the first diagram must be understood as

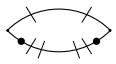

$$= r^2 \int_{\mathcal{D}} d\alpha\, d\theta \left[\partial_x \partial_{x'} C(\boldsymbol{r}, \boldsymbol{r}')\right] \left[\partial_x^2 \partial_y \partial_{x'}^2 \partial_{y'} C(\boldsymbol{r}, \boldsymbol{r}')\right] \cos\theta \sin\alpha. \tag{3.44}$$

Hence, in order to obtain the variance of f_x, we now simply have to calculate explicitly the contribution of each diagram. This can be done systematically since all diagrams share the same structure.

3.4.2 Calculation of each diagram

Since $C = G + G'$ (see Eq. (3.11)), each diagram can be separated into four terms. As a consequence, three different structures of diagrams are involved in Δf_x: diagrams involving only G, "mixed" diagrams involving G and G', and diagrams involving only G'. Let us take the diagram in Eq. (3.38) as an example again: we can write

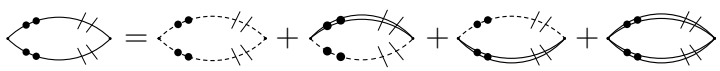

(3.45)

where the double line stands for $G'(\boldsymbol{r}, \boldsymbol{r}')$ while the dashed line stands for $G(\boldsymbol{r} - \boldsymbol{r}')$. In the particular example of Eq. (3.45), the two "mixed" diagrams are identical, but this is not the case for all the diagrams involved in Δf_x^2.

Using Eqs. (3.12) and (3.15), we can write each of these diagrams explicitly. For instance,

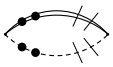

$$\begin{aligned} &= r^2 \int_{\mathcal{D}} d\alpha d\theta \left[\partial_y^2 \partial_{x'}^2 G'(\boldsymbol{r}, \boldsymbol{r}')\right] \left[\partial_y^2 \partial_{x'}^2 G(\boldsymbol{r} - \boldsymbol{r}')\right] \cos\theta \cos\alpha \\ &= -r^2 \int_{\boldsymbol{q},\boldsymbol{k},\boldsymbol{q}'} \frac{q_y^2 k_x^2\, \Delta_i(\boldsymbol{q}) M_{ij}^{-1} \Delta_j(\boldsymbol{k})}{q^4 k^4} \frac{q_y'^2 q_x'^2}{q'^4} \int_{\mathcal{D}} d\alpha d\theta \cos\theta \cos\alpha\, e^{i(\boldsymbol{q}+\boldsymbol{q}')\cdot\boldsymbol{r}} e^{i(\boldsymbol{k}-\boldsymbol{q}')\cdot\boldsymbol{r}'}, \end{aligned} \tag{3.46}$$

where we have introduced $\Delta_j(\boldsymbol{q}) = Q_j e^{-i\boldsymbol{q}\cdot\boldsymbol{R}_j}$ with $Q = (q_x^2,\ q_x q_y,\ q_y^2,\ q_x^2,\ q_x q_y,\ q_y^2)$. Note that we have used the shorthand introduced in Eq. (3.16).

a. Contour-dependence

In Sec. (3.3.2), we showed that the thermal average force $\langle f_x \rangle$ is independent of the integration contour as long as it surrounds exactly one inclusion. This is due to the fact that a piece of inclusion-free membrane is subject to a zero average force.

However, a piece of inclusion-free membrane is subject to a fluctuating force of finite variance [33], which entails that Δf_x^2 depends on the contour chosen to calculate f_x. Thus, in order to obtain the fluctuations of the Casimir-like force acting on an inclusion, we should take a contour that includes the inclusion and only it. We have seen in Sec. 3.2.3, by comparing the average force between point-like inclusions to that between circular inclusions, that the effective radius of the point-like inclusions is $a = 2/\Lambda$. Thus, the best we can do is to choose $r = a$.

b. Analytical insight

Let us first investigate the analytical calculations of the diagrams, on the example of the diagram in Eq. (3.46). Performing the angular integrals, its expression becomes

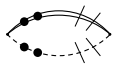

$$= 4\pi^2 r^2 \int_{\boldsymbol{q},\boldsymbol{k},\boldsymbol{q}'} \frac{q_y^2 k_x^2\, \Delta_i(\boldsymbol{q}) M_{ij}^{-1} \Delta_j(\boldsymbol{k})}{q^4 k^4}\, \frac{q_y'^2 q_x'^2}{q'^4} J_1(|\boldsymbol{q}+\boldsymbol{q}'|r) J_1(|\boldsymbol{k}-\boldsymbol{q}'|r) \cos\theta' \cos\alpha', \tag{3.47}$$

where J_1 is the Bessel function of the first kind and of the first order, while θ' (resp. α') denotes the angle of $\boldsymbol{q}+\boldsymbol{q}'$ (resp. $\boldsymbol{k}-\boldsymbol{q}'$) relative to the x-axis.

While the integrals on the wave vectors in Eq. (3.47) are difficult to calculate analytically for $r = a$, they become tractable in the limit $r \ll a$. Unfortunately, this limit is unphysical, given that the continuum theory we use breaks down at distances smaller than a (recall that $a = 2/\Lambda$, where Λ is the ultraviolet cutoff). However, the result will guide our understanding of the physical case $r = a$.

In the limit $r \ll a$, the arguments of J_1 in Eq. (3.47) are very small for all the wave vectors over which the integrals run. We can thus use a first-order expansion of J_1, yielding

$$= \pi^2 r^4 \int_{\boldsymbol{q},\boldsymbol{k},\boldsymbol{q}'} \frac{q_y^2 k_x^2\, \Delta_i(\boldsymbol{q}) M_{ij}^{-1} \Delta_j(\boldsymbol{k})}{q^4 k^4}\, \frac{q_y'^2 q_x'^2}{q'^4} (q_x + q_x')(k_x - q_x')\,, \tag{3.48}$$

which is now easy to calculate, using the explicit expression of M in Eq. (3.18). Recall that the wave vector moduli range from $1/\xi$ to $\Lambda = 2/a$ in these integrals (see Eq. (3.16)).

Performing the integrations over the wave vectors for all the diagrams in Δf_x^2 (see Eqs. (3.39), (3.41) and (3.43)) finally yields, in the limit $r \ll a$,

$$\Delta f_x^2 \sim \frac{r^4 (k_\mathrm{B} T)^2}{3\, a^6} \left[\ln\left(\frac{2\xi}{a}\right) - \frac{a^2}{d^2} + \mathcal{O}\left(\frac{a^4}{d^4}\right) \right], \tag{3.49}$$

where zero-average oscillations at the cutoff frequency, with amplitude in $(d/a)^{-5/2}$, have been discarded. Indeed, these oscillations are just an effect of our simple regularization scheme where the cutoff $\Lambda = 2/a$ is put in as an upper boundary of the integrals on the wave vectors. Using a smooth regularization, these oscillations would disappear.

c. Numerical calculations

In order to obtain Δf_x^2 in the physical case $r = a$, we have computed numerically the integrals involved in the diagrams. There is a large number of diagrams, but we can classify them in three groups of diagrams sharing the same structure: the diagrams involving only G, the "mixed" ones involving G and G', and those involving only G' (see Eq. (3.45)). To take profit of this, we wrote an algorithm that constructs formally all the diagrams and that calculates systematically the corresponding numerical integrals before adding them together. This algorithm was implemented in the software Mathematica.

Let us explain briefly our computation method on the example (3.46). First, we calculated analytically the integrals over the wave vectors $\boldsymbol{k}$, $\boldsymbol{q}$ and $\boldsymbol{q'}$, leaving only the final angular integrals over α and θ to be calculated numerically. Thanks to this partial analytical treatment, the numerical integrals we had to compute were double integrals, which made them tractable. Note that initially, there were either 6, 8 or 10 successive integrations in each diagram, depending on the diagram structure: for instance, there are 8 of them in Eq. (3.46), which is a "mixed" diagram involving both G and G'.

These computations were carried out for several radii r between $0.1\,a$ and $1.5\,a$, and we varied both d and ξ for each of these radii. The effect of varying r is presented in the Appendix, Sec. 3.7. In particular, comparing the numerical results for small r to the analytical result in Eq. (3.49) provided a consistency check. Here, we will focus on the physical case $r = a$, where the radius of the contour is equal to the effective radius of the inclusions.

Our numerical results for $r = a$, presented synthetically in Fig. 3.5, show that the leading behavior of Δf_x^2 in a/d is well described by the formula

$$\Delta f_x^2 \sim 0.112 \frac{(k_\mathrm{B}T)^2}{a^2} \left[\ln\left(\frac{2\xi}{a}\right) - 0.239 - \frac{a^2}{d^2} \right], \tag{3.50}$$

which has the same main features as the analytical result Eq. (3.49) found in the limit $r \ll a$: the scalings with ξ and d are the same. The only difference is the presence of the constant -0.239, which is negligible compared to the logarithmic term. As it can be absorbed in the definition of ξ, we shall discard it from now on. Note that, in the physical regime, corresponding to $\xi \gg a$ and $d > 2a$, (3.50) is always positive.

3.4.3 Interpretation of the result

a. Leading term and cutoff-dependence

Our main result Eq. (3.50) shows that Δf_x^2 is dominated by a distance-independent term, which corresponds to the fluctuations of the zero-average force exerted on a single inclusion by the membrane bulk. This term is proportional to $(k_\mathrm{B}T)^2/a^2$: it is strongly cutoff-dependent (recall that the ultraviolet cutoff of our theory is $\Lambda = 2/a$). Force fluctuations calculated in other cases using coarse-grained theories also feature a cutoff-dependence (see, e.g., Refs. [33, 111]). In fact, within a coarse-grained theory, the result obtained for the force variance generically depends on the coarse-graining scale, while the average force does not. This will be discussed in more detail in Sec. 4.5.3.

More precisely, our leading term $\Delta f_x^2 \propto (k_\mathrm{B}T)^2/a^2$ indicates that the shortest wavelengths allowed in our theory, which are of order a, are those which contribute most to the variance of the force. This can be understood qualitatively as follows. Let us consider a local deformation of the membrane with, e.g., a spherical-cap shape. Assuming that the deformation extends over a zone of area ℓ^2 of the membrane, and has a curvature $2/\ell$, our membrane Hamiltonian Eq. (3.1) shows that

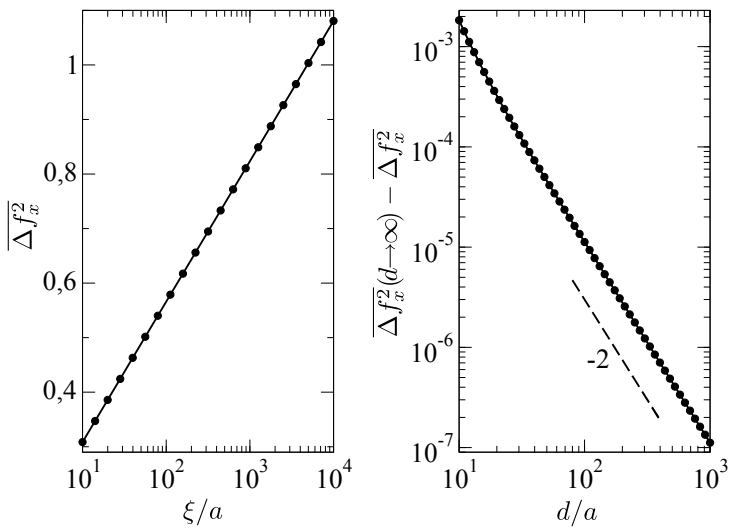

Figure 3.5: Results for $r = a$. Left: Non-dimensional force variance $\overline{\Delta f_x^2} = \beta^2 a^2 \Delta f_x^2$ for $d \to \infty$ as a function of ξ/a. The points are results from our numerical integrations, the line is the fit $\overline{\Delta f_x^2} = 0.112[\ln(2\xi/a) - 0.239]$. Right: d dependence of $\overline{\Delta f_x^2}$ for $\xi/a = 10^3$. Oscillations at the cutoff frequency have been smoothed out. The line is the fit $\overline{\Delta f_x^2}(d\to\infty) - \overline{\Delta f_x^2} = 0.112\, a^2/d^2 + 7.18\, a^4/d^4$. Similar results were obtained for other values of ξ/a (10^2 and 10^4), with the same coefficient in front of a^2/d^2.

its energy is $2\,\kappa$. Hence, the energetic cost of this local spherical-cap deformation is independent of its size. However, since the force we calculate depends on the local deformation of the membrane through the stress tensor, a membrane shape featuring a strong local deformation with a small extension at the place where the stress tensor is calculated will yield a large force. In particular, the membrane shapes featuring deformations over the shortest length allowed in our theory, $\ell = a$, will yield the largest forces. It is thus understandable that such membrane shapes should yield the dominant contribution to the variance of the force.

The strong cutoff dependence of the leading term seems to indicate that microscopic effects should be accounted for when calculating the force variance. In fact, it can be shown that the coarse-graining process leads to underestimating the force variance (see Sec. 4.5.3), as fluctuations with smaller length scales are disregarded. Let us thus continue discussing our result obtained within the continuum Helfrich theory, keeping in mind that it is probably slightly underestimated.

b. Signal-to-noise ratio

To leading order in a/d, the signal-to-noise ratio for the Casimir-like force (obtained from Eqs. (3.29) and (3.50)) verifies

$$\frac{\langle f_x \rangle}{\Delta f_x} \propto \left(\frac{a}{d}\right)^5 , \tag{3.51}$$

where the proportionality constant is $24\,[0.112 \ln(2\xi/a)]^{-\frac{1}{2}}$. This scaling law shows that the Casimir-like force is very small compared to its fluctuations in the physical case $d \gg a$: it is dominated by its fluctuations. If our result for the force variance is in fact underestimated, then this signal-to-noise ratio is even smaller.

c. Distance dependence

The subleading term in Eq. (3.50) shows that Δf_x^2 depends on the distance d between the inclusions. More precisely, when d is decreased from infinity, the variance of the Casimir-like force decreases as $-1/d^2$. This distance dependence of Δf_x^2 originates from the suppression of fluctuation modes by the constraints imposed by the two inclusions, so it shares a common physical origin with the Casimir-like effect.

To extract this d dependence, we can calculate

$$\frac{\partial \Delta f_x^2}{\partial d} \sim 0.224 \frac{(k_\mathrm{B}T)^2}{d^3}. \tag{3.52}$$

This quantity may be called the "Casimir-like effect relative to the fluctuations". It is independent of the cutoff, at least in the present case where point-like inclusions with effective radius a are considered. The question whether this universality holds for extended inclusions with dimension independent of the cutoff $\Lambda = 2/a$ would be interesting to address.

d. Comparison with the case of the scalar field

Ref. [111] investigated the variance of the Casimir-like force acting between two parallel (hyper)plates of dimension $\delta - 1$ imposing Dirichlet boundary conditions to a simple scalar field ϕ in dimension δ. The effective Hamiltonian, already mentioned in Eq. (2.14), reads

$$H[\phi] = \frac{\sigma}{2} \int d\boldsymbol{r}\ [\boldsymbol{\nabla}\phi(\boldsymbol{r})]^2 . \tag{3.53}$$

The variance obtained in this work features a leading cutoff-dependent term and a subleading universal distance-dependent term. These main features are shared by our result.

More precisely, let us focus on the two-dimensional situation ($\delta = 2$) to draw a comparison with the membrane: in this case, the (hyper)plates are long one-dimensional objects, i.e., rods. The signal-to-noise ratio of the Casimir-like force f_c obtained in Ref. [111] can then be put in the following form:

$$\frac{f_c}{\Delta f_c} \propto \frac{L^{\frac{1}{2}} a^{\frac{3}{2}}}{d^2} , \tag{3.54}$$

where d denotes the distance between the rods, L their length (see Fig. 2.4), and $a = 2/\Lambda$, where Λ is the ultraviolet cutoff. This ratio depends on L, a and d, and its domain of validity is $a \ll d \ll L$. Let us assume, e.g., that $a = 1$ nm and $L = 100\,\mu$m: then, the signal-to-noise ratio is equal to unity for $d = 56$ nm, and it can take large or small values depending whether d is smaller or larger than 56 nm. This is different from our result, where the signal-to-noise ratio is always small, as it scales as $(a/d)^5$. Another important difference regards the subleading, d-dependent term. In Ref. [111], when d is decreased from infinity, the variance of the Casimir-like force increases (as $1/d^{3/2}$ for $\delta = 2$), while in our results, the variance of the Casimir-like force then decreases as $-1/d^2$. It shows that this distance-dependent term in the variance, which stems from the suppression of fluctuating degrees of freedom, is nontrivial and quite tricky to understand qualitatively.

There are two main differences between the situation we have studied and the one investigated in Ref. [111]. The first one regards physics: the Hamiltonian and the stress tensor are different since different fields are considered, and the boundary conditions imposed by the objects are different too. The second one regards geometry: we have focused on point-like inclusions, while Ref. [111] dealt with (hyper)plates, i.e., rods in the two-dimensional case. The differences between the results can arise from both of these ingredients. In Chapter 5, we will discuss the average Casimir-like interactions between rods in membranes. It would be interesting to investigate the associated fluctuations and to compare the result to Eq. (3.54), in order to understand the effect of changing only the nature of the field while keeping the same geometry.

3.4.4 Other components

Until now, we have only discussed the variance of f_x. Recall that f_x is the projection along the x axis, which joins the two inclusions, of the force $\boldsymbol{f}$ exerted on inclusion 2 by the rest of the membrane containing inclusion 1. Let us now briefly discuss the variance of the other components of $\boldsymbol{f}$.

It is possible to calculate the variance of f_y and f_z using exactly the same method as for f_x. We have carried out these calculations analytically in the regime $r \ll a$, obtaining

$$\Delta f_y^2 \sim \frac{r^4 (k_\mathrm{B}T)^2}{3\,a^6} \left[\ln\left(\frac{2\xi}{a}\right) - 2\,\frac{a^2}{d^2} + \mathcal{O}\left(\frac{a^4}{d^4}\right) \right] , \tag{3.55}$$

$$\Delta f_z^2 \sim \frac{r^4 (k_\mathrm{B}T)^2}{3\,a^6} \left[4\pi\,\frac{\kappa}{k_\mathrm{B}T} + \mathcal{O}\left(\frac{a^4}{d^4}\right) \right] . \tag{3.56}$$

We observe that Δf_y^2 in Eq. (3.55) has a similar structure as Δf_x^2 in Eq. (3.49), while Δf_z^2 is different. Its leading term is proportional to $\kappa/(k_\mathrm{B}T)$, while κ did not appear in Δf_x^2 and Δf_y^2, and it features no logarithmic dependence in ξ/a. In addition, the dependence in a/d occurs at higher order in Δf_z^2 than in Δf_x^2 and Δf_y^2. These differences come from the fact that the z components of the stress tensor are first-order terms in h (see Eq. (3.25)), while the x and y components are

second-order terms in h (see Eqs. (3.23) and (3.24)). This fundamental difference arises in turn from the fact that the membrane is more deformable in the out-of-plane direction than in the in-plane directions. Note that such differences between the variance of in-plane and out-of-plane force components have been observed in Ref. [33] in the case of an inclusion-free membrane.

Summing the three contributions from Eqs. (3.49), (3.55) and (3.56) finally yields, for $r \ll a$:

$$\Delta \boldsymbol{f}^2 \sim \frac{r^4 (k_\mathrm{B}T)^2}{3\,a^6} \left[2\,\ln\left(\frac{2\xi}{a}\right) + 4\pi\,\frac{\kappa}{k_\mathrm{B}T} - 3\,\frac{a^2}{d^2} + \mathcal{O}\left(\frac{a^4}{d^4}\right) \right] , \tag{3.57}$$

Note that the contribution of Δf_z^2 to the d-independent term is large, given that $\kappa/(k_\mathrm{B}T) \simeq 25$ at ambient temperature: this contribution dominates over the one in $\ln(\xi/a)$ for $\xi = 100\,a$.

All the conclusions drawn in Sec. 3.4.3 from analyzing the behavior of Δf_x^2 also hold for the complete force variance $\Delta \boldsymbol{f}^2$, as the scaling laws in a and d are the same for Δf_x^2 and $\Delta \boldsymbol{f}^2$.

3.5 Inclusions inducing a nonzero curvature

Let us now consider inclusions imposing a finite local curvature (see, e.g., Fig. 3.1). In this case, the constraint Eq. (3.2) is replaced by

$$\mathbb{D}_i h(\boldsymbol{R}_i) = V \,, \tag{3.58}$$

for $i \in \{1, \ldots, 6\}$, where V contains the elements of the curvature tensors of the two inclusions. Let us restrict ourselves to two identical isotropic inclusions imposing a curvature $c \ll a^{-1}$ (see Fig. 3.6): this situation corresponds to $V = (c, 0, c, c, 0, c)$. The correspondence with finite-size inclusions imposing a contact angle variation α over a length a (see Fig. 2.5) is obtained for $c = \alpha/a$.

3.5.1 Partition function and average force

The partition function of the membrane containing the two curvature-inducing inclusions can be obtained using the same method as in the zero-curvature case (see Sec. 3.2.2) [72, 73]:

$$\begin{aligned} Z[u] = Z_0 \frac{(2\pi)^3}{\sqrt{\det M}} \exp\left[-\frac{1}{2} V_i M_{ij}^{-1} V_j + V_i\, M_{ij}^{-1} \int d\boldsymbol{r}\, u(\boldsymbol{r})\, \mathbb{D}_j G(\boldsymbol{r} - \boldsymbol{R}_j) \right] \\ \times \exp\left[\frac{1}{2} \int d\boldsymbol{r}\, d\boldsymbol{r}'\, u(\boldsymbol{r})\, C(\boldsymbol{r}, \boldsymbol{r}')\, u(\boldsymbol{r}') \right] , \end{aligned} \tag{3.59}$$

where the notations are those introduced in Eqs. (3.10), (3.11) and (3.12). Hence, there is an average deformation of the membrane due to the inclusions:

$$\langle h(\boldsymbol{r}) \rangle = \frac{1}{Z[0]} \left. \frac{\delta Z[u]}{\delta u(\boldsymbol{r})} \right|_{u=0} = V_i\, M_{ij}^{-1}\, \mathbb{D}_j G(\boldsymbol{r} - \boldsymbol{R}_j) \,, \tag{3.60}$$

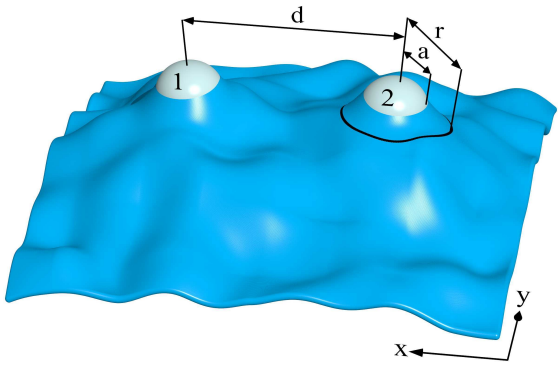

Figure 3.6: Two inclusions of radius a separated by a distance d in a fluctuating membrane. The inclusions impose an isotropic curvature to the membrane. The black line is a circular contour of radius r: its projection is used for the calculation of the Casimir-like force by integration of the stress tensor.

and the correlation function of the height of the membrane reads

$$\langle h(\boldsymbol{r})\, h(\boldsymbol{r}')\rangle - \langle h(\boldsymbol{r})\rangle\langle h(\boldsymbol{r}')\rangle = \frac{1}{Z[0]}\,\frac{\delta^2 Z[u]}{\delta u(\boldsymbol{r})\delta u(\boldsymbol{r}')}\bigg|_{u=0} - \langle h(\boldsymbol{r})\rangle\langle h(\boldsymbol{r}')\rangle = C(\boldsymbol{r},\boldsymbol{r}')\,. \tag{3.61}$$

Hence, within our harmonic description of the small deformations of the membrane with respect to the flat shape, the correlation function is the same for inclusions that impose a nonzero curvature as for inclusions that impose a zero curvature.

By integrating the average stress tensor over a contour that surrounds one inclusion but not the other (see Fig. 3.6), we obtain the following average force:

$$\langle f_x\rangle = 24\, k_{\mathrm{B}}T\,\frac{a^4}{d^5} - 32\pi\kappa\,\alpha^2\,\frac{a^4}{d^5} + \frac{1}{a}\,\mathcal{O}\!\left(\frac{a^7}{d^7}\right). \tag{3.62}$$

Again, this is identical to the result obtained by differentiating the free energy $F = -k_{\mathrm{B}}T\ln(Z[0])$ of the membrane with respect to d. We thus recover from the stress tensor the total membrane-mediated interaction [70–72], which includes an elastic force due to the average deformation of the membrane in addition to the Casimir-like force (see Eq. (3.29)), as described in Sec. 2.5.

3.5.2 Variance of the force

Studying the fluctuations of f_x is a straightforward generalization of the work presented above in the zero-curvature case. The only difference stems from the average deformation. Formally, Wick's theorem now applies to $h(\boldsymbol{r}) - \langle h(\boldsymbol{r})\rangle$ instead of $h(\boldsymbol{r})$, so that additional diagrams involving $\langle h(\boldsymbol{r})\rangle$ appear in the calculation. In the limit $r \ll a$, we obtain analytically

$$\Delta f_x^2 \sim \frac{r^4(k_{\mathrm{B}}T)^2}{3\,a^6}\left[\left(1+12\pi\beta\kappa\alpha^2\right)\ln\left(\frac{2\,\xi}{a}\right) - \left(1+8\pi\beta\kappa\alpha^2\right)\frac{a^2}{d^2} + \mathcal{O}\!\left(\frac{a^4}{d^4}\right)\right]. \tag{3.63}$$

The conclusions drawn in Sec. 3.4.3 in the vanishing curvature case still hold, as the scaling laws in a and d remain unchanged. Besides, here, the "Casimir-like effect relative to the fluctuations" introduced in Sec. 3.4.3 reads, for $r \ll a$,

$$\frac{\partial \Delta f_x^2}{\partial d} \sim \frac{2}{3}\left(1 + 8\pi\beta\kappa\alpha^2\right)\frac{r^4 (k_\mathrm{B}T)^2}{a^4 d^3}\,. \tag{3.64}$$

Thus, in the non-small curvature regime $\alpha > (8\pi\beta\kappa)^{-1/2}$ (see Sec. 2.5.1), we obtain

$$\frac{\partial \Delta f_x^2}{\partial d} \propto \frac{k_\mathrm{B}T\kappa\alpha^2}{d^3}. \tag{3.65}$$

The $k_\mathrm{B}T\kappa\alpha^2$ factor, which replaces the $(k_\mathrm{B}T)^2$ appearing in the pure Casimir-like case (see Eq. (3.52)), reveals the interplay between the Casimir-like force and the curvature-dependent force. These two effects, which are decoupled on average (see Eq. (3.62)), become coupled in the variance, which is a quadratic quantity.

3.6 Conclusion

The stress tensor is a powerful tool that allows for studying the Casimir-like force between membrane inclusions, especially its fluctuations.

Using a coarse-grained description in which the inclusions are point-like and impose local curvature constraints on the membrane, we have calculated the variance of the Casimir-like force. Our results show that the fluctuations dominate over the average force: the signal-to-noise ratio of the Casimir-like force scales as $(a/d)^5$, where a is the effective radius of the inclusions, and $d \gg a$ is the distance between them. In addition, we have studied the d-dependence of these fluctuations: when the distance d between the inclusions is decreased from infinity, the variance of the Casimir-like force decreases as $-1/d^2$. We have also shed light on the interplay in the force variance between the Casimir-like force and the force due to the average membrane deformation.

Further interesting developments would include treating the case of extended inclusions, and testing our results using coarse-grained membrane numerical simulations such as those in Ref. [103].

3.7 Appendix: Effect of varying the radius of the contour

In the main text, we presented analytical results obtained in the limit $r \ll a$, and numerical ones obtained for the physical case $r = a$. Let us now show how Δf_x^2 varies with the radius r of the integration contour. Numerical calculations of Δf_x^2 were conducted for different radii ranging from $0.1\,a$ to $1.5\,a$. Performing the same studies of the behavior of Δf_x^2 with d and ξ as those presented for $r = 1$ in Fig. 3.5 shows that, for all these values of r, Δf_x^2 is well described by the law

$$\Delta f_x^2 = \phi\left(\frac{r}{a}\right)\frac{(k_\mathrm{B}T)^2}{a^2}\left[\ln\left(\frac{2\xi}{a}\right) + \chi\left(\frac{r}{a}\right) - \psi\left(\frac{r}{a}\right)\frac{a^2}{d^2}\right]. \tag{3.66}$$

Note that Eq. (3.66) generalizes Eqs. (3.49) and (3.50). The graphs of the functions ϕ, ψ and χ are presented below, in Fig. 3.7.

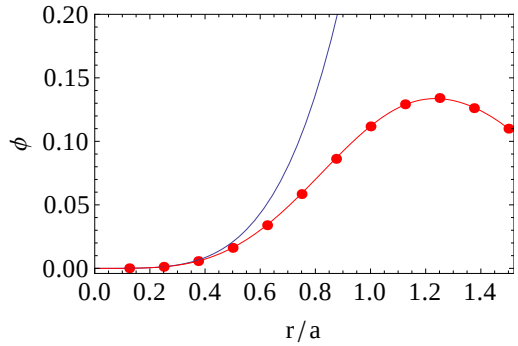

(a) Evolution of ϕ with r/a. Red dots: numerical results. Red line: polynomial interpolation (guide for the eye). Blue line: analytical result obtained for $r \ll a$: $\phi(r/a) = (r/a)^4/3$.

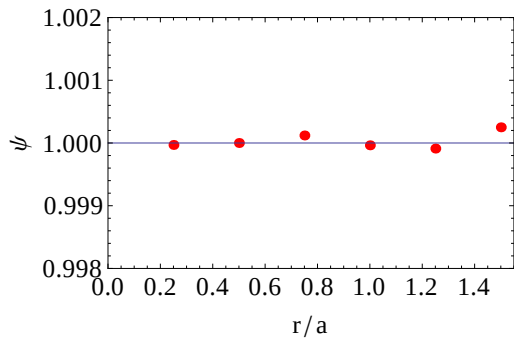

(b) Evolution of ψ with r/a. Red dots: numerical results. Blue line: analytical result obtained for $r \ll a$: $\psi(r/a) = 1$.

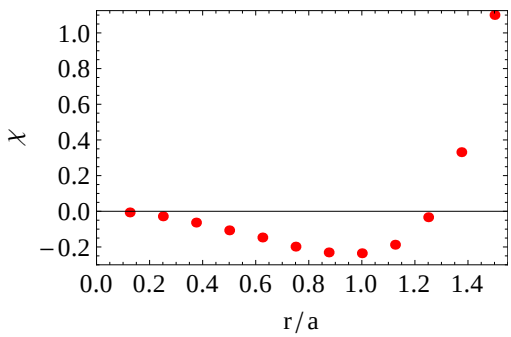

(c) Evolution of χ with r/a. Red dots: numerical results. The analytical calculation for $r \ll a$ gives $\chi(r/a) = 0$.

Figure 3.7: Evolution with r/a of the functions ϕ, ψ and χ involved in Δf_x^2 (see Eq. (3.66)). The numerical data is compared to the results of the analytical calculation conducted for $r \ll a$, which gives $\phi(r/a) = (r/a)^4/3$, $\psi(r/a) = 1$ and $\chi(r/a) = 0$ (see Eq. (3.49)).

For small r, we obtain good agreement between the numerical results and the analytical calculation conducted for $r \ll a$, which provides a consistency check. Besides, the fact that the law Eq. (3.66) describes well the data shows that the important features of our result, i.e., the scaling laws in a, d and ξ, are independent of the contour radius.

Chapter 4

Forces exerted by a correlated fluid on embedded inclusions

Contents

4.1 Introduction **76**

4.2 Embedded inclusion **77**

4.2.1 First route 79

4.2.2 Second route 80

4.2.3 Domain of application 82

4.2.4 Mean-field configuration 83

4.3 Non-embedded influencing object **83**

4.3.1 First route 84

4.3.2 Second route 85

4.3.3 Mean-field configuration 86

4.3.4 Formal relation between the two types of forces 86

4.4 Casimir-like force **87**

4.4.1 Embedded inclusions 87

4.4.2 Non-embedded influencing objects 89

4.5 A simple example of Casimir-like force **90**

4.5.1 The situation 90

4.5.2 Average Casimir-like force 92

4.5.3 Variance of the Casimir-like force 92

4.6 Discussion **96**

4.7 Conclusion **99**

4.8 Appendix **100**

4.8.1 Definition of the force f from the principle of virtual work 100

4.8.2 Derivation of the stress tensor T of the fluid medium . . 102

4.8.3 Stress tensor of the fluid medium with a perturbative embedded inclusion 104
4.8.4 Point-like embedded inclusion or non-embedded influencing object 105

4.1 Introduction

In Chapter 3, we presented our study of the fluctuations of the Casimir-like force between two membrane inclusions. This work has driven us to reflect upon the definition of the force exerted by a correlated fluid on an embedded inclusion in a given microstate of the fluid, which is a necessary ingredient to study the Casimir-like force beyond its thermal average value. Indeed, while we used the stress tensor to define this force in Chapter 3, another definition is also currently used in the literature, and these two definitions yield different results. We present here a study of the assumptions underlying these two definitions, and of their respective domains of application. Hence, this Chapter is strongly related to the previous one, while being more general. We will not only be concerned with inclusions in membranes, but with inclusions in correlated fluids.

Let us consider a fluid medium with long-range correlations, and inclusions embedded in this medium. Let us assume that, on a large scale, the state of the correlated fluid can be described by an effective scalar field theory. The inclusions, which are solid objects immersed in it, generically impose constraints on the field describing the state of the medium, and in particular, on its fluctuations. Due to these constraints, the force exerted by the medium on one inclusion depends on the position of the other inclusions, yielding Casimir-like interactions between inclusions (see Chapter 2).

The Casimir-like force between two inclusions is usually defined as $-\partial F/\partial \ell$, where F is the free energy of the fluid medium with two inclusions separated by a distance ℓ. However, this definition only provides a thermal average force. In order to study the fluctuations of the force, as well as out-of-equilibrium situations, it is necessary to define the force exerted on an inclusion by a fluid medium in each microstate of this medium. Two different definitions of this force are currently used. The first one uses the stress tensor of the medium [111, 114, 121–125]. It is the one we used in Chapter 3 to investigate the fluctuations of the Casimir-like force between two membrane inclusions. The second one is based on differentiating the effective Hamiltonian with respect to the position of the inclusion while keeping constant the field that describes the state of the medium [126–129]. The aim of the present work is to clarify the difference between these two definitions and to determine their respective domains of validity.

In this Chapter, we consider a correlated fluid medium described by a scalar field ϕ: each microstate of this effective field theory corresponds to a given ϕ. We study the force $\boldsymbol{f}$ exerted by this fluid medium on an embedded inclusion. This force $\boldsymbol{f}$ is defined as the negative gradient of the effective Hamiltonian H of the medium

together with the inclusion, with respect to the position of the inclusion. The validity of this fundamental definition in our coarse-grained description is justified in the Appendix, Sec. 4.8.1. In order to determine $\boldsymbol{f}$ in a given microstate of the medium, *the gradient of H must be taken in this microstate*. There are two distinct ways of interpreting these words, yielding two different routes to calculate the force. In the first route, the field ϕ is kept constant in the Eulerian sense, i.e., ϕ remains the same at each point in space. In the second route, ϕ is kept constant in the Lagrangian sense, i.e., each fluid particle of the medium keeps the same value of ϕ during the infinitesimal deformation that is associated with the displacement of the inclusion. We show that the second route gives the integral of the stress tensor of the medium on the boundary of the inclusion, which corresponds to the definition used in Refs. [111, 114, 121–125]. We argue that this definition is the right one for an embedded inclusion. We also consider the case of *non-embedded influencing objects*, which interact with the medium without being embedded in it, and we argue that the first route, which corresponds to the definition used in Refs. [126–129], is the right one in such situations.

This Chapter is organized as follows: in Sec. 4.2, we study the force $\boldsymbol{f}$ exerted on an inclusion by the fluid medium in a given microstate, starting from the variation of the total energy of the system when it undergoes a generic infinitesimal deformation, and we compare the two routes introduced above. In Sec. 4.3, we proceed similarly in the case of a non-embedded influencing object. In Sec. 4.4, we show the link between the thermal average of the force $\boldsymbol{f}$ and the Casimir-like force. In Sec. 4.5, we study a simple example of Casimir-like force, where we show that the variance of the force depends strongly on the route that is chosen. This example illustrates the importance of choosing the right definition when studying Casimir-like forces beyond their average value at thermal equilibrium. Finally, Sec. 4.6 is a discussion and Sec. 4.7 a conclusion.

The work presented in this Chapter has been published in: A.-F. Bitbol and J.-B. Fournier, *Forces exerted by a correlated fluid on embedded inclusions*, Physical Review E 83, 061107 (2011), cited as Ref. [130] here.

We thank Andrea Gambassi and David S. Dean for stimulating discussions on this subject.

4.2 Embedded inclusion

Let us consider an infinite d-dimensional fluid medium ($d \geq 1$) with short-range interactions, described in a coarse-grained fashion by a scalar field ϕ with Hamiltonian density $\mathcal{H}(\phi, \boldsymbol{\nabla}\phi)$. Note that including a dependence of $\mathcal{H}$ in higher-order derivatives of ϕ is necessary in many physical cases. In particular, membrane models involve the membrane curvature, and thus, second derivatives of the height of the membrane, which is then the relevant field ϕ. In the present Chapter, we will remain in the simple case where $\mathcal{H}$ only depends on ϕ and $\boldsymbol{\nabla}\phi$ for the sake of simplicity, but it is straightforward to adapt our work to other cases.

Let us assume that an embedded inclusion with center of mass in $\boldsymbol{\ell} \in \mathbb{R}^d$ extends

over a region $\mathcal{A}$ of the medium (see Fig. 4.1). The inclusion is made of a different material, typically a solid, where the physical field ϕ is not defined. For instance, in critical binary mixtures, ϕ is the order parameter, i.e., the shifted concentration in one component: $\phi = c - c^{\text{crit}}$, where c^{crit} is the critical concentration of this component [124][1], so ϕ is not defined in solid objects immersed in the mixture.

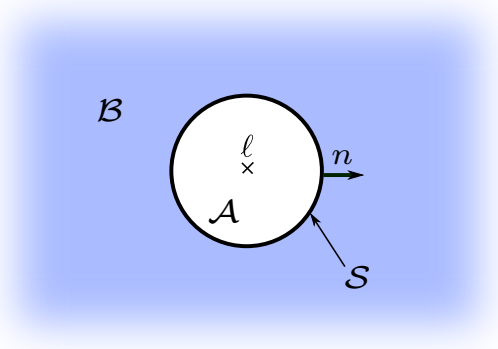

Figure 4.1: Schematic representation of an inclusion (white) embedded in a two-dimensional fluid medium (shaded). The inclusion extends over $\mathcal{A}$, which is centered on $\boldsymbol{\ell}$, so ϕ is defined only on $\mathcal{B} = \mathbb{R}^2 \setminus \mathcal{A}$. The contour of $\mathcal{A}$ is called $\mathcal{S}$, and $\boldsymbol{n}$ denotes its outward normal.

Since the embedded inclusion extends over the region $\mathcal{A}$, delimited by the hypersurface $\mathcal{S}$, ϕ is defined only in the region $\mathcal{B} = \mathbb{R}^d \setminus \mathcal{A}$ (see Fig. 4.1). We assume that the field ϕ is coupled to the inclusion at the interface $\mathcal{S}$ through short-range interactions modeled by a potential $V(\phi)$, so the effective Hamiltonian of the system reads

$$H = \int_{\mathcal{B}} \mathcal{H}(\phi, \boldsymbol{\nabla}\phi)\, d^d r + \int_{\mathcal{S}} V(\phi)\, d^{d-1} r + E_{\text{incl}}\,, \tag{4.1}$$

where E_{incl} represents the internal energy of the inclusion, which will not be varied in the following. Note that our work can be generalized to a more general coupling potential, such as $V(\phi, \boldsymbol{\nabla}\phi)$. While our proofs will be presented with $V(\phi)$ for the sake of simplicity, the final results for the force with $V(\phi, \boldsymbol{\nabla}\phi)$ will be mentioned.

Our aim is to calculate the force $\boldsymbol{f}$, which is defined as

$$\boldsymbol{f} = -\frac{\delta H}{\delta \ell_i}\, \boldsymbol{e}_i\,, \tag{4.2}$$

where $\boldsymbol{e}_i$ is a unit vector in the i direction. The Einstein summation convention has been used in Eq. (4.2), and will be used throughout. The validity of the fundamental definition Eq. (4.2) in our coarse-grained description is justified in the Appendix, Sec. 4.8.1, from the principle of virtual work.

In order to obtain $\boldsymbol{f}$, we must calculate the variation of H when the inclusion undergoes the infinitesimal displacement $\boldsymbol{\delta\ell}$. Since it is impossible to move an

[1] Note that Ref. [124] deals with critical systems in general, and thus ϕ is, more generally, the order parameter of the transition.

embedded inclusion without moving the fluid particles of the surrounding medium, we will consider a displacement field $\boldsymbol{\delta r}$ in the whole medium. We use the expression "fluid particle" in a similar way as in fluid mechanics [131]: it denotes a (macroscopically) closed mesoscopic part of the fluid medium, the state of which is described by the value of the coarse-grained field ϕ. Let us consider the generic infinitesimal transformation

$$\begin{cases} \boldsymbol{r} & \to & \boldsymbol{r} + \boldsymbol{\delta r}(\boldsymbol{r}) \,, \\ \phi(\boldsymbol{r}) & \to & \phi(\boldsymbol{r}) + \delta\phi(\boldsymbol{r}) \,. \end{cases} \tag{4.3}$$

More explicitly, the particle initially in $\boldsymbol{r}$ undergoes the infinitesimal displacement $\boldsymbol{\delta r}(\boldsymbol{r})$, and the value of ϕ at a fixed point $\boldsymbol{r}$ in space is modified by the quantity $\delta\phi(\boldsymbol{r})$. The functions $\boldsymbol{\delta r}$ and $\delta\phi$, defined respectively on $\mathbb{R}^d$ and on $\mathcal{B}$, are assumed to be regular and to take small values, of order ϵ (i.e., $\delta\phi = \mathcal{O}(\epsilon)$ and $|\boldsymbol{\delta r}|/L = \mathcal{O}(\epsilon)$ where L is the characteristic length of interest, e.g., the distance between two inclusions in a study of the Casimir-like force). During this transformation, the total (Lagrangian) variation of ϕ for the fluid particle initially in $\boldsymbol{r}$ is $\delta^T\phi(\boldsymbol{r}) = (\phi+\delta\phi)(\boldsymbol{r}+\boldsymbol{\delta r}) - \phi(\boldsymbol{r}) = \delta\phi(\boldsymbol{r}) + \boldsymbol{\nabla}\phi(\boldsymbol{r}) \cdot \boldsymbol{\delta r}(\boldsymbol{r})$ at first order in ϵ.

Let us assume that in the region $\mathcal{A}$, $\boldsymbol{\delta r}$ is constant, equal to $\boldsymbol{\delta \ell}$: thus, the inclusion undergoes an infinitesimal global translation that does not affect its internal energy E_{incl}. The total variation of the energy then reads, at first order in ϵ:

$$\begin{aligned} \delta H = & \int_{\mathcal{B}} \left[\frac{\partial \mathcal{H}}{\partial \phi} - \partial_i \left(\frac{\partial \mathcal{H}}{\partial(\partial_i \phi)} \right) \right] \delta\phi \, d^d r - \int_{\mathcal{S}} \left[\mathcal{H} \delta \ell_i + \frac{\partial \mathcal{H}}{\partial(\partial_i \phi)} \delta\phi \right] n_i \, d^{d-1} r \\ & + \int_{\mathcal{S}} \frac{\partial V}{\partial \phi} \left(\delta\phi + \partial_i \phi \, \delta \ell_i \right) \, d^{d-1} r \,, \end{aligned} \tag{4.4}$$

where we have introduced $\boldsymbol{n}$, the exterior normal to $\mathcal{S}$ (see Fig. 4.1), and we have used the notation $\partial_i \phi \equiv \partial\phi/\partial r_i$ for $i \in \{1, \ldots, d\}$. In this equation, the hypervolume integral on $\mathcal{B}$ contains the standard Euler-Lagrange term. Meanwhile, the first term of the first hypersurface integral comes from

$$\int_{\delta\mathcal{B}} \mathcal{H} \, d^d r = - \int_{\mathcal{S}} \mathcal{H} \delta \ell_i n_i \, d^{d-1} r \,, \tag{4.5}$$

while its second term is obtained via Stokes' theorem:

$$\int_{\mathcal{B}} \partial_i \left(\frac{\partial \mathcal{H}}{\partial(\partial_i \phi)} \delta\phi \right) d^d r = - \int_{\mathcal{S}} \frac{\partial \mathcal{H}}{\partial(\partial_i \phi)} \delta\phi \, n_i \, d^{d-1} r \,. \tag{4.6}$$

We may now calculate the force $\boldsymbol{f}$, as defined in Eq. (4.2), in a given microstate of the fluid medium. We will examine successively the two different routes presented in the introduction, which correspond to two different ways of keeping ϕ constant.

4.2.1 First route

The first way we may proceed is to keep ϕ constant at each point in space during the infinitesimal transformation, or, in other words, to keep the field ϕ constant in

the Eulerian sense. This amounts to taking $\delta\phi \equiv 0$ in Eq. (4.4), which gives:

$$\boldsymbol{f}^{(1)} = -\boldsymbol{e}_i \left.\frac{\delta H}{\delta \ell_i}\right|_{\phi,\,\mathrm{Eul.}} = \int_{\mathcal{S}} \left(\mathcal{H} n_i - \frac{\partial V}{\partial \phi} \partial_i \phi \right) d^{d-1}r \; \boldsymbol{e}_i \,. \tag{4.7}$$

In the case where the coupling potential is $V(\phi, \boldsymbol{\nabla}\phi)$ instead of $V(\phi)$, a term $-(\partial V/\partial(\partial_j\phi))\partial_i\partial_j\phi$ has to be added in the brackets in Eq. (4.7).

However, it is physically not clear why each point in space should keep the same value of ϕ during a displacement in which each fluid particle of the system moves by $\boldsymbol{\delta r}$. Another more formal argument also shows that it is artificial to keep the function ϕ constant while moving infinitesimally the inclusion: the domain of definition of ϕ itself depends on the position of the inclusion. For instance, when the inclusion is moved from $\mathcal{A}$ (centered on $\boldsymbol{\ell}$) to $\mathcal{A}'$ (centered on $\boldsymbol{\ell} + \boldsymbol{\delta\ell}$), the initial ϕ is not defined in the region $\mathcal{A} \smallsetminus \mathcal{A}'$ where it should exist after the transformation (see Fig. 4.2). One way to deal with this mathematical issue is to consider the analytic continuation of ϕ in this small region, and to truncate ϕ in $\mathcal{A}' \smallsetminus \mathcal{A}$, but the physical meaning of this process is unclear.

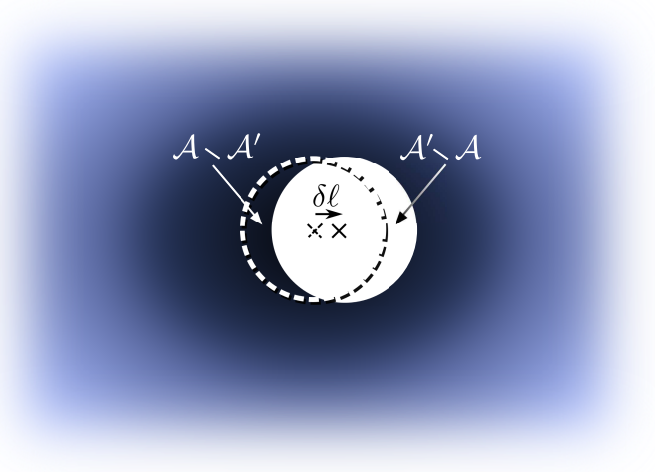

Figure 4.2: Schematic representation of an inclusion embedded in a two-dimensional fluid medium. The inclusion undergoes a small translation of $\delta\ell$. It is initially in the disk with dashed contour, which we call $\mathcal{A}$, while after the displacement, it stands in the white disk, which we call $\mathcal{A}'$. The initial ϕ is not defined in the region $\mathcal{A} \smallsetminus \mathcal{A}'$, and similarly, the final ϕ is not defined in the region $\mathcal{A}' \smallsetminus \mathcal{A}$.

In other words, this first route is not adapted to calculate the force on an embedded inclusion because the position $\boldsymbol{\ell}$ of the inclusion and the Eulerian field ϕ are not independent variables. Let us now move on to the second route.

4.2.2 Second route

Let us consider the example of critical binary mixtures, where ϕ is the (shifted) concentration: during a displacement that is smooth at the microscopic scale, each

fluid particle keeps the same concentration, so ϕ is transported by fluid particles. Similarly, in the case of liquid crystals, the order parameter field is transported. The case of membranes and interfaces is a little bit more complex (see the discussion in Sec. 4.2.3).

Let us focus on fields that are transported by fluid particles during a deformation[2]. For such a field ϕ, the correct force $\boldsymbol{f}$ will be provided by the second route defined in the introduction, where ϕ is kept constant in the Lagrangian sense, i.e., each fluid particle of the medium keeps a constant ϕ during the infinitesimal transformation. In this case, $\delta^T\phi \equiv 0$, so that $\delta\phi(\boldsymbol{r}) = -\boldsymbol{\nabla}\phi(\boldsymbol{r}) \cdot \boldsymbol{\delta r}(\boldsymbol{r})$ for all $\boldsymbol{r}$ in $\mathcal{B}$: Eq. (4.4) becomes

$$\delta H = -\int_{\mathcal{B}} \left[\frac{\partial \mathcal{H}}{\partial \phi} - \partial_j \left(\frac{\partial \mathcal{H}}{\partial(\partial_j \phi)}\right)\right] \partial_i \phi \, \delta r_i \, d^d r - \delta \ell_i \int_{\mathcal{S}} \left[\mathcal{H}\delta_{ij} - \frac{\partial \mathcal{H}}{\partial(\partial_j \phi)} \partial_i \phi\right] n_j \, d^{d-1} r \,. \tag{4.8}$$

Using the stress tensor $\boldsymbol{T}$ of the fluid medium, which is discussed and derived in the Appendix, in Sec. 4.8.2, and which reads

$$T_{ij} = \mathcal{H}\delta_{ij} - \frac{\partial \mathcal{H}}{\partial(\partial_j \phi)} \partial_i \phi \,, \tag{4.9}$$

and its divergence

$$\partial_j T_{ij} = \left[\frac{\partial \mathcal{H}}{\partial \phi} - \partial_j \left(\frac{\partial \mathcal{H}}{\partial(\partial_j \phi)}\right)\right] \partial_i \phi = \frac{\delta H}{\delta \phi} \partial_i \phi \,, \tag{4.10}$$

we can rewrite Eq. (4.8) as

$$\delta H = -\int_{\mathcal{B}} \partial_j T_{ij} \, \delta r_i \, d^d r - \delta \ell_i \int_{\mathcal{S}} T_{ij} n_j \, d^{d-1} r \,. \tag{4.11}$$

This relation being valid for any continuous displacement field $\boldsymbol{\delta r}$ such that $\forall \boldsymbol{r} \in \mathcal{A}$, $\boldsymbol{\delta r} = \boldsymbol{\delta \ell}$, it yields the force $\boldsymbol{f}^{(2)}$ exerted by the medium on the inclusion, and the hypervolume density $\boldsymbol{q}$ of internal forces in the fluid medium. Indeed, we can carry out an identification with Eq. (4.83), which comes from the principle of virtual work (see the Appendix, Sec. 4.8.1). We obtain

$$\boldsymbol{f}^{(2)} = -\boldsymbol{e}_i \left.\frac{\delta H}{\delta \ell_i}\right|_{\phi,\,\text{Lagr.}} = \int_{\mathcal{S}} T_{ij} n_j \, d^{d-1} r \, \boldsymbol{e}_i \,, \tag{4.12}$$

$$\forall \boldsymbol{r} \in \mathcal{B}, \;\; \boldsymbol{q}(\boldsymbol{r}) = -\frac{\delta H}{\delta r_i(\boldsymbol{r})} \boldsymbol{e}_i = \partial_j T_{ij}(\boldsymbol{r}) \, \boldsymbol{e}_i \,. \tag{4.13}$$

This second method of calculating $\boldsymbol{f}$ gives the integral of the stress tensor of the fluid medium on the boundary $\mathcal{S}$ of the inclusion. Contrary to $\boldsymbol{f}^{(1)}$, the force $\boldsymbol{f}^{(2)}$ does not depend on the short-range coupling V between the inclusion and the

[2]We make the following assumptions regarding the deformation field $\boldsymbol{\delta r}$: it is assumed to be a continuous function of $\boldsymbol{r}$, and it is assumed to be constant within the inclusion. Thus, the inclusion undergoes a rigid translation, but the surrounding fluid can undergo a more general motion.

medium (in particular, Eq. (4.12) holds for $V(\phi, \boldsymbol{\nabla}\phi)$ as well as for $V(\phi)$). This comes from the continuity of the function $\boldsymbol{\delta r}$: the fluid particles of the medium that are infinitesimally close to the inclusion undergo the same small displacement as the inclusion, so the short-range interaction between the medium and the inclusion does not vary during the displacement. In a real displacement in a viscous fluid, the displacement field has to be continuous at the inclusion boundary, and we consider virtual displacements consistent with this constraint. Note that although the force $\boldsymbol{f}^{(2)}$ in each microstate does not depend on V, the usual Casimir-like force, which is the thermal average of $\boldsymbol{f}^{(2)}$ (see Sec. 4.4), can depend on V since the statistical weight of each microstate depends on V.

Thus, the right definition of the force exerted by the medium on an embedded inclusion, obtained via the second route, is given by the integral of the stress tensor of the medium. This corresponds to the definition used in Refs. [111, 114, 121–125], and it is also very close to the definition used in Refs. [132, 133], which is based on integrating a density-dependent pressure on the boundary of the inclusion.

4.2.3 Domain of application

We have considered a Hamiltonian density $\mathcal{H}$ and a coupling potential V depending on ϕ and $\boldsymbol{\nabla}\phi$. More generally, $\mathcal{H}$ and V can depend on higher-order derivatives of ϕ. Our work can be adapted to such cases. In particular, the force $\boldsymbol{f}^{(2)}$ exerted on an inclusion can be expressed as the integral of the stress tensor of the medium also in these cases. The stress tensor associated with a Hamiltonian (or Lagrangian) density involving higher-order derivatives is discussed, e.g., in Refs. [134, 135].

We have focused on fields that are transported by fluid particles during a displacement, such as the order parameter field in a critical mixture or in a liquid crystal. However, our reasoning can be adapted to other cases, especially when the field ϕ has a direct relation to the position of the fluid particle. For instance, the Hamiltonian density of a membrane described in the Monge gauge depends on the height $\phi(x, y)$ of the membrane with respect to a reference plane: for a displacement $\boldsymbol{\delta r}(x, y)$ of the fluid particle initially in (x, y), the variation of the height ϕ at point (x, y) is $\delta\phi = \delta r_z - \partial_x\phi\,\delta r_x - \partial_y\phi\,\delta r_y$ instead of $\delta\phi = -\partial_i\phi\,\delta r_i$. The membrane stress tensor takes this particularity into account in its construction (see Refs. [101, 113], and Chapter 12 of the present thesis). Note that membrane models involve the membrane curvature, and thus, second derivatives of the membrane height ϕ.

In spite of this wider domain of application, the present work is restricted to the case of a fluid medium described by a scalar field ϕ such that its change during an infinitesimal displacement is a function of this infinitesimal displacement. More precisely, the relation $\delta\phi = -\partial_i\phi\,\delta r_i$ (or its equivalent for the membrane) is crucial in our derivation of $\boldsymbol{f}^{(2)}$. As a counterexample, let us consider a one-dimensional elastic solid described by a scalar deformation field $\phi(X) = x(X) - X$, where X is the position of a particle in the reference (nondeformed) configuration of the solid, while $x(X)$ is its position in the deformed configuration considered. In this case, changing the reference coordinate X of a particle has no link with changing the deformation field ϕ.

In addition, the assumption that the displacement $\boldsymbol{\delta r}$ is continuous at the boundary of the inclusion is valid for a viscous fluid, however small its viscosity, but not for an ideal fluid. In the latter case, only the component of the displacement normal to the inclusion boundary has to be continuous. Thus, our approach may not be fully adapted to a superfluid. However, it is adapted to study Casimir-like forces in a superfluid in the parallel plate geometry, which is the one usually considered. Indeed, modifying the distance between the plates involves a displacement perpendicular to the plates.

4.2.4 Mean-field configuration

The quantities $\boldsymbol{f}^{(1)}$ and $\boldsymbol{f}^{(2)}$ obtained via the two different routes are, in general, not equal. However, they cannot be distinguished in the most probable configuration of the field ϕ, i.e., in the mean-field configuration. Indeed, this configuration is such that the energy H is stationary with respect to variations of ϕ:

$$0 = \delta H = \int_{\mathcal{B}} \left[\frac{\partial \mathcal{H}}{\partial \phi} - \partial_i \left(\frac{\partial \mathcal{H}}{\partial(\partial_i \phi)} \right) \right] \delta\phi \, d^d r + \int_{\mathcal{S}} \left[\frac{\partial V}{\partial \phi} - \frac{\partial \mathcal{H}}{\partial(\partial_i \phi)} n_i \right] \delta\phi \, d^{d-1} r \,, \quad (4.14)$$

for any $\delta\phi$. The bulk equilibrium condition yields the usual Euler-Lagrange equation, valid on $\mathcal{B}$:

$$\frac{\partial \mathcal{H}}{\partial \phi} - \partial_i \left(\frac{\partial \mathcal{H}}{\partial(\partial_i \phi)} \right) = 0 \,, \quad (4.15)$$

while the boundary equilibrium condition gives the following relation, valid on $\mathcal{S}$:

$$\frac{\partial V}{\partial \phi} = \frac{\partial \mathcal{H}}{\partial(\partial_i \phi)} n_i \,. \quad (4.16)$$

When Eq. (4.16) holds, $\boldsymbol{f}^{(1)}$ (see Eq. (4.7)) and $\boldsymbol{f}^{(2)}$ (see Eq. (4.12)) are identical. Thus, the difference between the two routes is irrelevant when one considers the mean-field configuration.

4.3 Non-embedded influencing object

Let us now study the case of an object that interacts with the fluid medium without being embedded in it (see Fig. 4.3). For instance, it may be an optical trap creating a local electromagnetic field in the medium, or a protein binding very softly onto a lipid membrane so that the latter keeps its fluidity: in these cases, there is no material object immersed in the medium. We will refer to this type of object as an "influencing object", to make the distinction with the embedded inclusion. We will see that, contrary to the case of the embedded inclusion, it is here the first route that gives the correct force $\boldsymbol{f}$.

In the case of the influencing object, the field ϕ with Hamiltonian density $\mathcal{H}$ is defined everywhere in $\mathbb{R}^d$ (recall that the d-dimensional fluid medium is assumed to be infinite). In the region $\mathcal{A}$, the medium is affected by the influencing object: a term $V(\phi)$, representing the interaction between the influencing object and the

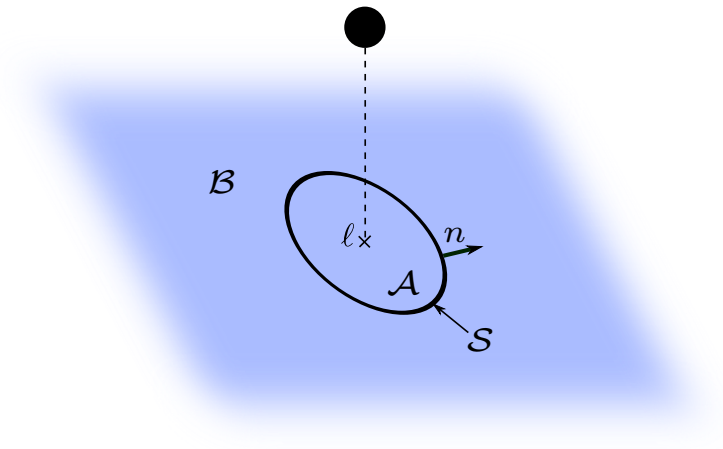

Figure 4.3: Schematic representation of a two-dimensional fluid medium with an influencing object. The object, represented by a black sphere, is not embedded in the medium (here, it is above the plane where the medium stands). It influences the medium, i.e., the field ϕ, in a region $\mathcal{A}$, which is centered on $\boldsymbol{\ell}$. The other notations are the same as in Fig. 4.1.

medium, adds to $\mathcal{H}$. The effective Hamiltonian H of the fluid medium with the influencing object reads

$$H = \int_{\mathbb{R}^d} \mathcal{H}(\phi, \boldsymbol{\nabla}\phi)\, d^d r + \int_{\mathcal{A}} V(\phi)\, d^d r = \int_{\mathbb{R}^d} [\mathcal{H} + V\, \mathbf{1}_{\mathcal{A}}]\, d^d r\,, \tag{4.17}$$

where $\mathbf{1}_{\mathcal{A}}$ is the indicator function of the region $\mathcal{A}$. Here too, our work can be generalized to $V(\phi, \boldsymbol{\nabla}\phi)$, and the final results for the force will be mentioned in this case.

In order to calculate the force $\boldsymbol{f}$ defined in Eq. (4.2), we can follow the same path as in the case of the embedded inclusion, by applying the generic transformation (4.3). The variation of H during this transformation reads, at first order:

$$\delta H = \int_{\mathbb{R}^d} \frac{\delta H}{\delta \phi}\, \delta\phi\, d^d r + \int_{\mathcal{S}} V(\phi)\, n_i\, \delta\ell_i\, d^{d-1} r\,, \tag{4.18}$$

where the functional derivative of H with respect to ϕ is

$$\frac{\delta H}{\delta \phi} = \frac{\partial \mathcal{H}}{\partial \phi} + \frac{\partial V}{\partial \phi}\mathbf{1}_{\mathcal{A}} - \partial_i \left(\frac{\partial \mathcal{H}}{\partial(\partial_i \phi)} \right)\,. \tag{4.19}$$

4.3.1 First route

If ϕ is kept constant in the Eulerian sense during the infinitesimal displacement (i.e., $\delta\phi \equiv 0$), we obtain

$$\boldsymbol{f}^{(1)} = -\boldsymbol{e}_i \left. \frac{\delta H}{\delta \ell_i} \right|_{\phi,\,\mathrm{Eul.}} = -\int_{\mathcal{S}} V(\phi)\, \boldsymbol{n}\, d^{d-1} r\,. \tag{4.20}$$

The result for $V(\phi, \boldsymbol{\nabla}\phi)$ is exactly similar.

In fact, since the influencing object is not embedded in the medium, the force exerted on it by the medium in a given microstate can be calculated directly by moving the object *with respect to the medium* in a given configuration of ϕ. In other words, $\boldsymbol{\ell}$ and the Eulerian field ϕ can be considered as independent variables. Then, we only need to take into account the variation of the interaction energy $E_p(\boldsymbol{\ell}) = \int_{\mathcal{A}} V(\phi)\, d^d r$ between the medium and the object when the position $\boldsymbol{\ell}$ of the object is modified:

$$\boldsymbol{f}^{(1)} = -\boldsymbol{e}_i \left.\frac{\delta E_p}{\delta \ell_i}\right|_{\phi,\,\mathrm{Eul.}} = -\int_{\mathcal{S}} V(\phi)\, \boldsymbol{n}\, d^{d-1} r\,. \tag{4.21}$$

This derivation is more physical than considering the full variation of H during the generic transformation (4.3). It shows that here, $\boldsymbol{f}^{(1)}$ is simply the negative gradient of the potential energy of interaction E_p between the medium and the influencing object.

This definition of the force, which is the correct one for influencing objects that are not embedded in the medium, is the one used in Refs. [126–129]. In these works, this definition of the force is used to investigate Casimir-like interactions out of equilibrium [126, 127]. Note however that Casimir-like interactions are usually studied between embedded inclusions and not between non-embedded influencing objects. Besides, this definition has also been used to investigate drag forces in classical fields [128, 129]. In the latter works, the example studied in detail is a point-like magnetic field moving through an Ising ferromagnet: it qualifies as an influencing object, since nothing material is embedded in the ferromagnet. However, the present work shows that the application of these results to the diffusion of inclusions embedded in membranes, which is discussed in Refs. [128, 129], should be taken with caution.

4.3.2 Second route

The Hamiltonian in Eq. (4.17) can be used to describe a medium coupled to an influencing object, but also a medium containing a "perturbative embedded inclusion", i.e., an inclusion that is only slightly different from the surrounding medium. Indeed, in the latter case, ϕ is defined everywhere in $\mathbb{R}^d$, and the energy density is perturbed by an extra term V inside the inclusion. For instance, in lipid membranes, domains with a lipid composition different from that of the rest of the membrane can be described as perturbative embedded inclusions, as well as similar structures in nematic liquid crystals.

As for any other inclusion, it is meaningless to move a perturbative inclusion while keeping ϕ constant in the Eulerian sense, since moving the inclusion displaces the surrounding fluid particles. If we assume, as before, that ϕ is transported by fluid particles, the second route is the right one to calculate the force exerted on a perturbative embedded inclusion. Let us now calculate this force.

If the field ϕ is kept constant in the Lagrangian sense during the infinitesimal

transformation, i.e., $\delta\phi(\boldsymbol{r}) = -\boldsymbol{\nabla}\phi(\boldsymbol{r}) \cdot \boldsymbol{\delta r}(\boldsymbol{r})$ for all $\boldsymbol{r}$ in $\mathbb{R}^d$, Eq. (4.18) becomes

$$\delta H = -\int_{\mathcal{B}} \frac{\delta H}{\delta\phi}\, \partial_i\phi\, \delta r_i\, d^d r - \left\{ \int_{\mathcal{A}} \frac{\delta H}{\delta\phi}\, \partial_i\phi\, d^d r - \int_{\mathcal{S}} V(\phi)\, n_i\, d^{d-1} r \right\} \delta\ell_i\,, \tag{4.22}$$

where, again, $\mathcal{B} = \mathbb{R}^d \smallsetminus \mathcal{A}$. This yields, using Eq. (4.19),

$$\begin{aligned} \boldsymbol{f}^{(2)} &= -\,\boldsymbol{e}_i \left.\frac{\delta H}{\delta \ell_i}\right|_{\phi,\,\text{Lagr.}} = \int_{\mathcal{A}} \frac{\delta H}{\delta\phi} \boldsymbol{\nabla}\phi\, d^d r - \int_{\mathcal{S}} V(\phi)\, \boldsymbol{n}\, d^{d-1} r \\ &= \int_{\mathcal{A}} \left[\frac{\partial \mathcal{H}}{\partial\phi} + \frac{\partial V}{\partial\phi} - \partial_j \left(\frac{\partial \mathcal{H}}{\partial(\partial_j\phi)} \right) \right] \boldsymbol{\nabla}\phi\, d^d r - \int_{\mathcal{S}} V(\phi)\, \boldsymbol{n}\, d^{d-1} r\,. \end{aligned} \tag{4.23}$$

Given the singularities in the energy density $\mathcal{H} + V\,\mathbf{1}_{\mathcal{A}}$ on $\mathcal{S}$, the integral over $\mathcal{A}$ has to be calculated using the procedure defined in the Appendix, Sec. 4.8.1, Eq. (4.88). Since $(\partial V/\partial\phi)\boldsymbol{\nabla}\phi = \boldsymbol{\nabla} V$, the two terms involving V in Eq. (4.23) cancel. Thus, using Eq. (4.10), we obtain

$$\boldsymbol{f}^{(2)} = \int_{\mathcal{A}} \partial_j T_{ij}\, d^d r\, \boldsymbol{e}_i = \int_{\mathcal{S}} T_{ij} n_j\, d^{d-1} r\, \boldsymbol{e}_i\,, \tag{4.24}$$

where $\boldsymbol{T}$ is the stress tensor of the fluid medium. This result, which is independent of V, remains the same for $V(\phi, \boldsymbol{\nabla}\phi)$.

The expression for $\boldsymbol{f}^{(2)}$ is the same here as for the embedded inclusion. In fact, a perturbative inclusion is a particular inclusion with $E_{\text{incl}} = \int_{\mathcal{A}} (\mathcal{H} + V)\, d^d r$, which verifies $\delta E_{\text{incl}} = 0$ during our transformation, and without any explicit boundary coupling.

Thus, while it is the first route that gives the correct force exerted by the medium on an influencing object, the second route is the right one in the case of a perturbative embedded inclusion.

4.3.3 Mean-field configuration

The two forces $\boldsymbol{f}^{(1)}$ and $\boldsymbol{f}^{(2)}$ are, in general, not equal, and we have seen that they are relevant to very different physical situations. However, as in the case of an embedded inclusion (see Sec. 4.2.4), these two quantities are equal in the mean-field configuration of the system. Indeed, in this configuration, $\delta H/\delta\phi \equiv 0$, so Eq. (4.23) shows that $\boldsymbol{f}^{(2)}$ is identical to $\boldsymbol{f}^{(1)}$.

4.3.4 Formal relation between the two types of forces

Independently of the physical interpretations of the forces $\boldsymbol{f}^{(1)}$ and $\boldsymbol{f}^{(2)}$, Eq. (4.23) gives a formal relation between these two forces:

$$\boldsymbol{f}^{(1)} = \boldsymbol{f}^{(2)} - \int_{\mathcal{A}} \frac{\delta H}{\delta\phi} \boldsymbol{\nabla}\phi\, d^d r\,. \tag{4.25}$$

Given the singularities in the energy density $\mathcal{H} + V\,\mathbf{1}_{\mathcal{A}}$ on $\mathcal{S}$, the integral over $\mathcal{A}$ has to be calculated using the procedure defined in the Appendix, Sec. 4.8.1, Eq. (4.88).

Let us introduce the stress tensor $\boldsymbol{T}'$ of the composite medium including the perturbative embedded inclusion: the force density at each point of the medium, even inside the perturbative embedded inclusion, is $\boldsymbol{q}' = \partial_j T'_{ij} \boldsymbol{e}_i$ (see the Appendix, Sec. 4.8.3). Thus, the basic definition Eq. (4.84) of the force $\boldsymbol{f}$ enables us to write:

$$\boldsymbol{f}^{(2)} = \int_{\mathcal{A}} \boldsymbol{q}'(\boldsymbol{r})\, d^d r\,. \tag{4.26}$$

Here again, the integral over $\mathcal{A}$ has to be calculated using the procedure defined in Eq. (4.88). Besides, if $\mathcal{C}$ is a region such that $\mathcal{A} \subset \mathcal{C}$, we have

$$\int_{\mathcal{C}} \boldsymbol{q}'(\boldsymbol{r})\, d^d r = \int_{\mathcal{C}} \frac{\delta H}{\delta \phi} \boldsymbol{\nabla} \phi\, d^d r - \int_{\mathcal{S}} V(\phi)\, \boldsymbol{n}\, d^{d-1} r\,, \tag{4.27}$$

where we have used the expression of $\boldsymbol{q}'$ in Eq. (4.98). Thus, we can write

$$\boldsymbol{f}^{(1)} = \int_{\mathcal{C}} \boldsymbol{q}'(\boldsymbol{r})\, d^d r - \int_{\mathcal{C}} \frac{\delta H}{\delta \phi} \boldsymbol{\nabla} \phi\, d^d r\,, \tag{4.28}$$

which corresponds exactly to formula (18) in [127]. However, this equation relates $\boldsymbol{f}^{(1)}$ and $\boldsymbol{f}^{(2)}$ only if $\mathcal{C} = \mathcal{A}$: the formal relation between $\boldsymbol{f}^{(1)}$ and $\boldsymbol{f}^{(2)}$ is given by Eq. (4.25).

4.4 Casimir-like force

4.4.1 Embedded inclusions

Let us consider a fluid medium including two embedded inclusions with respective centers of mass at the origin of the frame and at point $\boldsymbol{\ell}$, and let us introduce the unit vector $\boldsymbol{u} \equiv \boldsymbol{\ell}/\ell$. The Casimir-like force exerted on the inclusion in $\boldsymbol{\ell}$ by the other one is usually defined through $\boldsymbol{f}_C = -\boldsymbol{u}\, \partial F/\partial \ell$, where $F(\ell) = -k_{\mathrm{B}} T \ln Z(\ell)$ is the free energy of the system. We are going to show that $\boldsymbol{f}_C$ corresponds to the *average at thermal equilibrium* of the force $\boldsymbol{f}^{(2)}$ exerted on the inclusion in $\boldsymbol{\ell}$ by the medium containing the other inclusion.

Let us assume that the line joining the centers of mass of the two inclusions is a symmetry axis of the system. This assumption is valid in the standard case of parallel plates, as well as for point-like and spherical inclusions. Then, the effective Hamiltonian H of the system only depends on ϕ and on the distance ℓ between the two inclusions. At thermal equilibrium, the statistical weight of a configuration $([\phi], \ell)$ is given by $e^{-\beta H([\phi],\ell)}$, where the notation $[\phi]$ represents a functional dependence on ϕ. At a given ℓ, the partition function of the system is

$$Z(\ell) = \int \mathcal{D}\phi\; e^{-\beta H([\phi],\ell)}\,, \tag{4.29}$$

where the functional integral runs over the functions ϕ defined in the domain $\mathcal{B} = \mathbb{R}^d \smallsetminus (\mathcal{A}_{\boldsymbol{0}} \cup \mathcal{A}_{\boldsymbol{\ell}})$, where $\mathcal{A}_{\boldsymbol{\ell}}$ is the region where the inclusion with center of mass in $\boldsymbol{\ell}$ stands (and similarly for $\mathcal{A}_{\boldsymbol{0}}$).

Let us now introduce a replica of the system presented above, identical to it except that the center of mass of the second inclusion is at point $\boldsymbol{\ell} + \delta\ell\,\boldsymbol{u}$. The partition function of this replica reads

$$Z(\ell + \delta\ell) = \int \mathcal{D}'\tilde{\phi}\; e^{-\beta H([\tilde{\phi}],\ell+\delta\ell)}\,. \tag{4.30}$$

Here, the functional integral runs over the functions $\tilde{\phi}$ defined in the domain $\mathcal{B}' = \mathbb{R}^d \smallsetminus (\mathcal{A}_{\boldsymbol{0}} \cup \mathcal{A}_{\boldsymbol{\ell}+\delta\ell\boldsymbol{u}})$. This difference with respect to Eq. (4.29) is symbolized by a prime on the functional measure. Let us consider a smooth invertible function $\boldsymbol{r}' : \mathcal{B} \to \mathcal{B}'$, $\boldsymbol{r} \mapsto \boldsymbol{r}'(\boldsymbol{r}) = \boldsymbol{r} + \boldsymbol{\delta r}(\boldsymbol{r})$, where the infinitesimal virtual displacement field $\boldsymbol{\delta r}$ is such that $\boldsymbol{\delta r} = \boldsymbol{0}$ on the first inclusion while $\boldsymbol{\delta r} = \delta\ell\,\boldsymbol{u}$ on the second one, and $|\boldsymbol{\delta r}|/\ell$ is small, say of order ϵ. Let us assume that the function $\boldsymbol{r}'$ maps a field ϕ to a field $\tilde{\phi} = \phi + \delta\phi$ such that $\tilde{\phi}(\boldsymbol{r}'(\boldsymbol{r})) = \phi(\boldsymbol{r})$ for all $\boldsymbol{r} \in \mathcal{B}$, and $\delta\phi = -\boldsymbol{\delta r}\cdot\boldsymbol{\nabla}\phi$ at first order in ϵ. This is motivated by our assumption that each fluid particle of the medium keeps the same value of ϕ during any real smooth infinitesimal displacement. As this process can be inverted, $\boldsymbol{r}'$ yields a one-to-one mapping of the states $([\phi], \ell)$ of the first system to the states $([\phi + \delta\phi], \ell + \delta\ell)$ of the replica. We may thus write

$$\mathcal{D}\phi = \prod_{\boldsymbol{r}\in\mathcal{B}} d[\phi(\boldsymbol{r})] = \prod_{\boldsymbol{r}'(\boldsymbol{r})\in\mathcal{B}'} d[\tilde{\phi}(\boldsymbol{r}'(\boldsymbol{r}))] = \mathcal{D}'\tilde{\phi}\,, \tag{4.31}$$

where the continuous products must be understood as

$$\prod_{\boldsymbol{r}\in\mathcal{B}} d[\phi(\boldsymbol{r})] \equiv \lim_{N\to\infty} \prod_{n=1}^{N} d[\phi(\boldsymbol{r}_n)]\,, \tag{4.32}$$

where $\{\boldsymbol{r}_n\}$ is a regular mesh of $\mathcal{B}$ [136]. Hence, Eq. (4.30) can be rewritten as

$$Z(\ell + \delta\ell) = \int \mathcal{D}\phi\; e^{-\beta H([\phi+\delta\phi],\ell+\delta\ell)}\,, \tag{4.33}$$

so the difference of free energy between the replica and the original system reads at first order in ϵ:

$$\delta F = -k_{\mathrm{B}}T\,\frac{\delta Z}{Z} = \int \mathcal{D}\phi\; \frac{e^{-\beta H([\phi],\ell)}}{Z}\,\delta H = \langle \delta H\rangle\,, \tag{4.34}$$

where $\langle . \rangle$ denotes the average at thermal equilibrium, while $\delta Z \equiv Z(\ell + \delta\ell) - Z(\ell)$, and $\delta H \equiv H([\phi + \delta\phi], \ell + \delta\ell) - H([\phi], \ell)$.

The expression of δH is given by Eq. (4.11), so we obtain

$$\delta F = -\int_{\mathcal{B}} \langle q_i\rangle\,\delta r_i\,d^d r - \delta\ell \int_{\mathcal{S}} \langle T_{ui}\rangle n_i\,d^{d-1}r\,, \tag{4.35}$$

where the axes have been chosen so that one of them is along $\boldsymbol{u}$: $T_{ui}n_i\,d^{d-1}r$ denotes the component along this axis of the force transmitted through the infinitesimal

hypersurface $d^{d-1}r$. Recall that $\boldsymbol{q}$ represents the hypervolume density of internal forces in the medium, given by Eq. (4.13).

As no average external forces are imposed to the system, the hypervolume density of external forces $\boldsymbol{w}$ verifies $\langle \boldsymbol{w} \rangle = \boldsymbol{0}$. Neglecting inertia, which is possible if the timescales considered are sufficiently large, Newton's second law applied to each fluid particle of the medium gives $\boldsymbol{q} = -\boldsymbol{w}$ (see the Appendix, Sec. 4.8.1). Thus, we obtain $\langle \boldsymbol{q} \rangle = \boldsymbol{0}$. This relation can also be obtained formally: Eqs. (4.10) and (4.13) show that $\boldsymbol{q} = (\boldsymbol{\nabla}\phi)\, \delta H/\delta\phi$, and the thermal average of the latter quantity can be proved to vanish using the Schwinger-Dyson equation [127]. Thus, Eq. (4.35) becomes

$$\delta F = -\delta\ell \int_{\mathcal{S}} \langle T_{ui} \rangle n_i \, d^{d-1}r = -\delta\ell \, \langle \boldsymbol{f}^{(2)} \rangle \cdot \boldsymbol{u} \,, \tag{4.36}$$

where we have used the expression of $\boldsymbol{f}^{(2)}$ in Eq. (4.12). Note that Eq. (4.36) is independent of the virtual displacement field $\boldsymbol{\delta r}$ chosen at the beginning of this discussion to map the states of the system onto the state of its replica. We obtain from Eq. (4.36):

$$\boldsymbol{f}_C = -\frac{\partial F}{\partial \ell} \, \boldsymbol{u} = \big(\langle \boldsymbol{f}^{(2)} \rangle \cdot \boldsymbol{u} \big) \, \boldsymbol{u} \,. \tag{4.37}$$

Since $\langle \boldsymbol{f}^{(2)} \rangle$ is along $\boldsymbol{u}$ by symmetry, we can conclude that $\boldsymbol{f}_C = \langle \boldsymbol{f}^{(2)} \rangle$.

4.4.2 Non-embedded influencing objects

Although Casimir-like forces are usually studied between embedded inclusions, let us now consider non-embedded influencing objects. In this case, the partition function can also be written as

$$Z(\ell) = \int \mathcal{D}\phi \; e^{-\beta H([\phi],\ell)} \,, \tag{4.38}$$

but here the functional integral runs over the functions ϕ defined on $\mathbb{R}^d$. In contrast to the case of the embedded inclusions, ℓ can be varied at constant Eulerian field ϕ. Thus we can write directly

$$\frac{\partial F}{\partial \ell} = \int \mathcal{D}\phi \; \frac{e^{-\beta H([\phi],\ell)}}{Z} \, \frac{\partial H}{\partial \ell} = \left\langle \frac{\partial H}{\partial \ell} \right\rangle = -\langle \boldsymbol{f}^{(1)} \rangle \cdot \boldsymbol{u} \,. \tag{4.39}$$

Thus, in the case of influencing objects, it is the average of $\boldsymbol{f}^{(1)}$ that gives $-\boldsymbol{u}\, \partial F/\partial \ell$.

Some effective Hamiltonians, such as the one in Eq. (4.17) and the one studied in the next section, can describe both influencing objects and embedded inclusions. For such effective Hamiltonians, our results show that the thermal average of $\boldsymbol{f}$ is the same in these two physical cases, each of them being treated with the appropriate route. If there are two inclusions, this thermal average force corresponds to the Casimir-like force $-\boldsymbol{u}\, \partial F/\partial \ell$. Thus, the usual (i.e., thermal average) Casimir-like force does not depend on the route that is chosen. In spite of this degeneracy concerning thermal average, it is very important to distinguish the two physical cases as soon as one wishes to go beyond the thermal average force. This point will be illustrated in the next section.

4.5 A simple example of Casimir-like force

4.5.1 The situation

Let us now present a simple example with a Hamiltonian that can describe both influencing objects and embedded inclusions. In this example, we calculate the variance of the Casimir-like force, both in the usual case of embedded inclusions (via the second route) and in the particular case of non-embedded influencing objects (via the first route), and we find two very different results. Thus, this example illustrates the importance of the distinction between the two physical cases.

Let us consider an infinite one-dimensional fluid medium described by a dimensionless scalar field ϕ with Hamiltonian density

$$\mathcal{H} = \frac{\kappa}{2}\phi'^2 + \frac{m}{2}\phi^2 \,, \tag{4.40}$$

where $\phi' \equiv d\phi/dx$. The length scale $L = \sqrt{\kappa/m}$ which appears in $\mathcal{H}$ corresponds to the correlation length of ϕ, as shown in the following. The energy H_0 of the medium is such that

$$\beta H_0 = \beta \int_{\mathbb{R}} dx\ \mathcal{H}(x) = \frac{1}{2}\int_{\mathbb{R}^2} dx\, dy\ \phi(x)\mathcal{O}(x,y)\phi(y) \,, \tag{4.41}$$

where $\beta = (k_{\mathrm{B}}T)^{-1}$, and the symmetric operator $\mathcal{O}$ is defined by

$$\mathcal{O}(x,y) = \left[\beta m - \beta\kappa\frac{d^2}{dx^2}\right]\delta(x-y) \,. \tag{4.42}$$

Let us assume that there are two point-like inclusions or non-embedded influencing objects, in $x = 0$ and $x = \ell$, where $\ell > 0$, and that their coupling to the field ϕ is given by

$$\beta V = \frac{\alpha}{2}\left[\phi^2(0) + \phi^2(\ell)\right] \,. \tag{4.43}$$

Since ϕ is dimensionless, α is dimensionless too. When $\alpha \to \infty$, this quadratic coupling yields Dirichlet boundary conditions on the inclusions. Indeed, in this limit, the statistical weight $e^{-\beta(H_0+V)}$ of any configuration such that $\phi \neq 0$ on an inclusion goes to zero.

For the calculations that follow, let us assume that there is an external field u conjugate to ϕ:

$$\beta H_{\mathrm{ext}} = -\int_{\mathbb{R}} dx\, u(x)\phi(x) \,. \tag{4.44}$$

In order to calculate the partition function of the system

$$Z[u] = \int \mathcal{D}\phi\ e^{-\beta(H_0+V+H_{\mathrm{ext}})} \,, \tag{4.45}$$

let us carry out a Hubbard-Stratonovich transformation [119]. Using the relation

$$e^{-\beta V} = \frac{1}{2\pi\alpha} \int_{\mathbb{R}^2} d^2v \, \exp\left[-\frac{v^2}{2\alpha} + i\,(v_1\,\phi(0) + v_2\,\phi(\ell)) \right] , \tag{4.46}$$

where (v_1, v_2) is a two-dimensional vector, and performing the Gaussian integration on ϕ, we obtain

$$Z[u] = \frac{Z_0}{2\pi\alpha} \int_{\mathbb{R}^2} d^2v \, \exp\left[-\frac{v^2}{2\alpha} + \frac{1}{2} \int_{\mathbb{R}^2} dx\, dy \; S(x)\, G(x,y)\, S(y) \right] . \tag{4.47}$$

In this expression, Z_0 is the partition function of the medium with no inclusion or other influencing object, while $S(x) = u(x) + i\,v_1\,\delta(x) + i\,v_2\,\delta(x-\ell)$, and G is a Green's function of $\mathcal{O}$. The latter can be obtained using a Fourier transform since the medium is infinite and translation-invariant:

$$G(x,y) = \frac{k_{\mathrm{B}}T}{2\pi} \int_{\mathbb{R}} dq \, \frac{e^{i\,q(x-y)}}{\kappa\,q^2 + m} = \frac{k_{\mathrm{B}}T\,L}{2\,\kappa} \, \exp\left(-\frac{|x-y|}{L} \right) , \tag{4.48}$$

where $L = \sqrt{\kappa/m}$. In the absence of inclusions or other influencing objects, the correlation function of ϕ is G, so L represents the correlation length of ϕ. Therefore, we expect Casimir-like forces to be most important when the distance ℓ between the objects is such that $\ell \ll L$.

Performing the Gaussian integration on (v_1, v_2) in Eq. (4.47) yields

$$Z[u] = \frac{Z_0}{\alpha\sqrt{\det M}} \, \exp\left(\frac{1}{2} \int_{\mathbb{R}^2} dx\, dy \; u(x)\, C(x,y)\, u(y) \right) , \tag{4.49}$$

where $C(x,y) = G(x,y) - A^T(x)\, M^{-1} A(y)$, with $A^T(x) = (G(x,0)\,,\; G(x,\ell))$ and

$$M = \begin{pmatrix} G(0,0) + \alpha^{-1} & G(0,\ell) \\ G(0,\ell) & G(\ell,\ell) + \alpha^{-1} \end{pmatrix} . \tag{4.50}$$

It is straightforward to deduce the moments of the Gaussian variable $\phi(x)$ from Eq. (4.49):

$$\langle \phi(x) \rangle = -\frac{1}{Z[0]} \left. \frac{\delta Z}{\delta u(x)} \right|_{u=0} = 0 \, , \tag{4.51}$$

$$\langle \phi(x)\phi(y) \rangle = \frac{1}{Z[0]} \left. \frac{\delta^2 Z}{\delta u(x)\, \delta u(y)} \right|_{u=0} = C(x,y) \, . \tag{4.52}$$

Thus, the correlation function of the field ϕ in the presence of the two objects is

$$\langle \phi(x)\phi(y) \rangle - \langle \phi(x) \rangle \langle \phi(y) \rangle = C(x,y) = G(x,y) - A^T(x)\, M^{-1} A(y) \, . \tag{4.53}$$

4.5.2 Average Casimir-like force

The usual, average, Casimir-like force $\langle f \rangle$ between the two inclusions can be calculated by differentiating the free energy $F = -k_{\mathrm{B}}T\,\ln(Z[u=0])$ of the system, which can be obtained from Eq. (4.49):

$$\begin{aligned}\langle f \rangle &= -\frac{\partial F}{\partial \ell} = -\frac{k_{\mathrm{B}}T}{2}\,\frac{\partial(\ln\det M)}{\partial \ell} \\ &= \frac{-(k_{\mathrm{B}}T)^3\alpha^2 L\,e^{-\frac{2\ell}{L}}}{(k_{\mathrm{B}}T)^2\alpha^2L^2\left(1-e^{-\frac{2\ell}{L}}\right)+4\,k_{\mathrm{B}}T\,\alpha\,\kappa\,L+4\,\kappa^2}\,. \end{aligned} \tag{4.54}$$

Taking the hard-constraint limit $\alpha \to \infty$, which will be denoted in the following by a subscript index h, we obtain:

$$\langle f_h \rangle = \frac{k_{\mathrm{B}}T}{L\left(1-e^{\frac{2\ell}{L}}\right)} \underset{\ell \ll L}{\sim} -\frac{k_{\mathrm{B}}T}{2\,\ell}\,. \tag{4.55}$$

As expected, the Casimir-like force vanishes when $\ell \gg L$: when the distance between the inclusions is much larger than the correlation length of ϕ, one inclusion cannot feel the effect of the other one. We have emphasized the "critical regime" $\ell \ll L$, where the Casimir-like force is most important: it has a simple ℓ^{-1} power-law dependence.

Meanwhile, in the perturbative limit $\alpha \to 0$, which will be denoted in the following by a subscript index p, we obtain, to lowest order in α:

$$\langle f_p \rangle = -\frac{(k_{\mathrm{B}}T)^3\alpha^2 L\,e^{-\frac{2\ell}{L}}}{4\,\kappa^2} \underset{\ell \ll L}{\sim} -\frac{(k_{\mathrm{B}}T)^3\alpha^2\,(L-2\ell)}{4\,\kappa^2}\,. \tag{4.56}$$

Here too, we have emphasized the critical regime $\ell \ll L$: this time, the leading term is independent of ℓ, so the force is nearly constant in this regime.

4.5.3 Variance of the Casimir-like force

We are now going to illustrate the difference between embedded inclusions and non-embedded influencing objects by studying the variance of the Casimir-like force. The two routes to calculate the force $\boldsymbol{f}$ are detailed in the particular case of point-like embedded inclusions or non-embedded influencing objects in the Appendix, Sec. 4.8.4.

a. Preliminary remark

The variance we are going to study is that of the force $\boldsymbol{f}$ defined at the coarse-grained level where the system is described by $([\phi], \boldsymbol{\ell})$. This force is averaged over the fundamental microstates "$\mu \to ([\phi], \boldsymbol{\ell})$" that yield the coarse-grained field ϕ and the inclusion position $\boldsymbol{\ell}$. Indeed, it is shown in the Appendix, Sec. 4.8.1, that the

force $\boldsymbol{f}_\mu$ exerted by the medium on the inclusion in the fundamental microstate μ verifies

$$\langle \boldsymbol{f}_\mu \rangle_{\mu \to ([\phi],\boldsymbol{\ell})} = \boldsymbol{f}([\phi],\boldsymbol{\ell}) \,, \tag{4.57}$$

where $\langle . \rangle_{\mu \to ([\phi],\boldsymbol{\ell})}$ represents the statistical average at equilibrium over the fundamental microstates $\mu \to ([\phi],\boldsymbol{\ell})$. Therefore, the variance $\Delta^2 \boldsymbol{f}$ of the force $\boldsymbol{f}$ is smaller than $\Delta^2 \boldsymbol{f}_\mu$, since it is the variance of a force that is already partially averaged.

The difference between $\Delta^2 \boldsymbol{f}_\mu$ and $\Delta^2 \boldsymbol{f}$ is due to fluctuation modes with wavelengths smaller than the cutoff a of the field ϕ: such modes are averaged in the coarse-graining procedure leading to $\boldsymbol{f}$. Thus, we expect $\Delta^2 \boldsymbol{f}$ to decrease if a increases. The small-wavelength fluctuation modes are generically the fastest to equilibrate, so above a certain time resolution, it is right to consider $\Delta^2 \boldsymbol{f}$ instead of $\Delta^2 \boldsymbol{f}_\mu$, and for even longer time resolutions, it is appropriate to consider larger values of a. This subtelty, which is linked to the coarse-grained nature of the force $\boldsymbol{f}$, is relevant to all studies of the fluctuations of Casimir-like forces, in particular to the work we presented in Chapter 3 in the case of membranes, and to that of Ref. [111] in the case of the scalar field.

b. Embedded inclusions

In the case of point-like embedded inclusions, the force exerted on the inclusion in ℓ by the medium containing the other inclusion is obtained via the second route. It is given by Eq. (4.104) of the Appendix, adapted to $d = 1$: $f^{(2)} = T(\ell^+) - T(\ell^-)$.

Let us first show explicitly in the present example that the thermal average of $f^{(2)}$ gives back the Casimir force $\langle f \rangle$. Here, the stress tensor of the medium is

$$T = \mathcal{H} - \phi' \frac{\partial \mathcal{H}}{\partial \phi'} = -\frac{\kappa}{2} \phi'^2 + \frac{m}{2} \phi^2 \,, \tag{4.58}$$

and Eq. (4.52) enables to express its average as

$$\langle T(x) \rangle = -\frac{\kappa}{2} \, C_{xy}(x,x) + \frac{m}{2} \, C(x,x) \,, \tag{4.59}$$

where we have introduced the notation $C_{xy}(x,y) \equiv [\partial_x \partial_y C](x,y)$, which will be used henceforth. This average can be calculated thanks to Eq. (4.48) and (4.53). Note that $G_{xy}(x,x)$ has to be regularized using the short-distance cutoff a of the theory:

$$G_{xy}(x,x) \equiv \frac{k_\mathrm{B} T}{2\pi} \int_{-1/a}^{1/a} dq \, \frac{q^2}{\kappa \, q^2 + m} = \frac{k_\mathrm{B} T}{\pi \, \kappa} \left(\frac{1}{a} - \frac{\mathrm{Arctan}\left(\frac{L}{a}\right)}{L} \right) . \tag{4.60}$$

We then recover the result obtained in Eq. (4.54): $\left\langle f^{(2)} \right\rangle = \langle T(\ell^+) \rangle - \langle T(\ell^-) \rangle = \langle f \rangle$. Note that the cutoff-dependent term Eq. (4.60) vanishes when one calculates the difference between the average stress on each side of the inclusion. This is reminiscent of the calculation of the (average) quantum Casimir force, either from the energy [55] or from the radiation pressure [137], where two infinite quantities subtract to give a finite force. However, in the variance, this cutoff-dependent term will no longer vanish.

We may now proceed to calculate the variance $\Delta^2 f^{(2)}$ of $f^{(2)}$:

$$\Delta^2 f^{(2)} = K(\ell^-,\ell^-) + K(\ell^+,\ell^+) - 2\,K(\ell^-,\ell^+)\,, \tag{4.61}$$

where $K(x,y) \equiv \langle T(x)T(y)\rangle - \langle T(x)\rangle\,\langle T(y)\rangle$. Given the expression of the stress tensor in Eq. (4.58), its correlation function K involves quartic terms in ϕ (or ϕ'). Since $\phi(x)$ is a centered Gaussian variable, we can use Wick's theorem [120] to express K from the correlation function C of ϕ. It yields:

$$\begin{aligned}\Delta^2 f^{(2)} = \frac{\kappa^2}{2}\left[C_{xy}^2(\ell^-,\ell^-) + C_{xy}^2(\ell^+,\ell^+) - 2\,C_{xy}^2(\ell^-,\ell^+)\right]\\ - \kappa\, m\left[C_x^2(\ell^-,\ell^-) + C_x^2(\ell^+,\ell^+) - C_x^2(\ell^-,\ell^+) - C_y^2(\ell^-,\ell^+)\right]\,.\end{aligned} \tag{4.62}$$

This variance can be calculated from Eqs. (4.48), (4.53) and (4.60). Note that $G_x(x,x)$ and $G_y(x,x)$ can be obtained from a regularized Fourier transform:

$$G_x(x,x) = -G_y(x,x) \equiv \frac{k_{\rm B}T}{2\pi}\int_{-1/a}^{1/a} dq\,\frac{iq}{\kappa\,q^2+m} = 0\,. \tag{4.63}$$

The full analytical expression of $\Delta^2 f^{(2)}$ is quite heavy, so we will only present its limiting behaviors for large and small α, and we will focus on the regime where $a < \ell \ll L$, since the Casimir effect is strongest in the critical regime $\ell \ll L$. More precisely, in each limit, we carry out expansions in the small parameter a/L after setting $\ell = Ca$ where C is a constant.

Taking the hard-constraint limit $\alpha \to \infty$, and then keeping only the leading order in a/L, we obtain:

$$\Delta^2 f_h^{(2)} = \Delta^2 f^{(2)\dagger} + \Delta^2 f_h^{(2)\ddagger}\,, \tag{4.64}$$

where the first term is independent of ℓ and α:

$$\Delta^2 f^{(2)\dagger} \simeq \frac{(k_{\rm B}T)^2}{\pi^2 a^2}\,, \tag{4.65}$$

while the second one arises from the inclusions:

$$\Delta^2 f_h^{(2)\ddagger} \simeq -\frac{(k_{\rm B}T)^2}{\pi\,a\,\ell}\,. \tag{4.66}$$

If we consider inclusions imposing Dirichlet boundary conditions (i.e., $\phi(0) = \phi(\ell) = 0$) instead of inclusions imposing a potential V, we recover the result in Eqs. (4.64, 4.65, 4.66) for the force variance. In this case too, the average force can be obtained either directly from the free energy F or by using the stress tensor, and it gives back $\langle f_h\rangle$ in Eq. (4.55).

In the perturbative limit $\alpha \to 0$, let us keep the two lowest orders in α: the leading term corresponds to the situation where there is no inclusion, $\alpha = 0$, so the effect of the inclusions appears in the subleading term. We obtain

$$\Delta^2 f_p^{(2)} = \Delta^2 f^{(2)\dagger} + \Delta^2 f_p^{(2)\ddagger}\,, \tag{4.67}$$

where the first term is the one in Eq. (4.65), still at leading order in a/L, while

$$\Delta^2 f_p^{(2)\ddagger} \simeq -\frac{(k_\mathrm{B}T)^3\alpha}{\pi\,\kappa\,a}\left(1-\frac{\ell}{L}\right)\,, \tag{4.68}$$

where we have kept the two leading orders in a/L to see the ℓ-dependence. Note that these results can be obtained directly from a perturbative expansion of the stress tensor correlation function K at first order in βV. Besides, using this perturbative method, it is straightforward to study the more general problem of inclusions with a finite size s: we have checked that it gives back the average force Eq. (4.56) and the variance Eqs. (4.67, 4.68) in the small-size limit.

Both in the hard-constraint limit and in the perturbative limit (and also in the intermediary regime), the variance of the force features a term $\Delta^2 f^{(2)\dagger}$, expressed in Eq. (4.65), which is independent of ℓ and α. It corresponds to the variance of the zero-average fluctuating force exerted on a point of the medium, or on a single inclusion, by the rest of the medium, in the absence of any other inclusion. This term depends on the cutoff a, and it decreases when a increases, in agreement with the preliminary remark above. The other terms depend on ℓ, and this dependence has the same origin as the Casimir-like interaction itself: it comes from the constraints imposed by the inclusions on the fluctuations of ϕ. They also depend on the intensity of the coupling constant α, because they come from the constraints imposed by the inclusions. Obtaining a leading term that is cutoff-dependent but independent of the distance ℓ between the inclusions, and a subleading term that depends on ℓ, is strongly reminiscent of the results presented in Chapter 3 in the case of the membrane (see Sec. 3.4.3) and of those in Ref. [111].

c. Other influencing objects

In the case of point-like influencing objects that are not embedded in the fluid medium, the force exerted on the object in ℓ by the medium is obtained via the first route. It is given by Eq. (4.101), for $d=1$:

$$f^{(1)} = -\phi'(\ell)\frac{\partial V}{\partial\phi}(\phi(\ell)) = -\alpha\,k_\mathrm{B}T\,\phi'(\ell)\,\phi(\ell)\,. \tag{4.69}$$

Eq. (4.52) enables to express its average as

$$\left\langle f^{(1)}\right\rangle = -\alpha\,k_\mathrm{B}T\,C_x(\ell,\ell)\,, \tag{4.70}$$

which can be calculated from Eq. (4.48), (4.53) and (4.63), yielding once more the result obtained in Eq. (4.54): $\left\langle f^{(1)}\right\rangle = \langle f\rangle$. We have thus verified on the present example that all the definitions (i.e., the direct derivation from the free energy, and the two routes defined in the introduction) give the same result for the thermal average of the force.

In order to calculate the variance of $f^{(1)}$, we use Wick's theorem as above. It gives

$$\Delta^2 f^{(1)} = \alpha^2(k_\mathrm{B}T)^2\left[C(\ell,\ell)\,C_{xy}(\ell,\ell) + 2\,C_x^2(\ell,\ell)\right]\,. \tag{4.71}$$

This variance can be calculated from Eqs. (4.48), (4.53), (4.60) and (4.63). Here again, we will only present the limiting behaviors of $\Delta^2 f^{(1)}$, in the same regimes as for the embedded inclusion.

In the hard-constraint limit $\alpha \to \infty$, keeping the leading order in α, and then keeping the leading order in a/L, we obtain:

$$\Delta^2 f_h^{(1)} \simeq \frac{(k_\mathrm{B}T)^3\alpha}{\kappa\, a}\left(\frac{1}{\pi} - \frac{a}{4\,\ell}\right) . \tag{4.72}$$

In the perturbative limit $\alpha \to 0$, if we keep the two lowest orders in α (the lowest order term does not depend on ℓ, so we also keep the next one), we obtain:

$$\Delta^2 f_p^{(1)} \simeq \frac{(k_\mathrm{B}T)^4\alpha^2}{2\,\pi\,\kappa^2}\,\frac{L}{a} + \frac{(k_\mathrm{B}T)^5\alpha^3 L}{2\,\pi\,\kappa^3}\left(-\frac{L}{a} + \frac{\ell}{a} + \frac{\pi}{4}\right) , \tag{4.73}$$

where we have kept only the leading orders in a/L, and also the subleading one in the α^3 term to see the ℓ-dependence. This result can also be found directly from a perturbative expansion of $\left\langle (f^{(1)})^2 \right\rangle$ at second order in βV. This variance diverges when $L \to \infty$, but the correlation function itself diverges in this limit (see Eq. (4.48)).

The present results are very different from the ones concerning the embedded inclusions. First, there is no term independent of the coupling constant α here, since, as explained above, the first route amounts to taking the derivative of the potential energy of interaction between the medium and the influencing object. Besides, here, the variance diverges as α in the hard-constraint limit $\alpha \to \infty$, while it converged in the case of the embedded inclusion. Here follows a physical explanation of this divergence: for each microstate ϕ, let r and s be such that $|\phi(\ell)| = \alpha^r$ and $|\phi(0)| = \alpha^s$. For $\alpha \to \infty$, only the states such that $r \leq -1/2$ and $s \leq -1/2$ can keep a significant statistical weight: they are such that $\exp(-\beta V) \geq 1/e$, while for the others, $\exp(-\beta V) \to 0$ exponentially when $\alpha \to \infty$. Let us consider the statistically significant states with highest r, i.e., the ones such that $r = -1/2$: they will yield the largest forces $f^{(1)}$. For these states, $(f^{(1)})^2 \sim \alpha\,(k_\mathrm{B}T)^2\phi'^2(\ell)$. Since there is no particular constraint on $\phi'(\ell)$, $(f^{(1)})^2$ typically scales as α in these states, which explains the behavior of the variance. Much more qualitatively, if α is infinite, the only allowed states are such that $\phi(\ell) = 0$, but $\phi'(\ell)$ is generically nonzero, so $\phi(\ell + \delta\ell) \neq 0$: if it moved to this position, the object would have an infinite energy. Thus, it feels an infinite restoring force. While such contributions can cancel in the average, they add in the variance, which thus diverges with α.

4.6 Discussion

In the simple example studied above, we have found very different results for the variance of the Casimir-like force for embedded inclusions and for non-embedded influencing objects. It illustrates the importance of distinguishing these two physical cases and the associated routes for calculating the force.

The out-of-equilibrium behavior of Casimir-like forces also strongly depends on the route that is taken. The building of the Casimir-like force in a binary mixture after a quench from the high-temperature phase to the critical point has been studied for plates imposing boundary conditions to the field ϕ (i.e., the shifted concentration), using the second route in Ref. [124], and using the first route in Ref. [127][3]. During the quench, the correlation length increases towards infinity, and a Casimir-like force appears between the plates. The two routes give very different results in the case where one plate imposes Dirichlet boundary conditions while the other one imposes Neumann boundary conditions. Indeed, in Ref. [124], the force exerted on one plate, calculated via the second route, was found to differ from the one exerted on the other plate during the relaxation (while both converge to the same equilibrium value), as shown in Fig. 4.4. Conversely, in Ref. [127], which used the first route, it was proved that these two forces should always be equal, as the out-of-equilibrium system was mapped on an equilibrium one. Note that obtaining different forces on each plate is not ruled out by the action-reaction principle, since the forces involved are forces exerted by the medium containing one plate on the other plate, and not forces exerted by one plate on the other plate.

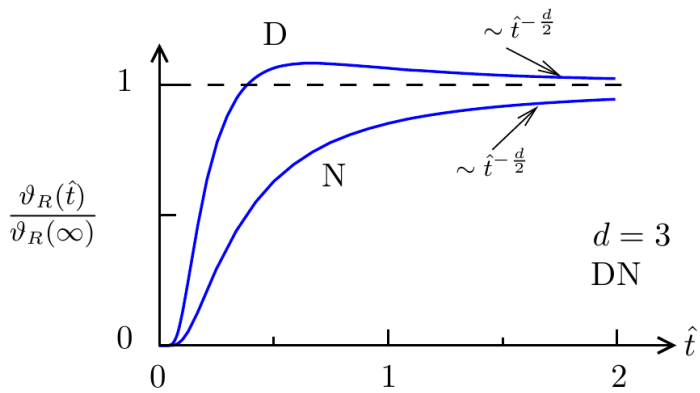

Figure 4.4: Casimir-like force in a binary mixture between one plate imposing Dirichlet boundary conditions (D) and another plate imposing Neumann boundary conditions (N) after a quench at time 0 from the high-temperature phase to the critical point. The universal scaling function ϑ_R characterizing the amplitude of the Casimir-like force is plotted versus rescaled (and dimensionless) time $\hat{t}$, for the D plate and for the N plate. The function ϑ_R is normalized by its asymptotic (equilibrium) value. In this study, the critical binary mixture is described by a Gaussian model with purely relaxational (i.e., model A) dynamics, and the dimension is $d = 3$ [124]. *Illustration reproduced from Ref. [124].*

We have shown that the difference underlying the two routes for calculating the force $\boldsymbol{f}$ stems from the hypotheses made on the infinitesimal virtual displacement of the inclusion that is used to calculate the corresponding variation of energy, which gives the force. This infinitesimal displacement, albeit being virtual, should be consistent with the physics of the system considered. For inclusions embedded in

[3]In Refs. [124] and [127], the fluid is described using model A dynamics. Note however that the actual dynamics of fluids involves features that are not present in this simple model [124].

fluid media, the Lagrangian hypothesis (i.e., our second route) is generally more realistic than the Eulerian one (i.e., our first route). For instance, in fluid membranes, simulations have shown that when a protein diffuses in the membrane, the surrounding lipids are dragged along with it [138], as shown, e.g., in Fig. 4.5. This confirms the relevance of the Lagrangian route, and consequently of the approach based on the stress tensor, in this system.

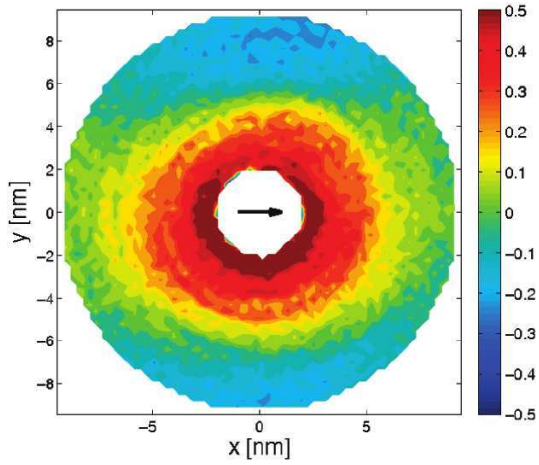

Figure 4.5: Two-dimensional lateral displacement correlation plot for membrane lipids around a protein moving towards positive values of x. The protein corresponds to the white disk in the middle. Results from an atomistic molecular dynamics simulation of a POPC bilayer membrane containing a single Kv1.2 ion channel [138]. *Illustration reproduced from Ref. [138].*

However, the question whether the surrounding fluid is dragged or not when an inclusion moves within it is a subtle one. In our second, i.e., Lagrangian, route, we assumed that the displacement $\boldsymbol{\delta r}$ is continuous at the boundary of the inclusion. As already mentioned in Sec. 4.2.3, this is fully valid in the usual parallel plate geometry where the infinitesimal displacement used to calculate the force is perpendicular to the plates. However, for other geometries, this hypothesis implies no local slipping at the interface. Thus, it may not be fully adapted to a superfluid. Even in viscous fluids, the issue of boundary conditions at small scale is a subtle one [139]. We could also imagine a field ϕ that is not fully transported by the fluid particles. This means that in some systems, the appropriate route might be an intermediate between the two routes discussed here. We have focused on the two extreme cases because they yield the two definitions that are currently used in the literature to study Casimir-like forces beyond their thermal average value.

This discussions lays the emphasis on the complexity of defining the force exerted on an inclusion embedded in a correlated fluid in a microstate of this medium. The thermal average force does not depend on these details, but as soon as one goes beyond this thermal average value, the difference between the two routes discussed here is really relevant.

4.7 Conclusion

We have investigated the force exerted on an inclusion by a fluid medium with long-range correlations, described by a scalar field ϕ in a coarse-grained theory. If a second inclusion is embedded in the medium, the thermal average of this force gives the Casimir-like force between the two inclusions. In order to go beyond the thermal average force, it is necessary to define properly the force $\boldsymbol{f}$ exerted on an inclusion by the medium in each microstate. In practice, one must take the negative gradient of the effective Hamiltonian with respect to the position of the inclusion in a given microstate of the medium. We have shed light onto the subtlety of this task, showing two routes that can be taken to calculate this gradient. In the first route, ϕ is kept constant in the Eulerian sense, while in the second one, ϕ is kept constant in the Lagrangian sense.

In the usual case of an embedded inclusion, the position of the inclusion and the Eulerian field ϕ are not independent variables, so one should not take the first route. Indeed, when an inclusion is displaced infinitesimally, the surrounding fluid particles are displaced too. In many physical cases, ϕ is transported by the fluid particles of the medium during a displacement, so the second route is the correct one. It gives the integral of the stress tensor of the medium on the boundary of the inclusion.

We have also considered the case of influencing objects that interact with the medium without being embedded in it. Contrary to inclusions, such objects can be moved with respect to the medium at a given Eulerian field ϕ. Thus, the first route is adapted to calculate the force exerted by the medium on an influencing object.

In a nutshell, the two formal routes for calculating the force $\boldsymbol{f}$ apply to two different physical cases. We have discussed the practical importance of this distinction. First, in the mean-field configuration, the two routes give the same result. Then, for effective Hamiltonians that can describe both physical cases, the two routes give the same thermal average of the force. However, the difference between these two routes becomes crucial as soon as one wants to study this force beyond its mean-field value and its thermal average. We have shown in a simple example that they yield very different results for the variance of the Casimir-like force. Besides, comparing Refs. [124] and [127] shows that the out-of-equilibrium behavior of Casimir-like forces also depends on the route that is taken.

Two definitions of the force, corresponding to our two routes, are currently used to study the fluctuations of the Casimir-like force and its out-of-equilibrium behavior. Our work shows that the second route, which gives the integral of the stress tensor, should be used when studying Casimir-like forces between embedded inclusions, in agreement with Refs. [111, 114, 121–125]. In contrast, the first route, which is used in Refs. [126–129], should be reserved to the case of non-embedded influencing objects.

4.8 Appendix

4.8.1 Definition of the force $\boldsymbol{f}$ from the principle of virtual work

The aim of the present Appendix is to provide a justification of the fundamental definition Eq. (4.2) in our coarse-grained, effective description. Let us consider, as in the main text, an infinite d-dimensional fluid medium with short-range interactions, and let us assume that an embedded inclusion extends over the region $\mathcal{A} \subset \mathbb{R}^d$ of this medium. Let us consider a "fundamental" microstate μ of the system constituted by the fluid medium with the inclusion, i.e., a microstate defined not by the coarse-grained field ϕ and by the position $\boldsymbol{\ell}$ of the center of mass of the inclusion, but by all the underlying microscopic degrees of freedom. Let us call $\boldsymbol{w}_\mu$ the hypervolume density of forces exerted by the exterior on the system, and $\boldsymbol{q}_\mu$ the hypervolume density of forces exerted on a piece of the system by the rest of the system, in the microstate μ. Both $\boldsymbol{w}_\mu$ and $\boldsymbol{q}_\mu$ can take different values in the different fundamental microstates "$\mu \to ([\phi], \boldsymbol{\ell})$" that yield the same coarse-grained field ϕ and inclusion position $\boldsymbol{\ell}$. The coarse-graining procedure regroups these microstates so that

$$Z([\phi], \boldsymbol{\ell}) = e^{-\beta H([\phi], \boldsymbol{\ell})} = \sum_{\mu \to ([\phi], \boldsymbol{\ell})} e^{-\beta E_\mu} \,, \tag{4.74}$$

where E_μ is the energy of the fundamental microstate μ, while $H([\phi], \boldsymbol{\ell})$ is the effective energy of the coarse-grained microstate $([\phi], \boldsymbol{\ell})$. Let us now introduce the average $\boldsymbol{q}([\phi], \boldsymbol{\ell})$ (respectively, $\boldsymbol{w}([\phi], \boldsymbol{\ell})$) of $\boldsymbol{q}_\mu$ (respectively, $\boldsymbol{w}_\mu$) over the microstates $\mu \to ([\phi], \boldsymbol{\ell})$: $\boldsymbol{q}$ and $\boldsymbol{w}$ are coarse-grained force densities. Explicitly, we have

$$\boldsymbol{q}([\phi], \boldsymbol{\ell}) \equiv \langle \boldsymbol{q}_\mu \rangle_{\mu \to ([\phi], \boldsymbol{\ell})} = \sum_{\mu \to ([\phi], \boldsymbol{\ell})} \boldsymbol{q}_\mu \frac{e^{-\beta E_\mu}}{Z([\phi], \boldsymbol{\ell})} \,, \tag{4.75}$$

and similarly for $\boldsymbol{w}$.

Let us consider a material particle of hypervolume $d^d r$ of the system: it can be a fluid particle of the medium in the sense defined in the main text, or a piece of the inclusion. Since it is a (macroscopically) closed particle, Newton's second law applies to it. In the fundamental microstate μ, it reads $\boldsymbol{w}_\mu \, d^d r + \boldsymbol{q}_\mu \, d^d r = d(\boldsymbol{p}_\mu \, d^d r)/dt$, where $\boldsymbol{p}_\mu$ is the hypervolume density of momentum in the microstate μ. This is equivalent to writing that $\boldsymbol{w}_\mu \cdot \boldsymbol{\delta r} \, d^d r + \boldsymbol{q}_\mu \cdot \boldsymbol{\delta r} \, d^d r = [d(\boldsymbol{p}_\mu \, d^d r)/dt] \cdot \boldsymbol{\delta r}$ for any smooth infinitesimal virtual displacement field $\boldsymbol{\delta r}$. The former relation can be integrated on the whole system:

$$\int_{\mathbb{R}^d} \boldsymbol{w}_\mu \cdot \boldsymbol{\delta r} \, d^d r + \int_{\mathbb{R}^d} \boldsymbol{q}_\mu \cdot \boldsymbol{\delta r} \, d^d r = \int_{\mathbb{R}^d} \frac{d(\boldsymbol{p}_\mu \, d^d r)}{dt} \cdot \boldsymbol{\delta r} \,. \tag{4.76}$$

The first integral in Eq. (4.77) represents the work δW_μ of the external forces on the whole system, and is therefore equal to the variation δE_μ of the energy of the

system during the infinitesimal displacement. Thus, averaging over the microstates $\mu \to ([\phi], \boldsymbol{\ell})$, we obtain

$$\langle \delta E_\mu \rangle_{\mu \to ([\phi],\boldsymbol{\ell})} = -\int_{\mathbb{R}^d} \boldsymbol{q}([\phi],\boldsymbol{\ell}) \cdot \boldsymbol{\delta r}\, d^d r + \int_{\mathbb{R}^d} \left\langle \frac{d(\boldsymbol{p}_\mu\, d^d r)}{dt} \right\rangle_{\mu \to ([\phi],\boldsymbol{\ell})} \cdot \boldsymbol{\delta r}\,, \tag{4.77}$$

where we have used Eq. (4.75). Neglecting the average inertial term in Eq. (4.77) yields

$$\langle \delta E_\mu \rangle_{\mu \to ([\phi],\boldsymbol{\ell})} = -\int_{\mathbb{R}^d} \boldsymbol{q}([\phi],\boldsymbol{\ell}) \cdot \boldsymbol{\delta r}\, d^d r\,. \tag{4.78}$$

It is possible to neglect the inertial term even out of equilibrium provided that the timescales considered are sufficiently large, as in case of the Langevin equation [140].

Let us consider the variation δH of the coarse-grained Hamiltonian H during the virtual displacement $\boldsymbol{\delta r}$. Let us denote by $\tilde{\phi} = \phi + \delta\phi$ the field after the displacement, and by $\boldsymbol{\ell} + \boldsymbol{\delta\ell}$ the position of the center of mass of the inclusion after the displacement. We can write at first order

$$\delta H([\phi],\boldsymbol{\ell}) \equiv H([\tilde{\phi}],\boldsymbol{\ell}+\boldsymbol{\delta\ell}) - H([\phi],\boldsymbol{\ell}) = \frac{k_{\mathrm{B}}T}{Z([\phi],\boldsymbol{\ell})} \Big(Z([\phi],\boldsymbol{\ell}) - Z([\tilde{\phi}],\boldsymbol{\ell}+\boldsymbol{\delta\ell}) \Big)\,. \tag{4.79}$$

We assume that the smooth infinitesimal virtual displacement $\boldsymbol{\delta r}$ yields a one-to-one mapping of each fundamental microstate $\mu \to ([\phi],\boldsymbol{\ell})$ to a fundamental microstate $\mu' \to ([\tilde{\phi}],\boldsymbol{\ell}+\boldsymbol{\delta\ell})$. In the present Appendix, we do not discuss the way ϕ is affected by the infinitesimal displacement —this problem is dealt with in the body of this Chapter— but we only assume that ϕ is modified by an amount $\delta\phi$, which is a function of $\boldsymbol{\delta r}$. Then,

$$Z([\tilde{\phi}],\boldsymbol{\ell}+\boldsymbol{\delta\ell}) = \sum_{\mu' \to ([\tilde{\phi}],\boldsymbol{\ell}+\boldsymbol{\delta\ell})} e^{-\beta E_{\mu'}} = \sum_{\mu \to ([\phi],\boldsymbol{\ell})} e^{-\beta(E_\mu + \delta E_\mu)}\,, \tag{4.80}$$

and we obtain at first order

$$\delta H([\phi],\boldsymbol{\ell}) = \langle \delta E_\mu \rangle_{\mu \to ([\phi],\boldsymbol{\ell})}\,, \tag{4.81}$$

so Eq. (4.78) becomes

$$\delta H([\phi],\boldsymbol{\ell}) = -\int_{\mathbb{R}^d} \boldsymbol{q}([\phi],\boldsymbol{\ell}) \cdot \boldsymbol{\delta r}\, d^d r\,. \tag{4.82}$$

Assuming that $\boldsymbol{\delta r}$ is constant in $\mathcal{A}$, equal to $\boldsymbol{\delta\ell}$ (so that the inclusion undergoes a translation), Eq. (4.82) becomes

$$\delta H([\phi],\boldsymbol{\ell}) = -\boldsymbol{f}([\phi],\boldsymbol{\ell}) \cdot \boldsymbol{\delta\ell} - \int_{\mathcal{B}} \boldsymbol{q}([\phi],\boldsymbol{\ell}) \cdot \boldsymbol{\delta r}\, d^d r\,, \tag{4.83}$$

where

$$\boldsymbol{f}([\phi],\boldsymbol{\ell}) = \int_{\mathcal{A}} \boldsymbol{q}([\phi],\boldsymbol{\ell})\, d^d r \tag{4.84}$$

is the force exerted by the fluid medium on the inclusion in the coarse-grained description. Thus, Eq. (4.83) gives

$$\boldsymbol{f}([\phi],\boldsymbol{\ell}) = -\frac{\partial H([\phi],\boldsymbol{\ell})}{\partial \ell_i}\boldsymbol{e}_i\,, \tag{4.85}$$

which corresponds to the fundamental definition Eq. (4.2).

Note that the force $\boldsymbol{f}([\phi],\boldsymbol{\ell})$ is relevant at the coarse-graining level where the system is described by $([\phi],\boldsymbol{\ell})$. It is a force averaged over the microstates $\mu \to ([\phi],\boldsymbol{\ell})$: indeed, in the fundamental microstate μ, the force exerted by the medium on the inclusion is

$$\boldsymbol{f}_\mu = \int_{\mathcal{A}} \boldsymbol{q}_\mu \, d^d r\,, \tag{4.86}$$

which verifies

$$\langle \boldsymbol{f}_\mu \rangle_{\mu\to([\phi],\boldsymbol{\ell})} = \int_{\mathcal{A}} \langle \boldsymbol{q}_\mu \rangle_{\mu\to([\phi],\boldsymbol{\ell})} \, d^d r = \boldsymbol{f}([\phi],\boldsymbol{\ell})\,, \tag{4.87}$$

where we have used Eq. (4.75) and (4.84).

If there are singularities in the energy density of the system at the boundaries of $\mathcal{A}$, the mathematical definition $\boldsymbol{f} = \int_{\mathcal{A}} \boldsymbol{q}\, d^d r$ can become ambiguous. This is the case for instance when such singularities yield Dirac terms in $\boldsymbol{q}$ at the boundaries of $\mathcal{A}$ (see, e.g., the Appendix, Sec. 4.8.3). However, the force $\boldsymbol{f}$ must take into account all the terms that come from the presence of the inclusion, including boundary terms. Thus, in general, the integral over $\mathcal{A}$ has to be carried out using the following procedure:

$$\int_{\mathcal{A}} \boldsymbol{q}\, d^d r = \lim_{\epsilon\to 0} \int_{\mathcal{A}_\epsilon} \boldsymbol{q}\, d^d r\,, \tag{4.88}$$

where $\mathcal{A}_\epsilon$ contains $\mathcal{A}$ and its boundary $\mathcal{S}$ plus a shell of hypervolume ϵ, so that each point of $\mathcal{A}$ and $\mathcal{S}$ is interior to $\mathcal{A}_\epsilon$ for all $\epsilon > 0$. This procedure amounts to performing the integral infinitesimally outside the inclusion, in order to ensure that the whole inclusion is enclosed in our hypersurface of integration. Using this procedure does not change the result in the case where $\boldsymbol{q}$ is a piecewise continuous function.

Note that we can also extract the hypervolume density $\boldsymbol{q}$ of internal forces in the medium, at the coarse-graining level where the system is described by $([\phi],\boldsymbol{\ell})$, from Eq. (4.82):

$$\boldsymbol{q}([\phi],\boldsymbol{\ell}) = -\frac{\delta H([\phi],\boldsymbol{\ell})}{\delta r_i}\boldsymbol{e}_i. \tag{4.89}$$

4.8.2 Derivation of the stress tensor $\boldsymbol{T}$ of the fluid medium

In this Appendix, we consider a fluid medium with Hamiltonian density $\mathcal{H}(\phi,\boldsymbol{\nabla}\phi)$ without any inclusion. The stress tensor associated to $\mathcal{H}$ can be derived from Noether's theorem (see, e.g., Ref. [141]). Indeed, it is the Noether current associated to the translation invariance of the system. It is obtained by considering the following infinitesimal translation:

$$\begin{cases} \boldsymbol{r} & \to \quad \boldsymbol{r} + \boldsymbol{\delta r}\,, \\ \phi(\boldsymbol{r}) & \to \quad \phi(\boldsymbol{r}) + \delta\phi(\boldsymbol{r})\,. \end{cases} \tag{4.90}$$

with constant $\boldsymbol{\delta r}$, and with $\delta\phi(\boldsymbol{r}) = -\boldsymbol{\nabla}\phi(\boldsymbol{r})\cdot\boldsymbol{\delta r}(\boldsymbol{r})$, i.e., $\delta^T\phi \equiv 0$. The stress tensor given directly by Noether's theorem is often called the *canonical* stress tensor (or more generally, in time-dependent field theories, the canonical energy-impulsion tensor). Indeed, it is its divergence that appears in the conservation law associated with translation invariance, so any tensor with vanishing divergence can be freely added to this canonical stress tensor. Such modifications of the stress tensor are often used in field theory, for instance to ensure its symmetry or its scale or conformal invariance [142]. However, in the case of perturbative embedded inclusions, where the stress tensor is defined everywhere in the system, even inside the inclusions (see the Appendix, Sec. 4.8.3), Stokes' theorem can be applied to the integral of the stress tensor on any closed hypersurface, so that the divergence-free "improvement" terms do not contribute to Casimir-like forces (this argument is used in Ref. [143]). We will not discuss these terms further.

In the present work, our field-theoretic model describes a fluid medium where the interactions are supposed to be short-ranged. Thus, another way of constructing the stress tensor of the medium is to adapt the definition of continuum mechanics. Let us define the stress tensor $\boldsymbol{T}$ by the relation

$$df_i = T_{ij} n_j \, d^{d-1}r \,, \tag{4.91}$$

where $\boldsymbol{df}$ is the infinitesimal force that one side of the medium (side 1) exerts onto the other side (side 2) through the hypersurface $d^{d-1}r$, and $\boldsymbol{n}$ denotes the normal to this hypersurface directed toward side 1 [131, 144]. The stress tensor $\boldsymbol{T}$ of the medium can be determined from its energy H using the principle of virtual work. For this, we start by cutting (virtually) a subpart $\mathcal{A}$ of the medium, with energy

$$H_{\mathcal{A}} = \int_{\mathcal{A}} \mathcal{H}(\phi, \boldsymbol{\nabla}\phi) \, d^d r \,. \tag{4.92}$$

Let us call $\mathcal{B}$ the rest of the medium (i.e., $\mathcal{B} = \mathbb{R}^d \smallsetminus \mathcal{A}$), and $\mathcal{S}$ the interface between $\mathcal{A}$ and $\mathcal{B}$. Let us now consider an infinitesimal transformation of the medium, as defined in Eq. (4.3). We consider that each fluid particle keeps the same ϕ during the displacement: $\delta\phi(\boldsymbol{r}) = -\boldsymbol{\nabla}\phi(\boldsymbol{r})\cdot\boldsymbol{\delta r}(\boldsymbol{r})$, i.e., $\delta^T\phi \equiv 0$. The variation during this transformation of the energy $H_{\mathcal{A}}$ of the closed system initially in $\mathcal{A}$ reads, at first order in ϵ:

$$\delta H_{\mathcal{A}} = -\int_{\mathcal{A}} \left[\frac{\partial\mathcal{H}}{\partial\phi} - \partial_j\left(\frac{\partial\mathcal{H}}{\partial(\partial_j\phi)}\right)\right] \partial_i\phi \, \delta r_i \, d^d r + \int_{\mathcal{S}} \left[\mathcal{H}\delta_{ij} - \frac{\partial\mathcal{H}}{\partial(\partial_j\phi)}\partial_i\phi\right] n_j \, \delta r_i \, d^{d-1}r \,. \tag{4.93}$$

This variation of energy can be equated to the work δW done during the transformation by the external forces acting on the closed system initially in $\mathcal{A}$:

$$\delta W = \int_{\mathcal{A}} w_i \, \delta r_i \, d^d r + \int_{\mathcal{S}} T_{ij} n_j \, \delta r_i \, d^{d-1}r \,, \tag{4.94}$$

where $\boldsymbol{w}$ is the hypersurface density of forces exerted by the exterior on the fluid medium, so that the integral on $\mathcal{A}$ represents the forces exerted by the exterior of the

medium on the closed system initially in $\mathcal{A}$. Meanwhile, the integral on $\mathcal{S}$ represents the force exerted by the rest of the medium on the closed system initially in $\mathcal{A}$, which has been expressed using the stress tensor thanks to its definition Eq. (4.92). Since the energy balance $\delta H = \delta W$ must hold for any virtual deformation field $\boldsymbol{\delta r}$, we can identify the stress tensor of the medium:

$$T_{ij} = \mathcal{H}\delta_{ij} - \frac{\partial \mathcal{H}}{\partial(\partial_j \phi)}\partial_i \phi \,. \tag{4.95}$$

In addition, the identification of the bulk term gives the hypervolume density $\boldsymbol{q}$ of internal forces in the medium. Neglecting inertia, which is possible if the timescales considered are sufficiently large, Newton's second law applied to each fluid particle of the medium gives $\boldsymbol{q} = -\boldsymbol{w}$, where $\boldsymbol{w}$ represents the hypervolume density of external forces (see the Appendix, Sec. 4.8.1). Thus, we obtain:

$$q_i = -w_i = \left[\frac{\partial \mathcal{H}}{\partial \phi} - \partial_j \left(\frac{\partial \mathcal{H}}{\partial(\partial_j \phi)}\right)\right] \partial_i \phi = \partial_j T_{ij} \,. \tag{4.96}$$

This derivation of the stress tensor shows that the stress tensor itself is built *by assuming that each fluid particle keeps the same ϕ during a displacement.* It is therefore not surprising that we find the stress tensor when we calculate the force $\boldsymbol{f}^{(2)}$ under this assumption.

With our mechanical definition of the stress tensor, we have obtained, from the principle of virtual work, a stress tensor $\boldsymbol{T}$ that is identical to the canonical stress tensor $\boldsymbol{T}^c$ given by Noether's theorem. In field theory, the stress tensor $\boldsymbol{T}^c$ generally written is in fact $T^c_{ij} = -T_{ji}$ [141, 142], but this apparent difference is just a matter of convention. Note that our stress tensor $\boldsymbol{T}$ is fully defined (not up to a term with vanishing divergence) because we have asked it to give the force exchanged through any infinitesimal hypersurface.

4.8.3 Stress tensor $\boldsymbol{T}'$ of the fluid medium with a perturbative embedded inclusion

Let us now consider the fluid medium with a perturbative embedded inclusion in it: its effective Hamiltonian H corresponds to Eq. (4.17). Carrying out the same reasoning as in the previous section, using a generic infinitesimal deformation $\boldsymbol{\delta r}$, enables to identify the stress tensor $\boldsymbol{T}'$ of the composite medium including the perturbative inclusion:

$$T'_{ij} = (\mathcal{H} + V\,\mathbf{1}_{\mathcal{A}})\,\delta_{ij} - \frac{\partial \mathcal{H}}{\partial(\partial_j \phi)}\partial_i \phi \,. \tag{4.97}$$

The same reasoning also enables to identify the hypervolume density of internal forces at each point of the composite medium as $q'_i = \partial_j T'_{ij}$. Explicitly, it gives

$$\boldsymbol{q}' = \frac{\delta H}{\delta \phi}\boldsymbol{\nabla}\phi + V\,\boldsymbol{\nabla}\mathbf{1}_{\mathcal{A}} \,, \tag{4.98}$$

where H is defined in Eq. (4.17), and its functional derivative with respect to ϕ is given by Eq. (4.19). Note that the gradient of $\mathbf{1}_{\mathcal{A}}$, and thus $\boldsymbol{q}'$, features Dirac singularities on the contour of $\mathcal{A}$, i.e., on $\mathcal{S}$.

4.8.4 Point-like embedded inclusion or non-embedded influencing object

Let us consider a point-like object in $\boldsymbol{r} = \boldsymbol{\ell}$ that is coupled to $\phi(\boldsymbol{\ell})$:

$$H = \int_{\mathbb{R}^d} \mathcal{H}(\phi, \boldsymbol{\nabla}\phi)\, d^d r + V(\phi(\boldsymbol{\ell})) = \int_{\mathbb{R}^d} \left[\mathcal{H} + V\delta(\boldsymbol{r} - \boldsymbol{\ell})\right]\, d^d r\,. \tag{4.99}$$

Here, the total variation of H during the infinitesimal transformation (4.3) reads, at first order:

$$\delta H = \int_{\mathbb{R}^d} \left[\frac{\partial \mathcal{H}}{\partial \phi} - \partial_i \left(\frac{\partial \mathcal{H}}{\partial(\partial_i \phi)}\right)\right] \delta\phi\, d^d r + \frac{\partial V}{\partial \phi}(\phi(\boldsymbol{\ell}))\left[\delta\phi + \boldsymbol{\nabla}\phi \cdot \boldsymbol{\delta\ell}\right]\,. \tag{4.100}$$

Thus, the first route, which corresponds to $\delta\phi \equiv 0$, yields

$$\boldsymbol{f}^{(1)} = -\boldsymbol{\nabla}\phi(\boldsymbol{\ell})\, \frac{\partial V}{\partial \phi}(\phi(\boldsymbol{\ell}))\,. \tag{4.101}$$

Meanwhile, if we follow the second route, i.e., if $\delta^{\mathrm{T}}\phi = \delta\phi + \boldsymbol{\nabla}\phi \cdot \boldsymbol{\delta r} \equiv 0$, Eq. (4.100) becomes

$$\delta H = -\int_{\mathbb{R}^d} \left[\frac{\partial \mathcal{H}}{\partial \phi} - \partial_j \left(\frac{\partial \mathcal{H}}{\partial(\partial_j \phi)}\right)\right] \partial_i \phi\, \delta r_i\, d^d r = -\int_{\mathbb{R}^d} \partial_j T_{ij}\, \delta r_i\, d^d r\,, \tag{4.102}$$

where we have used Eq. (4.10). In spite of this simple expression, we must remember that the energy density $\mathcal{H} + V\delta(\boldsymbol{r} - \boldsymbol{\ell})$ has a singularity in $\boldsymbol{\ell}$. To deal with it, let us write

$$\delta H = -\lim_{\epsilon \to 0} \int_{\mathbb{R}^d \setminus B_\epsilon^{\boldsymbol{\ell}}} \partial_j T_{ij}\, \delta r_i\, d^d r - \left\{\lim_{\epsilon \to 0} \int_{B_\epsilon^{\boldsymbol{\ell}}} \partial_j T_{ij}\, d^d r\right\} \delta \ell_i\,. \tag{4.103}$$

where $B_\epsilon^{\boldsymbol{\ell}}$ denotes the hyperball of radius ϵ centered on $\boldsymbol{\ell}$. This relation enables to identify $\boldsymbol{f}^{(2)}$ as

$$\boldsymbol{f}^{(2)} = \lim_{\epsilon \to 0} \int_{B_\epsilon^{\boldsymbol{\ell}}} \partial_j T_{ij}\, d^d r\, \boldsymbol{e}_i = \lim_{\epsilon \to 0} \int_{S_\epsilon^{\boldsymbol{\ell}}} T_{ij} n_j\, d^{d-1} r\, \boldsymbol{e}_i\,, \tag{4.104}$$

where $S_\epsilon^{\boldsymbol{\ell}}$ denotes the hypersphere of radius ϵ centered on $\boldsymbol{\ell}$ and $\boldsymbol{n}$ is its exterior normal.

Thus, the difference between the two ways of keeping ϕ constant while varying $\boldsymbol{\ell}$ remains for point-like objects. As in the case of extended objects, the force $\boldsymbol{f}^{(2)}$ is adapted to a point-like embedded inclusion, while the force $\boldsymbol{f}^{(1)}$ is adapted to a non-embedded point-like influencing object.

Chapter 5

Casimir-like interactions between rods in fluid membranes

Contents

5.1 Introduction **107**

5.2 Model **109**

5.2.1 Description of the membrane 109

5.2.2 Description of the rods 109

5.3 Simple rods with finite out-of-plane bending rigidity . . **111**

5.3.1 Partition function 112

5.3.2 Casimir-like interaction 113

5.3.3 Numerical results at all separations for rigid rods 114

5.4 Other types of rods **115**

5.4.1 Interactions between all types of rigid rods 115

5.4.2 Antagonistic constraints and repulsion 117

5.4.3 Zeta-function regularization method 118

5.5 Discussion **119**

5.5.1 Undulation instability 119

5.5.2 Effect of tension 122

5.6 Conclusion **122**

5.1 Introduction

In Chapter 3, we presented our study of the fluctuations of the Casimir-like force between membrane inclusions, and in Chapter 4, we exposed our subsequent work on the definition of the force exerted by a correlated fluid on an embedded inclusion in a given microstate of the fluid. We will now come back to Casimir-like forces in

biological membranes, but we will focus on the geometry of parallel rods instead of that of point-like inclusions discussed in Chapter 3. This geometry is interesting since it can yield stronger Casimir-like interactions. As mentioned in Sec. 2.4.2, the Casimir-like interaction energy between point-like membrane inclusions, albeit being long-range, is quite small compared to $k_{\mathrm{B}}T$ at relevant distances between inclusions. If one considers instead two parallel rigid rods with length L much larger than their separation d, one expects a constant scale-free Casimir-like interaction per unit length, i.e., a potential in $k_{\mathrm{B}}TL/d$ [76, 86], as discussed in Sec. 2.4.3. Effective attraction will thus result in the regime $d \ll L$ if the numerical prefactor involved in the potential is of order unity. Qualitatively, this difference is due to the fact that close parallel rods impose much more stringent constraints on the shape of the membrane than point-like inclusions.

The rods we are discussing can model stiff polymers adsorbed on membranes. Biologically relevant stiff polymers that can adsorb on membranes include actin filaments [145, 146], actin bundles formed of several filaments [146], FtsZ rings [147] and the β–amyloid fibrils involved in Alzheimer's disease [148, 149]. Adsorption of goethite nanorods on surfactant bilayers has also been reported [150]. Examples of such rods are shown in Fig. 5.1.

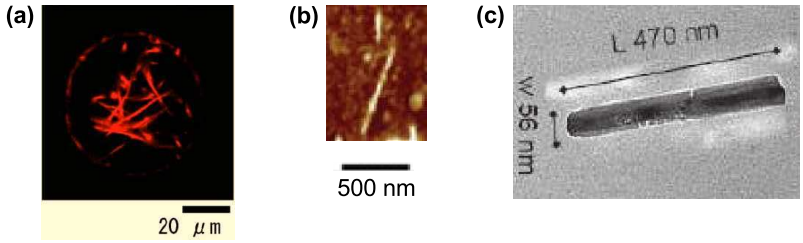

Figure 5.1: Examples of rods that can adsorb on membranes. (a): Fluorescent thick actin bundles adsorbed on a phospholipid monolayer covering a cell-sized water droplet immersed in oil, in the presence of Mg^{2+} ions. *Illustration reproduced from Ref. [146].* (b): β–amyloid fibrils adsorbed on the phospholipid bilayer membrane of a large unilamellar vesicle. *Illustration reproduced from Ref. [149].* (c): Magnetic goethite (α–FeOOH) nanorod that can adsorb onto surfactant bilayers, forming a hybrid mesophase. *Illustration reproduced from Ref. [150].*

In this Chapter, we study the Casimir-like interaction free energy $\mathcal{F}_{\mathrm{C}}$ between two parallel rods of length L adsorbed on a membrane, or embedded in it. We focus on short and intermediate separations $d \lesssim L$. This interaction free energy can be calculated by studying rods whose only effect is to restrict the membrane fluctuations: then, $\mathcal{F}_{\mathrm{C}}$ corresponds to the d-dependent part of the free energy of the system. The Casimir-like force can be obtained by direct differentiation of $\mathcal{F}_{\mathrm{C}}$.

We model rods as constraints imposed on the membrane curvature along a straight line. This allows to define four types of rods, according to whether the membrane can twist along the rod and/or curve across it. We present analytical calculations performed at short separations $d \ll L$. For stiff constraints, all the interaction potentials between the different types of rods are attractive and proportional to L/d. We obtain the exact expression and the value of the universal

numerical prefactors involved in these potentials. We also show that repulsion can occur between different rods for soft constraints. Numerical results obtained for all ranges of d/L in the case of stiff rods show that the attraction potential reaches $k_{\mathrm{B}}T$ for $d/L \simeq 0.2$. At separations smaller than $d_c \approx L(L/\ell_p)^{1/3}$, where ℓ_p is the rod persistence length, two rods with fixed ends will bend toward each other and finally come into contact because of the Casimir-like interaction.

The main results presented in this Chapter have been published in: A.-F. Bitbol, K. Sin Ronia and J.-B. Fournier, *Universal amplitudes of the Casimir-like interactions between four types of rods in fluid membranes*, EuroPhysics Letters 96, 40013 (2011), cited as Ref. [151] here.

5.2 Model

5.2.1 Description of the membrane

We will describe the membrane exactly as in Chapter 3 (see Sec. 3.2.1). Let us recall briefly the key elements of this description. We focus on small deformations around the flat shape, and we parametrize the membrane in the Monge gauge by its height $z = h(\boldsymbol{r})$ above a reference plane, where $\boldsymbol{r} = (x, y) \in \mathbb{R}^2$. We will refer to the latter coordinates as "in-plane" and to z as "out-of-plane". We use the Helfrich Hamiltonian [24] (see Eq. (1.8)) with zero spontaneous curvature, which corresponds to a symmetric membrane. The contribution of the Gaussian curvature can be disregarded since it is constant. Finally, we focus on membranes dominated by their bending rigidity κ, i.e., we assume that the length scale $\sqrt{\kappa/\sigma}$, which compares its effect to that of the membrane tension σ, is much larger than all other relevant lengths. Cases where tension is important will be briefly discussed in Sec. 5.5.2.

The effective Hamiltonian of the membrane thus reads:

$$\mathcal{H} = \int d\boldsymbol{r}\, \frac{\kappa}{2} \left[\nabla^2 h(\boldsymbol{r})\right]^2 . \tag{5.1}$$

5.2.2 Description of the rods

The presence of a rigid rod lying within the membrane (or absorbed on it) is traditionally described by imposing the constraint [84, 152]:

$$h(\boldsymbol{r}) = a + \boldsymbol{b} \cdot \boldsymbol{r} \tag{5.2}$$

for $\boldsymbol{r}$ in a narrow rectangle $[x_0 - \epsilon, x_0 + \epsilon] \times [0, L]$, where a and $\boldsymbol{b}$ describe translational and tilt degrees of freedom, respectively. This is fully equivalent to imposing in the same domain the constraints:

$$h_{yy} = 0\,, \qquad h_{xx} = 0\,, \qquad h_{xy} = 0\,, \tag{5.3}$$

where $h_{ij} \equiv \partial_i \partial_j h$. An infinitely narrow rod can be described by imposing conditions (5.3) for $x = x_0$ and $y \in [0, L]$.

The single condition $h_{yy} = 0$, however, is sufficient to specify a rod. In the absence of the other conditions, the membrane can curve across the rod and twist along it. It follows that we may consider four types of rods (see Fig. 5.2):

1. Curved-twisted (ct): $h_{yy} = 0$,
2. Curved-nontwisted ($\mathrm{c\bar{t}}$): $h_{yy} = h_{xy} = 0$,
3. Noncurved-twisted ($\mathrm{\bar{c}t}$): $h_{yy} = h_{xx} = 0$,
4. Noncurved-nontwisted ($\mathrm{\bar{c}\bar{t}}$): $h_{yy} = h_{xx} = h_{xy} = 0$.

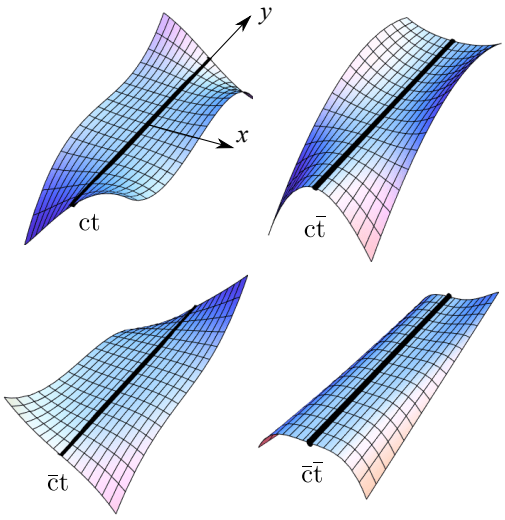

Figure 5.2: Four types of rods for which the membrane may or may not curve (c) across the rod or twist (t) along it.

The actual constraints imposed on the coarse-grained field h by a given rod depend on its microscopic properties, such as its width and its interactions with the lipids that constitute the membrane. In order to discuss this in more detail, let us introduce the natural short-length cutoff a of the theory, which is of order of the membrane thickness. No smaller cutoff can be considered since the membrane is modeled as a thin surface. The meaning of this cutoff is that the field h is constructed through a coarse-graining, for instance a simple moving average, of the height of each lipid molecule over the length scale a.

First, let us consider a rod with width smaller than a that interacts with the lipids through short-range (e.g., hydrophobic) interactions, which can be neglected at a distance a. Such a rod cannot affect h_{xx} or h_{xy}, and it will thus be of the "ct" type. On the contrary, a rod with a width equal to, or a little bit larger than a will be of the "$\mathrm{\bar{c}\bar{t}}$" type. Indeed, this width is sufficient for the thin flat region arising from the presence of the rod to remain after the coarse-graining. A rod which has strong anisotropic attractive interactions with the lipids, with a range at least of order a, would behave as a "$\mathrm{\bar{c}\bar{t}}$" rod too.

In the case of intermediate ranges of interactions, the rod could constrain the slope but not the curvature of the membrane, in which case one would obtain the "c$\bar{\text{t}}$" type. Finally, the "$\bar{\text{c}}$t" type could correspond to a rod with width of order a and with short-range interactions, but composed of units free to twist relative to one another.

In our coarse-grained description, all such rods can be treated as one-dimensional objects since their width is of order a or smaller. Hence, the microscopic properties of a rod (width, interactions) will only appear indirectly in our work, through the rod type.

5.3 Simple rods with finite out-of-plane bending rigidity

Let us first calculate the Casimir-like interaction between two parallel rods of the simplest "ct" type, in the $d \ll L$ regime (see Fig. 5.3). Let us assume periodic boundary conditions with period L along the y direction. This amounts to neglecting the effect of the edges of the rods, which is legitimate for $d \ll L$.

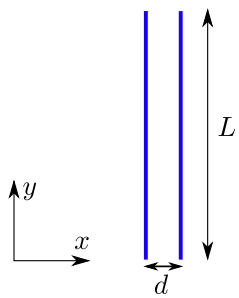

Figure 5.3: Two parallel rods of length L separated by a distance $d \ll L$.

Generalizing the hard constraint $h_{yy} = 0$ to rods with a finite out-of-plane bending rigidity, we account for the presence of the rods by adding to $\mathcal{H}$ the following interaction energies between each rod and the membrane:

$$\mathcal{H}_i' = \int_0^L dy\, \frac{\kappa_\perp}{2} h_{yy}^2(x_i, y), \tag{5.4}$$

for $i \in \{1, 2\}$, with $x_1 = 0$ and $x_2 = d > 0$. Thus, we allow out-of-plane fluctuations of the rods with a bending rigidity

$$\kappa_\perp = k_\mathrm{B} T \ell_\perp\,, \tag{5.5}$$

where $\ell_\perp$ plays the part of a persistence length. Note that $\kappa_\perp$ does not have the same dimension as κ, because $\kappa_\perp$ is a bending rigidity in one dimension (a polymer bending rigidity) while κ is a bending rigidity in two dimensions (a membrane bending rigidity). The hard constraint $h_{yy} = 0$ is recovered in the limit $\kappa_\perp \to \infty$. Note that we implicitly assume in any case an infinite in-plane rigidity $\kappa_\parallel \to \infty$. This hypothesis will be discussed in Sec. 5.5.1.

5.3.1 Partition function

The partition function of the membrane containing the two rods can be expressed as the functional integral

$$Z = \int \mathcal{D}h \, \exp\left[-\beta(\mathcal{H} + \mathcal{H}_1' + \mathcal{H}_2')\right] , \tag{5.6}$$

where $\beta = 1/(k_\mathrm{B}T)$. To calculate this partition function, we will adapt to our general constraints the field-theoretical method introduced by Li and Kardar in Ref. [76] for the calculation of Casimir-like forces between manifolds immersed in correlated fluids. These calculations will be reminiscent of those presented in Sec. 3.2.2 in the case of point-like inclusions.

Introducing two auxiliary fields ψ_i, which are assumed to be periodic with period L, carrying out a Hubbard-Stratonovitch transformation [119] and integrating twice by parts, we can write

$$\exp\left[-\beta\mathcal{H}_i'\right] = \int \mathcal{D}\psi_i \, \exp\left[-\frac{1}{2}\int dy \, \ell_\perp^{-1}\psi_i^2 + i\int d\boldsymbol{r} \, h(\boldsymbol{r})\psi_i''(y)\delta(x - x_i)\right] . \tag{5.7}$$

Substituting Eq. (5.7) into the partition function in Eq. (5.6) gives an expression of Z featuring a Gaussian functional integral over h. Performing it yields

$$Z = \int \mathcal{D}\psi_1 \, \mathcal{D}\psi_2 \, \exp\left[-\frac{1}{2L}\sum_{n\in\mathbb{Z}} \Psi^\dagger(q_n) M(d, q_n)\Psi(q_n)\right] , \tag{5.8}$$

where we have introduced the Fourier coefficients of the auxiliary fields ψ_i, for $q_n = 2\pi n/L$, where $n \in \mathbb{Z}$:

$$\psi_i(q_n) = \int_0^L dy \, \psi_i(y) e^{-iq_n y} , \tag{5.9}$$

and we have regrouped them into the vector $\Psi(q_n) = (\psi_1(q_n), \ \psi_2(q_n))^t$. Note that it verifies $\Psi^\dagger(q_n) = \Psi^t(-q_n)$, where $\dagger$ denotes Hermitian conjugation while t denotes transposition. Besides, the matrix M featured in Eq. (5.8) reads

$$M(d, q_n) = \begin{pmatrix} \ell_\perp^{-1} + \Gamma(0, q_n) & \Gamma(-d, q_n) \\ \Gamma(d, q_n) & \ell_\perp^{-1} + \Gamma(0, q_n) \end{pmatrix} , \tag{5.10}$$

where Γ is the Fourier transform along y of $\partial_y^4 G$, the function G being the correlation function of the rod-free membrane. As seen in Sec. 3.2.2, G is a Green's function of the differential operator associated with the membrane Hamiltonian in Eq. (5.1): $G(\boldsymbol{r} - \boldsymbol{r}') = \langle \boldsymbol{r}|(\beta\kappa\nabla^4)^{-1}|\boldsymbol{r}'\rangle$. Thus, Γ has the following explicit expression:

$$\Gamma(x, q) = \frac{k_\mathrm{B}T}{\kappa} q^4 \int_{-\infty}^{\infty} \frac{dp}{2\pi} \frac{e^{ipx}}{(p^2 + q^2)^2} = \frac{k_\mathrm{B}T}{4\kappa}|q| \left(1 + |q\,x|\right) e^{-|q\,x|}. \tag{5.11}$$

Note that the matrix M is Hermitian, given that $\Gamma(-d, q_n) = \Gamma(d, q_n)^*$, where $*$ denotes complex conjugation.

Performing the functional Gaussian integrals over the fields ψ_i finally yields

$$Z = Z_0 \prod_{n\in\mathbb{Z}} \left\{\det\left[M\left(d, q_n\right)\right]\right\}^{-\frac{1}{2}} , \tag{5.12}$$

where Z_0 is independent of d.

5.3.2 Casimir-like interaction

We have obtained an explicit expression of the partition function Z of the membrane containing two parallel "ct" rods (see Eqs. (5.12), (5.10) and (5.11)). The Casimir-like interaction free energy between these two rods corresponds to the d-dependent part of the free energy $-k_{\mathrm{B}}T\ln Z$. Hence, it reads

$$\mathcal{F}_{\mathrm{C}}^{\mathrm{ct|ct}}(d) = \frac{1}{2}k_{\mathrm{B}}T\sum_{n\in\mathbb{Z}}\ln\det\left[M(d,q_n)\right]\,. \tag{5.13}$$

Given that $L \gg d$, we can replace the series by an integral, which yields, using Eqs. (5.10) and (5.11),

$$\mathcal{F}_{\mathrm{C}}^{\mathrm{ct|ct}}(d) = \frac{k_{\mathrm{B}}TL}{2}\int_{\mathbb{R}}\frac{dq}{2\pi}\,\ln\left[1-\left(\frac{\Gamma(d,q)}{\ell_\perp^{-1}+\Gamma(0,q)}\right)^2\right] = k_{\mathrm{B}}T\frac{L}{d}\,\phi^{\mathrm{ct|ct}}(d)\,, \tag{5.14}$$

where we have introduced

$$\phi^{\mathrm{ct|ct}}(d) = \int_0^\infty\frac{dx}{2\pi}\ln\left[1-\left(\frac{1+x}{1+\bar{d}/x}\right)^2 e^{-2x}\right],\quad \text{with}\ \ \bar{d} = \frac{4\kappa}{k_{\mathrm{B}}T}\,\frac{d}{\ell_\perp}\,. \tag{5.15}$$

It can be shown that the integral expression of the Casimir-like interaction in Eq. (5.14) is consistent with Eqs. (4) and (8) of ref. [86]. Our method for calculating the Casimir-like interaction, however, is more direct, and we will extract explicit forms for the asymptotic behaviors and extend it to other types of rods.

Let us study the asymptotic regimes of Eq. (5.14). The one corresponding to $\bar{d} \ll 1$ is reached in the limit of small separations d for given rods, or equivalently, in the limit of large $\ell_\perp$ (i.e., large out-of-plane bending rigidity $\kappa_\perp$ of the rods, see Eq. (5.5)) at fixed d. We will call this limit the "hard" limit, and the opposite limit $\bar{d} \gg 1$ the "soft" limit, bearing in mind that hardness and softness are effective properties that depend on the separation between rods.

In the "hard" limit where $\bar{d}$ tends to zero ($\kappa_\perp \to \infty$), $\phi^{\mathrm{ct|ct}}$ reaches a constant limit, denoted by $A^{\mathrm{ct|ct}}$:

$$\mathcal{F}_{\mathrm{C}}^{\mathrm{ct|ct}}(d) \;=\; A^{\mathrm{ct|ct}}\,k_{\mathrm{B}}T\frac{L}{d}\,, \tag{5.16}$$

$$A^{\mathrm{ct|ct}} \;=\; \int_0^\infty\frac{dx}{2\pi}\ln\left[1-(1+x)^2\,e^{-2x}\right] \simeq -0.46237. \tag{5.17}$$

This "hard" limit corresponds to rods imposing $h_{yy} = 0$. In this limit, the Casimir-like interaction is universal: it depends only on $k_{\mathrm{B}}T$ and on the geometry of the system. Besides, given that the numerical prefactor $A^{\mathrm{ct|ct}}$ is close to unity, this attractive Casimir-like interaction is strong in this regime for $L \gg d$.

In the "soft" limit where $\bar{d}$ tends to infinity ($\kappa_\perp \to 0$), the integral in Eq. (5.15) can be performed analytically, yielding

$$\mathcal{F}_{\mathrm{C,soft}}^{\mathrm{ct|ct}}(d) = -\frac{7}{8\pi\,\bar{d}^2}k_{\mathrm{B}}T\,\frac{L}{d} = -\frac{7k_{\mathrm{B}}T}{128\pi}\,\frac{(\kappa_\perp/\kappa)^2L}{d^3}. \tag{5.18}$$

This interaction, which is attractive, scales as d^{-3}. Nevertheless, it is very small, since it is proportional to $\bar{d}^{-2}$, and we are dealing with the limit $\bar{d} \to \infty$.

The Casimir-like interaction free energy obtained in Eq. (5.14) is plotted versus d/L in Fig. 5.4. Our result Eq. (5.14) is valid in the limit $d \ll L$. We will show in Sec. 5.5.1 that the "hard" regime is the relevant one for ordinary rods in this limit, and we will also see that rods tend to bend toward each other below a critical value of the separation d. These informations are presented in Fig. 5.4: the white region corresponds to the one where our calculation is relevant.

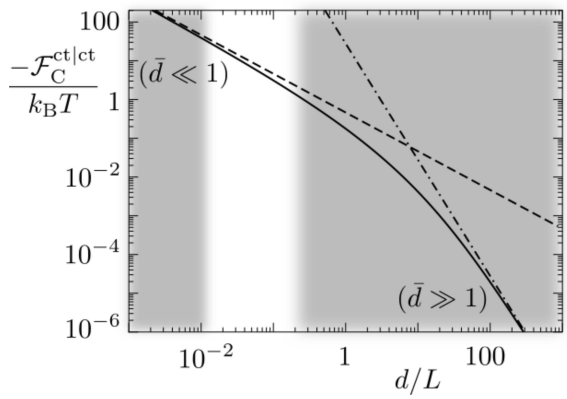

Figure 5.4: Logarithmic plot of the Casimir-like interaction free energy Eq. (5.14) between two "ct" rods of length L and separation d, calculated analytically under the assumption $d/L \ll 1$, for $L = 10^{-3}\ell_p \equiv 10^{-3}\ell_\perp$ and $\kappa = 25\,k_{\mathrm{B}}T$ (yielding $\bar{d} = 0.1d/L$). In the right shaded area the condition $d/L \ll 1$ is violated, and in the left shaded area the in-plane undulation instability discussed in Sec. 5.5.1 is expected to occur. The dashed lines show the asymptotic regimes (5.18) and (5.16). In the white region, a power-law fit indicates that one would measure $\beta\mathcal{F}_{\mathrm{C}}^{\mathrm{ct|ct}} \approx -0.2\,(L/d)^{1.2}$.

It is interesting to note that in the "hard" limit $\ell_\perp \to \infty$, the q^4 factors in $\Gamma(d,q)$ and $\Gamma(0,q)$ cancel each other out in Eq. (5.14). Hence, imposing $h_{yy} = 0$ on the rod is mathematically equivalent to setting $h = 0$ for $x = x_0$ and $y \in [0, L]$ (by means of external forces and torques). This indicates that the relative tilt of the rods is effectively frozen in this regime. Physically, this comes from the fact that we are in the $d \ll L$ regime: a relative tilt of these long rods would cost a lot of energy. More formally, as we use periodic boundary conditions with period L in the y direction in our calculation, which amounts to neglecting the effect of the edges of the rods, $h_{yy}(x_i, y) = 0$ for $y \in [0, L]$ entails that $h(x_i, y)$ is constant. Setting these constants to zero is legitimate since their presence simply corresponds to a possible change of reference plane.

5.3.3 Numerical results at all separations for rigid rods

Exact calculations of the fluctuation-induced interactions between rods at short separations $d \ll L$ were made possible by neglecting boundary effects, which results in translational invariance. Formally, this was implemented through periodic boundary conditions.

At larger separations, the effect of the edges of the rods cannot be neglected anymore. However, the Casimir-like interaction energy can be computed numerically for all d/L. Numerical schemes based on the method of Li and Kardar have been developed in Refs. [75, 153]. The idea is to discretize the functional integral over the auxiliary fields ψ_i that enforce the constraints.

Using such a discretization scheme [154], Sin Ronia and Fournier calculated the Casmir interaction between two rigid "ct" rods for all separations d (see Fig. 5.5). Although the microscopic cutoff wavelength is explicitly involved in their calculations, they obtained universal results that only depend on d/L. At large separations, they recovered the $(L/d)^4$ power-law obtained by Golestanian et al. [84]. At small separations, they recovered our result (5.16). As can be seen on Fig. 5.5, the Casimir-like interaction potential reaches $-k_\mathrm{B}T$ for $d/L \simeq 0.2$ (while using the asymptotic form would yield the overestimated value $d/L \simeq 2$). Thus, two rods approaching each other at separations less than half their length will effectively attract each other due to the Casimir-like effect.

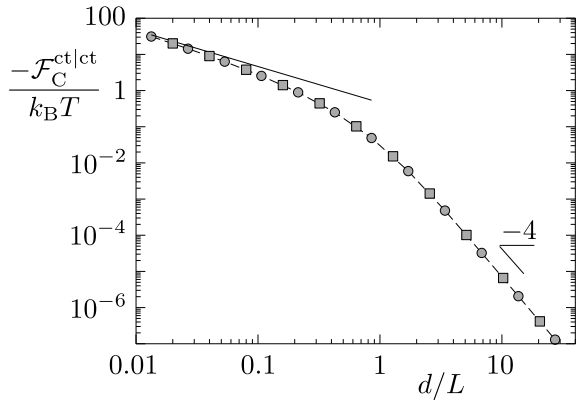

Figure 5.5: Logarithmic plot of the universal Casimir-like interaction between two rigid "ct" rods of length L and separation d, calculated numerically in all regimes of d/L [154]. Circles (resp. squares) corresponds to a length L of the rods $\simeq 75$ (resp. 50) times the microscopic cutoff. The straight line shows the analytical asymptotic behavior $\mathcal{F}_\mathrm{C}^{\mathrm{ct}|\mathrm{ct}}/(k_\mathrm{B}T) = A^{\mathrm{ct}|\mathrm{ct}}\, d/L$, valid for $d/L \ll 1$.

5.4 Other types of rods

5.4.1 Interactions between all types of rigid rods

Let us now calculate the Casimir-like interactions between the other pairs of rods (see Sec. 5.2.2) in the $d \ll L$ regime, focusing on the "hard" limit, i.e., on the situation where the conditions $h_{yy} = 0$, $h_{xy} = 0$ and $h_{xx} = 0$ are strictly imposed (see Fig. 5.2). Let us define a vectorial differential operator $\mathbb{D}^\alpha$ for each rod type $\alpha \in \{\mathrm{ct}, \mathrm{c\bar{t}}, \mathrm{\bar{c}t}, \mathrm{\bar{c}\bar{t}}\}$:

$$\begin{aligned} \mathbb{D}^{\mathrm{ct}} &= (\partial_y^2)\,, & \mathbb{D}^{\mathrm{c\bar{t}}} &= (\partial_x\partial_y,\, \partial_y^2)^t\,, \\ \mathbb{D}^{\mathrm{\bar{c}t}} &= (\partial_x^2,\, \partial_y^2)^t\,, & \mathbb{D}^{\mathrm{\bar{c}\bar{t}}} &= (\partial_x^2,\, \partial_x\partial_y,\, \partial_y^2)^t\,. \end{aligned} \tag{5.19}$$

The constraints imposed by a rod of type α can be expressed as $\mathbb{D}^\alpha h(x,y)=0$, for $x\in\{0,d\}$ and $y\in[0,L]$. Following the steps detailed above in the case of two "ct" rods, we obtain:

$$\mathcal{F}_{\mathrm{C}}^{\alpha|\beta}(d)=\frac{1}{2}k_{\mathrm{B}}T\sum_{n\in\mathbb{Z}}\ln\det\left[M^{\alpha|\beta}(d,q_n)\right], \tag{5.20}$$

where $M^{\alpha|\beta}$ is the following Hermitian block matrix:

$$M^{\alpha|\beta}(d,q)=\left(\begin{array}{c|c} G^{\alpha|\alpha}(0,q) & G^{\alpha|\beta}(-d,q) \\ \hline G^{\beta|\alpha}(d,q) & G^{\beta|\beta}(0,q)\end{array}\right), \tag{5.21}$$

in which $(G^{\alpha|\beta})_{ij}=\mathbb{D}_i^\alpha\mathbb{D}_j^\beta G$.

Note that when $\mathbb{D}_i^\alpha\mathbb{D}_j^\beta$ contains ∂_x^4 (e.g., for two "$\bar{\mathrm{c}}$t" rods), the corresponding element of $G^{\alpha|\alpha}(x,q)$ includes a term proportional to $\delta(x)$. This term is discarded in $x=0$, as in Ref. [76]. We will show in Sec. 5.4.3, in an example, that this regularization procedure is in agreement with zeta-function regularization.

We thus obtain the Casimir-like interaction between a rod of type α and a rod of type β:

$$\mathcal{F}_{\mathrm{C}}^{\alpha|\beta}(d)=A^{\alpha|\beta}k_{\mathrm{B}}T\frac{L}{d}, \tag{5.22}$$

with $A^{\alpha|\beta}(=A^{\beta|\alpha})$ given by

$$A^{\alpha|\beta}=\int_0^\infty\frac{dx}{2\pi}\ln\left[1-f^{\alpha|\beta}(x)\right]. \tag{5.23}$$

The function $f^{\alpha|\beta}$ depends on the types of rods considered:

$$\begin{aligned}
f^{\mathrm{ct}|\mathrm{ct}}(x) &= (1+x)^2\,e^{-2x}, && (5.24)\\
f^{\mathrm{ct}|\bar{\mathrm{c}}\bar{\mathrm{t}}}(x) &= \left(1+2\,x+2\,x^2\right)e^{-2x}, && (5.25)\\
f^{\mathrm{ct}|\bar{\mathrm{c}}\mathrm{t}}(x) &= (1+2\,x)\,e^{-2x}, && (5.26)\\
f^{\bar{\mathrm{c}}\bar{\mathrm{t}}|\bar{\mathrm{c}}\bar{\mathrm{t}}}(x) &= 2\left(1+2\,x^2\right)e^{-2x}-e^{-4x}, && (5.27)\\
f^{\bar{\mathrm{c}}\bar{\mathrm{t}}|\bar{\mathrm{c}}\mathrm{t}}(x) &= 4\,x\,e^{-2x}+e^{-4x}, && (5.28)\\
f^{\bar{\mathrm{c}}\mathrm{t}|\bar{\mathrm{c}}\mathrm{t}}(x) &= 2\,e^{-2x}-e^{-4x}. && (5.29)
\end{aligned}$$

We find that the results involving "$\bar{\mathrm{c}}\bar{\mathrm{t}}$" rods are strictly identical to those involving "ct" rods: $f^{\bar{\mathrm{c}}\bar{\mathrm{t}}|\beta}\equiv f^{\mathrm{ct}|\beta}$ for all β.

The numerical values of the $A^{\alpha|\beta}$ coefficients are given in Table 5.1. They are all negative, which means that all the rigid rods attract each other. We remark that the interactions increase upon going from "$\bar{\mathrm{c}}$t" to "ct/$\bar{\mathrm{c}}\bar{\mathrm{t}}$" then to "$\bar{\mathrm{c}}\bar{\mathrm{t}}$". Besides, as mentioned previously, "ct" and "$\bar{\mathrm{c}}\bar{\mathrm{t}}$" rods behave equivalently. Note that this equivalence holds only in the "hard" limit. Indeed, if we put a finite rigidity $\kappa_\perp$ on h_{yy}, as in Eq. (5.4), the "ct" rod vanishes altogether in the limit $\kappa_\perp\to 0$ while the "$\bar{\mathrm{c}}\bar{\mathrm{t}}$" rod becomes a different object: a flexible "ribbon" setting only $h_{xx}=0$.

α \ β	$\bar{\text{c}}\text{t}$	$\text{ct}/\bar{\text{c}}\bar{\text{t}}$	$\text{c}\bar{\text{t}}$
$\bar{\text{c}}\text{t}$	-0.262	-0.357	-0.549
$\text{ct}/\bar{\text{c}}\bar{\text{t}}$		-0.462	-0.672
$\text{c}\bar{\text{t}}$			-0.924

Table 5.1: Universal amplitudes $A^{\alpha|\beta}$ of the Casimir-like interactions between the various types of rods, rounded off to the third decimal place. The exact value of $A^{\bar{\text{c}}\text{t}|\bar{\text{c}}\text{t}}$ is $-\pi/12$.

5.4.2 Antagonistic constraints and repulsion

In the case of critical systems, Casimir-like interactions have been found to be attractive for like boundary conditions and repulsive for unlike boundary conditions [63]. For instance, in a critical binary mixture made of components A and B, if one wall features preferential adsorption of A while the other features preferential adsorption of B, these two walls will repel [63, 66]. Our results seem at variance with those regarding critical systems, since we have obtained attraction between all kinds of rigid rods (see Table 5.1). However, the case of rods is quite complex, given that all types of rods share the $h_{yy} = 0$ condition, while they differ on the other ones.

We have calculated the Casimir-like interaction between a flexible "ribbon" setting only $h_{xx} = 0$ and a "ct" rod imposing $h_{yy} = 0$, using exactly the same method as for rods. It gives $A^{\text{rib}|\text{ct}} \simeq 0.012 > 0$. Hence, these completely antagonistic constraints ($h_{yy} = 0$ vs. $h_{xx} = 0$) indeed yield a repulsion.

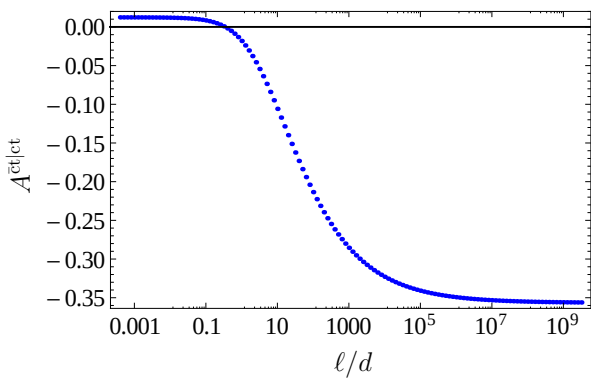

Figure 5.6: Coefficient $A^{\bar{\text{c}}\text{t}|\text{ct}}$ of the Casimir-like interaction between a rigid "ct" rod and a "$\bar{\text{c}}\text{t}$" rod that is rigid in the xx direction but that has a finite rigidity, characterized by $\kappa_\perp$, in the yy direction. This coefficient is plotted versus ℓ/d, where $\ell = \kappa_\perp/\kappa$. We have $\ell/d = 4/\bar{d}$, where $\bar{d}$ is defined in Eq. (5.15). The crossover between repulsion and attraction is obtained for $\ell/d \approx 0.3$.

The transition between repulsion and attraction can be studied by considering a rigid "ct" rod imposing $h_{yy} = 0$, and a "$\bar{\text{c}}\text{t}$" rod that is rigid in the xx direction but that has a finite rigidity, characterized by $\kappa_\perp$, in the yy direction. This interaction has been calculated for finite $\kappa_\perp$, using the same method as in Sec. 5.3.2. For $\kappa_\perp \to 0$, the "$\bar{\text{c}}\text{t}$" rod has no yy rigidity left at all and becomes a "ribbon" setting only $h_{xx} = 0$:

then, the Casimir-like interaction coefficient is $A^{\mathrm{rib}|\mathrm{ct}} \simeq 0.012$. Conversely, for $\kappa_\perp \to \infty$, we get back the interaction between two rigid rods, with the coefficient $A^{\mathrm{ct}|\bar{\mathrm{c}}\mathrm{t}} \simeq -0.357$ (see Table 5.1). The transition between these two asymptotic regimes is plotted in Fig. 5.6.

5.4.3 Zeta-function regularization method

In order to check the regularization procedure mentioned after Eq. (5.21), we have recalculated the interaction between two rigid rods of the "c̄t" type by using zeta-function regularization [155], which is rather straightforward for such rods.

To obtain the Casimir-like energy $\mathcal{F}_C^{\bar{\mathrm{c}}\mathrm{t}|\bar{\mathrm{c}}\mathrm{t}}(d)$, we calculate the partition function of the membrane patch $\mathcal{P} = [0, d] \times [0, L]$ situated between the rods. It will yield the Casimir-like interaction because the free energy of the rest of the membrane is independent of d. This partition function reads

$$Z = \int \mathcal{D}h \, \exp[-\beta \mathcal{H}_\mathcal{P}] \,, \tag{5.30}$$

where $\mathcal{H}_\mathcal{P}$ corresponds to the Hamiltonian Eq. (5.1) on the patch $\mathcal{P}$. The functional integral involved in Z runs over the functions h that comply with the boundary conditions imposed by the rods, i.e., $\mathbb{D}^{\bar{\mathrm{c}}\mathrm{t}} h(x, y) = 0$ for $x \in \{0, d\}$, and $y \in [0, L]$. Let us assume, in addition, that $h(x, y) = 0$ on the rods: it will not change the result since we have seen previously that the relative tilt of the rods is effectively frozen (see Sec. 5.3.2). Finally, let us take periodic boundary conditions with period L in the y direction, as before.

Under these hypotheses, it is possible to write

$$\mathcal{H}_\mathcal{P} = \frac{\kappa}{2} \int_\mathcal{P} d\boldsymbol{r} \, h(\boldsymbol{r}) \, \mathcal{O} \, h(\boldsymbol{r}) \,, \tag{5.31}$$

where $\mathcal{O}$ denotes the biharmonic operator ∇^4 on the domain $\mathcal{P}$ with the above-mentioned boundary conditions. Since $\mathcal{O}$ is positive definite Hermitian, we have

$$Z = \frac{Z_0}{\sqrt{\det(\mathcal{O})}} \,, \tag{5.32}$$

where Z_0 is independent of d. Thus, discarding d-independent terms, we obtain

$$\mathcal{F}_C^{\bar{\mathrm{c}}\mathrm{t}|\bar{\mathrm{c}}\mathrm{t}}(d) = \frac{k_\mathrm{B}T}{2} \ln\det(\mathcal{O}) = \frac{k_\mathrm{B}T}{2} \mathrm{Tr}\ln(\mathcal{O}) = \frac{k_\mathrm{B}T}{2} \sum_{n=1}^{\infty} \int_{-\infty}^{\infty} dm \, \ln(\lambda_{nm}) \,, \tag{5.33}$$

where λ_{nm} denote the eigenvalues of $\mathcal{O}$, which read

$$\lambda_{nm} \, = \, \pi^4 \left(\frac{n^2}{d^2} + \frac{4\, m^2}{L^2} \right)^2 , \;\; n \in \mathbb{N}^*, \;\; m \in \mathbb{Z} \,. \tag{5.34}$$

The associated eigenfunctions are $\sin(n\pi x/d) \times \exp(im2\pi y/L)$.

While Eq. (5.33) is divergent, it can be regularized by using the spectral Zeta function $\zeta_{\mathcal{O}}$ of the operator $\mathcal{O}$ [155]:

$$\zeta_{\mathcal{O}}(s) = \sum_{n=1}^{\infty} \int_{-\infty}^{\infty} dm\, \lambda_{nm}^{-s}\,, \tag{5.35}$$

which is finite for $s > 1/4$. It yields the Casimir-like interaction free energy expressed in Eq. (5.33) by analytical continuation:

$$\mathcal{F}_C^{\bar{\mathrm{ct}}|\bar{\mathrm{ct}}}(d) = -\frac{1}{2} k_{\mathrm{B}} T \lim_{s\to 0} \zeta'_{\mathcal{O}}(s) = -k_{\mathrm{B}} T \frac{\pi}{12} \frac{L}{d}\,. \tag{5.36}$$

This result is in agreement with the value $A^{\bar{\mathrm{ct}}|\bar{\mathrm{ct}}} = -\pi/12$ obtained above with the regularization of Li and Kardar. This agreement also implies that a half-plane imposing the same boundary conditions as a rod will yield the same Casimir-like interaction (in the regime $L \gg d$). Physically, this equivalence is due to the fact that the Casimir-like interaction arises from the confinement of the fluctuation modes between the rods (or the half-planes), i.e., in the patch $\mathcal{P}$.

Note that this method is an efficient one to calculate the Casimir-like interaction in other cases. For instance, let us consider two rods imposing Dirichlet boundary conditions on a standard scalar field (described by the Hamiltonian in Eq. (5.31), with $\mathcal{O} = \nabla^2$), in two dimensions. Then, the same scaling is obtained for the Casimir-like interaction, but with a prefactor $A = -\pi/24$.

5.5 Discussion

5.5.1 Undulation instability

a. Instability threshold

Golestanian [86] showed that the finite bending rigidity of semiflexible polymers, or polymer rods, embedded in membranes, has dramatic effects on their Casimir-like interaction at short separations: shape fluctuations, which locally reduce the separation of the polymer rods, become unstable. Precisely, the free energy eigenvalues of these modes were shown to be $\lambda(q) \simeq (\kappa_r/k_{\mathrm{B}}T)q^4 - (2A/\pi)/d^3$, where κ_r is the bending rigidity of the polymer rods and $A \simeq 2.91$. Instabilities occur if $\lambda(q_{\min}) < 0$ with $q_{\min} \simeq \pi/L$, i.e., for $d < d_c$, where

$$\frac{d_c}{L} \simeq \left(\frac{2A}{\pi^5}\right)^{1/3} \left(\frac{L}{\ell_p}\right)^{1/3}. \tag{5.37}$$

Here, $\ell_p = \kappa_r/(k_{\mathrm{B}}T)$ is the persistence length of the rod.

Let us check that the undulation instability discussed in Ref. [86] can be recovered from the Casimir-like interaction calculated in this Chapter. For this, let us consider the fundamental deformation mode, which has the lowest energetic cost. It reads:

$$u(y) = U \sin(\pi y/L')\,, \quad y \in [0, L']\,, \tag{5.38}$$

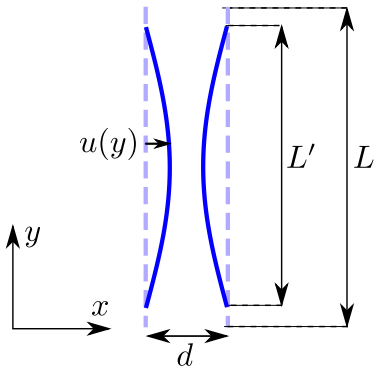

Figure 5.7: Two parallel rods of length L separated by a distance d deforming towards each other. The deformation $u(y)$, corresponding to the fundamental mode, is given by Eq. (5.38).

where u denotes the in-plane displacement of each rod in the direction of the other rod, while L' is the projection on the y-axis of the deformed rods (see Fig. 5.7). We focus on the case where $U \leq d/2$, so that the two rods do not overlap. Assuming that the rods are incompressible, we have $L' = L - \pi^2 U^2/(4L) + L\,\mathcal{O}(U^3/L^3)$.

In the limit $d \ll L$, we can use the proximity-force approximation (PFA), also called Derjaguin approximation [94], to calculate the Casimir-like interaction free energy between the two deformed rods. This approximation, valid when the distance between two objects is much smaller than their radius of curvature, amounts to integrating the known interaction per unit length between parallel rods separated by a varying distance (see Fig. 5.8).

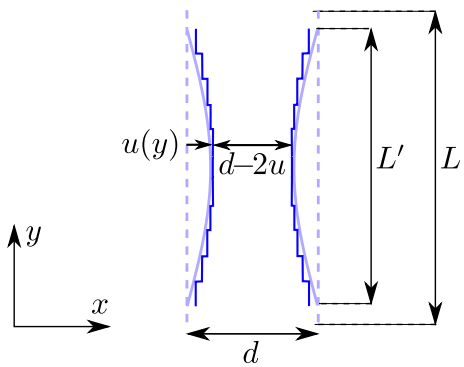

Figure 5.8: Qualitative view of the PFA: the deformed rods are replaced by (infinitesimal) parallel rods separated by a distance $d - 2u$.

The interaction free energy $\mathcal{F}_{\mathrm{PFA}}^{\alpha|\beta}$ between two deformed rods of types α and β in the PFA is

$$\frac{\mathcal{F}_{\mathrm{PFA}}^{\alpha|\beta}}{k_{\mathrm{B}}T} = \int_0^{L'} dy\, \frac{A^{\alpha|\beta}}{d - 2u}\,, \tag{5.39}$$

where u corresponds to Eq. (5.38) as we focus on the fundamental deformation mode. Let us call $\mathcal{F}_{\mathrm{def}}$ the total variation of the free energy of the system due to

the deformation. This variation of free energy arises both from the modification of the Casimir-like interaction and from the direct cost of bending the rods. It reads:

$$\begin{aligned}\frac{\mathcal{F}_{\text{def}}^{\alpha|\beta}}{k_{\text{B}}T} &= \frac{\mathcal{F}_{\text{PFA}}^{\alpha|\beta} + \mathcal{F}_{\text{bending}} - \mathcal{F}_{C}^{\alpha|\beta}}{k_{\text{B}}T} \\ &= \int_0^{L'} dy \left[\frac{A^{\alpha|\beta}}{d-2u} + \ell_p \left(\frac{d^2u}{dy^2}\right)^2\right] + \mathcal{O}\left(\frac{U^3}{L^3}\right) - \frac{A^{\alpha|\beta}L}{d} \\ &= \frac{A^{\alpha|\beta}L}{d}\frac{4U}{\pi d}\left(1+\frac{\pi U}{2d}\right) + \frac{\pi^4\ell_p}{2L}\frac{U^2}{L^2} + \mathcal{O}\left(\frac{U^3}{L^3}\right). \end{aligned} \tag{5.40}$$

Minimizing $\mathcal{F}_{\text{def}}$ with respect to U, we obtain the equilibrium deformation amplitude U_{eq}. Let us take as our instability criterion the fact that the two rods touch each other, i.e., $U_{\text{eq}} = d/2$. It occurs when $d = d_c'$, with

$$\frac{d_c'}{L} = \left(\frac{-4(2+\pi)A^{\alpha|\beta}}{\pi^5}\right)^{1/3}\left(\frac{L}{\ell_p}\right)^{1/3}. \tag{5.41}$$

This is very similar to the instability threshold of Eq. (5.37), obtained in Ref. [86]. For instance, considering two "ct" or "$\bar{\text{c}}\bar{\text{t}}$" rods, for which $A^{\alpha|\beta} \simeq -0.46$, we obtain 0.31 as the prefactor of $(L/\ell_p)^{1/3}$ in Eq. (5.41), while in Eq. (5.37), this prefactor is 0.27.

b. Implications

In light of this undulation instability threshold, we can be more specific about the domain of validity of our study, in which we have focused on rods with infinite in-plane bending rigidity. For actin filaments [145, 146] of length $L \simeq 100\,\text{nm}$, with $\ell_p \simeq 17\,\mu\text{m}$, and thus $L/\ell_p \simeq 6\times10^{-3}$, the instability threshold corresponds to $d_c/L \approx 5\times10^{-2}$. For $L/\ell_p \simeq 10^{-4}$, which may be realistic for actin bundles [146], it goes down to $d_c/L \approx 10^{-2}$. It is thus realistic to consider rods with infinite in-plane bending rigidity at separations in the range $0.01 \lesssim d/L \lesssim 1$.

We can also be more specific about the domain of application of the "hard" and "soft" limits studied analytically in Sec. 5.3.2 for $d \ll L$. Let us first focus on ordinary rods, which have identical in-plane and out-of-plane bending rigidities $\kappa_r = \kappa_\parallel = \kappa_\perp$ (and persistence lengths $\ell_p = \ell_\parallel = \ell_\perp$). Using the definition of $\bar{d}$ in Eq. (5.15), the condition $d \ll L$ can be rewritten $\bar{d} \ll 4\beta\kappa L/\ell_\perp$. Besides, we have seen that it is necessary to consider polymers such that $L/\ell_p \lesssim 10^{-2}$ in order to avoid the in-plane undulation instability for small d/L: given that $k_{\text{B}}T/(4\kappa) \approx 10^{-2}$, it yields $4\beta\kappa L/\ell_\perp \lesssim 1$. Combining these inequalities gives $\bar{d} \ll 4\beta\kappa L/\ell_\perp \lesssim 1$. Hence, the "hard" limit $\bar{d} \ll 1$ is the physical one for ordinary rods at separations $d \ll L$, and the relevant interaction is given by Eq. (5.16). This asymptotic regime is attained slowly, however, so that one might rather expect to see an intermediate effective power law (see Fig. 5.4). In principle, the "soft" limit $\bar{d} \gg 1$ could be relevant for strongly anisotropic rods with a large $\kappa_\parallel$ and a small $\kappa_\perp$, such that $\ell_\perp k_{\text{B}}T/(4\kappa) \ll d \ll L$.

5.5.2 Effect of tension

In this Chapter, we have assumed that the effect of the membrane tension σ is negligible with respect to that of its bending rigidity κ. This hypothesis is valid in usual flaccid membranes ($\sigma \approx 10^{-7}\,\mathrm{N/m}$) for rods shorter than $\sqrt{\kappa/\sigma} \approx 1\,\mu\mathrm{m}$. However, σ can be increased up to about $10^{-3}\,\mathrm{N/m}$ by applying an external tension to the membrane: in this case, the effect of tension will become important.

The methods presented here in the bending-rigidity–dominated regime can also be applied to the tension-dominated limit, where L and d are much larger than $\sqrt{\kappa/\sigma}$. For instance, the interaction between two "ct" rods imposing $h_{yy} = 0$ is then still given by Eq. (5.22), but with $A^{\mathrm{ct}|\mathrm{ct}} = -\pi/24$. We have obtained this result both through the method based on Ref. [76] and through zeta-function regularization. This tension-dominated interaction is relevant in liquid-vapor interfaces [156].

A general calculation of the Casimir-like interaction between two rods, including both κ and σ, is beyond the scope of this work, but it would be interesting. This problem has been addressed very recently in the simpler case of two small circular inclusions [92].

5.6 Conclusion

We have studied the Casimir-like interaction between two parallel rods adsorbed on a fluid membrane characterized by its bending energy and subject to thermal fluctuations. We have considered four types of constraints imposed by the rods, depending on whether the membrane can twist along the rod and/or curve across it. Whatever their type, rigid rods of length L at short separations $d \ll L$ experience an attractive Casimir-like interaction scaling as $k_{\mathrm{B}}TL/d$. In this regime, two of the four types of rods are equivalent, which yields six universal Casimir-like amplitudes. These amplitudes are of order unity, which means that the Casimir-like interaction free energy can be larger than $k_{\mathrm{B}}T$ in the regime $d \ll L$.

When taking into account the finite persistence length ℓ_p of the rod, we have found, in agreement with Ref. [86], that at separations smaller than $d_c \propto L(L/\ell_p)^{1/3}$, two rods will bend toward each other and finally come into contact because of the Casimir-like interaction. Besides, we have shown that rods with a very soft out-of-plane bending rigidity, but a large in-plane bending rigidity, still experience a power-law Casimir-like interaction (albeit small), which scales as d^{-3}. For a large, but not infinite out-of-plane bending rigidity, an effective power law in $d^{-\alpha}$ with α close to 1 would be observed. This nuances the conclusion of Ref. [86], according to which a finite out-of-plane rigidity, no matter how large, should destroy the long-range Casimir-like interaction. The study of rods with a finite out-of-plane rigidity has also enabled us to show that repulsion can exist between two objects imposing completely antagonistic constraints to the membrane.

We have also briefly presented numerical results regarding the Casimir-like interaction between two rods at any separations. They feature a crossover between the short separation d^{-1} behavior and the large separation d^{-4} behavior, occurring

at $d/L \approx 0.5$. Moreover, they show that the Casimir-like attraction reaches $k_{\mathrm{B}}T$ when $d/L \approx 0.2$.

In a nutshell, due to the Casimir-like interaction, long rods adsorbed on an effectively tensionless membrane will actually attract each other when their separation becomes significantly smaller than their length.

Part II

Inclusions and membrane thickness deformations

Chapter 6

Context: Membrane thickness deformations close to proteins

Contents

6.1 Introduction **127**

6.2 Experimental studies on gramicidin **129**

6.3 Models for local membrane thickness deformations . . . **132**

6.3.1 First models 132

6.3.2 Huang's model 133

6.3.3 Models based on the work of Dan, Pincus and Safran . . 134

6.4 Insight from numerical simulations **135**

6.5 Brief outline of our contribution **137**

6.1 Introduction

In Part I, we dealt with long-range membrane-mediated interactions between inclusions, which arise from the curvature constraints imposed by rigid inclusions to the membrane. There exist many other ways in which inclusions interact with the surrounding membrane and with other inclusions. Some are specific chemical interactions that need to be described at the microscopic level, but others are nonspecific, even if they do not feature the universal power-law behavior of Casimir-like interactions.

The study of these interactions was initiated before that of Casimir-like interactions in membranes (recall that the first study on the latter subject, Ref. [70], was published in 1993). In 1973, magnetic resonance studies conducted by Jost and coworkers showed that intrinsic membrane proteins, i.e., proteins that span the whole bilayer thickness, alter the properties of the neighboring lipids [157]. They obtained evidence for the existence of a boundary of immobilized lipids close to these hydrophobic proteins [157]. In 1976, Marčelja used a statistical mechanical

model describing the conformations of the lipid hydrophobic chains to study the local ordering of membrane lipids close to integral proteins [158]. This local ordering effect leads to a membrane-mediated attraction between proteins [158]. The following year, Schröder proposed an analytical treatment of such an interaction, using a generic order-parameter–based theoretical description. He obtained an interaction potential that decays exponentially for long distances, the decay length scale being the correlation length of the membrane order parameter [159]. In 1978, Owicki, Springgate and McConnell investigated theoretically the case where membrane proteins locally perturb the thickness of the membrane and the case where they couple preferentially to one component of a lipid mixture [160]. There are thus several ways through which membrane proteins can influence locally the structure of the membrane. In 1999, Fournier introduced a model that accounts for membrane shape, thickness and tilt, and he studied the interactions between proteins coupling to these various fields [22]. Very recently, Watson and coworkers proposed a membrane model that includes all these effects and also microscopic protrusions [23].

We are going to focus on the coupling of proteins to membrane thickness. Intrinsic membrane proteins can have a *hydrophobic mismatch* with the membrane: their hydrophobic thickness is slightly different from that of the unperturbed membrane. Hydrophobic mismatch is ubiquitous [161]. This can be realized by noting that the same membrane proteins can exist in different membranes, which have different thicknesses. For instance, in eukaryotic cells, the cell membrane is thicker than that of the endoplasmic reticulum, due to their different lipid composition. And yet, the proteins that are active in the cell membrane are first integrated in the endoplasmic reticulum membrane after being synthesized. Similarly, protein structures indicate that different proteins present in the same membrane are likely to have different hydrophobic thicknesses [161]. Hydrophobic mismatch has important biological consequences: the activity of many membrane proteins, e.g., ATP-ases and rhodopsin, has been shown to depend on membrane thickness [161]. Some specific mismatched proteins have been proved to serve as temperature sensors, since membrane thickness depends on temperature [162–164].

The membrane-protein system has to adapt to hydrophobic mismatch. As proteins are more rigid than membranes, it is generally the membrane that deforms due to hydrophobic mismatch. To avoid exposing part of its hydrophobic chains to water, the membrane can locally deform in the vicinity of the protein, and match its thickness. We will be interested in this local deformation of the membrane thickness. It yields an effective, membrane-mediated interaction between two such proteins, which can be relevant in the process of protein aggregation. Note that other adaptations to mismatch are possible: thin proteins with thicker hydrophobic part than the membrane can tilt, and the backbone conformation of the protein may sometimes change [161, 165].

Studying local membrane thickness deformations due to proteins and the resulting effective interaction between proteins is a key step to understand how the membrane responds to membrane proteins and influences their behavior. Many studies, of experimental, theoretical and numerical nature have focused on this subject. However, describing membrane thickness deformations is tricky since they

occur on the nanometer scale, which corresponds to the limit of validity of simple continuum theories where only long-scale terms are kept. In this introductory Chapter, we will first explain briefly the principle of experimental studies conducted on a particular integral membrane protein called gramicidin, which acts as a probe for membrane elasticity at the nanoscale. We will then present the main theoretical descriptions currently used to investigate local membrane thickness deformations. Finally, we will show how numerical simulations give a new insight into this subject.

6.2 Experimental studies on gramicidin

Gramicidin is a membrane protein with antibiotic activity. It is naturally produced by the soil bacterium *Bacillus brevis*, and it was one of the very first antibiotics to be used clinically, from 1939, shortly after being identified by Dubos in a bacterial culture. The promising applications of gramicidin stimulated research on other antibiotics such as penicillin[1] [167].

In lipid membranes, two gramicidin monomers, one on each side of the bilayer, associate via the N-terminus to form a dimer, which is stabilized by six intermolecular hydrogen bonds. This dimer is an integral protein which acts as an ion channel. While the monomers do not deform the membrane, the dimeric channel presents a hydrophobic mismatch with the membrane, so that dimer formation involves a local deformation of the bilayer [167], as shown in Fig. 6.1. The idea of this mismatch of gramicidin was originally inferred from experimental results showing the influence of membrane thickness and tension on gramicidin behavior [167].

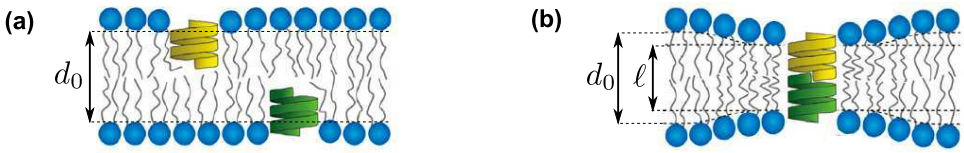

Figure 6.1: (a): Sketch representing two gramicidin monomers in a lipid bilayer. The unperturbed thickness of the membrane is denoted by d_0. (b): A gramicidin dimer in a lipid bilayer. The hydrophobic mismatch of the channel induces a deformation of the bilayer, which locally matches the hydrophobic thickness $\ell < d_0$ of the channel. *Original illustration from Ref. [168], adapted and modified.*

The gramicidin channel being large enough for the passage of monovalent cations, conductivity measurements [169] can detect its formation and lifetime, which are directly influenced by membrane properties. It thus constitutes a very convenient experimental system to probe local membrane thickness deformations and membrane elasticity on the nanoscale. An example of conductivity measurement in a vesicle

[1]Fleming discovered penicillin in 1928, but its purification was tricky. Florey and Chain realized the first successful purification of penicillin in 1942, and Florey credited Dubos' work on gramicidin for stimulating studies on penicillin [166]. Penicillin proved to be a much more efficient and convenient antibiotic than gramicidin. Nowadays, the therapeutic use of gramicidin is limited to local application on the skin, because it is quite toxic for eukaryotic cells too.

containing gramicidin channels is shown in Fig. 6.2. Such experiments enable to measure the formation rate and/or the lifetime of gramicidin channels.

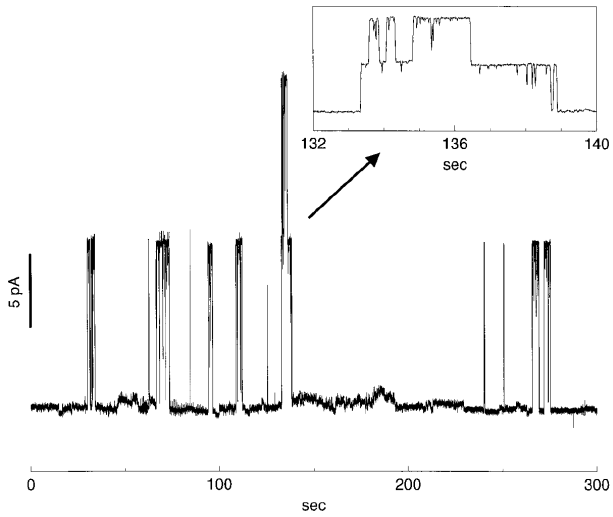

Figure 6.2: Time evolution of the current across a membrane "gigaseal", i.e., high-resistance seal, formed when the membrane of a vesicle fully adheres to a micropipette. The current is measured between one electrode in the micropipette and another one in the buffer which contains the vesicle. Each sudden rise of the current corresponds to the formation of a gramicidin channel in the membrane of the "gigaseal", and the subsequent sudden drop to the dissociation of this channel. In the inset, there is a phase where two channels are open simultaneously [170]. *Illustration reproduced from Ref. [170].*

Let us now explain how the formation rate and/or the lifetime of gramicidin channels can yield information on the membrane deformation caused by the channels. For this, let us describe the chemical equilibrium between the gramicidin monomers (M) and dimers (D) (see, e.g., Refs. [170–172]). It reads

$$2\,\mathrm{M} \underset{k_-}{\overset{k_+}{\rightleftharpoons}} \mathrm{D}\,, \tag{6.1}$$

where k_+ is the formation rate constant while k_- is the dissociation rate constant. The reactions involved being elementary, their kinetics are described by Van't Hoff's laws, yielding:

$$\frac{d[\mathrm{M}]}{dt} = k_+[\mathrm{M}]^2 - k_-[\mathrm{D}]\,, \tag{6.2}$$

where square brackets are used to denote concentration.

The rate constants can be related to the activation energies (i.e., the energy barriers) involved through Arrhenius' law:

$$k_+ = \nu_+ \exp\left[-\frac{\Delta G^\circ + \Delta G^\#}{k_\mathrm{B}T}\right], \tag{6.3}$$

$$k_- = \nu_- \exp\left[-\frac{\Delta G^\#}{k_\mathrm{B}T}\right], \tag{6.4}$$

where $\nu_\pm$ are constants, while ΔG° denotes the free energy difference between the dimer and the two monomers and $\Delta G^\#$ that between the transition state and the dimer, as illustrated in Fig. 6.3. In the transition state, i.e., at the peak of the energy barrier, the two monomers are separated by a distance δ, which corresponds roughly to the range of the hydrogen bonds that stabilize the dimer (see Fig. 6.3). Both ΔG° and $\Delta G^\#$ contain a specific chemical contribution, indicated by a subscript c in the following, and a contribution arising from membrane deformation. Denoting by $F(x)$ the free energy cost of the membrane deformation due to a gramicidin channel of hydrophobic thickness x, we have [170]:

$$\Delta G^\circ = \Delta G_c^\circ + F(\ell)\,, \tag{6.5}$$

$$\Delta G^\# = \Delta G_c^\# + F(\ell+\delta) - F(\ell)\,. \tag{6.6}$$

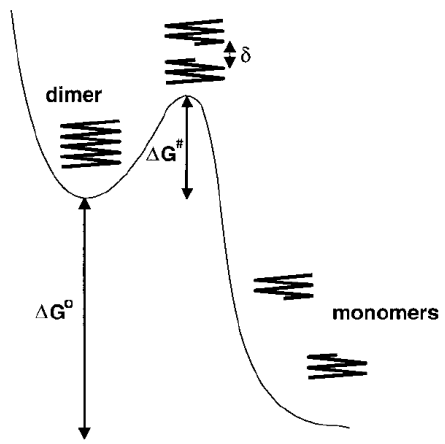

Figure 6.3: Free energy landscape regarding the formation (and dissociation) of the gramicidin channel. ΔG° denotes the free energy difference between the dimer and the two monomers, while $\Delta G^\#$ corresponds to the free energy difference between the transition state and the dimer. In the transition state, the two monomers are separated by a distance δ [170]. *Illustration reproduced from Ref. [170].*

As a consequence, both the formation rate and the lifetime of gramicidin channels depend on the membrane deformation. The formation rate f can be deduced from the differential equation Eq. (6.2):

$$f = k_+[\mathrm{M}]^2 = \nu_+[\mathrm{M}]^2 \exp\left[-\frac{\Delta G^\circ + \Delta G^\#}{k_\mathrm{B}T}\right], \tag{6.7}$$

where we have used Eq. (6.3). Thus, if [M] can be considered constant, which is the case if [M] $\gg$ [D], we obtain, using Eqs. (6.5) and (6.6):

$$\ln f = C - \frac{F(\ell+\delta)}{k_\mathrm{B}T}\,, \tag{6.8}$$

where C does not involve membrane elasticity [170]. Similarly, using Eqs. (6.2) and (6.4), the lifetime τ of gramicidin channels can be expressed as

$$\tau = \frac{1}{k_-} = \frac{1}{\nu_-}\exp\left[\frac{\Delta G^\#}{k_\mathrm{B}T}\right], \tag{6.9}$$

which yields, using Eq. (6.6),

$$\ln \tau = C' + \frac{F(\ell + \delta) - F(\ell)}{k_{\mathrm{B}}T}\,, \tag{6.10}$$

where C' does not involve membrane elasticity [172].

Hence, measurements of f and τ provide information on the deformation free energy F of a membrane due to the presence of a gramicidin dimer. Several such measurements have been conducted. In 1977, Kolb and Bamberg [173] studied the gramicidin channel lifetime variations arising from discrete changes of the hydrophobic mismatch. Various mismatches were obtained by using gramicidin varieties with different lengths in the same membrane. In 1983, Elliott and coworkers conducted a similar study, but they varied the mismatch through the membrane thickness, by studying a single variety of gramicidin channels in membranes of various compositions [171]. In 1998, Goulian and coworkers [170] measured the gramicidin channel formation rate as a function of applied tension.

Motivated by these experimental studies, sustained theoretical investigation has been conducted in order to construct a model describing local membrane thickness deformations [172, 174–176].

6.3 Models for local membrane thickness deformations

6.3.1 First models

The idea that the membrane hydrophobic thickness must locally match that of an intrinsic protein was first used in theoretical descriptions of lipid-protein interactions that focused on the thermodynamic phase behavior of the lipid-protein system and on protein aggregation. In 1978, Owicki, Springgate and McConnell implemented such a condition within a Landau-de Gennes model: they wrote the Hamiltonian density of the membrane as an expansion in an order parameter and its squared gradient [160, 177]. In 1984, Mouritsen and Bloom proposed a thermodynamic model, called the "mattress model", to describe the phase diagrams of lipid bilayers containing proteins. One key ingredient in their model was hydrophobic mismatch [178]. Such models are interesting to understand the phase behavior of membranes containing proteins, but they do not provide a precise description of the local membrane deformation or of the resulting free energy variation.

The first attempt to explain the dependence of gramicidin channel lifetime on the membrane thickness was provided by Elliott and coworkers in 1983 [171]. It is based on the idea that the membrane energy variation $F(\ell+\delta) - F(\ell)$ between the dimer state and the transition state is mostly due to membrane tension, which pulls the monomers apart until they are separated by δ (see Fig. 6.3). The estimate of δ obtained in Ref. [171] using this idea is $\delta \simeq 1.8$ nm. This is far larger than the separation required for the breaking of the hydrogen bonds that stabilize the dimer, which is of order 1 Å. Hence, this first model was not satisfactory.

6.3.2 Huang's model

In 1986, Huang proposed the first full continuum model describing membrane deformations [172]. He wrote the Hamiltonian density of the membrane as an expansion in powers of spatial derivatives of the thickness deformation. This corresponds to the generic method to construct a coarse-grained field theory (see, e.g., Ref. [119]). It is important to recall that neglecting higher-order derivatives is justified at length scales much larger than the range of microscopic interactions. Thickness deformations induced by mismatched protein typically decay over a few nanometers, which means that this hypothesis might not be fully valid.

Huang restricted his expansion to terms involving the membrane thickness deformation and its first and second derivatives. The terms included in the Hamiltonian density have to comply with the symmetry of the system [29, 119]. As a lipid bilayer has the same symmetry properties as a smectic liquid crystal, in which the elongated molecules organize in layers with the molecules oriented along the layers' normal (see Fig. 6.4), Huang based his model on the theory of smectic liquid crystals. The latter had been thoroughly studied before, starting in the late 1960s with de Gennes' work [179].

Figure 6.4: Sketch of the structure of a smectic (more precisely, smectic A) liquid crystal. *Illustration reproduced from Wikimedia Commons.*

The most important terms in the theory of smectic liquid crystals correspond to compression of the layers and splay distortion, i.e., curvature in the direction that is orthogonal to the planes. In addition to these terms, Huang included the contribution of the "surface tension" of the membrane. Restricting to symmetric deformations of the two monolayers, the effective Hamiltonian F of the membrane can then be expressed as [172]

$$F = \int dxdy \left[\frac{K_a}{2\,d_0^2}\, u^2 + \frac{\gamma}{4}\,(\boldsymbol{\nabla} u)^2 + \frac{\kappa}{8}\,\left(\nabla^2 u\right)^2 \right] , \tag{6.11}$$

In this expression, u denotes the thickness excess of the membrane relative to its equilibrium thickness d_0 (see Fig. 6.5), K_a corresponds to the stretching modulus of the membrane, d_0 to its equilibrium thickness, γ to its "surface tension", and κ is an elastic constant associated to splay. As usual, x and y denote the in-plane coordinates of the membrane, and the gradient and Laplacian featured in Eq. (6.11) are two-dimensional in-plane operators.

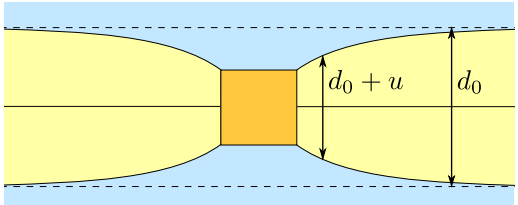

Figure 6.5: Cut of a bilayer membrane (yellow) containing a protein with a hydrophobic mismatch, represented as a square (orange). The equilibrium thickness of the bilayer is d_0, while the actual thickness is denoted by $d_0 + u$.

Huang assimilated γ to the tension of a Plateau border and κ to the Helfrich bending modulus [172]. Neither of these assumptions is actually obvious, as we will see in the following Chapter. Under these assumptions, he was able to neglect the contribution of his "tension" term. By minimizing the membrane effective Hamiltonian, he found analytical expressions for the membrane deformation profiles close to a gramicidin channel, obtaining a decay length of a few nanometers. He also reanalyzed the data obtained by Elliott and coworkers in Ref. [171], showing it to be consistent with $\delta \lesssim 1$ Å within his model [172]. This corresponds to the range of hydrogen bonds, and it is thus much more satisfactory than the higher value obtained previously by Elliott and coworkers using their tension-based model.

6.3.3 Models based on the work of Dan, Pincus and Safran

In 1993, Dan, Pincus and Safran investigated the membrane-mediated interaction between mismatched proteins [175]. For this, they used a construction of the membrane Hamiltonian density that is different from Huang's. They started by writing the effective Hamiltonian per lipid molecule in each monolayer as a second-order expansion in the variation of area per lipid and in the local "curvature" (i.e., Laplacian) of the monolayer thickness. Note that this "curvature" is different from the curvature of the average shape of the membrane involved in the Helfrich model, where the membrane is considered as a mathematical surface with no thickness. In Ref. [175], the simplified one-dimensional case was treated. Subsequently, in 1996, the same authors, together with Aranda-Espinoza and Berman, generalized the model to the two-dimensional case. We will present it directly in two dimensions. In the framework of Refs. [175, 176], the effective Hamiltonian per lipid molecule in a monolayer reads

$$f = f_0 + \frac{1}{2} f_0''(\Sigma - \Sigma_0)^2 + f_1 \nabla^2 t + f_1'(\Sigma - \Sigma_0)\nabla^2 t + f_2 \left(\nabla^2 t\right)^2 , \tag{6.12}$$

where t represents the thickness of the monolayer, Σ the area per lipid and Σ_0 the equilibrium area per lipid, while f_0, f_0'', f_1, f_1' and f_2 are constants. In the reference state, around which the expansion is performed, the membrane is flat and each lipid has an area Σ_0.

In Refs. [175, 176], incompressibility of the lipids was used to relate t and Σ. In addition, the focus was restricted to up-down symmetric deformations of the

membrane, as in Ref. [172]. Using the same notations as in Sec. 6.3.2, the membrane effective Hamiltonian they finally obtained can be written as:

$$F = \int dxdy \left[\frac{K_a}{2\,d_0^2} u^2 + \frac{\kappa\, c_0}{2} \nabla^2 u + \frac{\kappa}{2\,d_0} \left(c_0 - c_0' \Sigma_0 \right) u\, \nabla^2 u + \frac{\kappa}{8} \left(\nabla^2 u \right)^2 \right] . \quad (6.13)$$

The various constants that appear here can be expressed in terms of those involved in Eq. (6.12). Among them, K_a, d_0 and κ are interpreted in the same way as in Eq. (6.11). The constant c_0 corresponds to the spontaneous curvature of a monolayer, and c_0' denotes its derivative with respect to the area per molecule Σ. Here, we do not explain in detail how Eq. (6.13) can be derived from Eq. (6.12), but we will generalize this model in the next Chapter, and we will then present the full derivation.

The main difference between this model and Huang's model is that the effect of monolayer spontaneous curvature is included in Eq. (6.13). It was shown in Refs. [175, 176] that this can yield oscillations in the membrane deformation profile, and in the effective interaction potential between two mismatched proteins. Thus, the effective interaction is no longer monotonically attractive, which is a crucial difference with the predictions of Huang's model. Besides, note that no tension term is included in Eq. (6.13). This seems different from Huang's model, Eq. (6.11), but actually Huang neglected his "tension" term in all his calculations, as mentioned above.

The model of Refs. [175, 176] was generalized by Brannigan and Brown in 2006-2007 [180, 181]. First, in Refs. [180, 181] the deformations of the average shape of the membrane (i.e., those that are usually described by the Helfrich model) are accounted for, as well as the symmetric thickness deformations. Second, the effect of Gaussian curvature is taken into account in Ref. [181]. In the next Chapter, we will present a further generalization of the model elaborated in Refs. [175, 176, 180, 181].

6.4 Insight from numerical simulations

As numerical simulations become more and more realistic, they start providing insight into the behavior of microscopic systems, where direct experimental observation is difficult. Lipid membranes, with or without inclusions, are no exception. In the 2000s, several groups simulated bilayer systems over length- and time-scales long enough to give access to the material constants relevant for nanoscale deformations, using molecular dynamics. Both atomistic and coarse-grained simulations have been performed. In atomistic simulations, the individual interactions between atoms[2] are accounted for, via Lennard-Jones potentials and electrostatic interactions, the atomic charges being taken from previous ab initio quantum mechanical calculations [182]. In coarse-grained simulations, some atoms are regrouped into "beads". For instance, five beads can model a lipid [180]. These beads interact together through simplified effective potentials: chemical bonds can be modeled as

[2]Note that, in Ref. [182], united atoms were used for the CH_2 and CH_3 groups in the hydrophobic chains of the lipids. Apart from those, every single atom was accounted for separately.

springs, and the interaction between hydrophobic beads is modeled as a Lennard-Jones potential having an attractive part, while the other interactions are purely repulsive [183]. Such simulations provide interesting and stringent tests for continuum theoretical models, especially for those describing membrane elasticity at the nanoscale.

In these numerical simulations, thermal fluctuations of the membrane shape are visible, both at the scale of individual lipid molecules (protrusions), and at the nanoscopic scale, as collective deformations, as shown in Fig. 6.6. The fluctuation spectra of the average height and thickness of the simulated membranes can thus be measured precisely [180, 182–184]. By fitting these numerical spectra to theoretical formulas, it is possible to extract the numerical values of the membrane constants involved in continuum theories [180, 182–184].

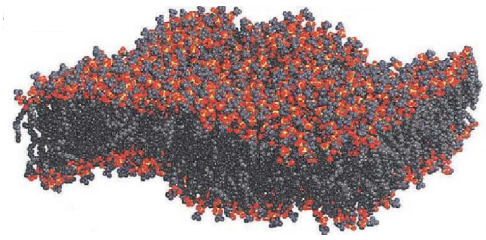

Figure 6.6: Snapshot from an atomistic molecular dynamics simulation of a phospholipid bilayer membrane in water. This system contains 1024 DPPC lipids, its linear size is 20 nm. The snapshot was taken after letting the system equilibrate for 10 ns, at a temperature scaled to 323 K [182]. Shape fluctuations on the nanoscopic scale have developed, and both undulations of the average shape and thickness deformations are visible. *Illustration reproduced from Ref. [182].*

Membranes containing mismatched inclusions have also been simulated. In Refs. [180, 181, 183], the thickness profile of a membrane containing one cylindrical inclusion with a hydrophobic mismatch has been obtained from coarse-grained numerical simulations (see Fig. 6.7). Comparing the average numerical thickness profiles to the equilibrium profiles predicted from theory is a very good test for continuum models regarding membrane thickness deformations. Atomistic simulations are currently being performed to investigate these situations [185], but no complete results are available yet.

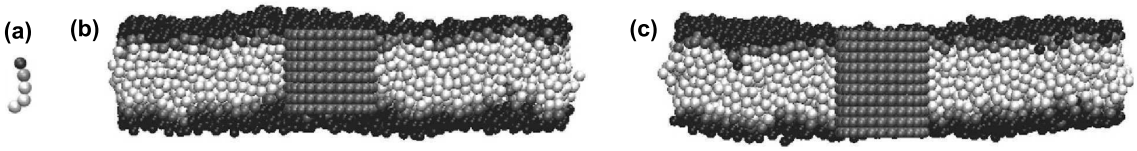

Figure 6.7: Coarse-grained molecular dynamics simulation of a lipid bilayer membrane containing a mismatched inclusion. (a) A coarse-grained lipid molecule composed of five beads. The black bead is the headgroup, the dark gray one constitutes the hydrophilic-hydrophobic interface and the light gray ones correspond to the hydrophobic chains. (b) Membrane containing a cylindrical inclusion (dark gray) with hydrophobic thickness smaller than that of the membrane. (c) Membrane containing an inclusion with hydrophobic thickness larger than that of the membrane. This system contains about 3000 coarse-grained lipids plus the inclusion, its linear size is about 30 nm [180, 181]. *Illustrations reproduced from Ref. [181].*

6.5 Brief outline of our contribution

In the next Chapter, we will put forward a modification of the models described in Sec. 6.3. We will reanalyze the recent numerical data mentioned just above, and the experimental data on gramicidin reviewed in Sec. 6.2, in order to test the predictions of this modified model regarding local membrane thickness deformations.

Chapter 7

Bilayer elasticity at the nanoscale: the need for new terms

Contents

7.1 Introduction **140**

7.2 Membrane model **140**

7.2.1 Starting point 140

7.2.2 Derivation of the effective Hamiltonian of the bilayer . . . 142

7.2.3 The case of symmetric thickness deformations 144

7.3 Comparison with existing models **146**

7.3.1 On the tension 146

7.3.2 On the constant K_a' 147

7.3.3 On the value of K_a'' 148

7.3.4 On the boundary terms 149

7.4 Comparison with numerical results **150**

7.4.1 Fluctuation spectra 150

7.4.2 Deformation profiles close to a mismatched protein 150

7.5 Comparison with experimental results **155**

7.5.1 Analysis of the experimental data of Elliott *et al.* 155

7.5.2 Analysis of the experimental data of Goulian *et al.* 158

7.6 Conclusion **165**

7.7 Appendix A: On our effective Hamiltonian **166**

7.7.1 Link with the Helfrich Hamiltonian 166

7.7.2 Stability criterion 166

7.7.3 Membrane submitted to an external tension 166

7.7.4 Estimating c_0' 168

7.8 Appendix B: Numerical fluctuation spectra **168**

7.9 Appendix C: Membrane containing a cylindrical mismatched protein 171

7.9.1 Equilibrium thickness profile 171

7.9.2 Deformation energy 173

7.1 Introduction

At length scales much larger than their thickness, the elasticity of lipid bilayers is well described by the Helfrich model [24] (see Sec. 1.3.2). However, nanometer-sized inclusions, such as membrane proteins, deform the membrane over smaller length scales. In particular, some integral membrane proteins locally affect the thickness of the membrane due to hydrophobic mismatch, as seen in the previous Chapter. Since these deformations regard membrane thickness, and since their characteristic amplitude and decay length are both of a few nanometers [172], they cannot be described using the Helfrich model. In fact, since the range of such deformations is of the same order as membrane thickness, one can wonder to what extent continuum elastic models in general still apply, and what level of complexity is required for an accurate description. In particular, which terms must be retained in a deformation expansion of the effective Hamiltonian?

Sustained theoretical investigation has been conducted in order to construct a model describing membrane thickness deformations [172, 174–176] (see Sec. 6.3). In this Chapter, we put forward a modification to the existing models. We argue that contributions involving the gradient (and the Laplacian) of the area per lipid should be accounted for in the effective Hamiltonian per lipid from which the effective Hamiltonian of the bilayer is constructed, following the approach of Refs. [175, 176]. We show that these new terms cannot be neglected *a priori* as they contribute to important terms in the bilayer effective Hamiltonian. We discuss the differences between our model and the existing ones. We compare the predictions of our model with numerical data giving the profile of membrane thickness close to a mismatched protein [180, 181, 183], and with experimental data regarding gramicidin lifetime [171] and formation rate [170].

The work presented in this Chapter was conducted in collaboration with Doru Constantin. The main results of this work have been published in: A.-F. Bitbol, D. Constantin and J.-B. Fournier, *Bilayer elasticity at the nanoscale: the need for new terms*, PLoS ONE 7(11), e48306 (2012), cited as Ref. [186] here.

7.2 Membrane model

7.2.1 Starting point

We consider a bilayer membrane constituted of two identical monolayers, labeled by $+$ and $-$, in contact with a reservoir of lipids with chemical potential μ. We write

the effective Hamiltonian per molecule in monolayer $\pm$ as

$$f_m^{\pm} = \frac{1}{2} f_0''(\Sigma^{\pm} - \Sigma_0)^2 \pm f_1\, H^{\pm} \pm f_1'(\Sigma^{\pm} - \Sigma_0) H^{\pm} + f_2\, (H^{\pm})^2 \\ + f_K\, K^{\pm} + \alpha\, (\boldsymbol{\nabla}\Sigma^{\pm})^2 + \beta\, \nabla^2 \Sigma^{\pm} + \zeta\, (\nabla^2 \Sigma^{\pm})^2 - \mu\,, \tag{7.1}$$

where $H^{\pm}$ is the average curvature of the monolayer, $K^{\pm}$ its Gaussian curvature, and $\Sigma^{\pm}$ is the area per lipid. All these quantities are defined on the hydrophobic-hydrophilic interface of each monolayer. Eq. (7.1) corresponds to an expansion of $f_m^{\pm}$ for small deformations around the equilibrium state where the membrane is flat and where each lipid has its equilibrium area Σ_0. Any constant term in the effective Hamiltonian per lipid is included in a redefinition of the chemical potential μ.

In the case where $\alpha = \beta = \zeta = 0$, Eq. (7.1) is equivalent to the model of Ref. [27], which corresponds to the basis of those developed in Refs. [175, 176, 180, 181]. To our knowledge, existing membrane models including a variable thickness or density do not feature terms in the gradient, or Laplacian, of such variables [187]. Disregarding such terms is justified when one deals with the large-scale behavior of membranes, since the correlation length of density fluctuations is typically not larger than the membrane thickness (far from a critical point). However, in order to investigate membrane elasticity at the nanoscale, and in particular the local membrane deformations due to a protein with a hydrophobic mismatch, it is necessary to account for such terms.

We are going to show that the terms in α, β and ζ cannot be neglected with respect to others *a priori*. We will then focus specifically on the influence of α, for which we provide a physical interpretation, and we will set $\beta = \zeta = 0$ to simplify our discussion and to avoid adding unknown parameters.

From now on, we will work in the Monge gauge. More precisely, each monolayer will be parametrized by the height $z = h^{\pm}(x, y)$ of its hydrophobic-hydrophilic interface, with respect to a reference plane (x, y), as shown on Fig. 7.1. In addition, we will consider small deformations of an infinite flat membrane. To second order in $\partial_i h^{\pm}$ and $\partial_i \partial_j h^{\pm}$, we have $H^{\pm} = \nabla^2 h^{\pm}/2$ and $K^{\pm} = \partial_x^2 h^{\pm} \partial_y^2 h^{\pm} - (\partial_x \partial_y h^{\pm})^2 = \det(\partial_i \partial_j h^{\pm})$. With our sign conventions, the upper monolayer corresponds to monolayer $+$ and the lower one to monolayer $-$.

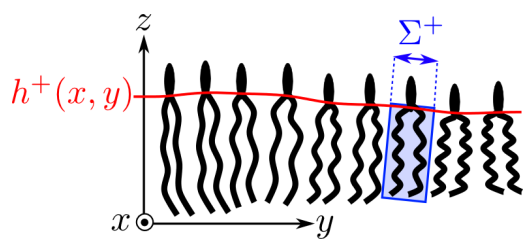

Figure 7.1: Two-dimensional sketch of monolayer $+$. The hydrophilic-hydrophobic interface corresponds to the red curve. Its height is denoted by h^+. The volume v of the hydrophobic chains per lipid is represented in blue for one of the lipids. The area per lipid, measured on the hydrophilic-hydrophobic interface, is Σ^+.

7.2.2 Derivation of the effective Hamiltonian of the bilayer

We will now construct the effective Hamiltonian of a bilayer from Eq. (7.1). For this, we will sum the Hamiltonian densities of the two monolayers, taking into account the constraint that there is no space between the two monolayers of the bilayer, and assuming that the hydrophobic chains of the lipids are incompressible.

Let us consider a patch of bilayer membrane with a fixed projected area A_p, at fixed chemical potential μ. The rest of the membrane (e.g., of the vesicle) plays the part of the reservoir that sets the chemical potential μ. The effective Hamiltonian per unit projected area in each monolayer is $f^\pm = f_m^\pm/\bar{\Sigma}^\pm$, where $f_m^\pm$ is given by Eq. (7.1), while the projected area $\bar{\Sigma}^\pm$ per molecule reads $\bar{\Sigma}^\pm = \Sigma^\pm[1-(\boldsymbol{\nabla} h^\pm)^2/2]$ to second order. Hence, Eq. (7.1) yields, to second order in the deformation and in the relative stretching of the monolayers,

$$\begin{aligned} f^\pm = &-\frac{\mu}{\bar{\Sigma}^\pm} + \frac{f_0''}{2}\bar{\Sigma}^\pm\left(\frac{\bar{\Sigma}^\pm-\Sigma_0}{\bar{\Sigma}^\pm}\right)^2 \pm \frac{f_1}{2}\frac{\nabla^2 h^\pm}{\bar{\Sigma}^\pm} \pm \frac{f_1'}{2}\left(\frac{\bar{\Sigma}^\pm-\Sigma_0}{\bar{\Sigma}^\pm}\right)\nabla^2 h^\pm \\ &+ \frac{f_2}{4}\frac{(\nabla^2 h^\pm)^2}{\bar{\Sigma}^\pm} + f_K\frac{\det(\partial_i\partial_j h^\pm)}{\bar{\Sigma}^\pm} + \alpha\frac{(\boldsymbol{\nabla}\bar{\Sigma}^\pm)^2}{\bar{\Sigma}^\pm} + \beta\frac{\nabla^2\bar{\Sigma}^\pm}{\bar{\Sigma}^\pm} + \zeta\frac{(\nabla^2\bar{\Sigma}^\pm)^2}{\bar{\Sigma}^\pm}\,, \end{aligned} \tag{7.2}$$

where a term involving third-order derivatives of $h^\pm$ has been discarded.

We assume that the hydrophobic chains of the lipids are incompressible. Following Refs. [175, 176, 180], we use the incompressibility condition $v = \bar{\Sigma}^\pm t^\pm$, where v is the constant hydrophobic volume per lipid, $t^\pm$ is the hydrophobic thickness of monolayer $\pm$ projected along the z direction and $\bar{\Sigma}^\pm$ is the area per molecule projected on the reference plane[1].

Let us denote by t_0 the equilibrium value of $t^\pm$ for a flat membrane parallel to the reference plane, and introduce

$$r^\pm = \frac{t^\pm - t_0}{t_0} = \frac{\Sigma_0 - \bar{\Sigma}^\pm}{\bar{\Sigma}^\pm}\,. \tag{7.3}$$

In all the following, we will keep only terms of second order and lower in the small dimensionless variables $r^\pm$, $t_0|\boldsymbol{\nabla} r^\pm|$, $t_0^2\nabla^2 r^\pm$, $|\boldsymbol{\nabla} h^\pm|$ and $t_0\nabla^2 h^\pm$ in $f^\pm$. In this framework, Eq. (7.2) becomes[2]

$$\begin{aligned} f^\pm = &-\frac{\mu}{\Sigma_0}\left(1+r^\pm\right) + \frac{K_a}{4}(r^\pm)^2 \pm \frac{\kappa_0\, c_0}{2}\nabla^2 h^\pm \pm \frac{\kappa_0}{2}(c_0 - c_0'\Sigma_0)\, r^\pm\, \nabla^2 h^\pm \\ &+ \frac{\kappa_0}{4}(\nabla^2 h^\pm)^2 + \frac{\bar{\kappa}}{2}\det(\partial_i\partial_j h^\pm) \\ &+ \frac{k_a' d_0^2}{4}\left(\boldsymbol{\nabla} r^\pm\right)^2 + \beta\left[\boldsymbol{\nabla}\cdot(r^\pm\boldsymbol{\nabla} r^\pm) - \nabla^2 r^\pm\right] + \frac{k_a''\, d_0^4}{4}(\nabla^2 r^\pm)^2\,. \end{aligned} \tag{7.4}$$

[1] In the incompressibility condition $v = \bar{\Sigma}^\pm t^\pm$, a correction arising from membrane curvature is neglected. Using the complete incompressibility condition instead of this one yields the same effective Hamiltonian Eq. (7.16), but with different expressions of c_0 and κ as a function of the constants involved in Eq. (7.1). These expressions depend on μ, and hence on the applied tension, but this dependence is negligible for realistic tension values. As the rest of our discussion is not affected by this, we keep the approximate incompressibility condition for the sake of simplicity. Note that the exact incompressibility condition was implemented very recently in Ref. [23].

[2] We use the relation $r^\pm\nabla^2 r^\pm = \boldsymbol{\nabla}\,(r^\pm\boldsymbol{\nabla} r^\pm) - (\boldsymbol{\nabla} r^\pm)^2$ to rewrite the term in β in Eq. (7.2).

In this expression, we have introduced the constitutive constants of a monolayer: $f_0''\Sigma_0 = K_a/2$ is the compressibility modulus of the monolayer, $f_2/(2\Sigma_0) = \kappa_0/2$ is its bending rigidity, $f_K/\Sigma_0 = \bar{\kappa}/2$ is its Gaussian bending rigidity, $f_1/f_2 = c_0$ is its spontaneous (total) curvature, and $f_1'/f_2 = c_0'$ is the modification of the spontaneous (total) curvature due to area variations. More precisely, $c_0' = dc_s/d\Sigma$ where $c_s(\Sigma) = c_0 + c_0'(\Sigma - \Sigma_0)$ is the lipid area-dependent (total) spontaneous curvature of the monolayer. In addition, we have introduced the constants

$$k_a' = 4\,\frac{\alpha\,\Sigma_0 + \beta}{d_0^2}\,, \tag{7.5}$$

$$k_a'' = 4\,\frac{\zeta\,\Sigma_0}{d_0^4}\,. \tag{7.6}$$

These two constants have the dimension of a surface tension, like K_a.

In our description, the state of monolayer $\pm$ is determined by the two independent variables $r^\pm$ and $h^\pm$ (or, equivalently, $t^\pm$ and $h^\pm$, see Fig. 7.2). Hence, the state of the bilayer membrane is *a priori* determined by four variables. However, given that there must be no space between the two monolayers, we have the following geometrical constraint (see Fig. 7.2):

$$h^+ - h^- = t^+ + t^- = t_0\left(2 + r^+ + r^-\right)\,. \tag{7.7}$$

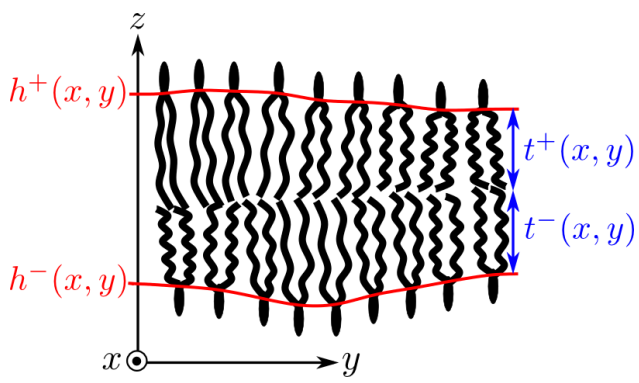

Figure 7.2: Two-dimensional sketch of a lipid bilayer membrane. The hydrophilic-hydrophobic interface of each monolayer corresponds to the red curve. The height of each of these interfaces is denoted by $h^\pm$. The hydrophobic thickness of each monolayer is $t^\pm$. The state of monolayer $\pm$ is described by the two fields $h^\pm$ and $t^\pm$.

This leaves us with only three independent variables to describe the state of the membrane. Let us choose the average shape h of the bilayer, the difference δt between the hydrophobic thicknesses of the two monolayers along z, and the excess thickness u along z of the bilayer:

$$h = \frac{h^+ + h^-}{2}\,, \tag{7.8}$$

$$\delta t = t^+ - t^-\,, \tag{7.9}$$

$$u = t^+ + t^- - d_0\left[1 + \frac{(\boldsymbol{\nabla} h)^2}{2}\right]\,, \tag{7.10}$$

where $d_0 = 2\,t_0$ is the equilibrium thickness of the flat bilayer, while $d_0[1+(\boldsymbol{\nabla} h)^2/2]$ is its equilibrium z-thickness (to second order).

In terms of the new variables h, u and δt, the effective Hamiltonian $f = f^+ + f^-$ per unit projected area of the membrane reads, to second order in the small dimensionless variables mentioned just before Eq. (7.4), and neglecting terms containing derivatives of order higher than two:

$$\begin{aligned} f = {} & \sigma \left[1 + \frac{u}{d_0} + \frac{(\boldsymbol{\nabla} h)^2}{2}\right] + \frac{K_a}{2\,d_0^2}\left(u^2 + \delta t^2\right) + \frac{\kappa_0}{2}\left[(\nabla^2 h)^2 + \frac{1}{4}(\nabla^2 u)^2\right] \\ & + \frac{\kappa_0\,c_0}{2}\,\nabla^2 u + \frac{\kappa_0}{2\,d_0}(c_0 - c_0'\Sigma_0)\left(u\,\nabla^2 u + 2\,\delta t\,\nabla^2 h\right) \\ & + \bar{\kappa}\left[\det(\partial_i\partial_j h) + \frac{1}{4}\det(\partial_i\partial_j u)\right] \\ & + \frac{k_a'}{2}\left[(\boldsymbol{\nabla} u)^2 + (\boldsymbol{\nabla}\delta t)^2\right] + \frac{k_a''\,d_0^2}{2}\left[(\nabla^2 u)^2 + (\nabla^2\delta t)^2\right] \\ & - \frac{2\,\beta}{d_0}\,\nabla^2 u + \frac{2\,\beta}{d_0^2}\left[\,\boldsymbol{\nabla}\cdot(u\boldsymbol{\nabla} u) + \boldsymbol{\nabla}\cdot(\delta t\boldsymbol{\nabla}\delta t)\,\right]\,, \end{aligned} \tag{7.11}$$

where we have introduced $\sigma = -2\mu/\Sigma_0$, which plays the part of an externally applied tension (see Appendix A, Sec. 7.7.3).

7.2.3 The case of symmetric thickness deformations

We wish to compare the predictions of our model to numerical and experimental results regarding hydrophobic mismatch, where proteins with up-down symmetry are considered (see Fig. 7.3). Hence, in the present study, we are not interested in the variable δt. In a coarse-graining procedure, this degree of freedom can be eliminated by integrating over it. In our Gaussian theory, it simply amounts to minimizing f with respect to δt. This variable is coupled to the membrane curvature $\nabla^2 h$, but not to u. In the case of a constant curvature, the constant value

$$\delta t = -\frac{d_0\,\kappa_0}{K_a}(c_0 - c_0'\Sigma_0)\;\nabla^2 h\,, \tag{7.12}$$

is a simple solution to the Euler-Lagrange equations in δt, for which the term involving δt in f reads

$$f_{\delta t} = -\frac{1}{2}\,\frac{\kappa_0^2}{K_a}(c_0 - c_0'\Sigma_0)^2\;(\nabla^2 h)^2\,. \tag{7.13}$$

As the variable δt varies spontaneously on length scales much shorter than the variable h, we can consider in a first approximation that δt will simply follow $\nabla^2 h$, in which case this constant solution is the valid one. Thus, after this partial minimization, this term provides a correction to κ_0.

We finally obtain

$$f = \sigma \left[1 + \frac{u}{d_0} + \frac{(\boldsymbol{\nabla} h)^2}{2}\right] + \frac{K_a}{2\,d_0^2}\,u^2 + \left[\frac{k_a'}{2} - \frac{\kappa_0}{2\,d_0}(c_0 - c_0'\Sigma_0)\right](\boldsymbol{\nabla} u)^2$$
$$+ \frac{\kappa}{2}(\nabla^2 h)^2 + \left(\frac{\kappa_0}{8} + \frac{k_a''\,d_0^2}{2}\right)(\nabla^2 u)^2 + \bar{\kappa}\left[\det(\partial_i\partial_j h) + \frac{1}{4}\det(\partial_i\partial_j u)\right]$$
$$+ \left[\frac{\kappa_0\,c_0}{2} - \frac{2\,\beta}{d_0}\right]\nabla^2 u + \left[\frac{\kappa_0}{2\,d_0}(c_0 - c_0'\Sigma_0) + \frac{2\,\beta}{d_0^2}\right]\boldsymbol{\nabla}\cdot(u\boldsymbol{\nabla} u)\,. \tag{7.14}$$

where the usual Helfrich bending rigidity κ, associated with the average shape, is related to κ_0 through

$$\kappa = \kappa_0 - \frac{1}{2}\frac{\kappa_0^2}{K_a}(c_0 - c_0'\Sigma_0)^2\,. \tag{7.15}$$

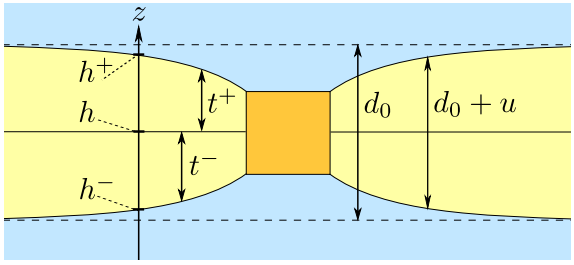

Figure 7.3: Cut of a bilayer membrane containing a protein with a hydrophobic mismatch, represented as a square (orange). The solidblack lines mark the boundaries of the hydrophobic part of the membrane (yellow), and the exterior corresponds to the hydrophilic lipid heads and the water surrounding the membrane (blue). The height of monolayer $\pm$ along z is denoted by $h^{\pm}$. In this up-down symmetric case, $h = (h^+ + h^-)/2$ is constant. The hydrophobic thickness of monolayer $\pm$ is denoted by $t^{\pm}$. The equilibrium hydrophobic thickness of the bilayer is d_0, while the actual hydrophobic thickness of the bilayer is denoted by $d_0 + u$.

In the present work, we are interested in variations of the membrane z-thickness u, and we thus focus on the case where the average shape of the membrane is flat, i.e., $h = 0$ (see Fig. 7.3). In this case, we obtain, from Eq. (7.14):

$$f = \frac{\sigma}{d_0}\,u + \frac{K_a}{2\,d_0^2}\,u^2 + \frac{K_a'}{2}\,(\boldsymbol{\nabla} u)^2 + \frac{K_a''}{2}\,(\nabla^2 u)^2$$
$$+ A_1\,\nabla^2 u + A_2\,\boldsymbol{\nabla}\cdot(u\boldsymbol{\nabla} u) + \frac{\bar{\kappa}}{4}\,\det(\partial_i\partial_j u)\,, \tag{7.16}$$

with

$$K_a' = -\frac{\kappa_0}{d_0}(c_0 - c_0'\Sigma_0) + k_a'\,, \tag{7.17}$$

$$K_a'' = \frac{\kappa_0}{4} + k_a''\,, \tag{7.18}$$

$$A_1 = \frac{\kappa_0\,c_0}{2} - \frac{2\,\beta}{d_0}\,, \tag{7.19}$$

$$A_2 = \frac{\kappa_0}{2\,d_0}(c_0 - c_0'\Sigma_0) + \frac{2\,\beta}{d_0^2}\,. \tag{7.20}$$

Note that the last three terms in Eq. (7.16) are boundary terms.

In our model Eq. (7.16), the constants K'_a, K''_a include contributions in k'_a and k''_a, which arise from α, β and ζ (see Eqs. (7.5) and (7.6)). Hence, the terms in gradient and Laplacian of Σ introduced in Eq. (7.1) cannot be neglected *a priori*, as they contribute to the terms in $(\boldsymbol{\nabla} u)^2$ and $(\nabla^2 u)^2$ that are traditionally accounted for in models describing membrane thickness deformations [170, 172, 175, 176, 180, 188]. Due to these contributions, the values of the constants K'_a and K''_a are not fully predicted by the constants involved in the Helfrich model. This stands in contrast with the models developed previously [170, 172, 175, 176, 180, 188]. In addition, the terms arising from α, β and ζ modify the relations between the various coefficients: in the previous models that accounted for boundary terms, assuming $\alpha = \beta = \zeta = 0$, one had $K'_a = -2\,A_2$ [180], which is no longer true here. This will affect the equilibrium thickness profile of a membrane containing a mismatched protein.

In the following, the membrane effective Hamiltonian we will use corresponds to Eq. (7.16). In addition, we will mostly concentrate on the effect of α, to simplify our discussion and to avoid adding unknown parameters. In the case where $\beta = \zeta = 0$, to which we will often restrict, the various constants introduced in Eq. (7.16) read:

$$K'_a = -\frac{\kappa_0}{d_0}(c_0 - c'_0\Sigma_0) + k'_a\,, \tag{7.21}$$

$$K''_a = \frac{\kappa_0}{4}\,, \tag{7.22}$$

$$A_1 = \frac{\kappa_0\, c_0}{2}\,, \tag{7.23}$$

$$A_2 = \frac{\kappa_0}{2\,d_0}(c_0 - c'_0\Sigma_0)\,, \tag{7.24}$$

with

$$k'_a = 4\,\frac{\alpha\,\Sigma_0}{d_0^2}\,. \tag{7.25}$$

7.3 Comparison with existing models

Our model Eq. (7.16) has a form similar to that of the models developed in [175, 176, 180, 181]. However, we have included the effect of an applied tension σ, and the various constants in Eq. (7.16) have different interpretations, and thus different values, from the ones in existing models. Let us discuss these differences in more detail.

7.3.1 On the tension

First of all, existing models [170, 172, 175, 176, 180, 181, 188] were constructed at zero applied tension, which means $\sigma = 0$ in Eq. (7.16). To our knowledge, our work is the first where the coefficient of the term linear in u is explicitly related to the applied tension (see Appendix A, Sec. 7.7.3) and to the tension of the Helfrich model (see Appendix A, Sec. 7.7.1).

In Ref. [170], the effect of applied tension was implemented in so far as it changes the equilibrium membrane thickness of a homogeneous membrane. Our description gives back this effect when applied to the particular case of a homogeneous membrane (see Appendix A, Sec. 7.7.3).

7.3.2 On the constant K'_a

In our model, restricting to the case where $\beta = \zeta = 0$, the constant K'_a features two contributions that have two different origins (see Eq. (7.21)).

The first contribution arises from the spontaneous curvature of a monolayer and from its variation with the area per lipid. More precisely, the term

$$\frac{\kappa_0}{2\,d_0}(c_0 - c'_0\Sigma_0)\,u\nabla^2 u = \frac{\kappa_0}{2\,d_0}(c_0 - c'_0\Sigma_0)\,\left[\boldsymbol{\nabla}\cdot(u\boldsymbol{\nabla}u) - (\boldsymbol{\nabla}u)^2\right] \tag{7.26}$$

arises when one constructs the membrane model starting from a monolayer Hamiltonian density such as Eq. (7.1). This term was first introduced in Ref. [175], and it was then included in Refs. [176, 180].

The second contribution, k'_a, arises from α (see Eq. (7.25)), i.e., from the term in $(\boldsymbol{\nabla}\Sigma)^2$ introduced in Eq. (7.1). This term was not included in Refs. [175, 176, 180], which started from a second-order expansion of the effective Hamiltonian per lipid molecule involving only the curvature and the area per lipid. However, a gradient of area per lipid (or, equivalently, of the thickness) in a monolayer has an energetic cost. Indeed, a greater part of the hydrophobic chains is in contact with water when a thickness gradient is present (see Fig. 7.4). The cost of the hydrocarbon-water interface is given by the interfacial tension γ, which is of order 40–50 mN/m [11, 189]. Such a term is often accounted for in microscopic membrane models (see, e.g., Ref. [190]). In the case of a symmetric membrane ($t^+ = t^- = t$) with flat average shape, the surface of the hydrocarbon-water interface is increased by a factor $[1 + (\boldsymbol{\nabla}t)^2/2]$ for each monolayer (see Fig. 7.4). Thus, to second order, the associated energetic cost per unit projected area is $\gamma(\boldsymbol{\nabla}t)^2 = \gamma(\boldsymbol{\nabla}u)^2/4$. In this framework, we should have

$$k'_a = \frac{\gamma}{2}\,. \tag{7.27}$$

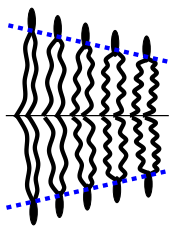

Figure 7.4: Bilayer with a symmetric thickness gradient. The dashed blue lines correspond to the hydrocarbon-water interfaces.

In the seminal article Ref. [172], where the membrane model was constructed by analogy with liquid crystals, a term in $(\boldsymbol{\nabla}u)^2$, interpreted as arising from tension,

was included in the effective Hamiltonian. However, its effect was neglected on the grounds that the value of its prefactor made it negligible with respect to the other terms. The value of this prefactor was taken to be that of the tension of a monolayer on the surface of a Plateau border [191]. The model introduced in Ref. [172] was further developed and analyzed in Refs. [170, 188], where the same argument was used to neglect the term in $(\boldsymbol{\nabla} u)^2$.

However, our construction of the membrane effective Hamiltonian shows that the tension involved through k'_a arises from local variations in the area per lipid. This stands in contrast with the case of the Plateau border, where whole molecules can move along the surface, yielding a smaller value of the tension. Ref. [191] stresses that the measured tension of a Plateau border is valid for long-wavelength fluctuations, but that it is largely underestimated for short-wavelength fluctuations (less than 10 nm) which involve significant changes in area per molecule.

Including the tension of the hydrocarbon-water interface instead of that of the Plateau border is a significant change, given that the former is of order 40–50 mN/m [11, 189], while the latter is of order 1.5–3 mN/m [170, 172, 188, 191]. In Refs. [170, 188], it is shown that the effect of the term in $(\boldsymbol{\nabla} u)^2$ is negligible if

$$K'_a \ll \frac{\sqrt{K_a K''_a}}{d_0}\,, \tag{7.28}$$

where we have used our own notations of the prefactors of the terms in $(\boldsymbol{\nabla} u)^2$, u^2 and $(\nabla^2 u)^2$. In the case of DOPC, taking $K''_a = \kappa/4$ and using the values of the membrane constants, this condition becomes $K'_a \ll 28$ mN/m. While this is well verified if K'_a corresponds to the tension of the Plateau border, it is no longer valid with our model.

Our model is the first that includes both contributions to K'_a, the one arising from spontaneous curvature and the one arising from interfacial tension. Besides, in Sec. 7.2.3, we have shown that, in the general case, β is also involved in K'_a, through k'_a (see Eq. (7.5)), which stresses the complexity of constructing a continuum model to describe membrane elasticity at the nanoscale: many terms involved in the expansion of the effective Hamiltonian cannot be neglected *a priori*.

In the following, we will analyze numerical and experimental data, looking for evidence for the presence of k'_a. In each case, we will compare the relative weight of the two contributions to K'_a.

7.3.3 On the value of K''_a

In the case where $\beta = \zeta = 0$, we have obtained $K''_a = \kappa_0/4$ (see Eq. (7.22)), where κ_0 is the bending rigidity of a symmetric membrane such that $\delta t = 0$. The elastic constant κ_0 is related to the bending rigidity κ of the Helfrich model (see Appendix A, Sec. 7.7.1) through

$$\kappa = \kappa_0 - \frac{1}{2}\frac{\kappa_0^2}{K_a}(c_0 - c'_0\Sigma_0)^2\,. \tag{7.29}$$

The difference between κ_0 and κ arises from integrating out δt (see Sec. 7.2.3). In the previous models, this procedure was not carried out, as one focused directly on

the symmetric case $\delta t = 0$. All the previous models consider that $K_a'' = \kappa/4$ [170, 172, 175, 176, 180, 188].

In addition, in Sec. 7.2.3, we have shown that, in the general case, ζ is also involved in K_a'', through k_a'' (see Eq. (7.6)), which stresses further the possible importance of such terms in order to describe membrane elasticity at the nanoscale.

7.3.4 On the boundary terms

The boundary terms, which correspond to the last three terms in Eq. (7.16), are the same as in Refs. [175, 176, 180]. However, we have accounted for the Gaussian bending rigidity $\bar{\kappa}$ in addition, as in Ref. [181]. When one wishes to describe the local membrane deformation due to a transmembrane protein, the boundary terms play an important part, as their integral on the contour of the protein contributes to the deformation energy.

Again, the situation is more complex when β is included, as the expressions of A_1 and A_2 then feature extra terms linear in β (see Eq. (7.20) in Sec. 7.2.3).

Now that we have presented our model and the differences with previous ones, we are going to test it against numerical results (Sec. 7.4) and experimental ones (Sec. 7.5).

7.4 Comparison with numerical results

As mentioned in Sec. 6.4, numerical simulations provide interesting tests for theoretical models describing membrane elasticity at the nanoscale. Let us compare the predictions of our model to recent numerical results.

7.4.1 Fluctuation spectra

Numerical simulations enable to measure precisely the fluctuation spectra of the average height h and the half thickness $t = u/2$ of a bilayer membrane [180, 182–184]. Microscopic protrusion modes, occurring at the scale of a lipid molecule, contribute to these spectra. While they are not described by continuum theory, it is possible to consider that they are decoupled from the larger-scale modes [180, 183]. By fitting the numerical spectra to theoretical formulas, it is possible to extract the numerical values of the membrane constants involved in the continuum theory. In our framework, the fluctuation spectra of the average height of the membrane give access to the Helfrich bending rigidity κ, while those regarding the thickness of the membrane give access to K_a, K'_a and K''_a.

We have reanalyzed the height and thickness spectra presented in Refs. [182–184] using the fitting formulas in Refs. [180, 183] (see Eq. (32) of Ref. [180]) and the method described in Ref. [180], except that we did not assume that $K''_a = \kappa/4$, in order to include the possible effect of the difference between κ and κ_0 (see Eq. (7.15)), and of k''_a, i.e., of ζ (see Eqs. (7.18)and (7.6)). More details on our analysis of these spectra are presented in Appendix B, Sec. 7.8.

Our results were similar to those obtained in Refs. [180, 183] assuming that $K''_a = \kappa/4$, and we obtained no systematic significant difference between K''_a and $\kappa/4$ (see Appendix B, Sec. 7.8), which means that the corrections to K''_a predicted by our model are negligible in these simulations. This gives a justification for focusing only on the correction k'_a to K'_a, as we do in this work. Besides, we obtained $K'_a < 0$ from all the fits, as reported in Refs. [180, 183], and we checked that all the values obtained for K'_a comply with the stability condition discussed in Appendix A (see Eq. (7.36)).

7.4.2 Deformation profiles close to a mismatched protein

In Refs. [180, 181, 183], the thickness profile of a membrane containing one cylindrical inclusion with a hydrophobic mismatch has been obtained from coarse-grained numerical simulations. Comparing the average numerical thickness profiles to the equilibrium profiles predicted from theory is a good test for our model, in particular to find clues for the presence of k'_a.

Let us denote the radius of the protein by r_0, and its hydrophobic length by ℓ: the mismatch stems from the difference between ℓ and the hydrophobic thickness d_0 of the membrane. The equilibrium shape of the membrane, which minimizes its deformation energy, is solution to the Euler-Lagrange equation associated with the effective Hamiltonian density in Eq. (7.16). We write down this equilibrium shape

explicitly in Appendix C, Sec. 7.9.1. In order to determine it fully, it is necessary to impose boundary conditions at the edge of the inclusion, i.e., in $r = r_0$. There is a consensus on the assumption of strong hydrophobic mismatch $u(r_0) = u_0 = \ell - d_0$, as it costs more energy to expose part of the hydrophobic chains to water than to deform the membrane, for typical mismatches of a few Å. However, there is some debate regarding the second boundary condition in r_0 (see, e.g., Ref. [180]), which depends on the precise interactions between the protein and the membrane. One can either assume that the protein locally imposes a fixed slope to the membrane [170, 188], or minimize the effective Hamiltonian in the absence of any additional constraint, which amounts to considering that the system is free to adjust its slope in r_0 [175, 176, 180, 181, 183]. In Appendix C, Sec. 7.9.1, we present the equilibrium profiles for these two types of boundary conditions. The latter, "free-slope" boundary condition (also called "natural" boundary condition [175, 180]) has the advantage of not introducing any extra unknown parameter in the description.

In Refs. [180, 181, 183], the free-slope boundary conditions (see Appendix C, Eq. (7.56)) are chosen. The membrane model of Refs. [180, 181, 183] is very similar to ours, except that $k'_a = 0$. It was shown in Ref. [183] that this model can reproduce very well the numerical results, *provided that the spontaneous curvature c_0 is adjusted for each deformation profile* (see Fig. 7.5).

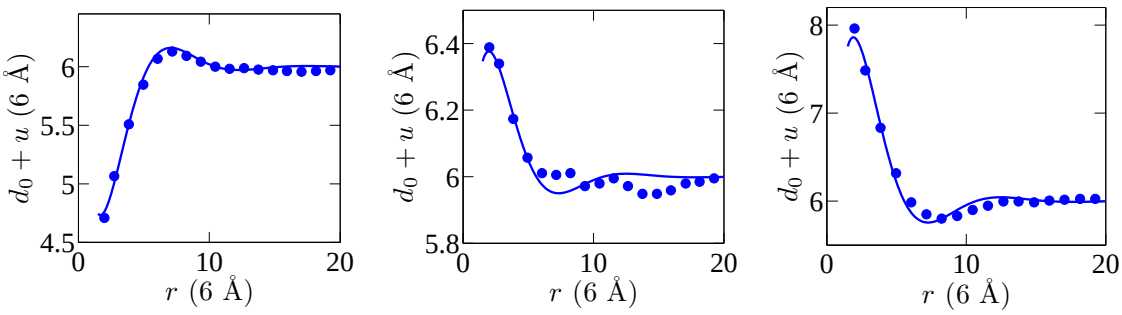

(a) $\ell \simeq 2.4$ nm **(b)** $\ell \simeq 3.6$ nm **(c)** $\ell \simeq 4.8$ nm

Figure 7.5: Thickness deformation profile from Ref. [183] for three mismatched inclusions with different hydrophobic thicknesses ℓ. Membrane thickness is plotted versus the radial distance r from the protein center. The equilibrium membrane hydrophobic thickness is $d_0 \simeq 3.6$ nm. Dots: numerical data (the error bars on the data, not reproduced here, are about 1 Å wide [183]). Lines: best fits. Exactly as in the original reference, the numerical data is fitted to Eqs. (7.51)-(7.58) in Appendix C, with $k'_a = 0$, taking u_0 and c_0 (i.e., in fact, $\tilde{c}_0$) as fitting parameters, the other constants being known from the fluctuation spectra.

In Ref. [183], the adjusted "renormalized spontaneous curvature" was found to depend linearly on the hydrophobic mismatch u_0, as shown[3] in Fig. 7.6. In our

[3]The renormalized spontaneous curvature $\tilde{c}_0$ we plot in Fig. 7.6 corresponds to twice that in Table 2 of Ref. [183], as we work with total curvatures while Ref. [183] (as well as Refs. [180, 181]) work with average curvatures. It is plotted as a function of the mismatch u_0, which corresponds to $2\,t_R^{\mathrm{el}}$ in Table 2 of Ref. [183]. The error bars on $\tilde{c}_0$ are those listed in Table 2 of Ref. [183].

model, the equilibrium profile corresponding to the free-slope boundary conditions (see Eqs. (7.51) and (7.58) in Appendix C) involves k'_a. We show in Appendix C, Sec. 7.9.1-b. that the quantity

$$\tilde{c}_0 = c_0 + \frac{k'_a}{\kappa} u_0 \,, \tag{7.30}$$

then plays the part of the renormalized spontaneous curvature of Ref. [183] in the equilibrium profile. This quantity is linear in u_0: our model, and more precisely, the presence of a nonvanishing k'_a, provides an explanation for the linear dependence observed in Ref. [183].

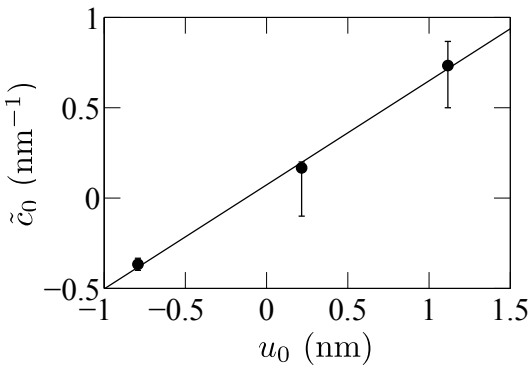

Figure 7.6: Renormalized spontaneous curvature $\tilde{c}_0$ as a function of the hydrophobic mismatch u_0. Data from Ref. [183], corresponding to fits of simulation results for inclusions with three different hydrophobic thicknesses (see Fig. 7.5). Line: linear fit, with equation $\tilde{c}_0\,(\mathrm{nm}^{-1}) = 0.073 + 0.576\ u_0\ (\mathrm{nm})$ and correlation coefficient $r^2 = 0.998$.

Using a linear fit of the data of Ref. [183] (see Fig. 7.6), together with Eq. (7.30) and the value $\kappa = 2.3 \times 10^{-20}$ J extracted from the spectra in Ref. [183], we obtain $k'_a = 13$ mN/m.

It is interesting to compare this value to K'_a, which is obtained from the fluctuation spectra in Ref. [183]: $K'_a = -9.2$ mN/m. This shows that the contribution of k'_a to K'_a is important. Besides, we may now estimate the other contribution to K'_a, which stems from the monolayer spontaneous curvature (see Eq. (7.21)): $-\kappa_0(c_0 - c'_0\Sigma_0)/d_0 = K'_a - k'_a = -22$ mN/m. Using values from the fluctuation spectra in Ref. [183], this yields $\xi \approx -6$ Å for the algebraic distance from the neutral surface of a monolayer to the hydrophilic-hydrophobic interface of this monolayer (see Appendix A, Sec. 7.7.4, for the relation between ξ and c'_0).

In Ref. [181], a different coarse-grained molecular simulation model was used to obtain the equilibrium membrane thickness profiles for cylindrical inclusions with two different hydrophobic thicknesses (one yielding a positive mismatch and the other a negative one), and with seven different radii r_0 (see Fig. 7.7). By fitting

each of these numerical profiles[4] in a similar way[5] as in Ref. [183], we found that $\tilde{c}_0$ does not depend on the radius of the inclusion, but that it depends significantly on the mismatch (see Fig. 7.8(a)). This is in good agreement with the predictions of our model (see Eq. (7.30)).

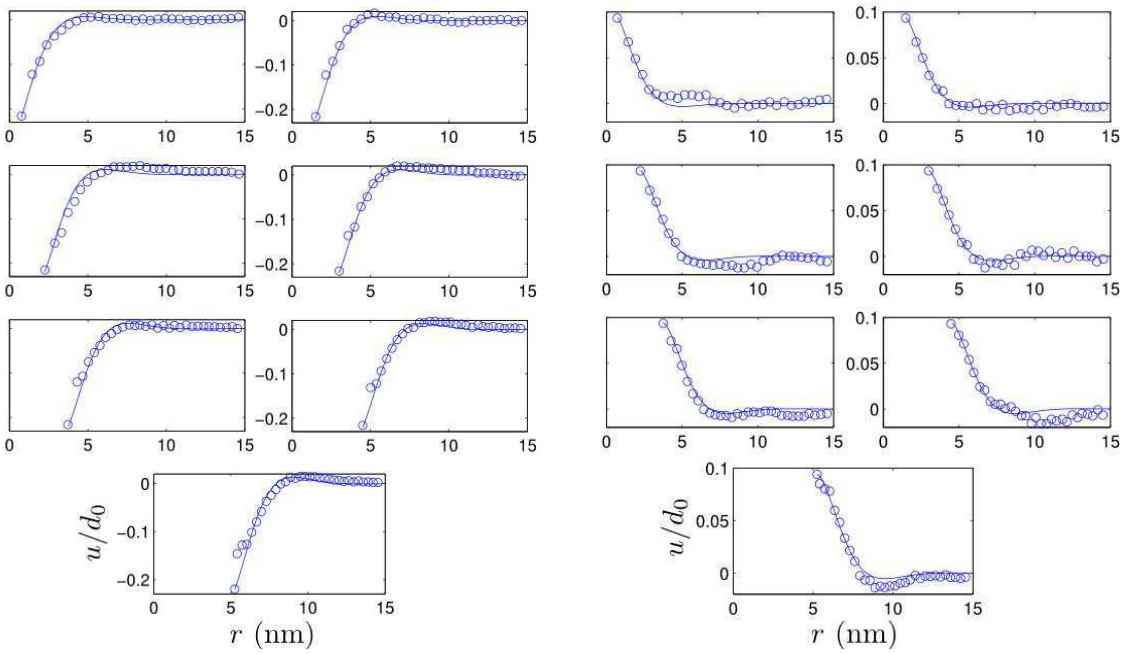

(a) $u_0 = -1.1$ nm. **(b)** $u_0 = 0.45$ nm.

Figure 7.7: Thickness deformation profiles from Ref. [181] for inclusions with two different thicknesses, yielding two hydrophobic mismatches u_0, and seven different radii, ranging from 0.75 nm to 5.25 nm. The equilibrium membrane hydrophobic thickness is $d_0 = 4.8$ nm. The numerical data (dots) was fitted to Eqs. (7.51)-(7.58) in Appendix C with $k'_a = 0$, taking only $\tilde{c}_0$ as fitting parameter, the other constants being known from the fluctuation spectra. In the lines shown here, $\tilde{c}_0$ was averaged over the seven results of the fits (corresponding to the different radii) for each of the two values of u_0.

For each of the two values of u_0, we averaged $\tilde{c}_0$ over the seven results corresponding to the different inclusion radii. The line joining these two average values of $\tilde{c}_0$ as a function of u_0 is plotted in Fig. 7.8(b). Using Eq. (7.30) and the value $\kappa = 1.4 \times 10^{-19}$ J [180, 181], the slope of this line yields $k'_a = 36$ mN/m: the order of magnitude of this value is the same as the one obtained from the data of Ref. [183].

Again, we can compare k'_a to K'_a, which is obtained from the spectra in Refs. [180, 181]: $K'_a = -11.9$ mN/m. Hence, the contribution of k'_a to K'_a is important here too. We also obtain $-\kappa_0(c_0 - c'_0\Sigma_0)/d_0 = K'_a - k'_a = -48\,\mathrm{mN/m}$, and $\xi \approx -3$ Å.

[4]We are referring to the profiles in Figs. 6 and 7 of Ref. [181]. The profiles corresponding to the inclusions with largest radii (5.25 nm) were not included in these figures: we thank Grace Brannigan for sharing this data with us.

[5]Here, c_0 was our only fitting parameter. However, taking u_0 as an additional fitting parameter (as in Ref. [183]) instead of taking its theoretical value yields $k'_a = 40$ mN/m: the difference is not significant.

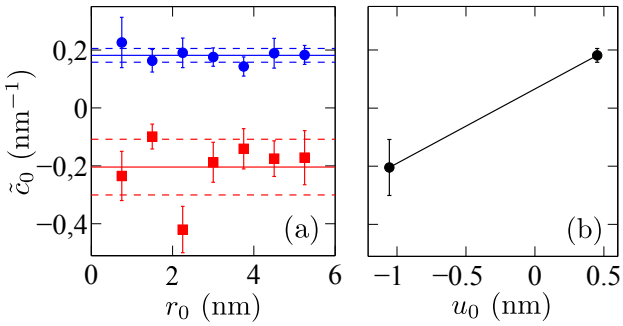

Figure 7.8: (a) Renormalized spontaneous curvature $\tilde{c}_0$ versus the inclusion radius r_0. The values of $\tilde{c}_0$ were obtained by fitting each thickness deformation profile of Ref. [181]. Circles (blue): positive mismatch, $u_0 = 0.45$ nm. Squares (red): negative mismatch, $u_0 = -1.1$ nm. Solid lines: average values; dotted lines: standard deviation over the seven data points (corresponding to the different r_0), for each value of u_0. (b) Average value of $\tilde{c}_0$ (see (a)) as a function of the hydrophobic mismatch u_0. The equation of the line joining the two data points is $\tilde{c}_0\,(\mathrm{nm}^{-1}) = 0.064 + 0.259\ u_0\ (\mathrm{nm})$.

In Ref. [181], the shortcomings of the model that disregards k_a' were explained by the local variation of the volume per lipid close to the protein. It was shown in Ref. [181] that including this effect yields

$$\tilde{c}_0 = c_0 - \frac{\eta}{v_0} v(r_0)\,, \tag{7.31}$$

where v_0 is the bulk equilibrium volume per lipid, while $v_0 + v(r_0)$ denotes the volume per lipid in $r = r_0$. However, the predicted linear dependence of $\tilde{c}_0$ in $v(r_0)/v_0$ is not obvious: in Fig. 7.9, we rather see two groups of points (one for each value of u_0) than a linear law. In other words, the data of Ref. [181] is more consistent with a value of $\tilde{c}_0$ that depends only on u_0 and not on v (or r_0), in agreement with the predictions of our model (see Eq. (7.30)). In Ref. [183], local modifications of the volume per lipid close to the inclusion were investigated too, as well as local modifications of the nematic order, of the shielding of the hydrophobic membrane interior from the solvent, and of the overlap between the two monolayers. None of these effects was found to explain the linear dependence of $\tilde{c}_0$ versus u_0 [183].

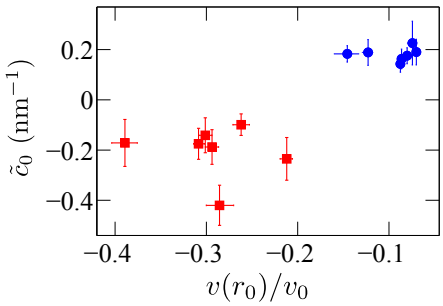

Figure 7.9: Renormalized spontaneous curvature $\tilde{c}_0$ extracted from fitting the data of Ref. [181] versus volume variation $v(r_0)/v_0$ on the inclusion edge, measured in Ref. [181].

To sum up, our model can explain the dependence of $\tilde{c}_0$ in u_0 observed in the numerical results of Refs. [181, 183] as a consequence of the presence of k'_a. Our explanation does not involve any local modification of the membrane properties, in contrast with those proposed in Refs. [181, 183]. Furthermore, the order of magnitude we obtain for k'_a from the data of Refs. [181, 183] is in agreement with our estimate based on the idea that $k'_a \approx \gamma/2 \approx 24$ mN/m (see Eq. (7.27)).

7.5 Comparison with experimental results

Data regarding gramicidin channels (see Sec. 6.2) originally motivated theoretical investigation on membrane models describing local thickness deformations [172, 174–176]. Such data now provides a great opportunity to test any refinement of these models. We will compare our model to the data of Ref. [171] regarding the lifetime of the gramicidin channel as a function of bilayer thickness, and then to the data of Ref. [170] regarding the formation rate of the gramicidin channel as a function of bilayer tension.

7.5.1 Analysis of the experimental data of Elliott *et al.*

It was shown in Ref. [188] that the detailed elastic membrane model introduced in Ref. [172] yields an effective linear spring model as far as the membrane deformation due to gramicidin is concerned [188, 192]: the energy variation F associated with the deformation can be expressed as $F = Hu_0^2$, where H is the effective spring constant, while u_0 is the thickness mismatch between the gramicidin channel and the membrane. This linear spring model was validated by comparison with experimental data regarding the lifetime of the gramicidin channel, measured as a function of bilayer thickness ([171, 173], summarized in [192]) and as a function of the channel length [193].

We will here focus on the data concerning virtually solvent-free bilayers, i.e., membranes formed using squalene. The elasticity of membranes containing hydrocarbons should be different. For instance, a local thickness change of the membrane could be associated with a redistribution of the hydrocarbons. In Ref. [192], the effective spring constant H of the membrane was estimated from data of Ref. [171] regarding gramicidin channel lifetime for three bilayers formed in squalene with monoglycerids that differed only through their chain lengths: the different thicknesses of these membranes yield different hydrophobic mismatches with a given type of gramicidin channels. The value $H_{\text{exp}} = 115 \pm 10$ mN.m^{-1} was obtained.

In Appendix C, Sec. 7.9.2, we use our model to calculate the deformation energy of the membrane due to the presence of a mismatched protein. Both in the case where the gramicidin channel imposes a vanishing slope on its circumference, and in the case of the free-slope boundary condition, this deformation energy can be expressed as a quadratic function of the mismatch u_0. The prefactor of u_0^2 in the deformation energy F corresponds to the effective spring constant of the system. Hence, although our model is different from the one of Refs. [170, 172, 188], it also

yields an effective linear spring model. This is not surprising since we are dealing with the small deformations of an elastic system. However, the detailed expressions of our spring constants as a function of the membrane parameters (see Eqs. (7.64) and (7.70)) are different from those obtained using the model of Refs. [170, 172, 188], due to the differences between the underlying membrane models[6]. In particular, in our model, k'_a is involved in H, through K'_a. Our aim will be to find out which value of k'_a gives the best agreement with the experimental value of H.

Using Eqs. (7.21), (7.22) and (7.24), and neglecting the difference between κ and κ_0, Eqs. (7.64) and (7.70) show that H depends on the elastic constants κ, $\bar{\kappa}$ and c_0 involved in the Helfrich model, on K_a, on $c'_0\Sigma_0$, which corresponds to the spontaneous curvature variation with the area per lipid, on d_0, on the radius r_0 of the gramicidin channel, and on k'_a. There is, to our knowledge, no direct experimental measurement of $c'_0\Sigma_0$ available, but, as shown in Appendix A, Sec. 7.7.4, we have $c'_0\Sigma_0 = K_a\xi/\kappa$, where ξ denotes the algebraic distance from the neutral surface of a monolayer to the hydrophilic-hydrophobic interface of this monolayer (see Eq. (7.46), neglecting the difference between κ and κ_0). Thus, in order to calculate the spring constant, we need values for κ, $\bar{\kappa}$, c_0, K_a and ξ, in the precise case of monoolein membranes.

In Ref. [194], the elastic constants κ, $\bar{\kappa}$ and c_0 were measured in a monoolein cubic mesophase, both at 25°C and at 35°C. The positions of the neutral surface and of the hydrophilic-hydrophobic interface were estimated on the same system in Ref. [195], but these results were flawed by a mathematical issue, which was corrected in Ref. [196]. This correction yielded other corrections on c_0, and on the ratio $\bar{\kappa}/\kappa$ [197]. These results regard a cubic phase, where the membrane is highly deformed with respect to a flat bilayer: the values of the various constants should be affected by the strains present in this phase. In another work [198], the constants of monoolein are determined in a highly hydrated doped HII phase, where the strains are better relaxed. However, these measurements were carried out at 37°C, while the experiments of Ref. [171] that we wish to analyze were performed at 23°C. Given that the data of Refs. [194, 195] include the most appropriate temperature, while the ones of Ref. [198] correspond to the most appropriate phase, we will present results corresponding to both sets of parameters. Finally, the experimental value of K_a for monoolein is provided by Ref. [191].

In Table 7.1, we present the results obtained for the spring constant H of monoolein bilayers, using the different experimental estimates of the membrane constants. The main difference between parameter sets 1 and 2 is the value and the sign of $\bar{\kappa}$ [194, 197]. However, $\bar{\kappa}$ is involved in H only in the free-slope case (see Eqs. (7.64) and (7.70)): the 3% difference between the values of H_0 obtained with parameter sets 1 and 2 stems only from the difference on c_0, while the 12% difference between H_f obtained with data sets 1 and 2 contains an important contribution from

[6]In addition, in the case of the free-slope boundary condition, we obtain $F = H_f\left(u_0 - u_0^{\min}\right)^2 + F^{\min}$ instead of $F = H_f u_0^2$ (see Appendix C, Sec. 7.9.2). The mismatch value $u_0^{\min}$ that minimizes F, and the corresponding deformation energy $F^{\min}$, are nonzero if $A_1 \neq 0$ due to the spontaneous curvature of each monolayer. The effect of monolayer spontaneous curvature was disregarded in Refs. [170, 172, 188].

$\bar{\kappa}$. The constants in parameter set 3, corresponding to Ref. [198], are significantly different from those of Refs. [194, 197], which yields a 30% difference on H_0 and a 20% difference on H_f. We also note that, as the value of the algebraic distance from the neutral surface to the hydrophilic-hydrophobic interface of a monolayer is very small compared to the other length scales involved ($\xi = -0.3$ Å [196]), the contribution of $c_0'\Sigma_0$ to H is negligible (it is of order 1%).

		Set 1	Set 2	Set 3
$s = 0$	H_0 if $k_a' = 0$	130	133	91
	k_a' if $H_0 = H_{\text{exp}} = 115$	< 0	< 0	7.5
Free s	H_f if $k_a' = 0$	41	46	33
	k_a' if $H_f = H_{\text{exp}} = 115$	25	24	26

Table 7.1: Spring constant H and constant k_a' of monoolein, calculated for the zero-slope boundary condition $s = 0$ (using Eq. (7.64)) and for the free-slope boundary condition (using Eq. (7.70)). All values of H and k_a' are given in mN.m^{-1}. The different columns correspond to three different data sets for the parameters of the membrane. Set 1 corresponds to the data from [194] at 25°C: $\kappa = 3.6 \times 10^{-20}$ J, $c_0 = -0.135$ nm^{-1}, $\bar{\kappa} = 8.8 \times 10^{-22}$ J. Set 2 takes into account the corrections on c_0 and $\bar{\kappa}$ in [197]: $c_0 = -0.196$ nm^{-1}, $\bar{\kappa} = -3.6 \times 10^{-21}$ J. Set 3 corresponds to the data from [198]: $\kappa = 1.2 \times 10^{-20}$ J, $c_0 = -0.503$ nm^{-1}, and $\bar{\kappa} = -1.2 \times 10^{-21}$ J deduced from $\bar{\kappa}/\kappa = -0.1$ [197]. In all cases, we have taken $r_0 = 1$ nm [192], $d_0 = 2.46$ nm [195], $\xi = -0.3$ Å [196], $K_a = 140$ mN/m [191, 192].

Let us first focus on the zero-slope boundary condition. The values obtained for H_0 assuming that $k_a' = 0$ are in quite good agreement with the experimental value $H_{\text{exp}} = 115 \pm 10$ mN.m^{-1} obtained in Ref. [192], for all the data sets we used (see line 1 of Table 7.1).

Conversely, for the free-slope boundary conditions, the spring constants H_f obtained assuming that $k_a' = 0$ are about three times smaller than the experimental values (see line 3 of Table 7.1). These conclusions are very similar to those in Ref. [192], which illustrates that accounting for monolayer spontaneous curvature and for boundary terms does not change much the value of H.

Interestingly, the value of the spring constant increases significantly with k_a'. In particular, H_f reaches the experimental value for $k_a' \approx 25$ mN/m for all three parameter sets (see line 4 of Table 7.1): while k_a' seems negligible if zero-slope boundary conditions are assumed, the presence of k_a' can improve the agreement with experiment if free-slope boundary conditions are assumed. The values of k_a' that yield the best agreement with experiment for these boundary conditions correspond to those expected if $k_a' \approx \gamma/2$.

We may compare these values of k_a' to the other contribution to K_a', which stems from the monolayer spontaneous curvature (see Eq. (7.21)): $-\kappa_0(c_0 - c_0'\Sigma_0)/d_0$. We estimate the value of this contribution to be between 0.26 and 1.2 mN/m, depending on which set of parameters is chosen. This is positive and much smaller in absolute value than the estimates obtained from the numerical data of Ref. [183] and of Ref. [181]: here, the neutral surface of a monolayer and its hydrophilic-hydrophobic

interface are very close, while ξ seemed to be significant in the numerical simulations. In the case of the free-slope boundary condition, our results imply that k'_a should be the dominant contribution to K'_a for the membranes studied in Ref. [171].

Here, our conclusions regarding the value of k'_a are somewhat dependent on the boundary conditions chosen. *A priori*, the free-slope boundary condition seems more satisfactory because one does not have to choose a specific slope, and also because the interactions between the membrane and the protein are very short-ranged. If free-slope boundary condition is indeed chosen, the above analysis of Ref. [171] yields some clues in favor of $k'_a \approx \gamma/2$.

7.5.2 Analysis of the experimental data of Goulian *et al.*

While the experiments cited in the previous Section dealt with discrete changes of the hydrophobic mismatch obtained by varying membrane composition, Goulian *et al.* [170] measured the gramicidin channel formation rate f in lipid vesicles as a function of the tension σ applied through a micropipette. As the tension is an externally controlled parameter that can be changed continuously for the same gramicidin-containing membrane, this approach can yield more information, and it has the advantage of limiting the experimental artifacts associated to new preparations. To date, the experiment in Ref. [170] remains the most significant in the field and should serve as a testing ground for any theoretical model. We will therefore discuss in detail the data and its interpretation by the original authors [170, 188] as well as in terms of our model (see Eq. (7.16)).

Within experimental precision, the data of Ref. [170] can be described by a quadratic dependence:

$$\ln f = g(\sigma) = C_0 + C_1\sigma + C_2\sigma^2. \tag{7.32}$$

Given that $\ln f$ is a linear function of the energy barrier associated with the formation of the gramicidin dimer, it is a sum of a chemical contribution, including, e.g., the energy involved in hydrogen bond formation, and of a contribution arising from membrane deformation due to the dimer (monomers do not deform the membrane) [170]. The latter contribution arises from the hydrophobic mismatch between the membrane and the dimer, and it depends on the applied tension σ, given that the membrane hydrophobic thickness depends on it (see Eq. (7.41) in Appendix A). Hence, expressing the deformation energy F of the membrane due to the presence of the dimer gives a theoretical expression for the σ-dependent part of $\ln f$. Quadratic elastic membrane models give a quadratic dependence of F on σ, in agreement with the form of Eq. (7.32). Comparing the experimental values of C_1 and C_2 to those predicted by theory provides a test for theoretical models [170].

Since the coefficients C_1 and C_2 can be described in terms of the elastic model (either that of Ref. [170] or ours), they are common to all vesicles. Conversely, the baseline C_0 depends on parameters such as the concentration of gramicidin molecules, so it can take a different value for each of the twelve vesicles studied in Ref. [170]. A global fit to the data of Ref. [170] using Eq. (7.32) involves minimizing

the goodness-of-fit function

$$\chi^2 = \sum_j (\ln f_j - g(\sigma_j))^2 \,, \tag{7.33}$$

where the index j runs over all the experimental points, with fitting parameters C_1, C_2, C_0^k, $k = 1, \ldots, 12$. The baseline C_0^k is then subtracted from each of the twelve curves. All the data is plotted in the same graph in Fig. 7.10. The best global fit, corresponding to $C_1 = 0.74 \pm 0.07\,\mathrm{m.mN^{-1}}$ and $C_2 = -0.09 \pm 0.015\,\mathrm{m^2.mN^{-2}}$, is shown on Fig. 7.10 as the dotted (black) line[7].

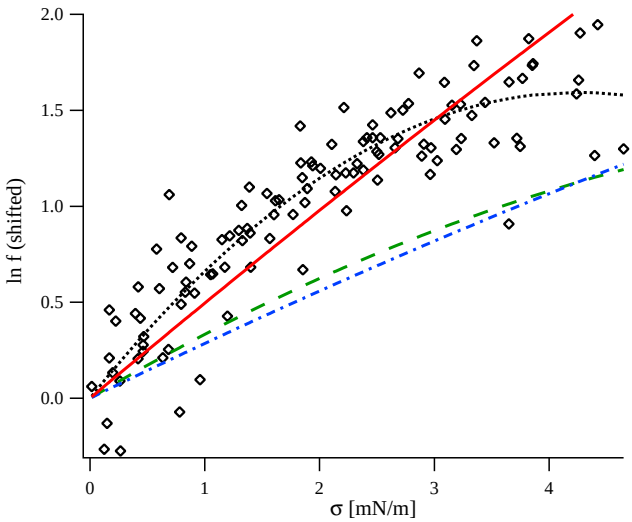

Figure 7.10: Formation rate f of gramicidin channels versus the applied tension σ. Diamonds: experimental data retrieved from Fig. 6b of Ref. [170], after subtraction of the baselines C_0^k. Dotted black line: best quadratic fit, with $C_1 = 0.74\,\mathrm{m.mN^{-1}}$ and $C_2 = -0.09\,\mathrm{m^2.mN^{-2}}$; $\chi^2_{\min} \equiv 1$. Dashed green line: results obtained from the elastic model of Ref. [188], with the constants given in [170]; $\chi^2 = 5.72$. Dashed-dotted blue line: *idem* with more recent values of the constants; $\chi^2 = 6.68$. Solid red line: results obtained by taking $s = 0$ and the recent values of the constants in the model of Refs. [172, 188]; $\chi^2 = 1.75$. The values of C_1 and C_2 corresponding to the curves on this graph are listed in Table 7.2.

In Ref. [170], the authors used published values of the material constants to calculate C_1 and C_2 in the framework of their elastic model [188], based on that of Ref. [172]. Using fixed-slope boundary conditions, they claimed good agreement with the experimental data for a reasonable value of the unknown slope s ($s = 0.3$). However, we need to raise the following points:

1. There was a mistake in their implementation of the formula of Ref. [188] giving

[7] It should be noted that the values obtained by fitting the individual curves are much more scattered: C_1 ranges from 0.4 to 1.5 $(\mathrm{mN/m})^{-1}$ and C_2 from -0.3 to 0 $(\mathrm{mN/m})^{-2}$.

C_1 and C_2 as a function of the material constants[8]. The actual values of C_1 and C_2 obtained using the same values of the constants as in Ref. [170] are in fact quite far from those corresponding to the best fit of the experimental data, as shown by the dashed green line in Fig. 7.10 (see also Fig. 7.11 and Table 7.2).

2. The estimates for the elastic constants used in Ref. [170] are somewhat different from more recent and more widely accepted values. Henceforth, we will use the following parameters, for a DOPC membrane: $d_0 = 2.7$ nm [170], $K_a = 265$ mN/m, $\kappa = 8.5 \times 10^{-20}$ J [34], $c_0 = -0.132$ nm^{-1} [199], and the dimensions of a gramicidin channel: $r_0 = 1$ nm, $\ell' = \ell + \delta = 2.3$ nm [170]. Implementing these more recent values in the model of Ref. [188] does not yield a better agreement with experiment, as shown by the dashed-dotted (blue) line in Figure 7.10 (see also Fig. 7.11 and Table 7.2).

A somewhat better agreement with the experimental data is obtained when taking $s = 0$ instead of $s = 0.3$ for the fixed slope (see Figs. 7.10, and 7.11 and Table 7.2). However, there is no physical justification for choosing $s = 0$ rather than $s = 0.3$. Besides, the downward inflection of the experimental curves at high σ is not adequately described for any value of s. In fact, C_2 is independent of s, and its absolute value given by the elastic model is 15 times smaller than the experimental one (see Table 7.2). We conclude that the elastic model of Refs. [172, 188] does not describe fully satisfactorily the data of Ref. [170] regarding the lifetime of the gramicidin channel under tension.

In Appendix C, Sec. 7.9.2, we calculate the deformation energy F in the framework of our model, both for the fixed-slope boundary condition and for the free-slope boundary condition. The resulting expressions of C_1 and C_2 are given in Appendix C, by Eqs. (7.66), (7.67), (7.72) and (7.73). In order to see which values of k'_a and which boundary conditions give the best agreement with the experiments of Ref. [170], we present a plot of the goodness-of-fit function χ^2 (see Eq. (7.33)) in a (C_1, C_2) graph in Fig. 7.11. On this graph, we have plotted the trajectories obtained from our model in the (C_1, C_2) plane when varying k'_a, for $s = 0$, for $s = 0.3$ and for the free-slope boundary condition.

In order to obtain numerical values of C_1 and C_2 from Eqs. (7.66), (7.67), (7.72) and (7.73), we used the above-mentioned parameter values, and the estimate $\bar{\kappa} = -0.8\kappa$ [183]. Finally, we estimated $c'_0\Sigma_0$ through the relation $c'_0\Sigma_0 = K_a\xi/\kappa$ (see Eq. (7.46) in Appendix A, Sec. 7.7.4). For this, the algebraic distance ξ from the neutral surface of a monolayer to the hydrophilic-hydrophobic interface of this monolayer was estimated by first determining the position of the pivot surface from the data of Ref. [199], and by calculating the distance between it and the neutral surface [200]: we found $\xi \approx -0.5$ Å. Here again, the neutral surface is close to the hydrophilic-hydrophobic interface. For the sake of simplicity, we took $c'_0 = 0$, and

[8] We found that a factor of 2 was missing in the expression of C_1 and a factor of 4 was missing in that of C_2 in the implementation of the formula of Ref. [188]. This was confirmed by Mark Goulian. We thank him for sharing a notebook containing some of the original calculations of Ref. [170] with us, and for email correspondence.

we checked that the results were not significantly different when taking $\xi = -0.5$ Å.

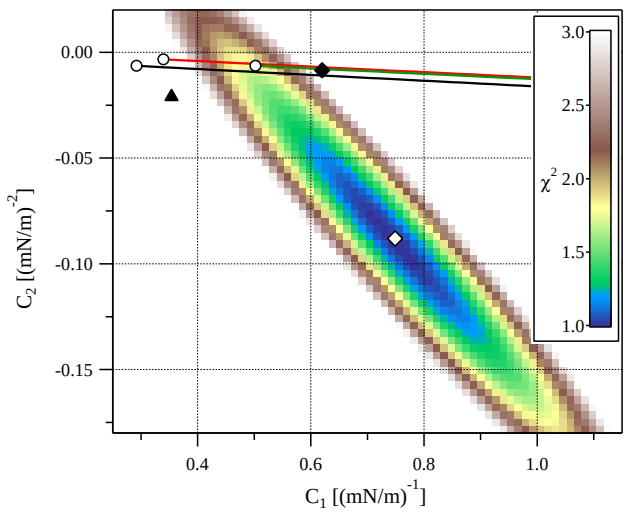

Figure 7.11: Colorscale: goodness-of-fit function χ^2 (see Eq. (7.33)) for the data of Ref. [170], as a function of the fitting parameters C_1 and C_2. White diamond: values of C_1 and C_2 that give the best fit. Black triangle: results obtained from the elastic model of Ref. [188], with the constants given in [170]. Lines: trajectories obtained from our model in the (C_1, C_2) plane when varying k'_a. Red: free slope; green: $s = 0$, black: $s = 0.3$. These three curves start by a white dot at $k'_a = 0$, and k'_a increases with C_1. The rightmost white dot ($k'_a = 0$, $s = 0$) roughly corresponds to the best agreement we can obtain between our model and the experiment fitted to the quadratic model (red curve on Fig. 7.10). The black diamond corresponds to the best agreement we can obtain between our model and the experiment fitted to the linear model at low tension (see Fig. 7.13).

The values of C_1 and C_2 corresponding to $k'_a = 0$ are very close to those obtained using the model of Ref. [170] with our values of the parameters, as shown in Table 7.2. This illustrates again that the influence of boundary terms is quantitatively small.

Model	Ref. [188]			Ours, with $k'_a = 0$		
Constants	Ref. [170]	Recent		Recent		
Slope s	0.3	0.3	0	0.3	0	Free
C_1 (10^{-3} m.mN^{-1})	354	282	480	292	502	339
$-C_2$ (10^{-6} m^2.mN^{-2})	21378	6108		6397		3343
χ^2	5.72	7.15	1.75	6.68	1.75	4.31

Table 7.2: Values of C_1 and C_2 obtained from the model of Ref. [188] and from our model with $k'_a = 0$, for the fixed-slope boundary condition (see Eqs. (7.66) and (7.67) in Appendix C), with slopes 0 and 0.3, and for the free-slope boundary condition (see Eqs. (7.72) and (7.73) in Appendix C). The corresponding values of χ^2 are also given. Recall that the best quadratic fit to the data of Ref. [170] yields $C_1 = 0.74\,\mathrm{m.mN^{-1}}$ and $C_2 = -0.09\,\mathrm{m^2.mN^{-2}}$ (see Fig. 7.10).

The ingredient in our model that can change significantly the results is k'_a. Fig. 7.11 shows that the experimental value of C_1 can be explained by our model. In addition, the values of k'_a that minimize χ^2, i.e., that give the best agreement with the experimental data of Ref. [170], are between 0 and 50 mN/m, depending on the boundary condition chosen, as shown in Fig. 7.12 and in Table 7.3. This range of values of k'_a is reasonable.

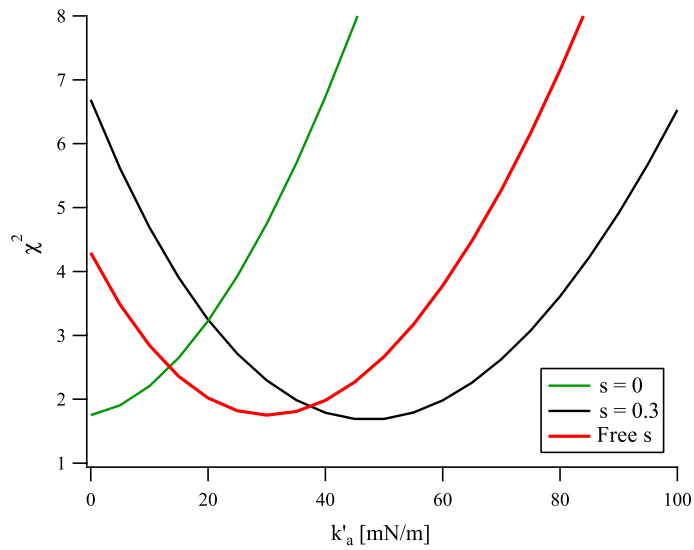

Figure 7.12: Goodness-of-fit function χ^2 (see Eq. (7.33)) for the data of Ref. [170], plotted as a function of k'_a within our model. These three curves can be viewed as cuts through the representation of χ^2 in the (C_1, C_2) plane shown in Fig. 7.11, along the three trajectories obtained from our model in the (C_1, C_2) plane when varying k'_a. Each curve corresponds to a different boundary condition; the colors are the same as in Fig. 7.11.

Slope s	0	0.3	Free
k'_a (mN.m^{-1})	0	45	30
C_1 (10^{-3} m.mN^{-1})	502	490	490
$-C_2$ (10^{-6} m^2.mN^{-2})	6397	9170	5290
χ^2	1.75	1.69	1.75

Table 7.3: Values of k'_a, C_1 and C_2 obtained from our model that yield the best agreement with the experimental results of Ref. [170], analyzed with a quadratic fit (see Eq. (7.32) and Fig. 7.10). Results are presented for the fixed-slope boundary condition (see Eqs. (7.66) and (7.67) in Appendix C), with slopes 0 and 0.3, and for the free-slope boundary condition (see Eqs. (7.72) and (7.73) in Appendix C).

However, the absolute values of C_2 we obtain remain much smaller than the one that matches best the experimental results, which is $C_2 = -0.09\,\mathrm{m}^2.\mathrm{mN}^{-2}$ (see Fig. 7.10). This can be seen in Fig. 7.11, as well as in Table 7.3. Hence, with our model, as with the one of Ref. [170], it seems impossible to explain the experimental value of C_2. Our model predicts that C_2 is proportional to the

effective spring constant H of the membrane discussed in the previous Section (see Eqs. (7.64) and (7.70)): it is thus quite unexpected to have a good agreement with the experimental values of H but not with those of C_2. This disagreement on C_2 could come either from a shortcoming of the model or from an undetected systematic error in the experimental data. The importance of C_2 is largest at highest tensions, as it is C_2 which gives the curve its concavity, and it should be noted that the maximum applied tension σ is around 4.5 mN/m in Ref. [170], which is comparable to the rupture threshold of $3 - 10$ mN/m [34]. The membrane properties may be affected at such high tensions in a way that is no longer well described by standard elastic models. It would be interesting to have more experimental data on the behavior of gramicidin channels under tension to see if this unexpected value of C_2 persists.

Following the hypothesis that high tensions are problematic, we conducted a linear fit of the data of Ref. [170], keeping only the points corresponding to $\sigma < 2$ mN/m: this yields $C_1 = (0.62 \pm 0.05)\,\mathrm{m.mN^{-1}}$ (see Fig. 7.13). In Table 7.4, we list, for each of the three usual boundary conditions, the value of k'_a which gives $C_1 = 0.62\,\mathrm{m.mN^{-1}}$, and the value of C_2 obtained from our model for this k'_a. These values correspond to those that give the best agreement between our model and the linear fit to the low-tension data of Ref. [170] presented in Fig. 7.13.

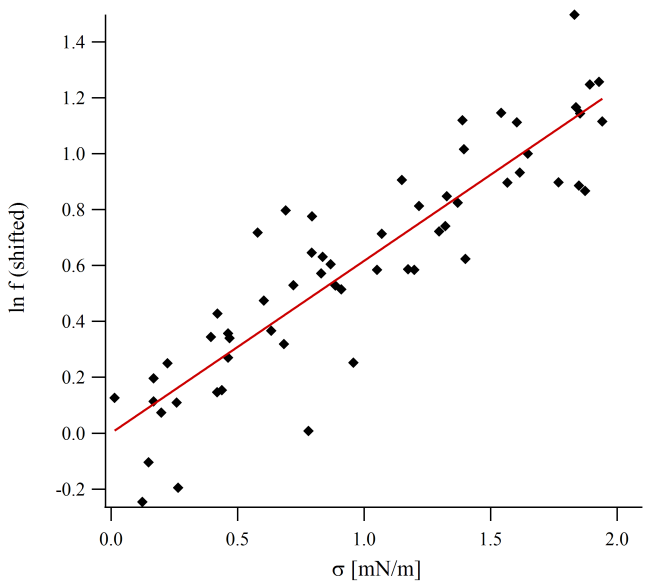

Figure 7.13: Formation rate f of gramicidin channels as a function of the applied tension σ, for $\sigma < 2$ mN/m. Diamonds: experimental data retrieved from Fig. 6b of Ref. [170], after subtraction of the baselines C_0^k (which are different from those of Fig. 7.10 since the fitting model is here linear instead of being quadratic). Line: best linear fit, yielding $C_1 = (0.62 \pm 0.05)\,\mathrm{m.mN^{-1}}$; correlation coefficient: $r = 0.894$.

Slope s	0	0.3	Free
k'_a (mN.m^{-1})	23	78	60
$-C_2$ (10^{-6} m^2.mN^{-2})	7896	10969	7042

Table 7.4: Values of k'_a and C_2 obtained from our model that yield the best agreement with the experimental results of Ref. [170] analyzed with the low-tension linear fit, i.e., that are associated with $C_1 = 0.62\,\mathrm{m.mN^{-1}}$. Results are presented for the fixed-slope boundary condition (see Eqs. (7.66) and (7.67) in Appendix C), with slopes 0 and 0.3, and for the free-slope boundary condition (see Eqs. (7.72) and (7.73) in Appendix C).

Our results show that for a fixed slope $s = 0$, the best agreement with the results of Ref. [170] analyzed with the complete quadratic fit is obtained for $k'_a = 0$. Conversely, for $s = 0.3$ and for the free-slope case, the best agreement is obtained for $k'_a \approx 40$ mN/m (see Table 7.3 and Fig. 7.11). This result is similar to that obtained in the previous Section, when analyzing the data of Ref. [171]: the conclusions on the value of k'_a seem to depend on the type of boundary condition that we choose. Here, we even observe a dependence on the value of the slope in the case of the fixed-slope boundary condition. Besides, if we only keep the low-tension data, as in Fig. 7.13, the values of k'_a that yield the best agreement with the experimental data are slightly higher, while remaining below 100 mN/m (see Table 7.4). These values are also boundary-condition–dependent.

Again, we may compare these values of k'_a to the other contribution to K'_a: here, $-\kappa_0(c_0 - c'_0\Sigma_0)/d_0 = -0.76\,\mathrm{mN/m}$. This is much smaller in absolute value than the estimates obtained from the numerical data of Ref. [183] and of Ref. [181]: here, as in the membranes studied in Ref. [171], the neutral surface of a monolayer and its hydrophilic-hydrophobic interface are very close, while ξ seemed to be of a few Å in the numerical simulations. This hints at a relevant difference between simulated membranes and real membranes. Besides, in the case of the free-slope boundary condition, our results imply that k'_a should be the dominant contribution to K'_a for the membranes studied in Ref. [170], as for those of Ref. [171].

As mentioned above, the free-slope boundary condition seems more satisfactory because one does not have to choose a specific slope, and also because the interactions between the membrane and the protein are very short-ranged, which means that the protein should not be able to impose a slope on our effective continuous profile that is not relevant at the Å scale. If we restrict ourselves to the free-slope boundary condition, our analyses of the numerical data of Ref. [183] and of Ref. [181], and our analyses of the experimental data of Ref. [171] and of Ref. [170] all converge toward a value of about a few tens of mN/m for k'_a, which is of the order of magnitude of the one expected if $k'_a = \gamma/2$. However, it is difficult to know what the real boundary conditions are.

7.6 Conclusion

We have put forward a modification of membrane elastic models used to describe thickness deformations at the nanoscale. We have shown that terms involving the gradient (and the Laplacian) of the area per lipid contribute to important terms of the effective Hamiltonian of the bilayer membrane. We have reanalyzed numerical and experimental data to find some signature of the presence of these terms. We have obtained consistent results showing that the term stemming from the gradient of the area per molecule has a prefactor k'_a of order 20 mN/m. This value is consistent with the idea that this terms corresponds to a contribution of the interfacial tension between water and the hydrocarbon-like hydrophobic part of the membrane. While this picture holds well for the "free-slope" boundary condition, the signature of our new term is less clear when the "fixed-slope" boundary condition is assumed instead.

Numerical simulations provide new insight in the nanoscale membrane behavior, and they enable to develop and to test more and more stringently theoretical models. For instance, models including lipid tilt have now been developed and compared with simulation results [23]. In particular, simulations should give important information on the effective boundary conditions that should be assumed in theoretical treatments. In works dealing with coarse-grained simulations, the authors favor "free-slope" boundary conditions [180, 181, 183]. Since the effective boundary condition at the protein boundary stems from the atomic-level protein-lipid interactions, it will be interesting to have data from all-atom simulations, as those described in Ref. [185].

Most of the practical applications of membrane elastic models regarding local thickness deformation and hydrophobic mismatch use the effective linear spring model [188, 192]. Thanks to this spring model, gramicidin is now widely used as a local probe of membrane properties, to investigate the influence of various molecules on membrane properties (see, e.g., Ref. [168]), among them new anticancer agents [201]. As other quadratic elastic models, our model results into an effective spring model, so it does not change such practical applications. However, the expressions of the spring constant from membrane elastic constants are modified in our model.

Besides, our analysis of the experimental data from Ref. [170] has shown that these nice experimental results were not as well understood as it was thought. Hence, it would be interesting to have more data regarding the behavior of gramicidin channels in membranes under tension.

Finally, it would be interesting to use our model to study the membrane-mediated interactions between gramicidin channels. The numerical results of Ref. [183] regarding these interactions are not explained satisfactorily by the elastic model with $k'_a = 0$, and the Landau-de Gennes model originally developed in Refs. [160, 177] tends to give a slightly better agreement with them, while fitting poorly the numerical profiles [183]: this is intriguing. From an experimental point of view, new data regarding the membrane-mediated interactions between gramicidin channels, obtained using X-ray scattering, is now available [202], which should motivate new comparisons with theory.

7.7 Appendix A: On our effective Hamiltonian

7.7.1 Link with the Helfrich Hamiltonian

Let us consider a membrane with a homogeneous thickness, equal to its equilibrium value d_0, so that $u = 0$: this membrane is simply characterized by its average shape h. In this case, we obtain at second order from Eq. (7.14)

$$f = \sigma \left[1 + \frac{(\boldsymbol{\nabla} h)^2}{2}\right] + \frac{\kappa}{2}(\nabla^2 h)^2 + \bar{\kappa}\det(\partial_i \partial_j h)\,, \tag{7.34}$$

which corresponds to the Helfrich Hamiltonian [24] for a membrane composed of two identical monolayers. Hence, in the homogeneous thickness case, our model restricts to the Helfrich model.

In particular, the term in σ has the standard form of a Helfrich tension term, conjugate to the actual area A of the membrane, since the element of area is $dA = dxdy\sqrt{1 + (\boldsymbol{\nabla} h)^2} = dxdy\,[1 + (\boldsymbol{\nabla} h)^2/2]$ to second order. Hence, σ can be viewed as an effective applied tension. This interpretation of σ is explained in more detail in Appendix A, Sec. 7.7.3.

7.7.2 Stability criterion

Let us focus on a membrane with flat average shape h, described by Eq. (7.16). Depending on the values of the constants K_a, K'_a and K''_a, a homogeneous thickness $u = 0$ can be less or more energetically favorable than an undulated shape. The physical situation we wish to describe is the one where the equilibrium state is the one with a homogeneous thickness.

To determine which sets of constants comply with this, let us calculate the effective Hamiltonian per unit projected area f_{def} of a membrane with harmonic undulations characterized by the wave vector q. In other words, let us perform a linear stability analysis. Neglecting boundary terms (by taking appropriate boundary conditions or by assuming that the undulations decay on some large length scale), we obtain

$$f_{\text{def}} \propto \frac{K_a}{d_0^2} + K'_a q^2 + K''_a q^4 \tag{7.35}$$

where the omitted prefactor is positive. The flat shape is favored if $f_{\text{def}} > 0$ for all q, and otherwise there exist some values of q for which it is unstable. We have $K_a > 0$ and $K''_a > 0$. Hence, the conditions for the stability of the flat shape is

$$K'_a > -2\frac{\sqrt{K_a K''_a}}{d_0}\,. \tag{7.36}$$

7.7.3 Membrane submitted to an external tension

We have derived the effective Hamiltonian of a bilayer membrane in the (μ, A_p) ensemble. This is the most convenient thermodynamic ensemble to work in. However,

in order to describe experiments where a vesicle is submitted to an external tension, one should work in the (N, τ) ensemble, where N is the number of lipids in the vesicle and τ is the externally applied tension. This is especially interesting in order to analyze the results of Ref. [170]. The ensemble change can be performed using a Legendre transformation: in the (N, τ) ensemble, the adapted effective Hamiltonian is $G(N, \tau) = F(\mu, A_p) + \mu N - \tau A_p$, where $F(\mu, A_p) = \int_{A_p} dxdy\, f$, with f expressed in Eq. (7.14), and

$$N = -\left.\frac{\partial F}{\partial \mu}\right|_{A_p}, \quad \tau = \left.\frac{\partial F}{\partial A_p}\right|_{\mu}. \tag{7.37}$$

Let us restrict to a homogeneous and flat membrane, i.e., to the case where h and u are constant. Then, using Eq. (7.37) to eliminate the variables μ and A_p from the expression of G, we obtain, to second order:

$$G(N, \tau) = N\,\frac{v}{d_0}\left[-\tau + \tau\frac{u}{d_0} + (K_a - 2\,\tau)\,\frac{u^2}{2\,d_0^2}\right]. \tag{7.38}$$

Minimizing G with respect to u yields the equilibrium excess thickness $u_{\rm eq}$ of the membrane at a given imposed tension τ. To first order, it reads

$$u_{\rm eq} = -\frac{\tau}{K_a}\,d_0\,, \tag{7.39}$$

Note that, since u/d_0 is assumed to be a first-order quantity, τ/K_a must be first-order too for our description to be valid for $u = u_{\rm eq}$. This property has been used to simplify the result in Eq. (7.39). In practice, $\tau \ll K_a$ is well verified, given that τ cannot exceed a few mN/m without the vesicle bursting, while K_a is of order 10^{-1} N/m. Since d_0 is the equilibrium hydrophobic thickness of this piece of homogeneous and flat membrane submitted to a vanishing external tension, it is consistent that $u_{\rm eq}$ vanishes when τ does, as u is the excess z-thickness with respect to d_0. Eq. (7.39) shows that the thickness of a membrane with fixed number of lipids decreases when the external tension increases, and is in agreement with Ref. [170].

We are now going to show that the constant σ in the (μ, A_p) ensemble (see, e.g., Eq. (7.14)) plays the part of an externally applied tension. For this, let us calculate the equilibrium thickness of a membrane patch with projected area A_p at a chemical potential μ, when it is homogeneous and flat. This amounts to minimizing f with respect to u. For a homogeneous and flat membrane, Eq. (7.14) becomes

$$f = \sigma\left(1 + \frac{u}{d_0}\right) + \frac{K_a}{2}\frac{u^2}{d_0^2}\,, \tag{7.40}$$

Minimizing f with respect to u then gives

$$u_{\rm eq} = -\frac{\sigma}{K_a}\,d_0\,. \tag{7.41}$$

Comparing Eq. (7.41) to Eq. (7.39) shows that σ plays the part of the externally applied tension τ. Hence, σ can be considered as an effective applied tension.

7.7.4 Estimating c_0'

Let us start from the effective Hamiltonian per molecule in monolayer + expressed in Eq. (7.1). All the quantities that are involved in this expression are defined on the hydrophobic-hydrophilic interface $\mathcal{S}$ of the monolayer.

Let us consider a surface $\mathcal{S}'$ parallel to $\mathcal{S}$, and let us call δ the algebraic distance from $\mathcal{S}'$ to $\mathcal{S}$. To second order, geometry gives [27]:

$$\Sigma' = \Sigma \left(1 + 2\,\delta\, H + \delta^2\, K\right) , \tag{7.42}$$

$$H' = H + \delta \left(K - 2\, H^2\right) , \tag{7.43}$$

$$K' = K\,. \tag{7.44}$$

Hence, we can rewrite f^+ using variables defined on $\mathcal{S}'$, to second order:

$$\begin{aligned} f^+ = {} & \frac{1}{2} f_0''(\Sigma' - \Sigma_0)^2 + f_1\, H' + (f_1' - 2\, f_0''\, \Sigma_0\, \delta)\, (\Sigma' - \Sigma_0)\, H' \\ & + \left(f_2 + 2 f_0''\, \Sigma_0^2\, \delta^2 - 2\, f_1'\, \Sigma_0\, \delta + 2\, f_1\, \delta\right) H'^2 + (f_K - f_1\, \delta)\, K' \\ & + \alpha\, (\boldsymbol{\nabla}\Sigma')^2 + \beta\, \nabla^2\Sigma' + \zeta\, (\nabla^2\Sigma')^2 - \mu\,, \end{aligned} \tag{7.45}$$

where we have neglected terms containing derivatives of order higher than two.

If $\mathcal{S}'$ is the neutral surface of the monolayer [27], by definition, the curvature and the area variations are decoupled, which entails $f_1' = 2\, f_0''\, \Sigma_0\, \xi$, where ξ denotes the algebraic distance from the neutral surface to the hydrophilic-hydrophobic interface of the monolayer. Hence, given that $f_0'' = K_a/(2\,\Sigma_0)$, $f_2 = \kappa_0\, \Sigma_0$, and $f_1'/f_2 = c_0'$ (see Sec. 7.2.2), we obtain

$$c_0' \Sigma_0 = \frac{K_a\, \xi}{\kappa_0}\,. \tag{7.46}$$

7.8 Appendix B: Numerical fluctuation spectra

Let us present in more detail our analysis of the fluctuation spectra obtained in the numerical simulations of Refs. [182–184]. In these studies, the variables considered are h and $t = u/2$. These works account for microscopic protrusion modes, occurring at the scale of a lipid molecule. Such modes are not described by our continuum theory. We include them assuming that they are decoupled from the larger-scale modes, following Ref. [180]. We fit the numerical data to the following formulas:

$$\left\langle |h(q)|^2 \right\rangle = k_{\mathrm{B}} T \left[\frac{1}{\kappa\, q^4} + \frac{1}{2\,(k_\lambda + \gamma_\lambda\, q^2)} \right] , \tag{7.47}$$

$$\left\langle |t(q)|^2 \right\rangle = k_{\mathrm{B}} T \left[\frac{1}{4\,(K_a/d_0^2 + K_a'\, q^2 + K_a''\, q^4)} + \frac{1}{2\,(k_\lambda + \gamma_\lambda\, q^2)} \right] . \tag{7.48}$$

In each of these two expressions, the first term corresponds to macroscopic modes described in our continuum theory: they are the spectra associated to the energy densities in Eq. (7.34) and Eq. (7.16), respectively, with $\sigma = 0$ given that the simulations are carried out at vanishing applied tension. The second term corresponds to microscopic protrusion modes, described as in Ref. [180].

We have carried out *simultaneous* fits of the height and thickness spectra to these formulas, using the method described in Ref. [180]. We have done this using two different assumptions:

(i) K_a'' and κ are independent constants. This corresponds to our model (see Eq. (7.22) in the case where $\beta = \zeta = 0$ and Eq. (7.18) in the most general version). Indeed, our model includes a difference between κ_0 and κ (see Eq. (7.15)), and in addition, k_a'' gives an additional contribution to K_a'' in the most general version, i.e., when $\zeta \neq 0$ (see Eq. 7.6).

(ii) $K_a'' = \kappa/4$. This corresponds to previous models [180, 183].

The spectra and the fitted functions are presented in Figs. 7.14, 7.15 and 7.16, and the obtained values of the fitting parameters are listed in Table 7.5.

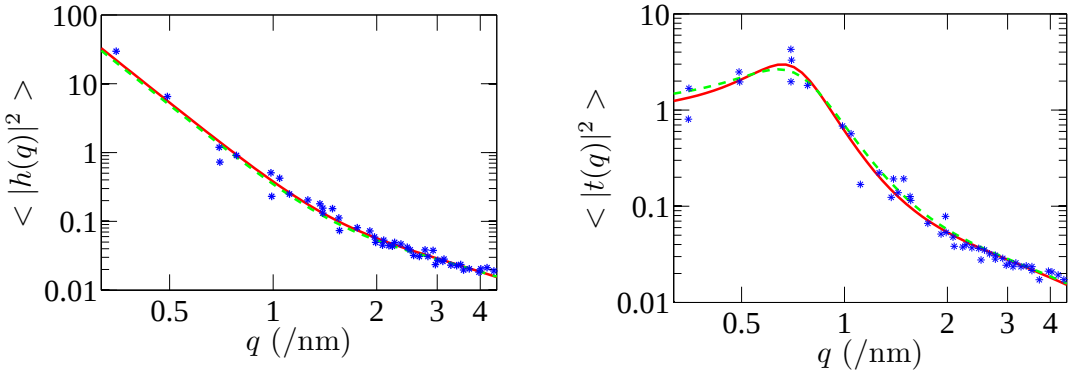

(a) Height fluctuation spectrum. **(b)** Thickness fluctuation spectrum.

Figure 7.14: Spectra corresponding to Ref. [182]: atomistic simulation of a DPPC membrane. Blue stars: numerical data. Plain red line: fit with $K_a'' \neq \kappa/4$ (case (i)). Dashed green line: fit with $K_a'' = \kappa/4$ (case (ii)).

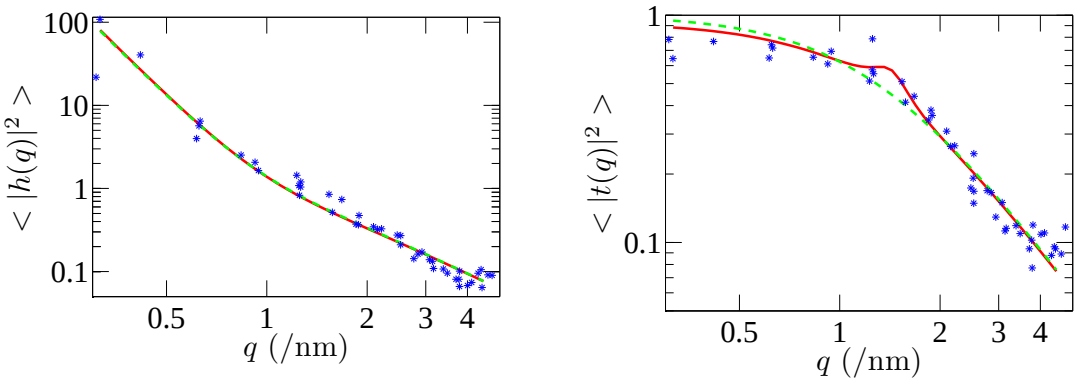

(a) Height fluctuation spectrum. **(b)** Thickness fluctuation spectrum.

Figure 7.15: Spectra corresponding to Ref. [184]: atomistic simulation of a GMO (glycerolmonoolein) membrane. Same notations as in Fig. 7.14.

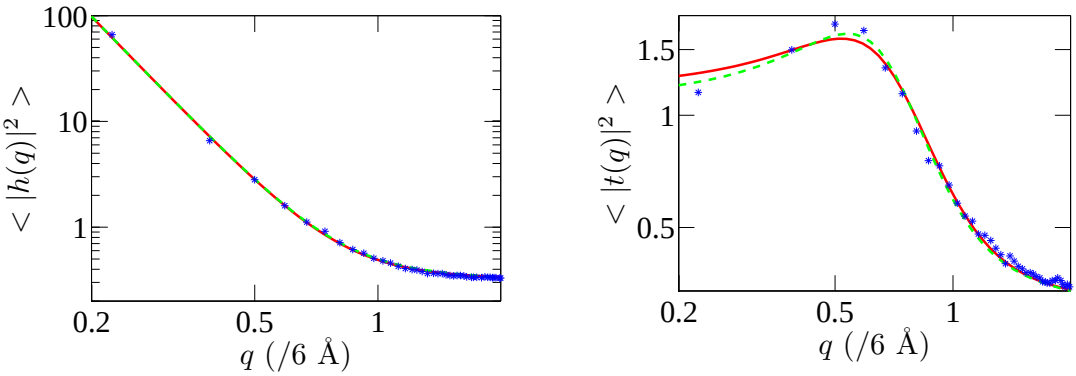

(a) Height fluctuation spectrum. **(b)** Thickness fluctuation spectrum.

Figure 7.16: Spectra corresponding to Ref. [183]: coarse-grained simulation, reproducing roughly the behaviour of DPPC. Same notations as in Fig. 7.14.

Data and assumptions	κ (10^{-20} J)	$4\ K''_a$ (10^{-20} J)	K_a (N/m)	$4\ K'_a$ (N/m)	k_λ (10^{16} J/m^4)	γ_λ (N/m)
[182]; $K''_a \neq \kappa/4$ (i)	**4.19**	**6.21**	**0.042**	**-0.0538**	**11.9**	**1.75 10^{-2}**
−	3.46	2.80	-0.045	-0.0807	5.21	9.59 10^{-3}
+	5.04	8.37	0.057	0.0128	18.3	2.19 10^{-2}
[182]; $K''_a = \kappa/4$ (ii)	**4.55**		**0.033**	**-0.0372**	**13.8**	**1.61 10^{-2}**
−	3.54		-0.060	-0.0414	10.1	1.11 10^{-2}
+	5.07		0.034	0.0197	17.9	1.87 10^{-2}
[184]; $K''_a \neq \kappa/4$ (i)	**5.20**	**70.3**	**6.8**	**-2.79**	**2.26**	**1.28 10^{-2}**
−	3.54	10.6	1.3	-5.88	1.93	1.22 10^{-2}
+	7.52	145	13.8	-1.01	2.69	1.34 10^{-2}
[184]; $K''_a = \kappa/4$ (ii)	**5.33**		**7.9**	**0.74**	**2.09**	**1.28 10^{-2}**
−	3.68		0.8	-0.24	1.80	1.22 10^{-2}
+	5.99		9.9	2.19	2.80	1.33 10^{-2}
[183]; $K''_a \neq \kappa/4$ (i)	**2.32**	**1.89**	**0.105**	**-0.0283**	**4.12**	**1.21 10^{-4}**
−	2.14	1.19	0.047	-0.0330	4.03	-6.10 10^{-5}
+	2.34	2.07	0.112	-0.0825	4.28	2.02 10^{-4}
[183]; $K''_a = \kappa/4$ (ii)	**2.31**		**0.118**	**-0.0374**	**3.98**	**2.48 10^{-4}**
−	2.22		0.109	-0.0392	3.82	-4.00 10^{-6}
+	2.43		0.121	-0.0351	4.14	4.02 10^{-4}

Table 7.5: Parameters extracted from the fits of the different numerical spectra represented in Figs. 7.14, 7.15 and 7.16. For each data set, we indicate the values of the fit parameters (lines in bold) and the bounds of the 95% confidence intervals calculated using the method explained in Ref. [180] (lines labeled '+' and '−'), both in case (i), i.e., for $K''_a \neq \kappa/4$ (6 fit parameters) and in case (ii), i.e., for $K''_a = \kappa/4$ (5 fit parameters).

It can be seen on Figs. 7.14, 7.15 and 7.16 that there is very little difference between the fits corresponding to cases (i) and (ii). Moreover, Table 7.5 shows that the values we find for K''_a and $\kappa/4$ in case (i), i.e., when they are treated as independent constants, are very close to each other, and to the result obtained in case (ii), in the three data sets analyzed. Hence, the effect of the difference between κ_0 and κ (and of k''_a) seems negligible. Besides, Table 7.5 shows that we obtain $K'_a < 0$,

which corresponds to the fact that the thickness spectra are non-monotonous (see Figs. 7.14, 7.15 and 7.16). We have checked that all the values obtained for K'_a comply with the stability condition Eq. (7.36) presented in Appendix A.

7.9 Appendix C: Membrane containing a cylindrical mismatched protein

In this Section, we write down explicitly the equilibrium shape and the deformation energy of a membrane which contains a single cylindrical transmembrane protein with a hydrophobic mismatch (see Fig. 7.3). This protein can correspond to a gramicidin channel in the dimer state. We focus on a membrane with a flat average shape, described by the effective Hamiltonian per unit projected area in Eq. (7.16). We denote the radius of the protein by r_0, and its hydrophobic thickness by ℓ. We take the center of the cylindrical protein as the origin of the frame, which yields cylindrical symmetry.

In order to treat the case where the membrane is submitted to a tension σ, we rewrite Eq. (7.16) in terms of the variable $\tilde{u} = u + \sigma d_0/K_a = t^+ + t^- - d_{\rm eq}(\sigma)$, which represents the excess thickness relative to the equilibrium thickness $d_{\rm eq}(\sigma) = d_0(1 - \sigma/K_a)$ of the bilayer at an applied tension σ (see Eq. (7.41)). It yields

$$f = \frac{K_a}{2\,d_0^2}\,\tilde{u}^2 + \frac{K'_a}{2}\,(\boldsymbol{\nabla}\tilde{u})^2 + \frac{K''_a}{2}\,(\nabla^2\tilde{u})^2 + A_1\,\nabla^2\tilde{u} + A_2\,\boldsymbol{\nabla}\cdot(\tilde{u}\boldsymbol{\nabla}\tilde{u}) + \frac{\bar{\kappa}}{4}\,\det(\partial_i\partial_j\tilde{u})\,. \tag{7.49}$$

7.9.1 Equilibrium thickness profile

Let us first review (see, e.g., Ref. [188]) the equilibrium thickness profile $\tilde{u}$ of the membrane containing the mismatched protein. This equilibrium shape is solution to the Euler-Lagrange equation associated with the effective Hamiltonian in Eq. (7.49),

$$\nabla^4\tilde{u} - \frac{K'_a}{K''_a}\nabla^2\tilde{u} + \frac{K_a}{K''_a d_0^2}\tilde{u} = 0\,. \tag{7.50}$$

Using the cylindrical symmetry of the problem and choosing solutions that vanish at infinity, we obtain, if the stability condition Eq. (7.36) is verified, the following solution to the Euler-Lagrange equation Eq. (7.50):

$$\tilde{u}(r) = A_+ K_0(k_+ r) + A_- K_0(k_- r)\,, \tag{7.51}$$

where K_n is the $n^{\rm th}$-order modified Bessel function of the second kind, and

$$k_\pm = \frac{1}{\sqrt{2}}\left\{-\frac{K'_a}{K''_a} \pm \left[\left(\frac{K'_a}{K''_a}\right)^2 - 4\frac{K_a}{K''_a d_0^2}\right]^{1/2}\right\}^{1/2}\,, \tag{7.52}$$

which are either both real or complex conjugate. The integration constants $A_\pm$ are determined by the boundary conditions in $r = r_0$.

a. Fixed slope

In the case where the boundary conditions in $r = r_0$ are

$$\begin{cases} \tilde{u}(r_0) = \tilde{u}_0 = \ell - d_0 \left(1 - \dfrac{\sigma}{K_a}\right) \\ \tilde{u}'(r_0) = s \end{cases} , \tag{7.53}$$

which corresponds to a strong hydrophobic coupling and a fixed slope s at $r = r_0$, we obtain:

$$A_\pm = \frac{K_0^\mp s + k_\mp K_1^\mp \tilde{u}_0}{k_\mp K_0^\pm K_1^\mp - k_\pm K_0^\mp K_1^\pm} , \tag{7.54}$$

where

$$K_n^\pm = K_n \left(k_\pm r_0\right) . \tag{7.55}$$

Note that A_+ and A_- are either both real or complex conjugate (like $k_\pm$), which ensures that the solution Eq. (7.51) is real.

b. Free slope

An alternative choice of boundary conditions in $r = r_0$ is

$$\begin{cases} \tilde{u}(r_0) = \tilde{u}_0 = \ell - d_0 \left(1 - \dfrac{\sigma}{K_a}\right) \\ \left(K_a'' \nabla^2 \tilde{u} + \dfrac{\bar{\kappa}}{4} \dfrac{\tilde{u}'}{r} + A_2 \tilde{u} + A_1\right)(r = r_0) = 0 \end{cases} . \tag{7.56}$$

The first of these conditions corresponds to a strong hydrophobic coupling, as before. The second one arises from minimizing the total effective Hamiltonian of the system without further constraints. It corresponds to the case where the slope at $r = r_0$ is free to adjust itself to yield the smallest deformation energy. With these "free-slope" boundary conditions, we obtain:

$$A_\pm = \pm \frac{\bar{\kappa}\, k_\mp K_1^\mp \tilde{u}_0 - 4 r_0 K_0^\mp \left[A_1 + \left(A_2 + K_a'' k_\mp^2\right) \tilde{u}_0\right]}{4 r_0 K_a'' \left(k_+^2 - k_-^2\right) K_0^+ K_0^- - \bar{\kappa} \left(k_+ K_0^- K_1^+ - k_- K_0^+ K_1^-\right)} , \tag{7.57}$$

which are, again, either both real or complex conjugate.

Let us now assume that $\beta = \zeta = 0$, as in the main text of this Chapter. In order to understand the impact of k_a' (i.e., of α) on $A_\pm$, let us express these coefficients as a function of k_a', r_0, d_0 and of the bulk constants K_a, K_a' and K_a'', whose values can be extracted from the fluctuation spectra in simulations. Using Eq. (7.52), the relation $A_1 = 2K_a'' c_0$, which can be derived from Eqs. (7.24) and (7.22), and the relation $A_2 = (k_a' - K_a')/2$, which stems from Eqs. (7.21) and (7.24), we obtain:

$$A_\pm = \pm \frac{\bar{\kappa}\, k_\mp K_1^\mp \tilde{u}_0 - 2 r_0 K_0^\mp \left\{4 K_a'' c_0 + \left[k_a' \pm K_a'' \left(k_-^2 - k_+^2\right)\right] \tilde{u}_0\right\}}{4 r_0 K_a'' \left(k_+^2 - k_-^2\right) K_0^+ K_0^- - \bar{\kappa} \left(k_+ K_0^- K_1^+ - k_- K_0^+ K_1^-\right)} . \tag{7.58}$$

For fixed values of r_0, d_0, K_a, K'_a and K''_a, the constants $A_\pm$ can be viewed simply as functions of k'_a and c_0: let us denote them by $A_\pm(k'_a, c_0)$. The following relation holds for all k'_a and c_0:

$$A_\pm\left(k'_a, c_0\right) = A_\pm\left(0, \tilde{c}_0\right) \,, \tag{7.59}$$

with

$$\tilde{c}_0 = c_0 + \frac{k'_a}{4K''_a}\tilde{u}_0 \,. \tag{7.60}$$

Hence, in the framework of a model that assumes $k'_a = 0$, the effect of a nonzero k'_a on the equilibrium membrane thickness profile would be that c_0 is replaced by a renormalized spontaneous curvature $\tilde{c}_0$, which depends linearly on $\tilde{u}_0$. At vanishing applied tension (in which case, $\tilde{u}_0 = u_0$), and neglecting the difference between $\kappa_0 = K''_a/4$ and κ, we obtain Eq. (7.30).

7.9.2 Deformation energy

Let us now calculate the deformation energy F of the membrane due to the presence of the mismatched protein. For the equilibrium shape of the membrane, which is solution to the Euler-Lagrange equation Eq. (7.50), the bulk energetic terms in Eq. (7.49) give a vanishing contribution, and we are left only with the boundary terms. In addition, sufficiently far away from the gramicidin channel, the deformation $\tilde{u}$ caused by the presence of the mismatched channel vanishes, so the only relevant boundary terms are those in $r = r_0$. We can write

$$\begin{aligned} F &= \int_{A_p} dxdy\, f = 2\pi \int_{r_0}^{\infty} r dr\, f \\ &= \pi \Bigg\{ K''_a\, r \left[\tilde{u}\, \frac{d}{dr}\left(\nabla^2 \tilde{u}\right) - \tilde{u}'\, \nabla^2 \tilde{u} - \frac{K'_a}{K''_a}\, \tilde{u}\, \tilde{u}' \right] \\ &\quad - 2\left[A_1\, r\, \tilde{u}' + A_2\, r\, \tilde{u}\, \tilde{u}' + \frac{\bar{\kappa}}{8}\, \tilde{u}'^2 \right] \Bigg\} \Bigg|_{r=r_0} \,, \end{aligned} \tag{7.61}$$

where $\tilde{u}' = d\tilde{u}/dr$. We have used the expression of the Gaussian curvature for small deformations in a system with cylindrical symmetry: $\det(\partial_i \partial_j \tilde{u}) = \tilde{u}'\tilde{u}''/r = (2\,r)^{-1}\, d(\tilde{u}'^2)/dr$. To express the deformation energy F explicitly, one has to use the boundary conditions in $r = r_0$.

a. Fixed slope

For the boundary conditions in Eq. (7.53), corresponding to a fixed slope in r_0, using Eqs. (7.51), (7.52) and (7.54), we can rewrite the deformation energy of the

membrane in Eq. (7.61) as

$$
\begin{aligned}
F = &-2\pi \left[A_1\, r_0\, s + A_2\, r_0\, \tilde{u}_0\, s + \frac{\bar{\kappa}}{8}\, s^2 \right] \\
&+ \frac{\pi\, r_0\, K_a''}{k_+ K_0^- K_1^+ - k_- K_0^+ K_1^-} \Big[k_+ k_- \left(k_+^2 - k_-^2 \right) K_1^+ K_1^- \tilde{u}_0^2 \\
&+ 2\, k_+ k_- \left(k_+ K_0^+ K_1^- - k_- K_0^- K_1^+ \right) \tilde{u}_0\, s + K_0^+ K_0^- \left(k_+^2 - k_-^2 \right) s^2 \Big] \,. \qquad (7.62)
\end{aligned}
$$

This expression shows that F is a second-order polynomial in $\tilde{u}_0$ and s.

Spring constant for $s = 0$. In the particular case where the fixed slope s vanishes, Eq. (7.62) becomes

$$F = H_0 \tilde{u}_0^2 \,, \qquad (7.63)$$

where the effective spring constant reads

$$H_0 = \frac{\pi\, r_0\, K_a''\, k_+ k_- \left(k_+^2 - k_-^2 \right) K_1^+ K_1^-}{k_+ K_0^- K_1^+ - k_- K_0^+ K_1^-} \,. \qquad (7.64)$$

Dependence on applied tension. Since $\tilde{u}_0 = \ell - d_0(1 - \sigma/K_a)$, Eq. (7.62) shows that F is a second-order polynomial in the applied tension σ. Thus, we can write

$$-\frac{F}{k_\mathrm{B} T} = C_0 + C_1 \sigma + C_2 \sigma^2 \,, \qquad (7.65)$$

with

$$
\begin{aligned}
C_1 = &\frac{2\pi d_0 r_0\, K_a''\, k_+ k_-}{k_\mathrm{B} T\, K_a \left(k_- K_0^+ K_1^- - k_+ K_0^- K_1^+ \right)} \Big[\left(k_+ K_0^+ K_1^- - k_- K_0^- K_1^+ \right) s \\
&+ \left(k_+^2 - k_-^2 \right) K_1^- K_1^+ \left(d_0 - \ell \right) \Big] + \frac{2\pi d_0 r_0}{k_\mathrm{B} T\, K_a}\, s A_2 \,, \qquad (7.66) \\
C_2 = &-\frac{d_0^2}{K_a^2} \frac{H_0}{k_\mathrm{B} T} \,, \qquad (7.67)
\end{aligned}
$$

where H_0 is the effective spring constant expressed in Eq. (7.64). Note that $\bar{\kappa}$ and A_1 do not appear in the coefficients C_1 and C_2, and that A_2 and s are only present in C_1.

b. Free slope

For the boundary conditions in Eq. (7.56), corresponding to a free slope in r_0, using Eqs. (7.51), (7.52) and (7.57), we can rewrite the deformation energy of the membrane (see Eq. (7.61)) as

$$\begin{aligned} F = & \frac{\pi r_0}{\bar{\kappa}\left(k_+ K_0^- K_1^+ - k_- K_0^+ K_1^-\right) - 4 r_0 K_a''\left(k_+^2 - k_-^2\right) K_0^+ K_0^-} \times \\ & \Bigg\{ \Big[4 r_0 \Big(k_+ K_0^- K_1^+ \left(A_2 + K_a'' k_-^2\right)^2 - k_- K_0^+ K_1^- \left(A_2 + K_a'' k_+^2\right)^2 \Big) \\ & + K_a'' \bar{\kappa}\left(k_+^2 - k_-^2\right) k_+ k_- K_1^+ K_1^- \Big] \tilde{u}_0^2 \\ & + 8 A_1 r_0 \Big[K_a'' k_- k_+ \left(k_- K_0^- K_1^+ - k_+ K_0^+ K_1^-\right) \\ & + A_2 \left(k_+ K_0^- K_1^+ - k_- K_0^+ K_1^-\right) \Big] \tilde{u}_0 + 4 A_1^2 r_0 \left(k_+ K_0^- K_1^+ - k_- K_0^+ K_1^-\right) \Bigg\} \end{aligned} \tag{7.68}$$

This expression shows that F is a second-order polynomial in $\tilde{u}_0$.

Spring constant. Eq. (7.68) can be expressed as

$$F = H_f \left(\tilde{u}_0 - \tilde{u}_0^{\min}\right)^2 + F^{\min}, \tag{7.69}$$

where the effective spring constant reads

$$\begin{aligned} H_f = & \frac{\pi r_0}{\bar{\kappa}\left(k_+ K_0^- K_1^+ - k_- K_0^+ K_1^-\right) - 4 r_0 K_a''\left(k_+^2 - k_-^2\right) K_0^+ K_0^-} \times \\ & \Big[4 r_0 \Big(k_+ K_0^- K_1^+ \left(A_2 + K_a'' k_-^2\right)^2 - k_- K_0^+ K_1^- \left(A_2 + K_a'' k_+^2\right)^2 \Big) \\ & + K_a'' \bar{\kappa}\left(k_+^2 - k_-^2\right) k_+ k_- K_1^+ K_1^- \Big], \end{aligned} \tag{7.70}$$

while $\tilde{u}_0^{\min}$ denotes the value of $\tilde{u}_0$ that minimizes F, and $F^{\min}$ is the minimum of F, obtained for $\tilde{u}_0 = \tilde{u}_0^{\min}$. Both $\tilde{u}_0^{\min}$ and $F^{\min}$ are nonzero if $A_1 \neq 0$ (see Eq. (7.68)), due to the spontaneous curvature of each monolayer.

Dependence on applied tension. Since $\tilde{u}_0 = \ell - d_0(1 - \sigma/K_a)$, Eq. (7.68) shows that F is a second-order polynomial in the applied tension σ. Thus, we can write

$$-\frac{F}{k_{\mathrm{B}} T} = C_0 + C_1 \sigma + C_2 \sigma^2, \tag{7.71}$$

with

$$C_1 = \frac{-2\pi r_0 d_0}{k_\mathrm{B}T\,K_a\left[\bar{\kappa}\left(k_+K_0^-K_1^+ - k_-K_0^+K_1^-\right) - 4r_0K_a''\left(k_+^2 - k_-^2\right)K_0^+K_0^-\right]}\times$$
$$\Bigg\{4A_1r_0\Big[K_a''k_-k_+\left(k_-K_0^-K_1^+ - k_+K_0^+K_1^-\right)$$
$$+ A_2\left(k_+K_0^-K_1^+ - k_-K_0^+K_1^-\right)\Big] + \Big[4r_0\Big(k_+K_0^-K_1^+\left(A_2 + K_a''k_-^2\right)^2$$
$$- k_-K_0^+K_1^-\left(A_2 + K_a''k_+^2\right)^2\Big) + K_a''\bar{\kappa}\left(k_+^2 - k_-^2\right)k_+k_-K_1^+K_1^-\Big](\ell - d_0)\Bigg\} \tag{7.72}$$

$$C_2 = -\frac{d_0^2}{K_a^2}\frac{H_f}{k_\mathrm{B}T}\,, \tag{7.73}$$

where H_f is the effective spring constant expressed in Eq. (7.70).

Part III

Dynamics of a membrane submitted to a local chemical modification

Chapter 8

Context: Local modification of the environment of a membrane

Contents

8.1 Introduction **179**

8.2 Experimental studies **180**

8.2.1 Microinjection experiments on GUVs 180

8.2.2 Local pH change close to a membrane 181

8.2.3 Dynamical local change versus static global change 183

8.3 Theory of local modifications of membranes **184**

8.3.1 The basis: membrane dynamics 184

8.3.2 Application to local membrane perturbations 187

8.4 Outline of Part III **188**

8.1 Introduction

In Parts I and II of this thesis, we presented studies about the interplay between the lipid bilayer membrane and the inclusions within it. Part I focused on long-range membrane-mediated interactions arising between rigid inclusions that impose local constraints on the membrane shape. Part II dealt with local thickness deformations of the membrane, which occur in the vicinity of many integral membrane proteins, due to hydrophobic mismatch.

Apart from inclusions, other factors can induce local perturbations of biological membranes. During cell life, membranes are subjected to an inhomogeneous and variable environment, which can be strongly coupled to biological processes. For instance, bacteria move along concentration gradients of some substances, e.g., glucose, in a process called chemotaxis [203]. In multicellular organisms, communication between cells involves local concentration gradients, e.g., in paracrine signaling.

Although these biological processes are generally complex and involve specific membrane receptors and signaling pathways within the cell, local concentration gradients can also directly affect the lipid bilayer membrane.

In Part III of this thesis, we will be concerned with the response of a lipid bilayer membrane to a local perturbation of its environment. In order to account for local inhomogeneities of membrane properties, we will have to go beyond the Helfrich model (see Sec. 1.3.2) and the area-difference elasticity (ADE) model (see Sec. 1.3.3), in a similar way as in Part II, where we investigated local modifications of the bilayer thickness. Although we focused on the effect of mismatched proteins in Part II while we will study local chemical modifications of the environment in Part III, both parts deal with local perturbations of lipid bilayer membranes. While in Part II, we investigated nanoscale perturbations, we will now be concerned with micron-scale ones.

8.2 Experimental studies

8.2.1 Microinjection experiments on GUVs

In order to understand the response of a pure lipid bilayer membrane to local changes of its environment, experiments are conducted on giant unilamellar vesicles (GUVs). These model membranes are made of amphiphilic lipid molecules that self-assemble into closed bilayers in water (see Sec. 1.2.3). Since their sizes and curvatures are similar to those of living cells and since their lipid bilayer membrane exhibits the basic properties of biological membranes, they are very attractive objects to study the physics of cellular phenomena. Although lacking membrane proteins and a cytoskeleton, they have been used as a minimal cell model to mimic various biological processes such as membrane budding and endocytosis, fusion and fission, transport phenomena across the membrane, lipid domain formation, etc. [204–209]. In addition, the fact that GUVs are pure lipid bilayers makes them ideal to test theoretical descriptions of membranes.

The radius of a GUV can reach 10 to 100 μm. It is thus possible to conduct controlled experiments on an individual GUV, obtaining data while exposing this vesicle to mechanical, biochemical, or chemical perturbations [210–213]. In particular, chemical perturbations can be created close to the membrane of a GUV by local injection from a micropipette. Such experiments were first described in 1996 by Wick, Angelova, Walde and Luisi [210]: a snake venom enzyme, phospholipase A2, was microinjected locally in the vicinity of individual GUVs, which made them burst. Subsequently, in 1999, Angelova, Hristova and Tsoneva investigated the effect of microinjecting DNA on GUVs, showing that endocytosis could occur if a specific bioactive molecule, sphingosine, is present in the membrane at sufficient concentration [211]. Locally injecting a reagent close to a membrane can thus yield various responses of the membrane, depending on the way this reagent interacts with the membrane lipids and on the injection conditions.

8.2.2 Local pH change close to a membrane

In the following, we will be mostly interested in local modifications of the pH close to a GUV, obtained by microinjection. Indeed, this case is simpler to understand than those involving enzymatic reactions or macromolecules, and it is also biologically relevant. When the pH on the membrane is modified, a diffusion-governed chemical equilibrium occurs between the membrane lipid headgroups and the protons or hydroxide ions that are microinjected.

a. Biological context: pH inhomogeneities in cell life

Local pH inhomogeneities at the cellular scale are ubiquitous and especially important. For instance, in various types of migrating cells, an actively generated intracellular pH gradient exists along the axis of movement, and it appears to be essential for cell migration [214]. The local intracellular pH in migrating cells was measured in Ref. [214] using a fluorescent pH indicator (see Fig. 8.1). The effect of an extracellular pH gradient on cell migration and morphology has also been demonstrated in the case of human melanoma cells [215].

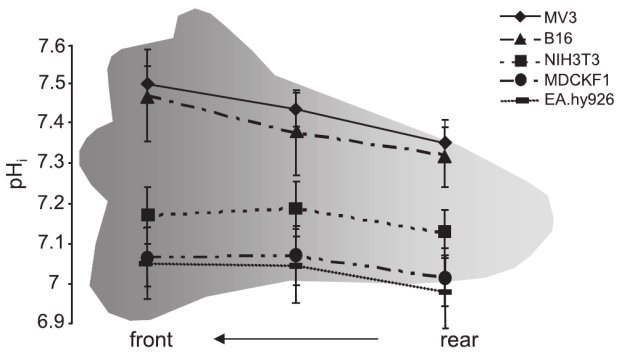

Figure 8.1: Results of local measurements of intracellular pH in migrating cells of five different cell lines (corresponding to the five different symbol types on the graph) [214]. *Illustration reproduced from Ref. [214].*

Local pH is also of great importance in mitochondria. The H^+–ATP synthase enzymes that synthesize adenosine triphosphate (ATP), the cell's fuel, are powered by the local pH difference across the inner membrane of mitochondria. Both the proton pumps that maintain actively this pH difference and the enzymes that use it are located in dynamic membrane invaginations called cristae, where pH heterogeneities are thought to be especially important [216]. The localization of the H^+–ATP synthase enzymes in the membranes of the cristae is shown in Fig. 8.2.

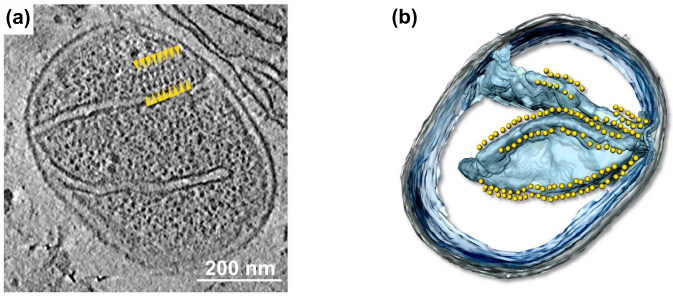

Figure 8.2: Whole mitochondrion observed using cryoelectron tomography, i.e., three-dimensional reconstruction from two-dimensional tilted images obtained using transmission electron microscopy at cryogenic temperature. (a) Tomographic slice. (b) Three-dimensional reconstitution. The invaginations correspond to cristae. The H^+–ATP synthase enzymes is shown in yellow [216]. *Illustration reproduced from Ref. [216].*

b. Local modification of the pH close to a GUV

In 2008, in Ref. [213], Khalifat, Puff, Bonneau, Fournier and Angelova reported experiments where an acidic solution is microinjected close to a GUV. Local inward deformations of the GUV membrane were observed when it contained negatively charged lipids. In particular, when the membrane composition included cardiolipin[1], a lipid with four hydrophobic chains that is specific of the inner membrane of mitochondria, dynamical cristae-like invaginations were observed, as shown on Fig. 8.3. Hence, membrane shape is tightly coupled to local pH inhomogeneities.

The narrow tubular connections in cristae are thought to slow down proton diffusion away from the cristae: hence, this shape might locally increase the pH difference across the inner membrane of mitochondria [217, 218]. The study of Ref. [213] shows that localized pH gradients could in turn stabilize the crista shape. Thus, this structure, which optimizes ATP synthesis, could self-maintain [213].

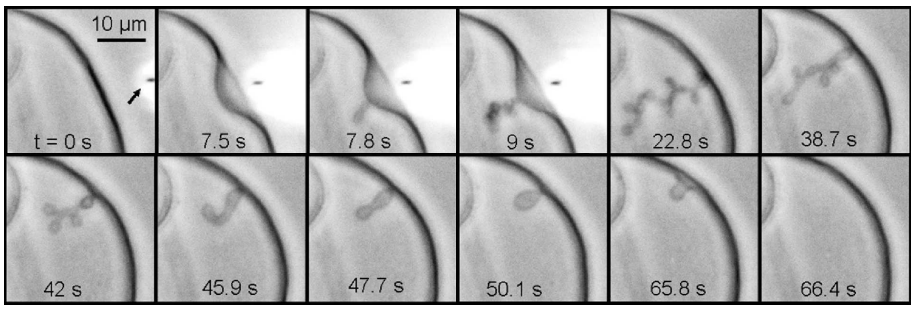

Figure 8.3: Snapshots of a microinjection of a chlorhydric acid solution (pH 1.8) close to a GUV composed of PC/PE/cardiolipin 60:30:10 mol/mol in a buffer at pH 8. The arrow in the first frame indicates the position of the micropipette tip. Cristae-like invaginations appear close to this tip, and the deformation fully relaxes when the injection is stopped (frames from 22.8 s) [213]. *Illustration reproduced from Ref. [213].*

[1]Cardiolipin features two hydroxyl groups, which can be protonated or not depending on the pH conditions. At pH 8, which is the buffer pH in Ref. [213], cardiolipin is negatively charged.

In 2009, in Ref. [219], Fournier, Khalifat, Puff and Angelova described experiments where a basic solution is microinjected close to a GUV. In this case, membrane deformations also occur, but in the opposite direction, i.e., outwards. There can be two phases in the membrane response. First, a smooth outward deformation develops. Then, if the concentration of the basic solution is high enough and the distance between the membrane and the micropipette small enough, a very thin tubule appears, and its length grows exponentially in the direction of the micropipette [219]. These two phases are visible on Fig. 8.4. The membrane of the GUVs used in Ref. [219] were composed of phosphatidylcholine (PC) and phosphatidylserine (PS)[2]. Note that PS is negatively charged at neutral pH.

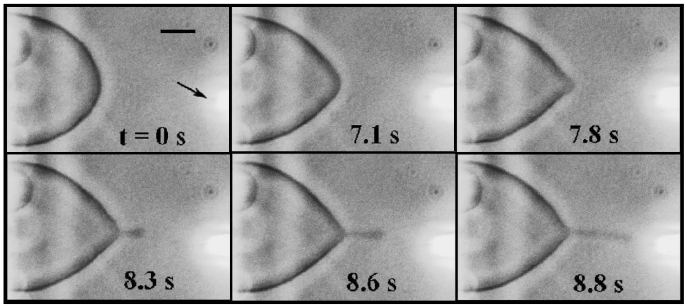

Figure 8.4: Snapshots of a microinjection of a sodium hydroxide solution (pH 13) close to a GUV composed of PC/PS 90:10 mol/mol in a buffer at pH 7.4. The arrow in the first frame indicates the position of the micropipette tip, and the scale bar represents 10 μm. The GUV deforms (frames 7.1–7.8 s) and a tubule appears and grows (frames 8.3–8.8 s) [219]. *Illustrations reproduced from Ref. [219].*

8.2.3 Dynamical local change versus static global change

The response of a vesicle to a static and uniform modification of its environment is well described by the area-difference elasticity (ADE) model presented in Sec. 1.3.3. The equilibrium shape of the vesicle changes when its environment is modified, as the values of the reduced volume v and of the combined quantity $\overline{\Delta a_0}$, which involves the spontaneous curvature and the preferred area difference between the two monolayers (see Sec. 1.3.3), change.

In 1999, Lee, Petrov and Döbereiner studied the equilibrium shape of a pure phosphatidylcholine (PC) GUV as a function of the external pH [220]. For this, the solution surrounding the GUVs was progressively replaced by a solution of different pH. The inside of the GUV can be considered unchanged during this process, given the low permeability of the lipid membrane to ions. Hence, different pH asymmetries between the inside and the outside of the membrane were obtained. It was found that increasing the external pH induced shape transitions toward outward curved shapes, whereas lowering it led to inward curved shapes, as shown in Fig. 8.5. In

[2]In Ref. [213], microinjection of chlorhydric acid was also performed on GUVs composed of PC/PS 90:10 mol/mol, and inward deformations were observed, but they were less pronounced than in membranes containing cardiolipin, and did not feature the characteristic cristae-like shapes.

light of the ADE model, and given that no visible change of the area or of the volume of the GUV occurred, which implies that v was constant, the authors interpreted this as a variation of $\overline{\Delta a_0}$ with the pH. More precisely, the cause of the shape variations was attributed to a change of the spontaneous curvature of the membrane, under the assumption that the preferred area per lipid was not modified [220]. While this assumption is a standard one in such studies [221, 222], it is not validated by any experimental proof, and the ADE model does not allow for distinguishing a change of the spontaneous curvature from a change of the preferred area difference.

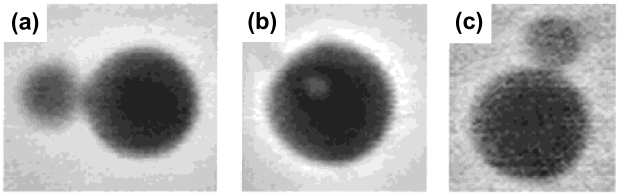

Figure 8.5: Successive snapshots of a single PC GUV (with radius about 3 μm) under different conditions of external pH. The equilibrium shape of the GUV changes as the external pH is modified. (a): pH = 10.1; budded shape. (b): pH = 5.5; stomatocyte shape. (c): pH = 10.1; the initial budded shape is reestablished [220]. *Illustrations reproduced from Ref. [220].*

There is a qualitative link between the membrane response to the static and global pH changes of Ref. [220] and the dynamical and local pH changes of Refs. [213, 219]: in both cases, the membrane tends to deform outwards when the external pH is increased and inwards when it is decreased. However, the theoretical description of the local and dynamical deformations described in Refs. [213, 219] is far more complex than the interpretation of the results of Ref. [220]. Indeed, as membrane properties can feature heterogeneities due to the local perturbation, a global theory such as the ADE model is no longer sufficient, and one must develop a local version of the ADE model. In addition, local modifications are intrinsically dynamical, as a local concentration heterogeneity will decay due to diffusion. Hence, a full dynamical description of the membrane is required. Let us now briefly review the studies that have been conducted in this direction.

8.3 Theory of local modifications of membranes

8.3.1 The basis: membrane dynamics

a. Description by Brochard and Lennon

In 1975, Brochard and Lennon investigated the dynamical flicker of red blood cells, a scintillation phenomenon observed under the microscope, which arises from thickness changes of the flat red blood cell [223]. They showed that these thickness changes were caused by thermal fluctuations of the membrane shape[3]. Using the Helfrich

[3]Many previous interpretations were based on the idea that the flicker is due to the red blood cell being a living cell, i.e., that it is related to active biological processes [223].

model [24] to describe the energetics of membrane shape changes (see Sec. 1.3.2), they elaborated a description of the dynamics of these changes.

They worked on small deformations of the membrane with respect to the flat shape, and they described the membrane in the Monge gauge, by its height $h(\boldsymbol{r})$, $\boldsymbol{r} = (x, y)$ with respect to the reference plane (x, y). They wrote a normal force balance involving the normal elastic force density in the membrane, obtained from a functional differentiation of the Helfrich Hamiltonian H (Eq. (1.6) with $c_0 = 0$, and discarding the Gaussian curvature contribution): $-\delta H/\delta h(\boldsymbol{r}) = -\kappa\nabla^4 h(\boldsymbol{r})$, and the viscous stress exerted by the cytoplasm on the membrane. The flow in the cytoplasm was described using Stokes' equation and assuming incompressibility. This flow results from the membrane deformations, and is related to it through boundary conditions, namely the continuity of velocity at the cytoplasm-membrane interface [223]. In the case of a red blood cell, the viscosity of the cytoplasm is much higher than that of the external fluid, and thus the viscous stress of the external fluid was neglected in Ref. [223]. However, in the case of a vesicle, it must also be accounted for.

The description of Ref. [223], adapted to the symmetric case where the fluid above and below the quasi-flat membrane are identical, yields the relaxation rate

$$\gamma = \frac{\kappa q^3}{4\eta}\,, \tag{8.1}$$

for a plane wave with wave vector of norm q deforming a membrane [224]. In this formula, κ is the bending rigidity of the membrane (see Eq. (1.6)), while η is the viscosity of the fluid that surrounds the membrane. Qualitatively, if the membrane deforms, it relaxes due to the bending rigidity κ, but the relaxation is slowed down by the viscosity η of the surrounding fluid, yielding the relaxation rate γ.

b. Description by Seifert and Langer

The description of membrane dynamics by Brochard and Lennon was based on the Helfrich model, in which the membrane is treated as a single surface. However, when the membrane curves, one monolayer locally stretches while the other is locally compressed. The resulting density heterogeneities within each monolayer relax by lateral lipid flow, since each monolayer is a two-dimensional fluid. From the late 1980s, Evans and coworkers stressed the importance of the coupling between bending and relative compression in membrane dynamics [225], and of the friction between the two monolayers of the membrane [226, 227]. This friction is crucial when the two monolayers move with respect to another, e.g., when a tether (i.e., a tubule) is pulled from the membrane by mechanical means [228].

In order to describe such effects, a membrane model including lipid density heterogeneities is needed. This corresponds in fact to a local version of the ADE model: while the ADE model involves the total area of each monolayer, which is sufficient as far as statics is concerned, a dynamical description needs to account for the local density in each monolayer. Such a model was presented in 1993 by Seifert and Langer, in Ref. [224]. Considering a membrane composed of two identical

monolayers, they wrote the following effective Hamiltonian:

$$H = \int_A dA \left[\frac{\kappa}{2} c^2 + \frac{k}{2} \left(r^+ + ec\right)^2 + \frac{k}{2} \left(r^- - ec\right)^2 \right], \tag{8.2}$$

where A is the area of the membrane measured on the midlayer $\mathcal{S}$ between the two monolayers (see Fig. 8.6), while c denotes the curvature of the membrane defined on $\mathcal{S}$, and $r^\pm = (\rho^\pm - \rho_0)/\rho_0$ represents the scaled two-dimensional lipid density in monolayer $\pm$, defined on $\mathcal{S}$ too, ρ_0 being a reference density. The constant κ is the bending rigidity of the membrane, while k is its stretching modulus[4], and e denotes the distance between $\mathcal{S}$ and the neutral surface $\mathcal{N}^\pm$ of monolayer $\pm$ [27, 229] (see Fig. 8.6). By definition, the neutral surface of a monolayer is the surface where the stretching and bending modes of the monolayer are decoupled [27]. Since $\mathcal{S}$ and $\mathcal{N}^\pm$ are parallel, the scaled density on $\mathcal{N}^\pm$ reads $r_n^\pm = r \pm ec + \mathcal{O}(e^2c^2)$: if F is written as a function of $r_n^\pm$ and c, it features no coupling between these variables.

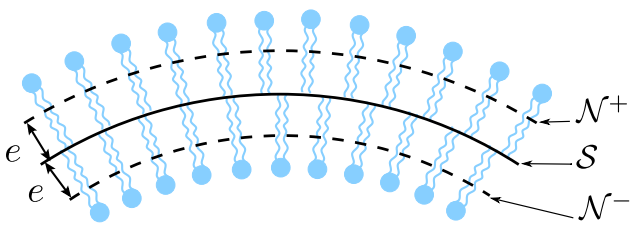

Figure 8.6: Two-dimensional sketch of a lipid bilayer composed of two identical monolayers. The curvature c and the scaled density $r^\pm$ of monolayer $\pm$ are defined on $\mathcal{S}$. The distance between $\mathcal{S}$ and the neutral surface $\mathcal{N}^\pm$ of monolayer $\pm$ is denoted by e. If the orientation convention is chosen in such a way that $c < 0$ on the drawing, the densities on $\mathcal{N}^\pm$ are $r_n^\pm = r^\pm \pm ec + \mathcal{O}(e^2c^2)$.

The approach taken in Ref. [224] to describe membrane dynamics is similar as in Ref. [223], except that the starting point is the effective Hamiltonian H in Eq. (8.2) instead of being the Helfrich Hamiltonian. Small deformations of the membrane with respect to the flat shape are considered, and the membrane is described by its height $h(\boldsymbol{r})$ with respect to the reference plane. The normal force balance involves the normal elastic force density in the membrane $-\delta H/\delta h(\boldsymbol{r})$ and the normal viscous stress exerted by the fluid above and below the membrane. In this description, a tangential force balance within each monolayer has to be accounted for as well. It involves the tangential viscous stress of the surrounding fluid, the "in-plane gradient of the surface pressure" $-\boldsymbol{\nabla}(\delta H/\delta r^\pm(\boldsymbol{r}))$, the viscous stress associated with the two-dimensional lipid flow, and finally, a term of intermonolayer friction, which reads $\mp b(\boldsymbol{v}^+ - \boldsymbol{v}^-)$, where b denotes the intermonolayer friction coefficient, while $\boldsymbol{v}^\pm$ is the in-plane velocity of the lipids in monolayer $\pm$.

Combining these equations and using mass conservation within each monolayer, Seifert and Langer obtained a system of linear differential equations coupling the

[4]The constant k corresponds to the one which was noted K_a in Part II.

in-plane Fourier transform of the height of the membrane to that of the antisymmetric density $r_a = r^+ - r^-$ [224]. Two relaxation rates are obtained from these equations. In particular, for modes of large wavelengths[5], these relaxation rates can be approximated by

$$\gamma_1 = \frac{kq^2}{2b}\,, \tag{8.3}$$

$$\gamma_2 = \frac{\kappa q^3}{4\eta}\,, \tag{8.4}$$

where q denotes the wave vector norm, while η is the viscosity of the fluid that surrounds the membrane. In this regime, γ_2 corresponds to a pure bending mode, and it is identical as Eq. (8.1), while γ_1 involves intermonolayer friction. Qualitatively, perturbations of the antisymmetric density relax due to the stretching modulus k, but this relaxation is slowed down by intermonolayer friction, which is characterized by b, yielding γ_1. Meanwhile, as above, shape deformations relax due to the bending rigidity, and the relaxation is slowed down by the viscosity of the surrounding fluid, yielding γ_2. Note that this qualitative view, which separates the two effects, is very simplified. A generic local perturbation of the membrane involves both a deformation and an antisymmetric density change, and the two relaxation mechanisms are coupled. In addition, the general expressions of the relaxation rates are more complicated than the above-mentioned large-wavelength asymptotic expressions (see Ref. [224]).

In Ref. [224], Seifert and Langer used their model successfully to analyze the dynamical fluctuation spectra of bilayer membranes. This model constitutes the basis of the studies of the dynamics of local chemical modifications of a membrane.

8.3.2 Application to local membrane perturbations

a. Study by Sens

In 2004, Sens investigated the deformation of a membrane resulting from a local and sudden flip of some lipids from one monolayer to the other in an initially flat membrane [230]. His aim was to describe the formation of a spherical bud due to the local asymmetry of the density between the two monolayers created by the flip. Sens started from Seifert and Langer's effective Hamiltonian, Eq. (8.2). In order to describe a spherical bud, the usual quasi-flat approximation is not sufficient. Given the difficulty of a full nonlinear treatment of large deformations, Sens restricted his study to the case where the perturbed zone of the membrane has a spherical cap shape and a uniform density asymmetry [230].

This approach showed that transient budding can occur due to the local density asymmetry, before this density asymmetry finally relaxes with a diffusive behavior. In addition, it was shown that the conversion of the initial density asymmetry into

[5] More precisely, the expressions in Eqs. (8.3) and (8.4) are valid if $q \ll 2\eta k/[b(\kappa + 2ke^2)]$, which typically corresponds to wavelengths larger than a few microns.

a budding deformation is optimized if the length scale of the initial perturbation is of order be^2/η, which typically corresponds to one micron [230].

b. Study by Fournier *et al.*

In 2009, in Ref. [219], Fournier, Khalifat, Puff and Angelova proposed a theoretical description of their experiments where a basic solution is microinjected close to a GUV. They started from a membrane effective Hamiltonian similar to that of Seifert and Langer, Eq. (8.2), to which they added the effect of membrane tension. They considered that the local lipid chemical modification of the external monolayer, which arises from the microinjection, modifies the preferred area per lipid [219]. This yields a local asymmetry between the two monolayers. This situation is reminiscent of that studied in Ref. [230], but the asymmetry has a different origin.

Focusing on the regime of small deformations with respect to the flat shape, they adapted Seifert and Langer's approach to write the dynamical equations. They investigated the relaxation dynamics of an instantaneous chemical modification of the external monolayer involving only one wavelength. They found that, due to intermonolayer friction, the asymmetry between the two monolayers yields a transient deformation before it relaxes through lateral redistribution of the lipids, i.e., monolayer expansion [219].

In addition, they discussed the threshold of tubule formation, and they interpreted the subsequent growth of the tubule as arising from a Marangoni effect. Indeed, the pH gradient on the membrane, which is due to the local injection of the basic solution, can induce a tension gradient. They deduced an exponential law for the tubule growth, which matches very well the experimental data [219].

8.4 Outline of Part III

Part III is in the continuity of Refs. [213, 219]. It is the result of a close collaboration with the experimental group of Miglena I. Angelova and Nicolas Puff, and it contains experimental results together with a theoretical description.

Chapter 9 presents the bases of our theoretical description. We start by showing that the generic effect of a chemical modification on a monolayer is twofold: both the equilibrium density and the spontaneous curvature are changed. We then derive the equations of linear membrane dynamics from first principles, following the same lines as Seifert and Langer [224], and adapting their description to a chemically modified membrane. In our dynamical equations, we use a general expression of the elastic force density in the membrane, which is valid for monolayers with density and composition heterogeneities. The calculation of this force density, and of the stress tensor from which it derives, is exposed at the end of this Part, in Chapter 12, as it is somewhat technical. In Chapter 9, we also present a calculation of the fraction of the chemically modified lipids in the membrane that arises from the local injection of a reagent above the membrane.

In Chapter 10, we compare the predictions of the theoretical description presented in Chapter 9 to new experimental results corresponding to brief and local

microinjections of a basic solution close to a GUV, in the regime of small deformations. In this work, we aim at describing the experimental situation as closely as possible. In particular, we take into account the time-dependent profile of the reagent concentration due to diffusion in the solution above the membrane. We obtain good agreement between theory and experiment.

In Chapter 11, we investigate theoretically the effect of a continuous local injection of a reagent on a membrane. We show that the effect of the evolution of the reagent concentration profile on the dynamics of the membrane becomes negligible after some time. It then becomes possible to extract interesting properties of the membrane response to the chemical modification. We find that a local density asymmetry between the two monolayers relaxes by spreading diffusively in the whole membrane. We show how the ratio of the spontaneous curvature change to the equilibrium density change induced by the chemical modification can be extracted from the dynamics of the membrane deformation. This ratio cannot be deduced from the study of global and static modifications of the environment of a membrane (see Sec. 8.2.3).

Finally, as mentioned above, Chapter 12 is devoted to the derivation of a fundamental tool: the stress tensor of a membrane monolayer of variable shape, variable lipid density and variable composition. We construct a Hamiltonian density for one and two-component monolayers, which is shown to be a local version of the ADE model, and we derive the associated stress tensor, using the principle of virtual work.

Chapter 9

Theoretical description of the dynamics of a membrane submitted to a local chemical modification

Contents

9.1 Introduction **192**

9.2 Effective Hamiltonian of a monolayer **192**

9.2.1 In the absence of chemical modification 192

9.2.2 Chemically modified monolayer 193

9.2.3 Effect of the chemical modification 194

9.3 Force densities in the membrane **195**

9.3.1 Expression of the force densities 195

9.3.2 Spontaneous curvature change versus equilibrium density change 196

9.4 Membrane dynamics **199**

9.4.1 Hydrodynamics of the surrounding fluid 199

9.4.2 Dynamical equations for the membrane 200

9.4.3 Relaxation rates for large wavelengths 202

9.5 Profile of the fraction of the chemically modified lipids **203**

9.6 Resolution of the dynamical equations **205**

9.7 Conclusion **206**

9.1 Introduction

In this Chapter, we present the bases of our description of the dynamics of a membrane submitted to a local chemical modification. Chapters 10 and 11 build upon this description. We first write down the Hamiltonian density in each monolayer in a local version of the area-difference elasticity membrane model. We show that the generic effect of a chemical modification on a monolayer is twofold: both the equilibrium density and the spontaneous curvature are changed. We then express the elastic force density in the chemically modified membrane. Using this force density, we derive linear dynamical equations for a chemically modified membrane, which generalize those of Ref. [224]. We also present a calculation of the fraction of the chemically modified lipids in the membrane that arises from the local injection of a reagent above the membrane. Finally, we explain how our dynamical equations can be solved in the case of a local injection of a reagent above the membrane.

Part of the work presented in this Chapter has been published in: A.-F. Bitbol, J.-B. Fournier, M. I. Angelova and N. Puff, *Dynamical membrane curvature instability controlled by intermonolayer friction*, Journal of Physics: Condensed Matter 23, 284102 (2011), cited as Ref. [231] here. The rest, together with the work presented in Chapter 11, is the subject of an article currently under review: A.-F. Bitbol and J.-B. Fournier, *Membrane properties revealed by spatiotemporal response to a local inhomogeneity* (2012).

9.2 Effective Hamiltonian of a monolayer

9.2.1 In the absence of chemical modification

Our description of the bilayer membrane is based on a local version of the area-difference elasticity membrane model [224, 232]. Before the chemical modification, the local state of monolayer $\pm$ is described by two variables: the total curvature c defined on the membrane midlayer, which is common to both monolayers, and the scaled two-dimensional lipid density $r^{\pm} = (\rho^{\pm} - \rho_0)/\rho_0$, defined on the midlayer of the membrane, ρ_0 being a reference density. The sign convention for the curvature is chosen in such a way that a spherical vesicle has $c < 0$. The outer monolayer corresponds to monolayer $+$, while the inner one corresponds to monolayer $-$.

We write the effective Hamiltonian $f^{\pm}$ per unit area in monolayer $\pm$ as:

$$f^{\pm} = \frac{\sigma_0}{2} + \frac{\kappa}{4}c^2 \pm \frac{\kappa c_0}{2}c + \frac{k}{2}\left(r^{\pm} \pm ec\right)^2 , \tag{9.1}$$

where σ_0 represents the tension of the bilayer and κ its bending modulus, while k is the stretching modulus of a monolayer, and e denotes the distance between the neutral surface [27] of a monolayer and the midsurface of the bilayer. As we assume that the two monolayers of the membrane are identical before the chemical modification, these constants are the same for both monolayers. The two monolayers have opposite spontaneous curvature constants, noted $\mp c_0$, since their lipids are oriented in opposite directions.

The expression for $f^{\pm}$ in Eq. (9.1) corresponds to a general second-order expansion in the small variables $r^{\pm}$ and ec, around the reference state which corresponds to a flat membrane with uniform density $\rho^{\pm} = \rho_0$. It is valid for small deformations around this reference state: $r^{\pm} = \mathcal{O}(\epsilon)$ and $ec = \mathcal{O}(\epsilon)$, where ϵ is a small nondimensional parameter. The construction of the Hamiltonian density Eq. (9.1) is explained in detail in Sec. 12.3.1-a. Writing the monolayer effective Hamiltonian as a second-order expansion in the curvature and the local stretching[1] is reminiscent of Chapter 7 (see Eq. (7.1)). However, the gradient terms that were investigated in Chapter 7 are discarded here, because we now restrict to length scales much larger than the correlation length of the density fluctuations, which should not exceed the monolayer thickness (far from a critical point). In the present Part, we focus on micron-scale phenomena and not on nanoscale ones.

Note that Eq. (9.1) does not include any Gaussian curvature contribution. Indeed, we will remain at fixed topology, which implies that this contribution is constant[2]. In Sec. 12.3.2, we show explicitly that the Hamiltonian densities in Eq. (9.1) give back the ADE model after minimization with respect to $r^{\pm}$: our model is a local version of the ADE model, which extends it to the case of inhomogeneous densities.

The effective Hamiltonian H of the bilayer membrane reads

$$H = \int_A dA \left(f^+ + f^-\right) = \int_A dA \left[\sigma_0 + \frac{\kappa}{2}c^2 + \frac{k}{2}\left(r^+ + ec\right)^2 + \frac{k}{2}\left(r^- - ec\right)^2\right] , \quad (9.2)$$

which is consistent with Seifert and Langer's model [224] (see Eq. (8.2)). Note that here, we have taken into account the effect of the membrane tension σ_0, which was not implemented in Ref. [224].

9.2.2 Chemically modified monolayer

Let us now focus on the way the membrane effective Hamiltonian is affected by the local chemical modification. We consider that the reagent source, which corresponds to the micropipette tip in an experiment, is localized in the fluid that surrounds the vesicle. Besides, membrane permeation and flip-flop are neglected given their long timescales. Hence, the chemical modification only affects the outer monolayer, i.e., monolayer +, and not the inner one.

Let us denote by ϕ the mass fraction of the lipids of the upper monolayer that are chemically modified, and let us assume that the reagent concentration remains

[1] This stretching can be represented equivalently by the relative variation of the two-dimensional lipid density ρ (as here), or by that of the area per lipid molecule Σ (as in Chapter 7): these two variables are related by $\rho = m/\Sigma$, where m is the mass of a lipid.

[2] The Gaussian bending rigidity $\bar{\kappa}$ may be locally affected by the chemical modification. The Gauss-Bonnet theorem implies that $\int_A dA\, c_1 c_2$ depends only on topology, where $c_1 c_2$ is the Gaussian curvature of the membrane. *A priori*, with an inhomogeneous $\bar{\kappa}$, this does not imply that the contribution $\int_A dA\, \bar{\kappa}\, c_1 c_2$ to the effective Hamiltonian of the membrane is constant. However, the effect of the inhomogeneity of $\bar{\kappa}$ would be third-order. Hence, the contribution of the Gaussian curvature can safely be discarded throughout, even for heterogeneous membranes.

small enough to have $\phi = \mathcal{O}(\epsilon)$. We thus have to include this third small variable in our second-order expansion of f^+. We obtain

$$\begin{aligned} f^+ &= \frac{\sigma_0}{2} + \sigma_1\phi + \frac{\sigma_2}{2}\phi^2 + \tilde{\sigma}\left(1 + r^+\right)\phi\ln\phi + \frac{\kappa}{4}c^2 \\ &\quad + \frac{\kappa}{2}\left(c_0 + \tilde{c}_0\phi\right)c + \frac{k}{2}\left(r^+ + ec\right)^2 , \end{aligned} \tag{9.3}$$

where the constants σ_1, σ_2, and $\tilde{c}_0$ describe the response of the membrane to the chemical modification. These constants depend on the reagent that is injected. Besides, the non-analytical mixing entropy term $\tilde{\sigma}\left(1 + r^+\right)\phi\ln\phi$ (see, e.g., Ref. [233]) has been added to our second-order expansion.

The construction of the Hamiltonian density Eq. (9.3) is explained in detail in Sec. 12.3.1-b.

9.2.3 Effect of the chemical modification

Let us now investigate the physical effect of the chemical modification on monolayer +. For this, we study how the equilibrium state of the monolayer described by the Hamiltonian density Eq. (9.3) is affected by the presence of a nonzero ϕ.

For a homogeneous monolayer (e.g., monolayer +) with constant mass, the spontaneous curvature and the equilibrium density can be obtained by minimizing the Hamiltonian per unit mass f^+/ρ^+ with respect to r^+ and c. First, the minimization with respect to r^+ gives, to first order in ϵ:

$$r^+_{\text{eq}} = \frac{\sigma_0}{2\,k} + \frac{\sigma_1\phi}{k} - ec\,. \tag{9.4}$$

Then, the minimization with respect to c yields[3] to first order, using Eq. (9.4):

$$c_{\text{eq}} = -c_0 - \bar{c}_0\phi - \frac{\sigma_0 e}{\kappa}\,, \tag{9.5}$$

where we have introduced

$$\bar{c}_0 = \tilde{c}_0 + \frac{2\sigma_1 e}{\kappa}\,. \tag{9.6}$$

Note that, since we assume that $r^+ = \mathcal{O}(\epsilon)$ and $ec = \mathcal{O}(\epsilon)$, we must have $c_0 e = \mathcal{O}(\epsilon)$ and $\sigma_0/k = \mathcal{O}(\epsilon)$ for our description to be valid for the values of r^+ and c that minimize f^+/ρ^+. This property has been used to simplify the results of the minimization.

The scaled lipid density r^+_n on the neutral surface of the monolayer is related to r^+ through $r^+_n = r^+ + ec$ to first order. This relation arises from the geometry of

[3] One might wonder why the spontaneous curvature c_{eq} found by minimization in Eq. (9.5) is not simply $-c_0$ for $\phi = 0$. This is due to the fact that we work on the membrane midsurface, which is more convenient to study the membrane dynamics. If the monolayer effective Hamiltonian had been originally written using variables and constants defined on the neutral surface, then the spontaneous curvature found by minimization would correspond exactly to the constant c_0^n that plays the part of c_0 when everything is defined on the neutral surface.

parallel surfaces [27], given that the membrane midlayer and the monolayer neutral surface are parallel surfaces separated by a distance e. Hence, Eq. (9.4) can be rewritten as

$$r^{+}_{n,\,\mathrm{eq}} = \frac{\sigma_0}{2\,k} + \frac{\sigma_1 \phi}{k}\,. \tag{9.7}$$

This result is independent of the curvature c, contrary to that in Eq. (9.4). Indeed, by definition, on the neutral surface, curvature and density are decoupled [27], while these two variables are coupled on other surfaces.

Eq. (9.7) shows that, due to the chemical modification, the scaled equilibrium density on the neutral surface of monolayer + is changed by the amount

$$\delta r^{+}_{n,\,\mathrm{eq}} = r^{+}_{n,\,\mathrm{eq}}(\phi) - r^{+}_{n,\,\mathrm{eq}}(0) = \frac{\sigma_1 \phi}{k} \tag{9.8}$$

to first order. Besides, Eq. (9.5) indicates that the spontaneous curvature of monolayer + is changed by the amount

$$\delta c_{\mathrm{eq}} = c_{\mathrm{eq}}(\phi) - c_{\mathrm{eq}}(0) = -\bar{c}_0 \phi \tag{9.9}$$

to first order.

In a nutshell, the effect of the chemical modification (i.e., of ϕ) on the upper monolayer is twofold. First, the scaled equilibrium density on the neutral surface of the upper monolayer is changed by the amount $\sigma_1 \phi / k$ to first order. Second, the spontaneous curvature of the upper monolayer is changed by the amount $-\bar{c}_0 \phi$ to first order. Hence, the constants σ_1 and $\bar{c}_0$ describe the linear response of the monolayer equilibrium density and of its spontaneous curvature, respectively, to the chemical modification. This description is generic, but the values of σ_1 and $\bar{c}_0$ depend on the chemical modification considered.

9.3 Force densities in the membrane

9.3.1 Expression of the force densities

The elastic force densities in a monolayer described by the Hamiltonian densities in Eqs. (9.1–9.3) are derived in Chapter 12 to first order in ϵ, using the principle of virtual work. More precisely, in Chapter 12, we derive the stress tensor of a monolayer featuring density and composition inhomogeneities. The force density is obtained by taking its divergence (see Sec. 12.5.1). We also obtain this force density through a direct covariant calculation (see Sec. 12.5.2).

Let us focus on small deformations of an infinite flat membrane. Such a description is adapted to practical cases where the distance between the reagent source and the membrane is much smaller than the vesicle radius. It is thus convenient to describe the membrane in the Monge gauge by the height $z = h(\boldsymbol{r})$, $\boldsymbol{r} \in \mathbb{R}^2$, of its midlayer with respect to the reference plane $z = 0$. Then, $ec = e\nabla^2 h + \mathcal{O}(\epsilon^2)$ for small deformations such that $\partial_i h = \mathcal{O}(\epsilon)$ and $e\partial_i\partial_j h = \mathcal{O}(\epsilon)$ where $i, j \in \{x, y\}$. Recall that we denote the upper monolayer by + and the lower one by −.

The force densities in the membrane then read to first order in ϵ (see Sec. 12.5.1):

$$\boldsymbol{p}_t^+ = -k\,\boldsymbol{\nabla}\left(r^+ + e\nabla^2 h - \frac{\sigma_1}{k}\phi\right)\,, \tag{9.10}$$

$$\boldsymbol{p}_t^- = -k\,\boldsymbol{\nabla}\left(r^- - e\nabla^2 h\right)\,, \tag{9.11}$$

$$p_z = \sigma_0\nabla^2 h - \tilde{\kappa}\nabla^4 h - ke\,\nabla^2 r_a - \left(\frac{\kappa\bar{c}_0}{2} - \sigma_1 e\right)\nabla^2\phi\,, \tag{9.12}$$

where $\boldsymbol{p}_t^\pm$ is the tangential component of the force density in monolayer $\pm$, while $p_z = p_z^+ + p_z^-$ is the total normal force density in the membrane. In these formulas, we have introduced the antisymmetric scaled density $r_a = r^+ - r^-$, and the constant $\tilde{\kappa} = \kappa + 2ke^2$.

9.3.2 Spontaneous curvature change versus equilibrium density change

Our general expressions Eqs. (9.10), (9.11) and (9.12) of the force densities in a chemically modified membrane allow for a comparison of the effects produced by an equilibrium density change and by a spontaneous curvature change. Affecting the local spontaneous curvature of a bilayer membrane can yield membrane deformation and budding [234–236]. Changing non-symmetrically the equilibrium density in each monolayer can also result in membrane deformation or budding [219, 230, 237]. However, to our knowledge, no previous study has considered these two effects at the same time and compared them.

Eq. (9.10) shows that the equilibrium density change (i.e., σ_1) can yield a tangential force density and induce tangential lipid flow. In addition, Eq. (9.12) shows that both the equilibrium density change and the spontaneous curvature change (i.e., both σ_1 and $\bar{c}_0$) can yield a normal force density, and thus a deformation of the membrane. More precisely, changing the spontaneous curvature produces a destabilizing normal force density $\delta p_z^{\mathrm{c}} = -\frac{1}{2}\kappa\bar{c}_0\nabla^2\phi$, while changing the equilibrium density yields $\delta p_z^{\mathrm{d}} = \sigma_1 e\nabla^2\phi$. Let us compare the effects of these two destabilizing normal force densities.

a. Equilibrium state of a chemically modified membrane

Let us assume that a membrane has been chemically modified in such a way that there is a static spatial profile of the mass fraction ϕ of the modified lipids in monolayer $+$[4].

In the case where only the equilibrium density is affected, which corresponds to $\sigma_1 \neq 0$ and $\bar{c}_0 = 0$, the membrane deformation would vanish once the scaled lipid

[4] A static ϕ can occur if the membrane is in chemical equilibrium with a reagent that is continuously injected from a local source, once the stationary profile of reagent concentration in the fluid above the membrane has been reached. This situation will be studied in Chapter 11. Another possibility is an irreversible modification of the lipids, but the lateral diffusion of the modified lipids would lead to their uniform repartition. In any case, on long timescales, membrane permeability to the reagent or flip-flop yield an equilibration between the two monolayers: we restrict to timescales short with respect to those.

density on the neutral surface of monolayer + has reached its equilibrium profile $r^+_{n,\mathrm{eq}}$, defined in Eq. (9.7). Indeed, the equilibrium condition $p_n = p_i^\pm = 0$ of the membrane is then satisfied for $\nabla^2 h = 0$, which means that the flat shape is an equilibrium shape.

In contrast, in the case where only the spontaneous curvature is changed, where $\sigma_1 = 0$ and $\bar{c}_0 \neq 0$, a deformation persists. Indeed, the equilibrium condition $p_n = p_i^\pm = 0$ can be satisfied only if $\sigma_0 \nabla^2 h - \kappa \nabla^4 h = \frac{1}{2}\kappa \bar{c}_0 \nabla^2 \phi$, which implies that $\nabla^2 h \neq 0$ if $\nabla^2 \phi \neq 0$, so that the plane shape is not an equilibrium shape for a generic inhomogeneous ϕ.

Thus, although both mechanisms should lead to membrane deformations, they are not physically equivalent. We will study the differences between them in more detail in Sec. 11.3. Generic chemical modifications result both in a change of the spontaneous curvature and in a change of the equilibrium density, so in general both mechanisms are involved.

b. Relative importance of the two deformation driving forces

It is interesting to study the relative importance of the spontaneous curvature change and of the equilibrium density change, through the ratio

$$\left|\frac{\delta p_z^{\mathrm{c}}}{\delta p_z^{\mathrm{d}}}\right| = \frac{\kappa|\bar{c}_0|}{2e|\sigma_1|} \tag{9.13}$$

of the destabilizing normal force densities associated with each of these two effects.

To quantify this ratio, let us estimate the variation δc_0 of the spontaneous curvature and the variation $\delta r^+_{n,\mathrm{eq}}$ of the scaled equilibrium density on the neutral surface induced by the chemical modification. We focus on a chemical modification that affects the lipid headgroups by effectively changing their preferred area. For instance, in the experimental case of an injection of sodium hydroxide on a membrane composed of PC and PS lipids, we expect that the acid-base reaction between the headgroups and the hydroxide ions increases the negative charge of the headgroups and hence the preferred area per lipid headgroup (see Sec. 10.3.3).

It is now necessary to resort to a microscopic model to express δc_0 and $\delta r^+_{n,\mathrm{eq}}$ as a function of the variation of the preferred area per lipid headgroup. We will present two very simple such models.

Simple geometrical model. Let us assume that each lipid is constituted of a headgroup with area $a_{\mathrm{h0}} = l_{\mathrm{h0}}^2$ and of a chain group with a different (e.g., to fix ideas, smaller) area $a_{\mathrm{c0}} = l_{\mathrm{c0}}^2$, situated at a fixed distance s from each other, as shown in Fig. 9.1(a). Both the head and the chain are supposed to be incompressible, and to favor close-packing. In this crude model, the equilibrium density on the neutral surface (i.e., here, on the surface of the headgroups) is equal to m/a_{h0}, where m is the mass of a lipid (see Fig. 9.1 (a)). The spontaneous curvature is obtained when the area per chain is equal to a_{c0} and the area per head is equal to a_{h0} (see Fig. 9.1 (b)): geometry yields $|c_0| = 2(l_{\mathrm{h0}} - l_{\mathrm{c0}})/(l_{\mathrm{c0}} s)$. If the preferred area per headgroup a_{h0}, or equivalently l_{h0}, is modified, it gives $|\delta r_{n,\mathrm{eq}}| = 2|\delta l_{\mathrm{h0}}|/l_{\mathrm{h0}}$ and

$|\delta c_0| = 2|\delta l_{\mathrm{h0}}|/(l_{\mathrm{c0}} s)$. Thus, given that $|c_0|s \gg 1$ (since lipids spontaneously organize into planar membranes), we obtain

$$|\delta c_0| \approx \frac{1}{s} |\delta r_{n,\mathrm{eq}}| \,. \tag{9.14}$$

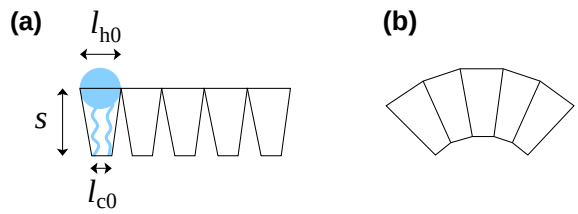

Figure 9.1: Two-dimensional illustration of the geometrical model: the lipid headgroups (resp. chains) have a characteristic size l_{h0} (resp. l_{c0}). (a) Plane shape: the area per lipid is given by $a_{\mathrm{h0}} = l_{\mathrm{h0}}^2$. (b) The spontaneous curvature c_0 of the monolayer is obtained when both the heads and the chains are close-packed.

Model based on Ref. [39]. Let us consider that the head and chain of a lipid have respective preferred areas a_{h0} and a_{c0}, while their actual areas are a_{h} and a_{c}, and let us write the elastic energy per molecule in a decoupled harmonic approximation [39]:

$$g(a_{\mathrm{h}}, a_{\mathrm{c}}) = \frac{K_{\mathrm{h}}}{2} a_{\mathrm{h0}} \left(\frac{a_{\mathrm{h}}}{a_{\mathrm{h0}}} - 1 \right)^2 + \frac{K_{\mathrm{c}}}{2} a_{\mathrm{c0}} \left(\frac{a_{\mathrm{c}}}{a_{\mathrm{c0}}} - 1 \right)^2 , \tag{9.15}$$

where K_{h} and K_{c} are stretching moduli. It was shown in Ref. [39] that the ADE model can be derived from Eq. (9.15). Following the same lines, we find that Eq. (9.15) yields the following Hamiltonian density, per unit area of a monolayer:

$$f^{\pm} = \frac{\kappa}{4} c^2 \pm \frac{\kappa c_0}{2} c + \frac{k}{2} \left(r^{\pm} \pm ec \right)^2 , \tag{9.16}$$

which corresponds to Eq. (9.1) with $\sigma_0 = 0$. Ref. [39] gives

$$c_0 = \frac{(K_{\mathrm{h}} a_{\mathrm{c0}} + K_{\mathrm{c}} a_{\mathrm{h0}})(a_{\mathrm{h0}} - a_{\mathrm{c0}})}{s(K_{\mathrm{h}} + K_{\mathrm{c}}) a_{\mathrm{h0}} a_{\mathrm{c0}}} , \tag{9.17}$$

$$\rho_{n,\mathrm{eq}} = m \frac{K_{\mathrm{h}} a_{\mathrm{c0}} + K_{\mathrm{c}} a_{\mathrm{h0}}}{(K_{\mathrm{h}} + K_{\mathrm{c}}) a_{\mathrm{h0}} a_{\mathrm{c0}}} , \tag{9.18}$$

where m is mass of a lipid. Using these expressions, it is straightforward to express $|\delta c_0|$ and $|\delta r_{n,\mathrm{eq}}|$ as a function of δa_{h0}, and it yields

$$|\delta c_0| \approx \frac{K_{\mathrm{h}} + K_{\mathrm{c}}}{s\, K_{\mathrm{h}}} |\delta r_{n,\mathrm{eq}}| , \tag{9.19}$$

where we have used $|c_0|s \ll 1$. The values of K_{h} and K_{c} should be of the same order, and we may hint at $K_{\mathrm{c}} < K_{\mathrm{h}}$ since the chains are able to reorganize spatially. Note that Eq. (9.14) is recovered when $K_{\mathrm{h}} \to \infty$ while K_{c} is finite. Since $s \approx e$, the results from both models, Eqs. (9.14) and (9.19), can be put in the form

$$|\delta c_0| \approx \frac{\alpha}{e} |\delta r_{n,\mathrm{eq}}| , \tag{9.20}$$

where the order of magnitude of α is one.

Conclusion. Using Eqs. (9.8), (9.9) and (9.20), we obtain

$$\left|\frac{\bar{c}_0}{\sigma_1}\right| \approx \frac{\alpha}{e\,k}\,. \tag{9.21}$$

Hence, the ratio of the destabilizing normal force densities associated with the spontaneous curvature change and with the equilibrium density change, expressed in Eq. (9.13), is such that

$$\left|\frac{\delta p_z^{\mathrm{c}}}{\delta p_z^{\mathrm{d}}}\right| \approx \frac{\alpha\,\kappa}{2\,e^2 k}\,. \tag{9.22}$$

Using the standard orders of magnitudes $\kappa \approx 10^{-19}$ J, $e \approx 1$ nm and $k \approx 0.1$ J/m^2 [27] shows that the order of magnitude of the ratio in Eq. (9.22) should be one. Hence, we expect that the effect of the spontaneous curvature change and that of the equilibrium density change have a comparable importance, for a chemical modification of the lipid headgroups which effectively modifies their preferred area. It is thus important to take into account both effects in the dynamics of the membrane.

9.4 Membrane dynamics

Using the elastic force densities in Eqs. (9.10–9.12), we describe the dynamics of the membrane to first order in the spirit of Ref. [224]. The dynamical equations are best expressed using two-dimensional Fourier transforms of the various fields involved, denoted with hats: for any field f which depends on $\boldsymbol{r}$ and on time t, $\hat{f}$ is such that

$$\hat{f}(\boldsymbol{q},t) = \int_{\mathbb{R}^2} d\boldsymbol{r}\, f(\boldsymbol{r},t) e^{-i\boldsymbol{q}\cdot\boldsymbol{r}}\,. \tag{9.23}$$

The dynamics of the membrane involves the forces specific to the membrane, among which the elastic force densities in the membrane given by Eqs. (9.10), (9.11) and (9.12), but also the viscous stresses exerted by the fluid above and below the membrane. Let us thus study the hydrodynamics of this fluid, before proceeding to the dynamical equations of the membrane.

9.4.1 Hydrodynamics of the surrounding fluid

We wish to determine the velocity field $\boldsymbol{W}^{\pm} = (\boldsymbol{w}^{\pm}, W_z^{\pm})$ in the fluid above (+) and below (−) the membrane. This flow is caused by the deformation of the membrane and by the lateral flow in the membrane: mathematically, it is determined by the boundary conditions corresponding to the continuity of velocity at the interface between the fluid and the membrane.

Given the short length scales considered, the dynamics of $\boldsymbol{W}^{\pm}(\boldsymbol{r},z,t)$ can be described using Stokes' equation. Adding the incompressibility condition, we have:

$$\eta(-q^2 + \partial_z^2)\hat{\boldsymbol{W}}^{\pm} = (i\boldsymbol{q} + \boldsymbol{e}_z\partial_z)\hat{P}^{\pm}\,, \tag{9.24}$$

$$i\boldsymbol{q}\cdot\hat{\boldsymbol{w}}^{\pm} + \partial_z \hat{W}_z^{\pm} = 0\,, \tag{9.25}$$

where $P^{\pm}$ is the excess pressure field in the fluid: the total pressure is $\mathcal{P}^{\pm} = P_0 + P^{\pm}$, where P_0 is a constant and $P^{\pm}$ goes to zero far from the membrane. Taking the scalar product of $\boldsymbol{q}$ and Eq. (9.24), and using Eq. (9.25) yields

$$\hat{P}^{\pm} = -\eta \partial_z \hat{W}_z^{\pm} + \frac{\eta}{q^2} \partial_z^3 \hat{W}_z^{\pm} \,. \tag{9.26}$$

Taking the scalar product of $\boldsymbol{e}_z$ and Eq. (9.24), and using Eq. (9.26) yields

$$q^4 \hat{W}_z^{\pm} - 2\, q^2 \partial_z^2 \hat{W}_z^{\pm} + \partial_z^4 \hat{W}_z^{\pm} = 0 \,. \tag{9.27}$$

These equations are solved with the following boundary conditions at infinity: $\hat{W}_z^{\pm} \to 0$ for $z \to \pm\infty$, and at the water–membrane interface: $\hat{W}_z^{\pm}(\boldsymbol{q}, 0, t) = \partial_t \hat{h}(\boldsymbol{q}, t)$ and $\hat{\boldsymbol{w}}^{\pm}(\boldsymbol{q}, 0, t) = \hat{\boldsymbol{v}}^{\pm}(\boldsymbol{q}, t)$, where $\boldsymbol{v}^{\pm}$ denotes the in-plane velocity of the lipids in monolayer $\pm$. Note that, since $\phi = \mathcal{O}(\epsilon)$, and since the lipid flow is induced by the chemical modification, one has $|\boldsymbol{v}^{\pm}| = \mathcal{O}(\epsilon)$. We obtain

$$\hat{P}^{\pm} = \pm 2\, \eta \left[q\, (\partial_t \hat{h}) \mp i \boldsymbol{q} \cdot \hat{\boldsymbol{v}}^{\pm} \right] e^{\mp q z} \,, \tag{9.28}$$

$$\hat{\boldsymbol{w}}^{\pm} = \left\{ \hat{\boldsymbol{v}}^{\pm} - \left[i \boldsymbol{q}\, (\partial_t \hat{h}) \pm q\, \hat{\boldsymbol{v}}^{\pm} \right] z \right\} e^{\mp q z} \,, \tag{9.29}$$

$$\hat{W}_z^{\pm} = \left\{ \partial_t \hat{h} \pm \left[q\, (\partial_t \hat{h}) \mp i \boldsymbol{q} \cdot \hat{\boldsymbol{v}}^{\pm} \right] z \right\} e^{\mp q z} \,. \tag{9.30}$$

For our study of the dynamics of the membrane, what is needed is the stress exerted by the fluid on the membrane, i.e., since we are working at first order in the membrane deformation, the stress in $z = 0$. The viscous stress tensor of the fluid is defined by

$$T_{\alpha\beta} = -(P^{\pm} + P_0)\delta_{\alpha\beta} + \eta \left(\partial_\beta W_\alpha^{\pm} + \partial_\alpha W_\beta^{\pm} \right) \,, \tag{9.31}$$

where $\alpha \in \{x, y, z\}$ and $\beta \in \{x, y, z\}$. Hence, using Eqs. (9.28, 9.29, 9.30), we obtain

$$\hat{T}_{zz}^{+}(z = 0) - \hat{T}_{zz}^{-}(z = 0) = -4\, \eta\, q\, \partial_t \hat{h} \,, \tag{9.32}$$

$$\hat{\boldsymbol{T}}_{tz}^{\pm}(z = 0) = \mp 2\, \eta\, q\, \hat{\boldsymbol{v}}^{\pm} \,, \tag{9.33}$$

where we have introduced the tangential part $\boldsymbol{T}_{tz}^{\pm} = (T_{xz}^{\pm}, T_{yz}^{\pm})$ of the stress tensor of the fluid above and below the membrane.

9.4.2 Dynamical equations for the membrane

The first dynamical equation we use is a balance of forces per unit area acting normally to the membrane [224]. It involves the normal elastic force density in the membrane given by Eq. (9.12) and the normal viscous stresses exerted by the fluid above and below the membrane, Eq. (9.32). It reads:

$$-\left(\sigma_0\, q^2 + \tilde{\kappa}\, q^4 \right) \hat{h} + k\, e\, q^2\, \hat{r}_a + \frac{\kappa\, \tilde{c}_0}{2}\, q^2 \hat{\phi} - 4\, \eta\, q\, \partial_t \hat{h} = 0 \,, \tag{9.34}$$

where η denotes the viscosity of the fluid above and below the membrane.

Besides, as each monolayer is a two-dimensional fluid, we write down generalized Stokes equations describing the tangential force balance in each monolayer [224]. The first force involved is the density of elastic forces given by Eqs. (9.10) and (9.11). The second one arises from the viscous stress in the two-dimensional flow of lipids. The third one comes from the viscous stress exerted by the water, Eq. (9.33). The last force that has to be included is the intermonolayer friction [228]. We thus obtain:

$$-i\,k\,\boldsymbol{q}\left(\hat{r}^{+}-e\,q^{2}\,\hat{h}-\frac{\sigma_1}{k}\,\hat{\phi}\right)-\left(\eta_2\,q^{2}+2\,\eta\,q\right)\hat{\boldsymbol{v}}^{+}-b\left(\hat{\boldsymbol{v}}^{+}-\hat{\boldsymbol{v}}^{-}\right)=0\,, \tag{9.35}$$

$$-i\,k\,\boldsymbol{q}\left(\hat{r}^{-}+e\,q^{2}\,\hat{h}\right)-\left(\eta_2\,q^{2}+2\,\eta\,q\right)\hat{\boldsymbol{v}}^{-}+b\left(\hat{\boldsymbol{v}}^{+}-\hat{\boldsymbol{v}}^{-}\right)=0\,, \tag{9.36}$$

where $\boldsymbol{v}^{\pm}$ denotes the velocity in monolayer $\pm$, while η_2 is the two-dimensional viscosity of the lipids and b is the intermonolayer friction coefficient.

Finally, we use the conservation of mass in each monolayer to first order:

$$\partial_t\hat{r}^{\pm}+i\,\boldsymbol{q}\cdot\hat{\boldsymbol{v}}^{\pm}=0\,. \tag{9.37}$$

Considering that each monolayer has a fixed total mass is justified as long as we restrict to timescales much shorter than the flip-flop characteristic time, which is of the order of hours or days in vesicles, depending on the lipid type [5], and which is assumed not to be significantly modified by the local chemical modification. The timescales of the microinjection experiments investigated in Chapter 10, which are about 10 seconds, verify this hypothesis.

Combining Eqs. (9.34), (9.35), (9.36) and (9.37) yields a system of first-order linear differential equations on the two-dimensional variable $X=(q\,\hat{h},\hat{r}_a)$:

$$\frac{\partial X}{\partial t}(\boldsymbol{q},t)+M(q)\,X(\boldsymbol{q},t)=Y(\boldsymbol{q},t)\,, \tag{9.38}$$

where we have introduced the matrix which describes the dynamical response of the membrane [224]:

$$M(q)=\begin{pmatrix}\dfrac{\sigma_0 q+\tilde{\kappa}q^3}{4\eta} & -\dfrac{keq^2}{4\eta}\\[2ex] -\dfrac{keq^3}{b} & \dfrac{kq^2}{2b}\end{pmatrix}. \tag{9.39}$$

Here, we have assumed that $\eta_2 q^2 \ll b$ and $\eta q \ll b$. This is true for all the wave vectors with significant weight in $\hat{\phi}$, if the modified lipid mass fraction ϕ has a smooth profile with a characteristic width larger than 1 μm. Indeed, $\eta=10^{-3}\,\mathrm{J\,s/m^3}$ for water, and typically $\eta_2=10^{-9}\,\mathrm{J\,s/m^2}$ and $b=10^{9}\,\mathrm{J\,s/m^4}$ [238, 239]. Besides, the forcing term in Eq. (9.38) reads:

$$Y(\boldsymbol{q},t)=\begin{pmatrix}\dfrac{\kappa\tilde{c}_0 q^2}{8\eta}\hat{\phi}(\boldsymbol{q},t)\\[2ex] \dfrac{\sigma_1 q^2}{2b}\hat{\phi}(\boldsymbol{q},t)\end{pmatrix}. \tag{9.40}$$

Eqs. (9.38) and (9.39) show that the membrane deformation is coupled to the antisymmetric density: the symmetry breaking between the monolayers causes the deformation of the membrane. Here, the symmetry breaking is caused by the chemical modification of certain membrane lipids in the external monolayer, i.e., to the presence of ϕ. And indeed, Eq. (9.40) shows that the forcing term in Eq. (9.38) is proportional to $\hat{\phi}(\boldsymbol{q}, t)$.

Note that Eqs. (9.34), (9.35), (9.36) and (9.37) also yield a decoupled evolution equation for the symmetric scaled density $r_s = r^- + r^+$:

$$\frac{\partial \hat{r}_s}{\partial t} = -\frac{kq}{2\eta}\left(\hat{r}_s - \frac{\sigma_1}{k}\hat{\phi}\right) , \tag{9.41}$$

where we have assumed that $\eta_2 q \ll \eta$, which is true for all the wave vectors with significant weight in $\hat{\phi}$, if the modified lipid mass fraction ϕ has a smooth profile with a characteristic width larger than 1 μm.

The present theoretical description is general and applies to any local chemical modification of monolayer $+$, if ϕ remains small and if its profile is smooth with a characteristic width larger than 1 μm. What changes with the nature of the reagent is the value of the constants σ_1 and c_0, which describe the linear response of the membrane to the chemical modification.

9.4.3 Relaxation rates for large wavelengths

Let us focus on the case where the modified lipid mass fraction ϕ has a smooth profile with a characteristic width larger than about 10 μm. Then, the wave vectors with significant weight in its Fourier transform $\hat{\phi}$ verify $q \lesssim 10^6\,\mathrm{m}^{-1}$. Let us study the eigenvalues of $M(q)$ in this large-wavelength regime.

Membrane tensions are such that $\sigma_0 \geq 10^{-8}\,\mathrm{N/m}$, and standard values of the other parameters involved in $M(q)$ are $\kappa = 10^{-19}\,\mathrm{J}$, $k = 0.1\,\mathrm{N/m}$, $e = 1$ nm, $b = 10^9\,\mathrm{J.s.m}^{-4}$ and $\eta = 10^{-3}\,\mathrm{J\,s/m}^3$. Hence, in the large-wavelength regime, we have $q \ll \sqrt{\sigma_0/\tilde{\kappa}}$, and the eigenvalues of $M(q)$ can be approximated by

$$\gamma_1 = \frac{kq^2}{2b} , \tag{9.42}$$

$$\gamma_2 = \frac{\sigma_0 q}{4\eta} . \tag{9.43}$$

Indeed, for $q \ll \sqrt{\sigma_0/\tilde{\kappa}}$, the coefficient keq^3/b in $M(q)$ is much smaller than all the other ones (see Eq. (9.39)), so that $M(q)$ can be approximated by an upper triangular matrix.

The eigenvalues of $M(q)$ represent the relaxation rates of a deformation of the membrane. We observe that γ_1, which involves intermonolayer friction, is identical to Eq. (8.3) in Seifert and Langer's description [224] (see Sec. 8.3.1-b.), while γ_2 is different, because the effect of tension, which was disregarded in Seifert and Langer's description, is actually dominant over that of bending rigidity for large wavelengths.

It is also interesting to compare γ_1 and γ_2 to the relaxation rate γ_s of the symmetric density, which appears in Eq. (9.41):

$$\gamma_s = \frac{kq}{2\eta} \,. \tag{9.44}$$

The rupture threshold of a membrane corresponds to a tension of a few mN/m [5]. Hence, $\sigma_0 \ll k$ for all realistic membrane tensions, which yields $\gamma_s \gg \gamma_2$. Besides, as mentioned above, we have $\eta q \ll b$ for all the wave vectors with significant weight in $\hat{\phi}$, so that $\gamma_s \gg \gamma_1$. Hence, the relaxation of the symmetric density is much faster than that of the antisymmetric density and of the deformation of the membrane, for all modes in the large-wavelength limit.

9.5 Profile of the fraction of the chemically modified lipids

The time evolution of the deformation of the chemically modified membrane can be determined by solving Eq. (9.38). To this end, we first need to determine $\hat{\phi}(\boldsymbol{q}, t)$, which is involved in the forcing term $Y(\boldsymbol{q}, t)$ (see Eqs. (9.38–9.39)).

The profile $\phi(\boldsymbol{r}, t)$ of the mass fraction of the chemically modified lipids in the external monolayer arises from the local reagent concentration increase. We focus on reagents that react reversibly with the membrane lipid headgroups. Besides, we assume that the reaction between the lipids and the reagent is diffusion-controlled (see, e.g., Ref. [240]). In other words, the molecular reaction timescales are very small compared to the diffusion timescales. For such a reversible diffusion-controlled chemical reaction, $\phi(\boldsymbol{r}, t)$ is instantaneously determined by the local reagent concentration on the membrane, which results from the diffusion of the reagent in the fluid above the membrane.

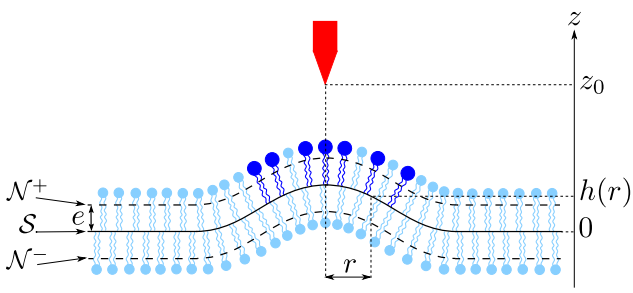

Figure 9.2: Sketch of the situation described (not to scale). Due to the injection of a reagent from the micropipette (red) standing at z_0 above the membrane, some lipids are chemically modified (dark blue) in the external monolayer. The mass fraction of these modified lipids is denoted by ϕ. The membrane deforms because of this local chemical modification: the shape of its midlayer $\mathcal{S}$ is described by $h(r)$. The variables $c \simeq \nabla^2 h$ and $r^\pm$ used in our theory are defined on $\mathcal{S}$, which is at a distance e from the neutral surface $\mathcal{N}^\pm$ of monolayer $\pm$.

We consider that the reagent source is localized in $(\boldsymbol{r}, z) = (\mathbf{0}, z_0 > 0)$, which would represent the position of the micropipette tip in an experiment (see Fig. 9.2). The cylindrical symmetry of the problem then implies that the fields involved in our description only depend on $r = |\boldsymbol{r}|$. We focus on the regime of small deformations $h(r,t) \ll z_0$, and we work at first order in $h(r,t)/z_0$. Besides, we study the linear regime where $\phi(r,t)$ is proportional to the reagent concentration on the membrane: denoting by $C(r,z,t)$ the reagent concentration field, we have $\phi(r,t) \propto C(r, h(r,t), t)$. To first order in the membrane deformation, this can be simplified into $\phi(r,t) \propto C(r,0,t)$.

The field C is determined by the diffusion of the reagent from the local source in the fluid above the membrane. In microinjection experiments, there is also a convective transport of the reagent due to the injection, but the Péclet number remains so small that diffusion dominates. Besides, since the membrane is a surface and $\phi \ll 1$, we can neglect the number of reagent molecules that react with the membrane when calculating C. Hence, C can be obtained by solving the diffusion equation

$$\partial_t C - D\nabla^2 C = S\,, \tag{9.45}$$

where D is the diffusion coefficient of the reagent in the fluid above the membrane, and the source term reads

$$S(\boldsymbol{r}, z, t) = S_0 \delta(\boldsymbol{r})\delta(z - z_0)F(t). \tag{9.46}$$

This corresponds to an injection flow from the source, with time evolution described by the function F. In practice, we will only consider the two following simple cases:
1) $F = \mathbf{1}_{[0,T]}$, where $\mathbf{1}_{[0,T]}$ is the indicator function of the interval $[0,T]$: this corresponds to an injection with constant flow, starting at $t = 0$ and stopping at $t = T$ (see Chapter 10).
2) $F = \theta$, where θ denotes Heaviside's function: this corresponds to a continuous injection with constant flow, starting at $t = 0$ (see Chapter 11).
In addition, the membrane imposes a Neumann boundary condition, which reads $\partial_z C\left(r, h(r,t), t\right) = 0$. This relation, which corresponds to a vanishing flux across the membrane, can be simplified to first order into

$$\partial_z C\left(r, 0, t\right) = 0\,. \tag{9.47}$$

The solution to this diffusion problem reads

$$\begin{aligned} C\left(r,z,t\right) &= \int_0^t dt' \int_{\mathbb{R}^2} d\boldsymbol{r'} \int_0^{+\infty} dz'\, S\left(\boldsymbol{r'}, z', t'\right)\, G\left(|\boldsymbol{r} - \boldsymbol{r'}|, z, z', t - t'\right) \\ &= S_0 \int_0^t dt'\, G\left(r, z, z_0, t - t'\right)\, F(t')\,, \end{aligned} \tag{9.48}$$

where the causal Green's function G of our diffusion problem can be expressed using the method of images [241]:

$$G\left(r, z, z', t\right) = G_\infty\left(r, z - z', t\right) + G_\infty\left(r, z + z', t\right)\,, \tag{9.49}$$

where we have introduced the infinite-volume causal Green's function of the diffusion equation:

$$G_\infty(r,z,t) = \frac{\theta(t)}{(4\,\pi\,D\,t)^{3/2}}\,\exp\left(-\frac{r^2+z^2}{4\,D\,t}\right). \tag{9.50}$$

For the two simple functions F cited above, combining Eqs. (9.48), (9.49) and (9.50) provides an analytical expression for $C(r,z,t)$, and for $\hat{C}(q,z,t)$. Since $\hat{\phi}(q,t) \propto \hat{C}(q,0,t)$, we thus obtain an analytical expression for $\hat{\phi}$ too (see Secs. 10.4.1 and 11.2.1).

9.6 Resolution of the dynamical equations

Once one has determined $\hat{\phi}(q,t)$, which is involved in the forcing term $Y(q,t)$ of the dynamical equations (see Eqs. (9.38–9.39)), the time evolution of the membrane deformation can be obtained by solving the differential equation Eq. (9.38). This can be done thanks to the method of variation of parameters. The square matrix $M(q)$ defined in Eq. (9.39) has two real positive and distinct eigenvalues for all $q > 0$. Let us call these eigenvalues γ_1 and γ_2, and let us introduce the associated eigenvectors $V_1 = (v_1, w_1)$ and $V_2 = (v_2, w_2)$. For the initial condition $X(q, t = 0) = (0,0)$, corresponding to a non-perturbed membrane (i.e., flat and with identical density in the two monolayers), we can write:

$$q\,\hat{h}(q,t) = \int_0^t ds\,\left[v_1\,e^{-\gamma_1\,t}A(s) + v_2\,e^{-\gamma_2\,t}\,B(s)\right], \tag{9.51}$$

where $A(t)$ and $B(t)$ are the solutions of the linear system

$$V_1\,A(t)\,e^{-\gamma_1\,t} + V_2\,B(t)\,e^{-\gamma_2\,t} = Y(q,t)\,. \tag{9.52}$$

Then, in order to obtain the membrane deformation profile at time t, we perform an inverse Fourier transform:

$$h(r,t) = \frac{1}{2\pi}\int_0^{+\infty} dq\;J_0(q\,r)\;q\,\hat{h}(q,t)\,, \tag{9.53}$$

where we have used the cylindrical symmetry of the problem, introducing the Bessel function of the first kind and of zero order J_0. Thus, using Eq. (9.51), we finally obtain

$$h(r,t) = \frac{1}{2\pi}\int_0^{+\infty} dq\,J_0(q\,r)\int_0^t ds\,\left[v_1\,e^{-\gamma_1\,t}A(s) + v_2\,e^{-\gamma_2\,t}\,B(s)\right]. \tag{9.54}$$

Hence, we can obtain the spatiotemporal evolution of the membrane deformation during and after the microinjection by carrying out the integrals in Eq. (9.54) numerically.

9.7 Conclusion

This Chapter constitutes the basis of our study of the dynamics of a membrane submitted to a local chemical perturbation of its environment. In Chapter 10, we will confront this description to experimental results corresponding to microinjection experiments on giant unilamellar vesicles. Then, in Chapter 11, we will analyze further the response of a membrane to a continuous reagent injection.

Chapter 10

Lipid membrane deformation in response to a local pH modification: theory and experiments

Contents

10.1 Introduction **207**

10.2 Materials and methods **208**

10.2.1 Membrane composition and vesicle preparation 208

10.2.2 Microscopy imaging and micromanipulation 209

10.2.3 Steady-state fluorescence measurements 209

10.3 Experiments **210**

10.3.1 Observation of the membrane deformation 210

10.3.2 Observation of the pH profile on the membrane 211

10.3.3 Chemical effect of a pH increase on the lipids 213

10.4 Comparison between theory and experiments **213**

10.4.1 Calculation of ϕ 213

10.4.2 Membrane deformation height 215

10.5 Conclusion **219**

10.1 Introduction

Local pH inhomogeneities at the cellular scale are ubiquitous and play important biological roles (see Sec. 8.2.2-a.). In order to understand the fundamental phenomena involved in the response of a biological membrane to a local pH modification, microinjection experiments of acidic or basic solutions on GUVs are performed in

the group of Miglena I. Angelova and Nicolas Puff [213, 219, 231, 237, 242]. These studies, which were shortly described in Sec. 8.2.2-b., show that locally modifying the pH on a GUV through microinjection results into a local dynamic membrane deformation: the membrane shape is tightly coupled to local pH inhomogeneities. These experimental results were interpreted in light of linear membrane dynamics, focusing on the simple case of a constant modification of the membrane involving only one wavelength, in Refs. [219, 231]. It was first assumed that the chemical modification resulted only in an equilibrium density change in Ref. [219], and then we took into account the spontaneous curvature change as well in Ref. [231].

In Chapter 9, we presented linear membrane dynamics, taking into account both the equilibrium density change and the spontaneous curvature change induced by the chemical modification. Moreover, we explained how to fully account for the time-dependent profile of the fraction of chemically modified lipids in the membrane. In the present Chapter, we compare the results of this extended theoretical description to experimental measurements of the height of the membrane deformation during and after the local injection of a basic solution, in the regime of small deformations. In addition, we present a direct experimental visualization of the pH profile on the membrane during and after the microinjection, obtained using a pH-sensitive fluorescent membrane marker. These experiments were performed by the group of Miglena I. Angelova and Nicolas Puff, in collaboration with Yuka Sakuma and Masayuki Imai[1]. We will first present the experiments, and then move on to the comparison with our theoretical model.

The work presented in this Chapter has been published in: A.-F. Bitbol, N. Puff, Y. Sakuma, M. Imai, J.-B. Fournier and M. I. Angelova, *Lipid membrane deformation in response to a local pH modification: theory and experiments*, Soft Matter 8, 6073–6082 (2012), cited as Ref. [243] here.

10.2 Materials and methods

10.2.1 Membrane composition and vesicle preparation

The following lipids, from Avanti Polar Lipids, were used without further purification: egg yolk L-α-phosphatidylcholine (PC), brain L-α-phosphatidylserine (PS), and the fluorescent lipid analog 1,2-dioleoyl-*sn*-glycero-3-phosphoethanolamine-N-(carboxyfluorescein) ammonium salt (DOPE-CF). All other chemicals were of highest purity grade: calcein and NaOH, Sigma.

Giant unilamellar vesicles were formed in a thermostated chamber, by the liposome electroformation method [18], which is briefly described in Sec. 1.2.3. Liposome preparations for phase contrast microscopy experiments were made with a unique

[1]Until recently, Yuka Sakuma and Masayuki Imai worked at Ochanomizu University in Tokyo, Japan. They have now moved to Tohoku University in Sendai, Japan. Yuka Sakuma was able to come to the MSC laboratory in Paris thanks to the JSPS Core-to-Core Program "International research network for non-equilibrium dynamics of soft matter", and she performed microinjection experiments on GUVs in the group of Miglena I. Angelova and Nicolas Puff.

lipid mixture of PC and PS with PC/PS 90:10 mol/mol. For fluorescence observations, 1% (mol) of the fluorescent lipid analog DOPE-CF was added to this mixture. The particular electroformation protocol used in this work was the following: lipid mixture solutions were prepared in chloroform/diethyl ether/methanol (2:7:1) with a total lipid concentration of 1 mg/ml. A droplet of this lipid solution (1 μl) was deposited on each of the two parallel platinum wires constituting the electroformation electrodes, and dried under vacuum for 15 min. An AC electrical field, 10 Hz, 0.26 Vpp, was applied to the electrodes. Water (temperature 25°C) was added to the working chamber, avoiding agitation. The voltage was gradually increased, for more than two hours, up to 1 Vpp and maintained during 15 more minutes, before switching the AC field off. The GUVs were then ready for further use. In each preparation at least 10 GUVs of diameter 50-80 μm were available.

Large unilamellar vesicles (LUVs) were prepared using the extrusion method [244], implemented as in Ref. [237]. Samples were prepared by dissolving and mixing the above-mentioned lipids in chloroform/methanol (9.4:0.6 vol/vol) to obtain the desired composition (PC/PS 90:10 mol/mol, to which 1% mol of DOPE-CF was then added).

10.2.2 Microscopy imaging and micromanipulation

We used a Zeiss Axiovert 200M microscope, equipped with a charged-coupled device camera (CoolSNAP HQ; Photometrics). The experiments were computer-controlled using the Metamorph software (Molecular Devices). The morphological transformations and the dynamics of the membrane were followed by phase contrast and fluorescence microscopy (Zeiss filter set 10, Ex/Em = 475/520 nm).

Tapered micropipettes for the local injection of NaOH were made from GDC-1 borosilicate capillaries (Narishige), pulled on a PC-10 pipette puller (Narishige). The inner diameter of the microcapillary used for performing the local injections onto a GUV was 0.3 μm. For these local injections, a microinjection system (Eppendorf femtojet) was used. The micropipettes were filled with basic solutions of NaOH with concentrations ranging from 5 to 100 mM. The injected volumes were of the order of picoliters and the injection pressure was 200 hPa. The positioning of the micropipettes was controlled by a high-graduation micromanipulator (MWO-202; Narishige). The injections were performed at different distances from the GUV surface, taking care to avoid any contact with the lipid membrane.

10.2.3 Steady-state fluorescence measurements

Steady-state fluorescence measurements of LUV samples were carried out with a Cary Eclipse spectrofluorimeter (Varian Instruments) equipped with a thermostated cuvette holder (±0.1°C). Excitation and emission slits were adjusted to 5 nm. Fluorescence emission spectra were all recorded at 25°C. All fluorescence measurements were carried out at a total lipid concentration of 0.2 mM. In the experiments, the pH of the LUV samples was gradually modified by adding aliquots of acidic or basic

solutions. The measurements were carried out after a few minutes of equilibration under agitation.

10.3 Experiments

10.3.1 Observation of the membrane deformation

The chemical modification of the membrane was achieved by locally delivering a basic solution of NaOH close to the vesicle. This local increase of the pH should affect the headgroups of the phospholipids PS and PC forming the external monolayer of the membrane [231], as well as the fluorescent marker (when present).

Fig. 10.1 shows a typical microinjection experiment. We inject the basic solution during a time $T = 4$ s. One can see in Fig. 10.1 the vesicle before any microinjection (frame 0 s). A smooth local deformation of the vesicle develops toward the pipette during the microinjection (first line of images). Once the injection is stopped, the membrane deformation relaxes (second line of images). This deformation is fully reversible. For the sake of clarity, the deformation presented in Fig. 10.1 is actually the largest this Chapter deals with. Indeed, we focus on the regime of small deformations in order to remain in the framework of our linear theory. In particular, it is necessary that the deformation height be much smaller than the distance between the membrane and the micropipette for our theory to be valid.

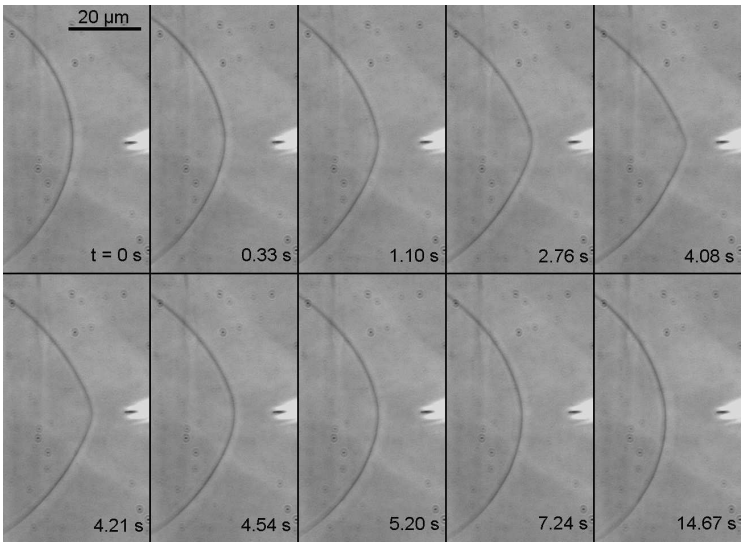

Figure 10.1: Typical microinjection experiment, lasting $T = 4$ s, observed using phase contrast microscopy. A local modulation of the pH on the vesicle membrane induces a smooth deformation of the vesicle (frames 0.33 to 4.08 s). The deformation is completely reversible when the NaOH delivery is stopped (frames 4.21 s to the end).

10.3.2 Observation of the pH profile on the membrane

We present here a direct experimental visualization of the pH profile on the membrane during and after the local microinjection of NaOH. For this, we use a pH-sensitive fluorescent membrane marker (DOPE-CF). The fluorescein group is a weak acid whose conjugate base has a strong fluorescence, and which is attached to phosphatidylethanolamine lipids.

First of all, the dependence of the fluorescence on the pH was verified on a solution of LUVs (see Fig. 10.2). The dependence of the mean intensity of the LUV solution on the pH is well described by the sigmoidal shape characteristic of an acid-base titration (see Fig. 10.2). The steep intensity rise is observed around pH 7.5, which makes this marker adequate to investigate pH increases starting from a neutral pH.

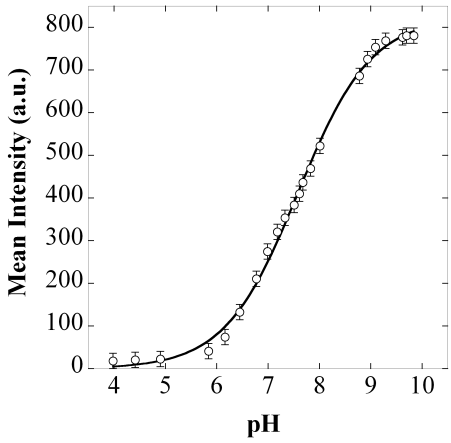

Figure 10.2: Mean (fluorescence) intensity as a function of the pH in a solution of LUVs whose membranes contain a pH-sensitive fluorescent marker (DOPE-CF). Dots: experimental data. Solid line: sigmoidal fit.

Using this fluorescent marker within a preparation of GUVs, it is possible to observe the pH profile on the membrane during and after the local microinjection of NaOH. Typical results are presented in Fig. 10.3. The pH profile on the membrane is visualized directly together with the deformation of the membrane. The vesicle deforms progressively in response to the local pH increase (frames from 0 to 3.6 s). The increase of the intensity in front of the micropipette and the lateral spreading of the bright zone during the injection are visible in the three first images. This illustrates the local pH increase on the membrane in front of the micropipette, and then on the sides, as the HO^- ions diffuse from the micropipette tip towards the membrane. Later on, photobleaching occurs, and its effect is visible faster in the zone where the onset of fluorescence occurred sooner, i.e., just in front of the micropipette. The deformation fully relaxes when the NaOH injection is stopped (frames from 4.4 s to the end), and the fluorescence decreases at the same time, both due to the diffusion of the injected basic solution in the water surrounding the membrane after the end of the injection, and to photobleaching.

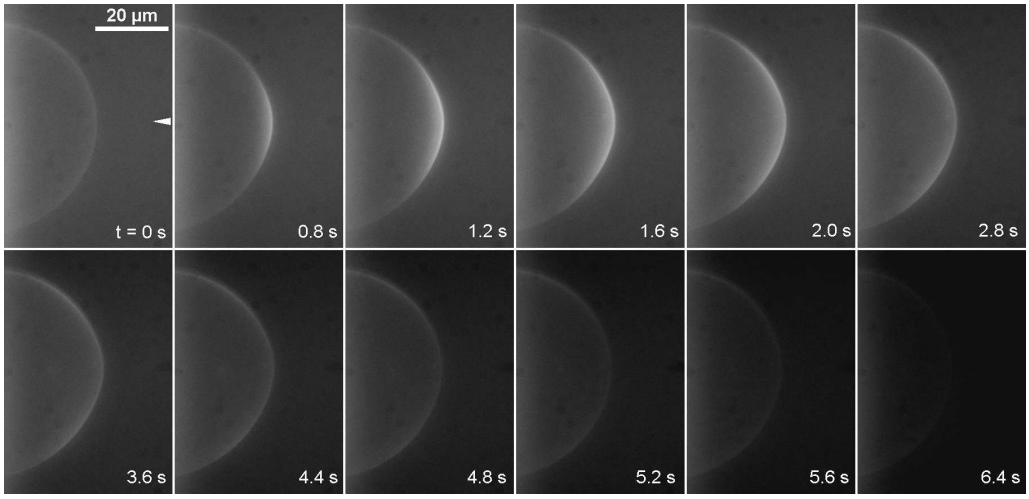

Figure 10.3: Typical microinjection experiment, lasting $T = 4$ s, observed using fluorescence microscopy. The white arrow represents the micropipette tip. The pH profile on the membrane is visualized directly together with the deformation of the membrane. The vesicle deforms progressively in response to the local pH increase (frames from 0 to 3.6 s). The increase of the intensity illustrates the pH increase. The deformation fully relaxes when the NaOH injection is stopped (frames from 4.4 s to the end). The initial fluorescence of the membrane at $t = 0$, i.e., at pH 7, is weak but visible (see Fig. 10.2). The global darkening of the images with time is due to photobleaching.

The membrane shape profiles and the membrane intensity profiles have been extracted from the images in Fig. 10.3, using the software Image J supplemented by our own plugins[2]. The corresponding results are shown in Fig. 10.4 for the frames corresponding to times 0, 0.8, 1.2 and 2.8 s in Fig. 10.3. One can see first the local increase of intensity, and thus of pH, in front of the micropipette, as the membrane deforms (red curves), and the subsequent spreading of the high-pH zone while the pH increase continues (blue curves). In the last (green) curves, the effect of photobleaching is visible, as the central intensity decreases while the injection still continues and the membrane keeps deforming.

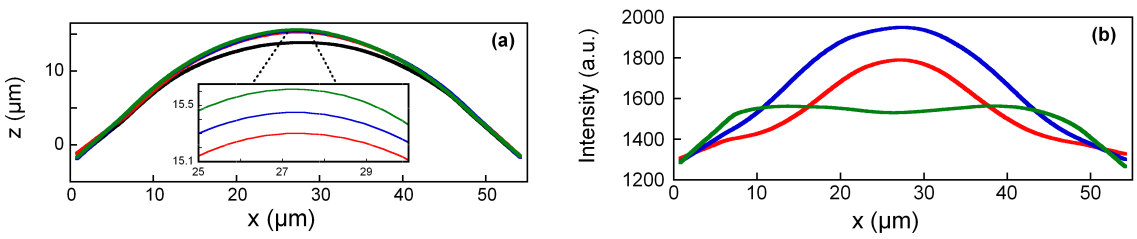

Figure 10.4: (a) Membrane shape profiles during the experiment presented in Fig. 10.3 (black: $t = 0$ s, red: $t = 0.8$ s, blue: $t = 1.2$ s, green: $t = 2.8$ s). Inset: zoomed-in image of the central zone. (b) Intensity profiles on the membrane at the times 0.8, 1.2 and 2.8 s (same colors as in (a)).

[2]We thank Rémy Colin for his precious help with writing the image treatment plugins.

10.3.3 Chemical effect of a pH increase on the lipids

The following control experiments have been carried out:
1) We have checked that no deformation occurs if only buffer solution is injected.
2) In order to verify that the observed effects were not simply due to charge screening and/or osmotic effects, a local injection of salt solution (NaCl instead of NaOH) has been performed. The typical smooth and reversible deformation has not been observed in these control experiments.
This shows that the pH increase is here the crucial of membrane deformation.

The local pH increase should affect the headgroups of the phospholipids PS and PC forming the membrane. Indeed, the amino group of the PS headgroup deprotonates at high pH, its intrinsic pKa being about 9.8 in vesicles constituted of a PC/PS 90:10 mol/mol mixture [245]. Besides, the positively charged trimethylammonium group of the PC headgroup associates with hydroxide ions at high pH, the dissociation constant K of this equilibrium being such that $\mathrm{pK} = 14 - \mathrm{pKa}^{\mathrm{eff}}$, where $\mathrm{pKa}^{\mathrm{eff}} = 11$ [220]. Both reactions increase the negative charge of the lipids, which should entail an effective local increase of the preferred area per lipid headgroup in the outer monolayer of the membrane.

10.4 Comparison between theory and experiments

In Chapter 9, we presented a theoretical description of the membrane deformation in response to the microinjection of a reagent close to a membrane. We are now going to compare its predictions with experimental data. First, let us show that our method for calculating the mass fraction ϕ of the chemically modified lipids in the external monolayer, presented in Sec. 9.5, is well adapted to the present experimental case, and let us write down the analytical expression of ϕ.

We keep the notations of Chapter 9: in particular, we denote by $C\,(r, z, t)$ the local concentration in hydroxide ions in the water that surrounds the vesicle, and we assume that the unperturbed flat membrane is in the plane $z = 0$, and that the micropipette stands at $z_0 > 0$ above it (see Fig. 9.2).

10.4.1 Calculation of ϕ

The acid-base (and complexation) reactions that occur between the lipid headgroups and the injected hydroxide ions are reversible and diffusion-controlled [240]. Hence, the local mass fraction $\phi(r, t)$ of the chemically modified lipids is determined by an instantaneous equilibrium with the hydroxide ions that are above the membrane. In addition, in the experimental conditions, the pH on the membrane remains well below the effective pKa of the lipids. Thus, the mass fraction of the chemically modified lipids after the reaction is proportional to the concentration of HO^- ions just above the membrane: $\phi(r, t) \propto C(r, z = 0, t)$. This corresponds to the assumption made in Sec. 9.5 to deduce ϕ from C.

In addition, in our experiments, the NaOH solution is injected from a micropipette of inner diameter $d = 0.3\,\mu$m and length $L \simeq 2$ cm, with an injection pressure $\Delta P = 200$ hPa. Hence, we can estimate the average velocity v_0 of the NaOH solution when it just gets out the pipette, treating the flow in the micropipette as a Poiseuille flow:

$$v_0 = \frac{\Delta P\, d^2}{32\,\eta L} \simeq 2\,\mu\text{m.s}^{-1}. \tag{10.1}$$

Thus, given the small length scales and velocities involved in the microinjection, the Péclet number Pe is very small:

$$\text{Pe} = \frac{v_0 z_0}{D} \approx 10^{-2}, \tag{10.2}$$

where the order of magnitude of z_0 is $10\,\mu$m, while D is the diffusion coefficient of sodium hydroxide in water, which is given by $D = 2/(1/D_{\text{OH}^-} + 1/D_{\text{Na}^+}) = 2125\,\mu\text{m}^2/\text{s}$ at infinite dilution and at $20\,^\circ$C [246]. Hence, once the NaOH solution is out of the pipette, its dynamics is dominated by diffusion. This fact can also be verified experimentally by injecting a fluorescent substance in the conditions under which the basic solution is injected in our experiments. The observed quasi-spherical fluorescent "cloud", presented in Fig. 10.5, illustrates well the dominant effect of diffusion. Thus, we can consider that the NaOH solution simply diffuses from the micropipette tip, situated in $(r = 0, z_0)$, where we take the same notations as in Chapter 9 (see Fig. 9.2).

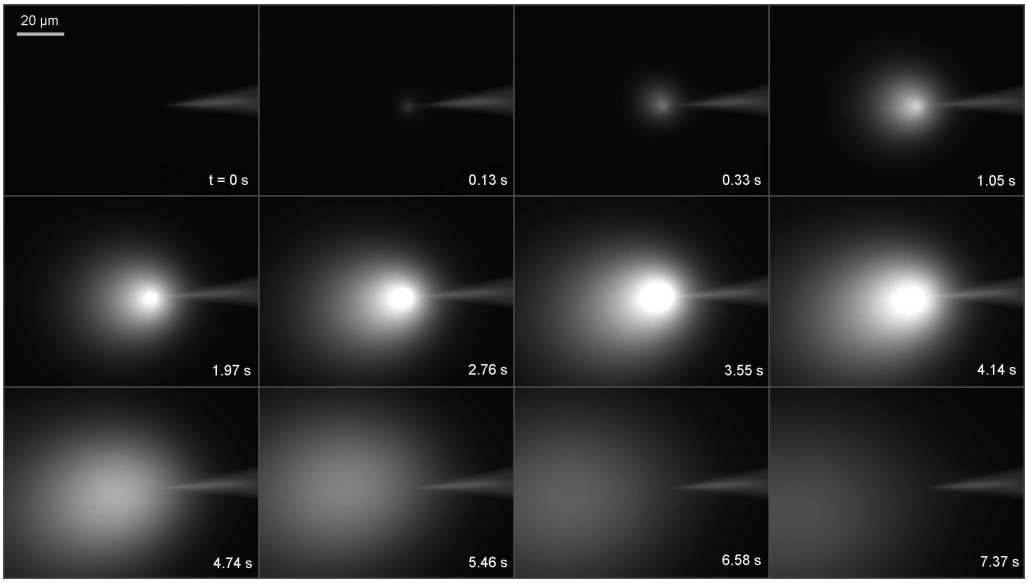

Figure 10.5: Injection of a water solution containing a fluorescent marker (calcein 96 mM) from a micropipette in the conditions under which the basic solution is injected in our experiments: injection pressure $\Delta P = 200$ hPa, microcapillary inner diameter 0.3 μm, injection duration $T = 4$ s.

As a consequence, the hypotheses in the calculation of C presented in Sec. 9.5 are well verified in our experiments. We can use Eq. (9.48) to express the concentration

field C of hydroxide ions outside the vesicle. Here, since we have injections that last for a given time T at constant injection pressure, the function F that describes the time evolution of the injection flow is $F = \mathbf{1}_{[0,T]}$, where we have chosen the injection start as our time origin $t = 0$. Hence, Eq. (9.48) yields

$$C\left(r, z, t\right) = S_0 \int_0^{\min(t,\, T)} dt'\, G\left(r, z, z_0, t - t'\right) \ , \tag{10.3}$$

where G is defined in Eqs. (9.49) and (9.50).

Using Eqs. (10.3), (9.49) and (9.50), it is straightforward to obtain an analytical expression for $C(r, z, t)$, and for its in-plane Fourier transform $\hat{C}(q, z, t)$. Since $\hat{\phi}(q, t)$ is proportional to $\hat{C}\left(q, z = 0, t\right)$, we also obtain its analytical expression, which reads

$$\hat{\phi}\left(q, t\right) = \hat{\phi}_1\left(q, t\right) - \theta(t - T)\, \hat{\phi}_1\left(q, t - T\right) \ , \tag{10.4}$$

with

$$\hat{\phi}_1\left(q, t\right) \propto \operatorname{erf}\left(q\sqrt{Dt} - \frac{z_0}{2\sqrt{Dt}}\right) \frac{\cosh\left(qz_0\right)}{qz_0} - \frac{\sinh\left(qz_0\right)}{qz_0}, \tag{10.5}$$

where erf denotes the error function. The value of the proportionality constant in this expression is not crucial for our study since all our dynamical equations are linear: it only affects the deformation and the antisymmetric scaled density by a multiplicative constant.

Now that we have determined $\hat{\phi}(q, t)$, which is involved in the forcing term $Y(q, t)$ of the dynamical equations (see Eqs. (9.38–9.39)), the time evolution of the membrane deformation during and after the microinjection can be determined by solving the differential equation Eq. (9.38). For this, we apply the method presented in Sec. 9.6. Hence, we can obtain the spatiotemporal evolution of the membrane deformation during and after the microinjection by carrying out the integrals in Eq. (9.54) numerically.

10.4.2 Membrane deformation height

In order to compare the predictions of our theoretical description to experimental results, we measured the height $H(t) = h(r = 0, t)$ of the membrane deformation in front of the micropipette during the microinjection experiments described in the experimental section (see, e.g., Fig. 10.1). Several microinjection experiments were carried out on GUVs, with an injection lasting $T = 4$ s, and with various distances z_0 between the micropipette and the membrane.

Given that our theory is linear, we expect it to be valid in the regime where $\phi \ll 1$ and $H \ll z_0$. Besides, as the unperturbed membrane is considered flat in our theory, its domain of validity is restricted to $z_0 \ll R$, where R is the radius of the GUV. Hence, we strived to remain in these conditions, and we shall present here only the experimental results that match these conditions best. In practice, the radii of our largest GUVs were of order 60 to 80 μm. We thus focused on values of z_0 in the range 10 to 30 μm. Besides, we adjusted the HO^- concentration for the various z_0 in order to obtain small but observable deformations, of order 1 to 5 μm. As long

as we remain in the linear regime, the absolute value of the concentration of the injected solution only affects the deformation by a global proportionality constant. This was checked experimentally, albeit in a rough fashion given the uncertainty on the radii of the different micropipettes used.

In order to compare the experimental data on $H(t)$ during and after the microinjection to the solutions of our theoretical equations, we normalize our experimental data on $H(t)$ by the value of $H(t = 4\,\mathrm{s})$, corresponding to the end of the injection, for each experiment. This eliminates the effect of the unknown proportionality constant in our theoretical expression of $\hat{\phi}$ (see Eqs. (10.4–10.5)), as well as the experimental effect of the different concentrations and of the slightly different micropipette diameters.

The membrane deformation $H(t) = h(r = 0, t)$ predicted theoretically using Eq. (9.54) together with Eq. (9.52) and Eqs. (10.4–10.5) was calculated numerically. This was done in the case of four-second injections, with the values of z_0 corresponding to the different experiments, and taking typical values of the membrane constitutive constants: $\kappa = 10^{-19}\,\mathrm{J}$, $k = 0.1\,\mathrm{N/m}$, $b = 10^9\,\mathrm{J.s.m^{-4}}$ and $e = 1$ nm, and $\eta = 10^{-3}\,\mathrm{J.s.m^{-3}}$ for the viscosity of water.

In order to solve the dynamical equations, it was also necessary to assign a value to the parameter

$$\alpha = -\frac{ke\bar{c}_0}{\sigma_1}\,, \tag{10.6}$$

which quantifies the importance of the change of the spontaneous curvature relative to the change of the equilibrium density of the external monolayer as a result of the chemical modification (see Sec. 9.3.2-b., Eq. (9.21)). This parameter cannot be determined from an analysis of static and global modifications of the environment of the vesicle. Indeed, the ADE model predicts that the equilibrium shape of a vesicle is determined by a combined quantity which involves both the equilibrium density and the spontaneous curvature [39, 220], as explained in Sec. 1.3.3. Rough microscopic lipid models, presented in Sec. 9.3.2-b., yield $\alpha \approx 1$: the effect of the change of the spontaneous curvature and that of the equilibrium density should have the same order of magnitude. In the absence of any experimental measurement of α, we took $\alpha = 1$ in our calculations. We also checked that the agreement between theory and experiment was not as good for $\alpha = 0.1$ and $\alpha = 10$ as it is for $\alpha = 1$.

Figs. 10.6 and 10.7 show the results obtained for several values of z_0, on two different vesicles. As these vesicles have the same lipid composition, their membranes share the same constitutive constants, as well as the same constants σ_1 and $\bar{c}_0$ that describe their response to ϕ. On the contrary, the membrane tension σ_0 is highly variable among vesicles. We did not measure this tension during the experiments, but since the vesicles are flaccid, σ_0 should be in the range $10^{-8} - 10^{-6}$ N/m. It was visible that the vesicle corresponding to Fig. 10.6 was more flaccid than that corresponding to Fig. 10.7. The parameter σ_0 was adjusted in these two cases, with all the other parameters kept constant at the above-mentioned values. More precisely, we integrated numerically our dynamical equations assuming various values of the tension σ_0. For each of the two vesicles, we calculated the total chi-square between these numerical results and the three experimental data sets

that respected best the hypotheses of our theory, i.e., small deformation and stable injection pressure (see Figs. 10.6(a) and 10.7(a)). For the vesicle corresponding to Fig. 10.6, the best match between theory and experiments, i.e., the lowest chi-square, was obtained for $\sigma_0 = (1.5 \pm 0.5) \times 10^{-8}$ N/m, and for the vesicle corresponding to Fig. 10.7, it was obtained for $\sigma_0 = (5 \pm 1) \times 10^{-7}$ N/m. These values are in the expected range, and the data corresponding to the most flaccid vesicle is best matched by the lowest tension, which is satisfactory.

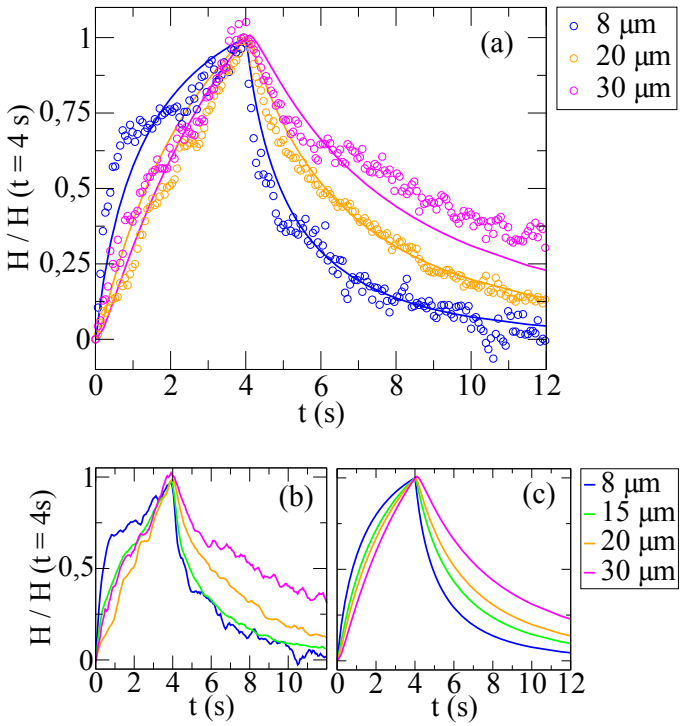

Figure 10.6: Normalized height $H(t)/H(t = 4\text{ s})$ of the membrane deformation, during and after microinjections lasting $T = 4$ s. The microinjections were carried out on the same GUV at different distances z_0, corresponding to the different colors. (a) Comparison between experimental data and theoretical calculations for three experiments. Dots: raw experimental data (one data point was taken every 57 ms). Solid lines: numerical integration of our dynamical equations with $\sigma_0 = 1.5 \times 10^{-8}$ N/m. (b) Full set of experimental data; a moving average over 4 successive points was performed to reduce the noise. (c) Full set of numerical data for values of z_0 corresponding to those of the experiments.

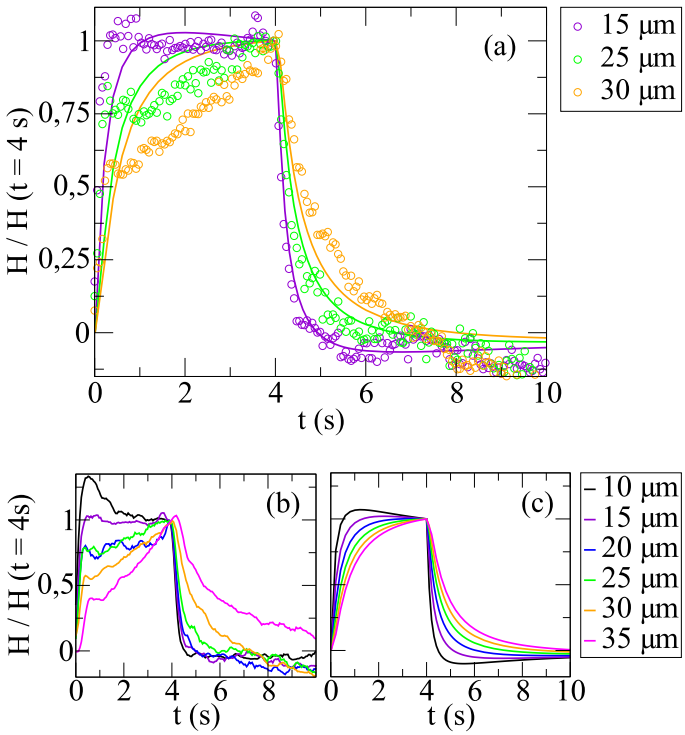

Figure 10.7: Similar data as on Fig. 10.6, but for another, less flaccid, vesicle. Here, the numerical integration of our dynamical equations was carried out for $\sigma_0 = 5 \times 10^{-7}$ N/m.

The experimental data presented in Figs. 10.6 and 10.7 is slightly noisy. This is due to the fact that we have focused on small deformations, of 1 to 5 μm, in order to remain in the domain of application of our linear theoretical description. For such small deformations, all sources of noise (e.g., vibrations) become important, and the pixel size also becomes limiting. Our image treatment plugins were equipped with subpixel resolution in order to improve this point (see, e.g., Ref. [247])[3]. Besides, it can be noted that the injection phase is more noisy than the relaxation phase, especially on Fig. 10.7. This is due to fluctuations of the injection pressure, which seem to occur mostly at the beginning of the injection phase. In particular, the excessive overshoots observed at the beginning of the injection on Fig. 10.7 are very likely due to this artifact.

Figs. 10.6 and 10.7 show a good agreement between our experimental data and the results of our theoretical description. In particular, our theory predicts the right timescales of deformation and of relaxation, and also the right variation of these timescales with the distance z_0 between the membrane and the micropipette. The increase of the timescales with z_0 comes from two different factors. First, the diffusion of the HO^- ions takes longer if z_0 is larger. Second, when z_0 increases, the width of the modified membrane zone that deforms increases, so that smaller wave vectors have a higher importance in $\hat{h}(q,t)$. As the relaxation timescales of the membrane, which correspond to the inverse of the eigenvalues of M, all increase

[3]We thank Rémy Colin for his precious help with writing the image treatment plugins.

when q decreases (see Eq. (9.39)), this yields longer timescales.

Besides, the timescales involved are shorter if the vesicle is more tense, for instance they are shorter in Fig. 10.7 than in Fig. 10.6. This can be understood as follows: one of the relaxation timescales of the membrane, which corresponds to the inverse of one of the eigenvalues of M (see Eq. (9.39)), can be approximated by $4\eta/\sigma_0 q$ for the wave vectors q with largest weight in $\hat{h}(q)$. This timescale decreases when σ_0 increases. More qualitatively, a tense membrane will tend to relax faster once it has been deformed.

While we have focused our discussion on the height $H(t) = h(r = 0, t)$ of the membrane deformation in front of the micropipette, the full deformation profiles $h(r, t)$ are available both experimentally and theoretically in our work. We observe qualitative agreement between theory and experiment regarding the spatial profile of h (and ϕ), but the effect of vesicle curvature makes it difficult to push further the quantitative analysis away from the micropipette axis.

10.5 Conclusion

We have studied experimentally and theoretically the deformation of a biomimetic lipid membrane in response to a local pH increase obtained by microinjecting a basic solution close to the membrane. Experimentally, we have measured the deformation height during and after the injection, and we have observed directly the pH profile on the membrane at the same time, using a pH-sensitive fluorescent membrane marker. Theoretically, our description of the phenomenon takes into account the linear dynamics of the membrane, and it also fully accounts for the time-dependent profile of the fraction of chemically modified lipids in the membrane. This profile results from the diffusion of the basic solution in the water that surrounds the membrane during and after the microinjection. We have compared experimental data regarding the height of the deformation to the results of our theoretical description, in the regime of small deformations, and we have obtained good agreement between theory and experiments.

Experimentally, it would be interesting to measure the vesicle tension through a micropipette [35] at the same time as the microinjection is performed. It would perhaps become possible to adjust the intermonolayer friction coefficient b (and hence to measure it) if the tension was known precisely. However, since high tensions yield shorter timescales and smaller deformations, it would be necessary to control precisely very small tensions through the micropipette.

From a theoretical point of view, our description is general and applies to a local injection of any substance that reacts reversibly with the membrane lipids. It could be improved by taking into account the curvature of the vesicle instead of taking a flat membrane as a reference state. Besides, it would be interesting to include nonlinear effects in order to describe larger, more dramatic, deformations, such as tubulation [219].

The study of the response of a membrane to a local modification of its environment is a promising field. From the point of view of membrane physics, studying

the spatiotemporal response of a membrane to a local modification can give access to membrane properties that were not accessible before. For instance, the ratio of the spontaneous curvature change to the equilibrium density change caused by a chemical modification cannot be determined from an analysis of static and global modifications [220]. In Chapter 11, we will present a way of determining this ratio from the study of the dynamical response of a membrane to a continuous local injection. Hence, an interesting perspective would be to study continuous injections experimentally, which could yield an experimental measurement of this ratio. However, the injection pressure would have to be very stable for this to be done satisfactorily. More generally, we hope that studying the response of a biomimetic membrane to a local modification of its environment will help to shed light onto the relation between cellular phenomena and small-scale environment changes.

Chapter 11

Membrane properties revealed by spatiotemporal response to a local inhomogeneity

Contents

11.1 Introduction **221**

11.2 Theoretical description **222**

11.2.1 Profile of the fraction of chemically modified lipids 222

11.2.2 Dimensionless form of the description 224

11.3 Extreme cases **225**

11.3.1 Equilibrium density change only 225

11.3.2 Spontaneous curvature change only 228

11.3.3 Qualitative picture of the dynamics 230

11.4 General case **232**

11.5 Conclusion **234**

11.1 Introduction

In Chapter 9, we presented a theoretical description of the dynamics of a lipid bilayer membrane submitted to a local chemical change of its environment. We focused on the case of a concentration increase of a substance that reacts reversibly and instantaneously with the membrane lipid headgroups, and we restricted to the regime of small deformations. In Chapter 10, we compared the predictions of this theoretical description to results of experiments in which a basic solution is microinjected close to a biomimetic membrane, and we obtained good agreement between theory and experiments. In the present Chapter, we investigate further the implications of our theoretical description. In general, the dynamics of the locally modified membrane is quite complex, as it involves the evolution of the

reagent concentration profile simultaneously as the response of the membrane. The spatiotemporal profile of the fraction of chemically modified lipids results from the local reagent concentration increase: it is determined by the reagent diffusion in the fluid above the membrane. Focusing on the case of a continuous reagent injection, we show that the effect of the evolution of the reagent concentration profile on the membrane dynamics becomes negligible some time after the beginning of the reagent concentration increase. Subsequently, the dynamics corresponds to the response of the membrane to an instantaneously imposed chemical modification. Studying this regime enables to extract properties of the membrane response.

This Chapter is organized as follows. In Sec. 11.2, we give the explicit expression of the spatiotemporal profile of the fraction of chemically modified lipids in the case of the continuous injection, and we present a dimensionless form of our theoretical description. We then move on to the analysis of the results of this description. In Sec. 11.3, we study separately the dynamics associated with each of the two effects that can arise from a chemical modification, namely a spontaneous curvature change and an equilibrium density change of the upper monolayer. We find that a local asymmetric density perturbation between the two monolayers of the membrane relaxes by spreading diffusively in the whole membrane. Intermonolayer friction plays a crucial part in this behavior. Then, in Sec. 11.4, we treat the general case where both effects are present, and we show how the ratio of the spontaneous curvature change to the equilibrium density change induced by the local chemical modification can be extracted from the dynamics, while it cannot be deduced from the study of static and global modifications [220].

The work presented in this Chapter is the subject of an article accepted for publication: A.-F. Bitbol and J.-B. Fournier, *Membrane properties revealed by spatiotemporal response to a local inhomogeneity*, Biochimica et Biophysica Acta: Biomembranes, in press (2012), cited as Ref. [248] here.

11.2 Theoretical description

In Chapter 9, we presented a theoretical description of the membrane deformation in response to the concentration increase of a reagent injected from a local source close to the membrane. In order to solve Eq. (9.38), which yields the evolution of the deformation profile of the membrane, we need to express explicitly the profile of the mass fraction ϕ of chemically modified lipids in the upper monolayer. Indeed, $\hat{\phi}(\boldsymbol{q}, t)$ is involved in the forcing term $Y(\boldsymbol{q}, t)$ of Eq. (9.38). The profile $\phi(\boldsymbol{r}, t)$ of the mass fraction of chemically modified lipids in the upper monolayer arises from the local reagent concentration increase.

11.2.1 Profile of the fraction of chemically modified lipids

We make the same assumptions regarding geometry and reagent behavior as in Chapter 9. Let us recall them briefly. We consider that the reagent source is localized in $(\boldsymbol{r}, z) = (\boldsymbol{0}, z_0 > 0)$, while the unperturbed membrane stands in the

plane $z = 0$ (see Fig. 9.2). The cylindrical symmetry of the problem then implies that the fields involved in our description only depend on $r = |\boldsymbol{r}|$. We focus on the regime of small deformations $h(r,t) \ll z_0$, and we work at first order in $h(r,t)/z_0$. In addition, we focus on reagents that react reversibly with the membrane lipid headgroups, and we assume that the reaction between the lipids and the reagent is diffusion-controlled. We restrict to the linear regime where $\phi(r,t)$ is proportional to the reagent concentration on the membrane: denoting by $C(r,z,t)$ the reagent concentration field, we have $\phi(r,t) \propto C(r,h(r,t),t)$. To first order in the membrane deformation, this can be simplified into $\phi(r,t) \propto C(r,0,t)$.

The field C is determined by the diffusion of the reagent from the local source in the fluid above the membrane. The calculation of C was presented in Sec. 9.5, and the general result is given by Eq. (9.48). Here, since we consider the case of a constant reagent flow from the local source, beginning at time $t = 0$, the function F that describes the time evolution of the injection flow is $F = \theta$, where θ denotes Heaviside's function. Hence, Eq. (9.48) yields

$$C\left(r,z,t\right) = S_0 \int_0^t dt'\, G\left(r,z,z_0,t-t'\right)\,, \tag{11.1}$$

where G is defined in Eqs. (9.49) and (9.50). The only difference with our description of the experimental situation in Sec. 10.4 is that the injection flow is continuous instead of stopping after time T. Mathematically, here, $F = \theta$, while in Sec. 10.4, we had $F = \mathbf{1}_{[0,T]}$.

Combining Eqs. (11.1), (9.49) and (9.50) provides an analytical expression for $C(r,z,t)$, and for $\hat{C}(q,z,t)$. Since $\hat{\phi}(q,t) \propto \hat{C}\left(q,0,t\right)$, we thus obtain an analytical expression for $\hat{\phi}$, which reads

$$\hat{\phi}\left(q,t\right) \propto \mathrm{erf}\left(q\sqrt{Dt} - \frac{z_0}{2\sqrt{Dt}}\right)\frac{\cosh\left(qz_0\right)}{qz_0} - \frac{\sinh\left(qz_0\right)}{qz_0}\,, \tag{11.2}$$

where erf denotes the error function, and D is the diffusion coefficient of the reagent. As expected, this is identical to Eq. (10.5), which gives the expression of $\hat{\phi}$ for $t < T$ in the case of an injection of duration T.

When $t \to \infty$, $\hat{\phi}(q,t)$ converges toward the stationary profile

$$\hat{\phi}_s(q) \propto \frac{e^{-qz_0}}{qz_0}\,. \tag{11.3}$$

Now that we have determined $\hat{\phi}(q,t)$, the time evolution of the membrane deformation can be determined by solving the differential equation Eq. (9.38), using the method presented in Sec. 9.6: the spatiotemporal evolution of the membrane deformation is obtained by carrying out the integrals in Eq. (9.54) numerically. While in Chapter 10, our aim was to compare with experimental data, in this Chapter, we wish to extract general properties of the membrane response. For this, let us put our description in dimensionless form before solving the equations. This is interesting both for physical understanding and for computational efficiency.

11.2.2 Dimensionless form of the description

Ten parameters are involved in our dynamical description (see Eqs. (9.38), (9.39), (9.40) and Eq. (11.2)): the membrane tension σ_0, its bending rigidity κ, its stretching modulus k, the distance e between the membrane midlayer and the monolayer neutral surfaces, the intermonolayer coefficient b, the constants σ_1 and $\bar{c}_0$ which describe the linear response of the membrane to the reagent, the viscosity η of the fluid above the membrane, the diffusion coefficient D of the reagent in this fluid, and the distance z_0 between the membrane and the reagent source.

Using the Buckingham Pi theorem and choosing z_0 as the distance unit, bz_0^2/k as the time unit and $\sigma_0 b^2 z_0^4/k^2$ as the mass unit, these ten parameters yield seven dimensionless numbers:

$$L_1 = \frac{1}{z_0}\sqrt{\frac{\kappa}{\sigma_0}}\,,\ L_2 = \frac{e}{z_0}\,,\ \Sigma_0 = \frac{\sigma_0}{k}\,,$$
$$\Delta = \frac{Db}{k}\,,\ \mu = \frac{\sigma_0 b z_0}{\eta k}\,,\ \Sigma_1 = \frac{\sigma_1}{k}\,,\ G = \bar{c}_0 z_0\,. \tag{11.4}$$

The parameters L_1 and L_2 compare the characteristic length scales $\sqrt{\kappa/\sigma_0}$ and e of the membrane to z_0, while Σ_0 is a dimensionless version of the membrane tension σ_0. Besides, the parameter Δ quantifies the importance of the reagent diffusion on the membrane dynamics. We will briefly discuss the effect of varying Δ in the following.

In the case of a lipid membrane in water, the only dimensional parameters that can span various orders of magnitudes are σ_0 and z_0. For $\sigma_0 \geq 10^{-8}\,\mathrm{N/m}$, i.e., for realistic membrane tensions, and for $z_0 \geq 5\,\mu\mathrm{m}$, we will see in the following that the only relevant dimensionless parameters in the dynamics of the membrane are μ and

$$\tilde{\alpha} = -\frac{\Sigma_0 L_1^2}{L_2}\frac{G}{\Sigma_1} = -\frac{\kappa\,\bar{c}_0}{\sigma_1 e}\,. \tag{11.5}$$

The first one, μ, then quantifies the ratio of the two eigenvalues of $M(q)$ for $q = 1/z_0$, and hence it is a crucial element of the membrane dynamical response. The second one, $\tilde{\alpha}$, quantifies the relative weight of the spontaneous curvature change and of the equilibrium density change of the upper monolayer due to the chemical modification. It is related to the parameter α used in Chapters 9 and 10 (see Eq. (10.6)) through

$$\tilde{\alpha} = \frac{\kappa}{k\,e^2}\,\alpha\,. \tag{11.6}$$

The effect of varying μ and $\tilde{\alpha}$ will thus be discussed in the following.

For our numerical calculations, we initially take

$$L_1 = 10^{-1},\ L_2 = 10^{-4},\ \Sigma_0 = 10^{-6},\ \Delta = 21.25,\ \mu = 10. \tag{11.7}$$

These values correspond to the injection of NaOH in water ($D = 2125\,\mu\mathrm{m}^2/\mathrm{s}$ [246]; $\eta = 10^{-3}\,\mathrm{J.s.m}^{-3}$) from a source at $z_0 = 10\,\mu\mathrm{m}$ above a floppy membrane with typical constants $\sigma_0 = 10^{-7}\,\mathrm{N/m}$, $\kappa = 10^{-19}\,\mathrm{J}$, $k = 0.1\,\mathrm{N/m}$, $e = 1$ nm and $b = 10^9\,\mathrm{J.s.m}^{-4}$. Note that the time unit bz_0^2/k is then equal to one second.

11.3 Extreme cases

In this Section, we will study the two extreme cases $G = 0$ and $\Sigma_1 = 0$. In other words, we will study separately the dynamics associated with an equilibrium density change and with a spontaneous curvature change of the upper monolayer. We will see that these two manifestations of the chemical modification of the membrane due to the reagent concentration increase yield different spatiotemporal evolutions of the membrane deformation[1]. The general case where both effects are present will then be discussed in Sec. 11.4.

A priori, the dynamics of the membrane deformation is quite complex, as it involves the evolution of the reagent concentration profile, due to diffusion, simultaneously as the response of the membrane. In order to investigate the effect of the reagent diffusion on the dynamics of the deformation, and to see when the effect of the evolution of the reagent concentration profile becomes negligible, we will compare the two following cases:
(i) the realistic case where $\hat{\phi}(q,t)$ is given by Eq. (11.2),
(ii) the theoretical case where the stationary modification ϕ_s in Eq. (11.3) is imposed instantaneously: $\hat{\phi}(q,t) = \hat{\phi}_s(q)\theta(t)$. Note that this case corresponds to the limit of very large Δ.

11.3.1 Equilibrium density change only

Let us first focus on the case where $G = 0$, in which only the equilibrium density of the upper monolayer is affected by the chemical modification. Fig. 11.1 shows the evolution with dimensionless time $\tau = kt/(bz_0^2)$ of the membrane deformation height $H(\tau) = h(0,\tau)$ in front of the source, and of the full width at half-maximum $W(\tau)$ of the deformation. The cases (i) and (ii) introduced above are presented. On these graphs, we also show $\Phi(\tau) = \phi(0,\tau)/\phi_s(0)$ and the full width at half-maximum W_ϕ of ϕ in case (i).

Fig. 11.1 shows that the membrane undergoes a transient deformation that relaxes to zero while getting broader and broader. The local asymmetric density perturbation relaxes by spreading in the whole membrane. However, this process is slowed down by intermonolayer friction, so the density asymmetry is transiently solved by a deformation of the membrane [230, 231]. This deformation is downwards if $\Sigma_1 > 0$, and upwards if $\Sigma_1 < 0$.

[1]This can be expected from the differences between the equilibrium states obtained with a static spatial profile of the mass fraction ϕ. These equilibrium states were studied in the two extreme cases $G = 0$ and $\Sigma_1 = 0$ in Sec. 9.3.2-a.

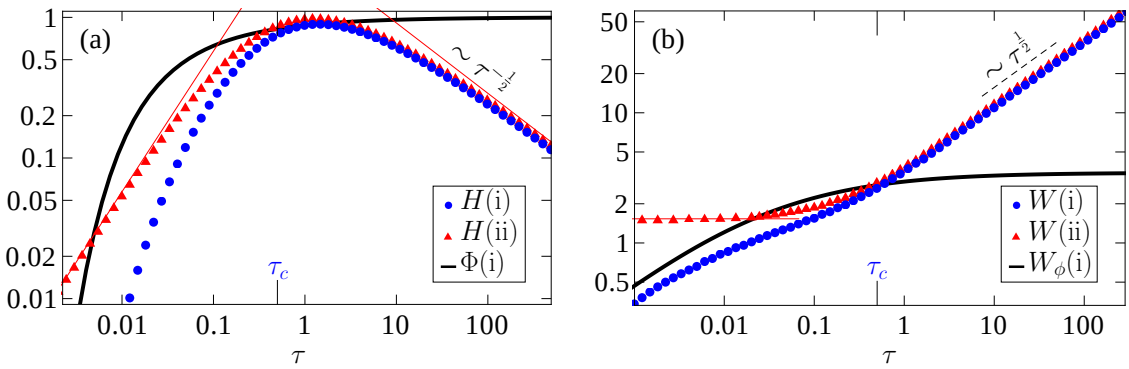

Figure 11.1: Dynamics of the membrane deformation in the extreme case $G = 0$, where only the equilibrium density is changed. The values taken for the other dimensionless numbers are those in Eq. (11.7). Both the realistic case (i) where reagent diffusion is accounted for, and the simpler case (ii) where the chemical modification is imposed instantaneously, are considered. (a) Logarithmic plot of the height of the membrane deformation H and of the fraction Φ of modified lipids in front of the reagent source versus dimensionless time τ. Both in case (i) and in case (ii), H is plotted in units of the extremal value it attains in case (ii). (b) Logarithmic plot of the width W of the membrane deformation and of the width W_ϕ of the fraction of modified lipids versus τ. Both W and W_ϕ are plotted in units of z_0. It can be seen on graphs (a) and (b) that cases (i) and (ii) yield similar dynamics for $\tau \gg \tau_c \approx 0.5$. The thin red (gray) lines correspond to the analytical laws mentioned in the text.

a. Effect of reagent diffusion

In the realistic case (i), at short times, the membrane dynamics is governed by the evolution of ϕ due to the reagent diffusion. Conversely, at long times, once ϕ is close enough to its steady-state profile ϕ_s, the dynamics of the membrane deformation is similar in case (i) and in case (ii). This can be seen in Fig. 11.1: first, H(i) and W(i) follow Φ and W_ϕ, and then, they have an evolution very similar to those of H(ii) and W(ii). Thus, after some time, the effect of reagent diffusion on the dynamics of the membrane deformation becomes negligible, and the dynamics of the realistic case (i) can be well approximated by that of the simpler case (ii), which corresponds to the response of the membrane to an instantaneously imposed modification.

The transition time, noted τ_c, between the diffusion-dominated regime and the membrane-response–dominated regime is determined by the convergence of ϕ to ϕ_s. As the reagent takes a dimensionless time $1/\Delta$ to diffuse from the source to the membrane, we expect $\tau_c \propto 1/\Delta$. We studied the dynamics of the deformation height for $\Delta \in [10^{-3}, 10^3]$ by integrating Eq. (9.38) numerically, and we found that this law is very well verified. For our standard value of Δ (see Eq. 11.7), used in Fig. 11.1, we have $\tau_c \approx 0.5 \approx 10/\Delta$.

b. Analytical insight

Let us discuss analytically the simple case (ii). The long-time behaviors obtained in this case are especially interesting, since they also apply to the realistic case (i). Let

us focus on $\sigma_0 \geq 10^{-8}$ N/m, i.e., on realistic membrane tensions, and let us keep the standard values of the other parameters involved in $M(q)$ (see below Eq. (11.7)), as these parameters cannot vary significantly for a membrane in water. The eigenvalues of $M(q)$ can then be approximated by $\gamma_1 = kq^2/(2b)$ and $\gamma_2 = \sigma_0 q/(4\eta)$ for all wave vectors with significant weight in $\hat{\phi}_s$ if $z_0 \geq 5\,\mu$m (see Sec. 9.4.3)[2]. This leads to a simple expression of the solution of the dynamical equation Eq. (9.38):

$$\hat{h}(p,\tau) \propto \frac{e^{-p\mu\tau/4} - e^{-p^2\tau/2}}{\mu - 2p}\,\hat{\phi}_s(p)\,, \tag{11.8}$$

with $p = qz_0$. This expression shows that the only parameter that is relevant in the dynamics is μ. Note that, in the realistic case (i), the value of Δ is relevant too.

In the long-time limit, as the deformation spreads, we have $2p \ll \mu$ for all the wave vectors with significant weight in $\hat{h}(p,\tau)$. In this case, calculating the inverse Fourier transform of Eq. (11.8) for $r = 0$ yields

$$H \sim 1/\sqrt{\tau}\,, \tag{11.9}$$

and the numerical results for W are in excellent agreement with

$$W \sim \sqrt{\tau}\,, \tag{11.10}$$

as can be seen in Fig. 11.1(b). This law can also be obtained analytically if ϕ_s is replaced by a Gaussian.

In the short-time limit, Eq. (11.8) yields $H \sim \tau$ and $W \to 2(2^{2/3} - 1)^{1/2} z_0$. These asymptotic behaviors, both for the short-time limit and for the much more interesting long-time limit, are plotted in red (gray) lines on Fig. 11.1.

The transition between the two asymptotic regimes is determined by the value of μ, which is the only parameter that controls the dynamics in case (ii). In particular, it is possible to show that the long-term scaling laws are valid for $\tau \gg \max(1, 1/\mu^2)$. We studied the dynamics of the deformation height for $\mu \in [10^{-3}, 10^3]$ by integrating Eq. (9.38) numerically, and we found that this law is very well verified.

c. Diffusive spreading of an antisymmetric density perturbation

The long-term scaling $W \sim \sqrt{\tau}$ shows that the local antisymmetric density perturbation spreads diffusively. Let us emphasize that this diffusive behavior is not related to the diffusion of the reagent in the solution above the membrane, as in the long-term limit, ϕ has reached its steady-state profile ϕ_s. The fact that the long-term scaling $W \sim \sqrt{\tau}$ holds in case (ii), where the profile ϕ_s is established instantaneously, as well as in case (i) (see Fig. 11.1(b)), illustrates that this scaling law is not related to the reagent diffusion.

[2] In Sec. 9.4.3, we assume that ϕ has a smooth profile with a characteristic width larger than about 10 μm. Since we consider here that $z_0 \geq 5\,\mu$m, and since the full width at half-maximum of ϕ_s is $2\sqrt{3}z_0$ (see Eq. 11.3), this condition is verified. In addition, we have checked that with $z_0 = 5\,\mu$m, taking $\gamma_1 = kq^2/(2b)$ and $\gamma_2 = \sigma_0 q/(4\eta)$ only yields an error of a few percent on the deformation profile.

The long-term diffusive spreading of the antisymmetric density perturbation can be understood as follows. At long times, the difference between the Stokes equations for each monolayer Eq. (9.35) and Eq. (9.36) can be approximated by

$$k\boldsymbol{\nabla}\left(r_a - \frac{\sigma_1}{k}\phi\right) + 2b\left(\boldsymbol{v}^+ - \boldsymbol{v}^-\right) = 0\,, \tag{11.11}$$

in real space. To obtain this equation from the difference between Eq. (9.35) and Eq. (9.36), we have used $\eta_2 q^2 \ll b$ and $\eta q \ll b$ (see below Eq. (9.39)), and also $|2e\,q^2\,\hat{h}| \ll |\hat{r}_a - \sigma_1\hat{\phi}/k|$, which holds for $\tau \gg 1$. The last relation can be shown using Eq. (11.8) in the long-time limit. Using Eq. (11.11), the antisymmetric convective mass current $\boldsymbol{j}_a = \boldsymbol{j}^+ - \boldsymbol{j}^-$ can be expressed to first order as

$$\boldsymbol{j}_a = \rho_0\left(\boldsymbol{v}^+ - \boldsymbol{v}^-\right) = -\rho_0\,\frac{k}{2b}\boldsymbol{\nabla}\left(r_a - \frac{\sigma_1}{k}\phi\right): \tag{11.12}$$

this current has a diffusive form. Combining this with the mass conservation relations in Eq. (9.37) finally yields the diffusion equation

$$\partial_t r_a - \frac{k}{2b}\nabla^2\left(r_a - \frac{\sigma_1}{k}\phi\right) = 0\,. \tag{11.13}$$

Hence, the local asymmetry in density between the two monolayers finally relaxes by spreading diffusively, with an effective diffusion coefficient $k/(2b)$. This slow relaxation is due to intermonolayer friction. Note that we can now interpret the dimensionless number Δ defined in Eq. (11.4) as (half) the ratio of the reagent diffusion coefficient D to this effective diffusion coefficient.

The fact that a local density asymmetry in the two monolayers of a membrane relaxes by spreading diffusively is generic. Here, the asymmetry is due to a local chemical modification of one monolayer, but it can also be caused, e.g., by a sudden flip of some lipids from one monolayer to the other [230]. Our description of this diffusive behavior generalizes that of Ref. [230], which focused on a perturbation with a spherical cap shape and a uniform density asymmetry.

11.3.2 Spontaneous curvature change only

Let us now focus on the second extreme case, where $\Sigma_1 = 0$, i.e., where only the spontaneous curvature of the upper monolayer is affected by the chemical modification. Fig. 11.2 shows that the deformation converges to a deformed profile, in contrast with the previous case: while a local density asymmetry spreads on the whole membrane, a local spontaneous curvature modification leads to a locally curved equilibrium shape. This is in agreement with our qualitative discussion of Sec. 9.3.2. The deformation is upwards if $G > 0$, and downwards if $G < 0$.

As in Sec. 11.3.1, in the realistic case (i), the membrane dynamics is governed by the reagent diffusion at short times $\tau \ll \tau_c$, while at long times $\tau \gg \tau_c$, it is similar in case (i) and in case (ii). The long-time dynamics thus corresponds to the response of the membrane to an instantaneously imposed chemical modification.

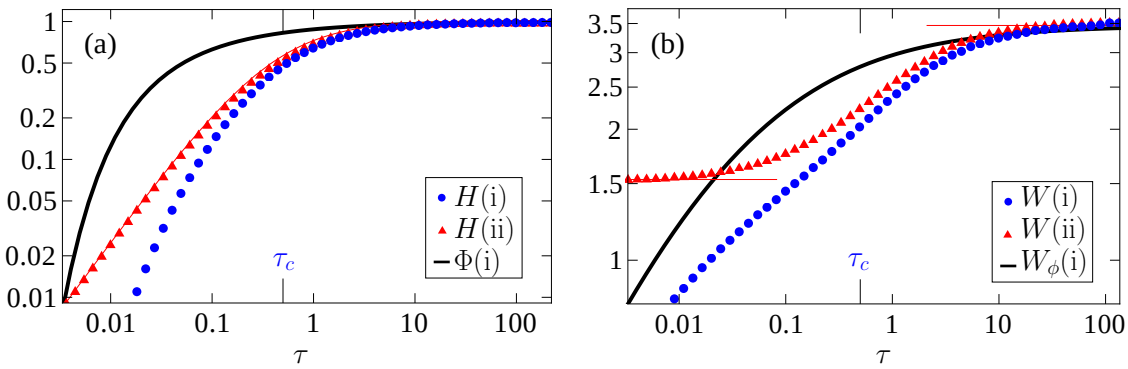

Figure 11.2: Dynamics of the membrane deformation in the extreme case $\Sigma_1 = 0$, where only the spontaneous curvature is changed. The values taken for the other dimensionless numbers are those in Eq. (11.7). Both the realistic case (i) where reagent diffusion is accounted for, and the simpler case (ii) where the chemical modification is imposed instantaneously, are considered. (a) Logarithmic plot of the height of the membrane deformation H and of the fraction Φ of modified lipids in front of the reagent source versus dimensionless time τ. Both in case (i) and in case (ii), H is plotted in units of the extremal value it attains in case (ii). (b) Logarithmic plot of the width W of the membrane deformation and of the width W_ϕ of the fraction of modified lipids versus τ. Both W and W_ϕ are plotted in units of z_0. It can be seen on graphs (a) and (b) that cases (i) and (ii) yield similar dynamics for $\tau \gg \tau_c \approx 0.5$. The thin red (gray) lines correspond to the analytical laws mentioned in the text.

In the simple case (ii), the approximations on γ_1 and γ_2 introduced in Sec. b. yield

$$\hat{h}(p,\tau) \propto \left(1 - e^{-p\mu\tau/4}\right) \hat{\phi}_s(p)\,, \tag{11.14}$$

where we have used the notation $p = qz_0$ as above. Calculating the inverse Fourier transform of this function for $r = 0$ yields

$$H \propto \frac{\mu\tau}{\mu\tau + 4}\,, \tag{11.15}$$

for all $\tau > 0$. This analytical law for the deformation height H is plotted in red (gray) lines in Fig. 11.2(a).

Let us focus on the long-time limit, which is especially interesting, since the results found in case (ii) also apply to the realistic case (i). Eq. (11.14) shows that in this limit, $\hat{h}(p,\tau) \propto \hat{\phi}_s(p)$, so that the long-time profile of the membrane deformation is fully determined by that of ϕ. In particular, for $\tau \to \infty$, $W_\phi \to 2\sqrt{3}\,z_0$ and $W \to 2\sqrt{3}\,z_0$.

For $\tau \to 0$, we find $W \to 2(2^{2/3} - 1)^{1/2} z_0$ again. These asymptotic behaviors regarding the deformation width W are plotted in red (gray) lines in Fig. 11.2(b), both for the short-time limit and for the much more interesting long-time limit.

As in Sec. 11.3.1, in case (ii), μ is the only relevant parameter in the dynamics of the membrane deformation (see Eq. (11.14)), and it determines the transition time between the two asymptotic regimes. In the realistic case (i), the value of Δ is relevant too.

11.3.3 Qualitative picture of the dynamics

Before moving on to the general case, which involves both an equilibrium density change and a spontaneous curvature change, let us present a qualitative picture of the dynamics in the two extreme cases we just studied. In Fig 11.3, we introduce a schematic representation of lipids: the preferred shape of a lipid is represented by a cone, superimposed on the lipid. The area per lipid on the neutral surface corresponds to the upper surface of this cone, while the spontaneous curvature is symbolized by the angle of the cone.

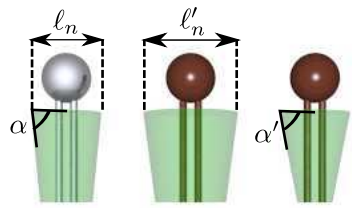

Figure 11.3: First lipid (light gray): non-modified lipid. The length ℓ_n represents the preferred diameter per lipid on the neutral surface, while the angle α quantifies the spontaneous curvature. Second and third lipids (brown): modified lipids. For the second lipid, the modification affects the preferred density on the neutral surface, but not the spontaneous curvature. It is the contrary for the third lipid.

We will now use this schematic representation to represent qualitatively the dynamics of a locally chemically modified membrane, in the simple case (ii) of an instantaneously imposed chemical modification.

a. Equilibrium density change only

Let us first focus on the case where only the equilibrium density is affected by the chemical modification. At $t = 0$, the preferred area per lipid suddenly increases for the lipids of the upper monolayer that are chemically modified. Thus, these modified lipids are effectively compressed (see Fig. 11.4(b)). In Sec. 9.4.3, we showed that, for large wavelengths, the dynamics of the symmetric density r_s is much faster than the coupled dynamics of the antisymmetric density r_a and of the deformation h. Hence, restricting to large wavelengths, we may consider that at $t = 0^+$, the equilibrium state $r_s = \sigma_1\phi/k$ (see Eq. (9.41)) has been reached, while $r_a = 0$ still holds. This yields $r^{\pm}(0^+) = \frac{1}{2}\sigma_1\phi/k$: half the compression of the lipids of the upper monolayer has relaxed, but the flow of the lipids of the upper monolayer has dragged the lipids of the lower monolayer, because of intermonolayer friction (see Fig. 11.4(c)).

After this very fast first step, the time evolution of the membrane deformation corresponds to that described in Sec. 11.3.1. The density asymmetry is transiently solved by a deformation of the membrane (see Fig. 11.4(d)). The final state corresponds to a non-deformed membrane (see Fig. 11.4(e)), once the local density asymmetry has relaxed by spreading in the whole membrane, through a relative sliding of the two monolayers, which is slowed down by intermonolayer friction.

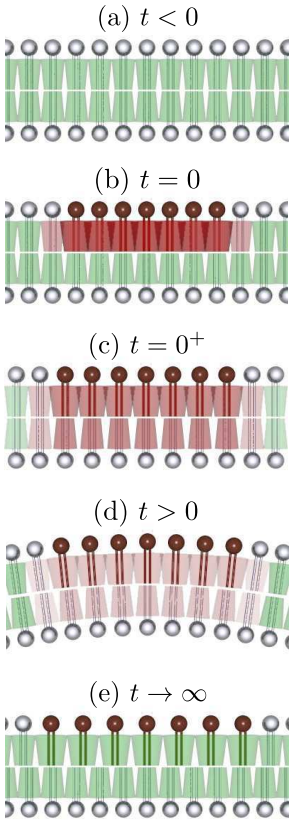

Figure 11.4: Qualitative representation of the dynamics if $G = 0$. The lipids that become chemically modified at $t = 0$ are represented in brown. The cones are in red for the lipids experiencing compression or dilation with respect to their preferred area and in light green otherwise. The intensity of the red color represents the degree of the compression or dilation.

b. Spontaneous curvature change only

Let us now discuss the opposite case, where only the spontaneous curvature is modified (see Sec. 11.3.2). At $t = 0$, the preferred curvature per lipid suddenly increases for the lipids of the upper monolayer that are chemically modified (see Fig. 11.5(b)). The membrane locally curves to accommodate the local increase of spontaneous curvature, and it reaches a deformed final state (see Fig. 11.5(c)).

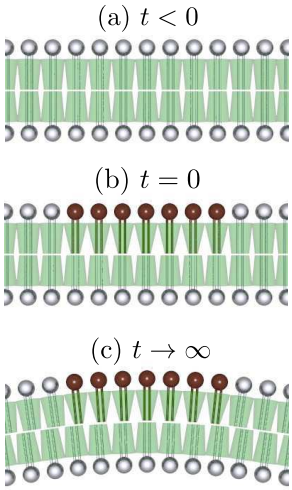

Figure 11.5: Qualitative description of the dynamics if $\Sigma_1 = 0$. Here, the modification affects the preferred curvature, but not the preferred density on the neutral surface.

11.4 General case

Generically, a chemical modification will affect both the equilibrium density and the spontaneous curvature of the upper monolayer. The general solution of Eq. (9.38) is a linear combination of the two solutions obtained for the two extreme cases: $G = 0$ (see Sec. 11.3.1) and $\Sigma_1 = 0$ (see Sec. 11.3.2). In this Section, we will only discuss the realistic case (i) where the reagent diffusion is taken into account. As in the two extreme cases, the effect on the membrane dynamics of the evolution of ϕ due to reagent diffusion is crucial for $\tau \ll \tau_c$, while it becomes negligible for $\tau \gg \tau_c$.

For a lipid membrane in water such that $\sigma_0 \geq 10^{-8}\,\mathrm{N/m}$ and for $z_0 \geq 5\,\mu\mathrm{m}$, we have seen that in both extreme cases, the dynamics is influenced only by μ and Δ (see Secs. 11.3.1–11.3.2). Hence, in the general case, the dynamics is influenced by μ, Δ, and by the parameter $\tilde{\alpha}$, defined in Eq. (11.5), which quantifies the relative importance of the spontaneous curvature change and of the equilibrium density change of the upper monolayer due to the chemical modification. Indeed, Eq. (9.13) shows that the absolute value of the ratio of the destabilizing normal force density arising from the spontaneous curvature change to that arising from the equilibrium density change is equal to $2|\tilde{\alpha}|$. The effect of varying Δ was discussed in Secs. 11.3.1–11.3.2, and in addition, Δ cannot vary much for a reagent injected in water above a lipid membrane. Hence, we will focus on the influence of μ and $\tilde{\alpha}$ on the membrane dynamics.

The value of $\tilde{\alpha}$ is *a priori* unknown, as σ_1 and $\bar{c}_0$, which are involved in Σ_1 and G, respectively (see Eq. (11.4)), are unknown. The actual values of σ_1 and $\bar{c}_0$ depend on the reagent as well as on the membrane itself, as these two parameters describe the linear response of the membrane to a reagent (see Sec. 9.3.2). Let us assume that $\tilde{\alpha} > 0$, i.e., that the equilibrium density change and the spontaneous

curvature change induce deformations in the same direction. This is true, e.g., for a chemical modification that affects the lipid headgroups in such a way that it yields an effective change of the preferred area per headgroup, as seen in Sec. 9.3.2-b. The rough microscopic models presented in that Section show that the destabilizing normal force densities due to the two effects should have similar magnitudes[3]. Thus, we expect $\tilde{\alpha} \approx 1$.

Fig. 11.6(a) shows the evolution of H in the realistic case (i) for three different values of $\tilde{\alpha}$. The deformation height features an extremum H_e, and then a relaxation. This behavior is due to the change of the equilibrium density (see Sec. 11.3.1). Conversely, the nonzero asymptotic deformation H_∞ arises from the change of the spontaneous curvature (see Sec. 11.3.2). The relative importance of H_e to H_∞ thus depends on $\tilde{\alpha}$. This means that studying the dynamics of the membrane deformation in response to a local chemical modification provides information on the ratio of the spontaneous curvature change to the equilibrium density change induced by this chemical modification.

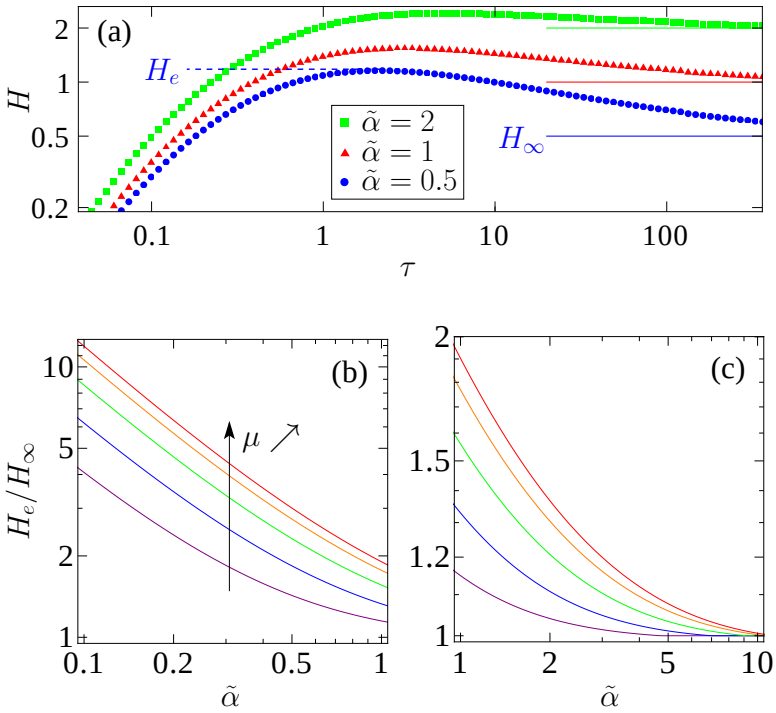

Figure 11.6: (a): Logarithmic plot of the height of the membrane deformation H in front of the reagent source versus dimensionless time τ in the realistic case (i), for different values of $\tilde{\alpha}$. The values taken for the other dimensionless numbers are those in Eq. (11.7). In each case, H is plotted in units of its asymptotic value in the case $\tilde{\alpha} = 1$. The lines show the asymptotic values H_∞ of H for $\tau \to \infty$ in each case, and H_e denotes the extremal value of H. (b) and (c): Logarithmic plot of H_e/H_∞ versus $\tilde{\alpha}$ in the realistic case (i), for different values of μ. From down to up: $\mu = 1$; $\mu = 10^{0.5} \simeq 3.2$; $\mu = 10$; $\mu = 10^{1.5} \simeq 32$; $\mu = 10^2$.

[3]More precisely, the rough microscopic models presented in Sec. 9.3.2-b. yield $\alpha \approx 1$. Using Eq. (11.6) and the typical values of k, e and κ given after Eq. (11.7) yields $\tilde{\alpha} \approx \alpha$, so that $\tilde{\alpha} \approx 1$.

In Fig. 11.6(b)–(c), the ratio H_e/H_∞ is plotted versus $\tilde{\alpha}$ for different values of μ. Indeed, as mentioned above, the membrane dynamics is determined both by $\tilde{\alpha}$ and by μ (at constant Δ). The order of magnitude of H_e can be estimated assuming an equilibrium density change and/or a spontaneous curvature change of a few percent: H_e is of order $1 - 10\,\mu$m for flaccid membranes, and smaller than $0.1\,\mu$m if $\sigma_0 \geq 10^{-5}\,$N/m. Hence, we choose $\sigma_0 \in [10^{-8}, 10^{-6}]\,$N/m, which yields $\mu \in [1, 100]$ for $z_0 = 10\,\mu$m: such values are taken in Fig. 11.6(b)–(c).

Our study shows that one can deduce $\tilde{\alpha}$, and thus the relative importance of the spontaneous curvature change to the equilibrium density change due to a chemical modification, from the measurement of H_e/H_∞. This is very interesting, given that such information cannot be deduced from the study of static and global membrane modifications [39, 220] (see Sec. 8.2.3). Indeed, the equilibrium vesicle shapes in the ADE model are determined by the combined quantity $\overline{\Delta a_0}$, which involves both the equilibrium density and the spontaneous curvature [39] (see Sec. 1.3.3). As mentioned in Sec. 8.2.3, the vesicle shape variations due to global modifications of the vesicle environment are usually interpreted as coming only from a change of the spontaneous curvature, under the assumption that the preferred area per lipid is not modified [220–222].

In order to determine $\tilde{\alpha}$ in a practical case, it is necessary to know the value of μ (see Fig. 11.6(b)–(c)). However, as μ does not involve any parameter that depends on the reagent (see Eq. (11.4)), it is possible to compare the effects of different reagents on the same membrane, i.e., their values of $\tilde{\alpha}$, even without knowing the precise value of μ.

11.5 Conclusion

In general, the dynamics of the deformation of a membrane submitted to a local chemical heterogeneity is quite complex, as it involves the evolution of the reagent concentration profile due to diffusion, simultaneously as the response of the membrane. We have shown that, some time after the beginning of the reagent concentration increase, the effect of the evolution of the reagent concentration becomes negligible.

Studying this regime enables to extract interesting properties of the membrane response. We have shown that a local density asymmetry between the two monolayers relaxes by spreading diffusively in the whole membrane. Intermonolayer friction plays a crucial part in this behavior. In addition, we have shown how the relative importance of the spontaneous curvature change to the equilibrium density change can be extracted from the dynamics of the membrane response to the local chemical modification. Such information cannot be deduced from the study of a static and global modification.

Our description provides a theoretical framework for experiments involving the microinjection of a reagent close to biomimetic membranes. In Chapter 10, we have used our theoretical model to analyze experimental results corresponding to brief microinjections of a basic solution. The results of the present Chapter show that

it would be interesting to conduct experiments with a continuous injection phase, where $\tilde{\alpha}$ could be determined.

In biomimetic membranes as well as in cells, remarkable phenomena occur in the regime of larger deformations: cristae-like invaginations [213], tubulation [219], pearling [235], budding, exo- or endocytosis [211], etc. To study such phenomena, it would be useful to pursue our study in the nonlinear regime.

Chapter 12

A tool: the membrane stress tensor in the presence of density and composition inhomogeneities

Contents

12.1 Introduction **238**

12.2 Stress tensor formal derivation **238**

12.3 Monolayer model **242**

12.3.1 Hamiltonian density in terms of local variables 242

12.3.2 Consistency with the ADE model 245

12.4 Projected stress tensor **247**

12.4.1 Stress tensor of a monolayer 247

12.4.2 Comparison with the stress tensor associated with the Helfrich model 248

12.4.3 Stress tensor in the ADE model 249

12.5 Force density in a monolayer **250**

12.5.1 Calculation from the projected stress tensor 250

12.5.2 Direct covariant calculation 251

12.5.3 Comparison between the two results 253

12.6 Applications **254**

12.6.1 Forces arising from a modification of composition 255

12.6.2 Forces arising from a local deformation at uniform density 256

12.7 Conclusion **258**

12.8 Appendix A: Covariant calculation of the force density **259**

12.9 Appendix B: Tangential stress tensor at second order . **261**

12.1 Introduction

In this Chapter, we derive a fundamental tool: the stress tensor of a membrane monolayer of variable shape, variable lipid density and variable composition. Understanding forces in complex membranes with various degrees of freedom is crucial to understand their equilibrium shape and their dynamics [249, 250]. The divergence of the stress tensor gives the density of elastic forces in the membrane, which is the basis of a dynamical description, as seen in Chapter 9. Moreover, the stress tensor provides the forces exchanged through a boundary. This is a valuable information that can be used, for instance, in the calculation of membrane-mediated interactions [251]. In Chapter 3, we used the stress tensor associated with the Helfrich model to calculate the fluctuations of the Casimir-like force between two membrane inclusions [114].

The present Chapter is organized as follows: in Sec. 12.2, we express formally the membrane stress tensor as a function of the Hamiltonian density by means of the principle of virtual work. In Sec. 12.3, following Ref. [224], we construct a Hamiltonian density for one and two-component monolayers, which is shown to be a local version of the area-difference elasticity (ADE) model. In Sec. 12.4, we derive the stress tensor associated with this Hamiltonian density. This stress tensor generalizes the one associated with the Helfrich model [101, 113], and can be specialized to obtain the one associated with the ADE model. In Sec. 12.5, we derive the force density in the membrane from our stress tensor, and we also directly obtain this force density in covariant formalism. Finally, in Sec. 12.6, we show how our results enable to understand the forces and the dynamics in the case of a local perturbation of a membrane by the microinjection of a reagent.

The work presented in this Chapter has been published in: A.-F. Bitbol, L. Peliti and J.-B. Fournier, *Membrane stress tensor in the presence of lipid density and composition inhomogeneities*, European Physical Journal E 34, 53 (2011), cited as Ref. [187] here.

12.2 Stress tensor formal derivation

Let us consider one monolayer of the bilayer. We describe its shape in the Monge gauge by the height $z = h(x, y)$ of a surface $\mathcal{S}$ parallel to its hydrophobic interface with the other monolayer, with respect to a reference plane (x, y). We do not assume yet that the membrane is weakly deformed. Let $\bar{\rho}(x, y)$ be the *projected* mass density, i.e., the lipid mass per unit area of the reference plane (x, y). In order to study the case of a two-component monolayer, let us denote by $\phi(x, y)$ the local mass fraction of one of the two lipid species, say species number 1. The case of a one-component monolayer can be obtained by setting $\phi = 0$.

Let $\bar{f}(\bar{\rho}, \phi, h_i, h_{ij})$ be the projected Hamiltonian density of the monolayer (i.e., the effective Hamiltonian per unit area of the reference plane). Here and in the following, Latin indices represent either x or y (not z) and $h_i \equiv \partial_i h$, $h_{ij} \equiv \partial_i \partial_j h$, etc. Note that we are assuming that the effective Hamiltonian depends only on the mass density, on the local lipid composition, and on the slope and curvature of the

monolayer. In contrast with what we did in Part II, we neglect the gradients of the lipid density. It means that the model presented here is valid at length scales much larger than the correlation length of the density fluctuations, which should not exceed the monolayer thickness (far from a critical point). Here, our aim is not to describe bilayer elasticity at the nanoscale. In addition, we discard terms involving the gradient of the curvature, and higher-order derivatives: this approximation has already proven successful in membrane descriptions [24, 39].

Let us consider an infinitesimal cut separating a region 1 from a region 2 in the monolayer, and let us denote by $\boldsymbol{m}$ the normal to the *projected* cut directed toward region 1 (see Fig. 12.1). The *projected stress tensor* $\boldsymbol{\Sigma}$ relates linearly the force $d\boldsymbol{f}$ that region 1 exerts onto region 2 to the vectorial length $\boldsymbol{m}\,ds$ of the projected cut through

$$d\boldsymbol{f} = \boldsymbol{\Sigma}\,\boldsymbol{m}\,ds\,. \tag{12.1}$$

This defines the six components of the projected stress tensor: Σ_{ij} and Σ_{zj}, where $i \in \{x, y\}$ and $j \in \{x, y\}$ [113].

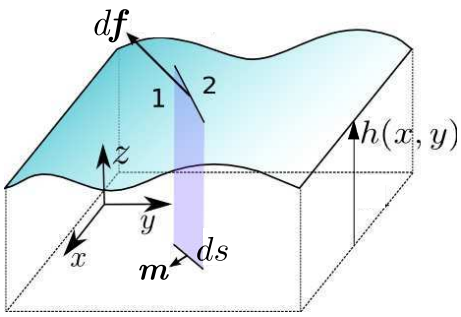

Figure 12.1: Sketch of a membrane in the Monge gauge, featuring an infinitesimal cut between separating a region 1 from a region 2. *Original illustration from Ref. [33], adapted and modified.*

To determine the projected stress tensor, we will follow the method presented in Ref. [113], which is based on the principle of virtual work. Let us consider a monolayer patch standing above a domain Ω of the reference plane. This patch is supposed to be a *closed system* with fixed total mass of each lipid species. Its effective Hamiltonian reads

$$F = \int_\Omega d^2r\, \bar{f}\left(\bar{\rho}, \phi, h_i, h_{ij}\right)\,. \tag{12.2}$$

In order to deal with arbitrarily deformed states of the monolayer patch, we assume that in addition to the boundary forces (and torques) exerted by the rest of the monolayer, the patch is submitted to a surface density $\boldsymbol{w}(x, y)$ of external forces, and to individual external forces acting on the molecules and deriving from a one-body potential energy $v_\alpha(x, y)$ for the lipid species $\alpha \in \{1, 2\}$. The former forces control the shape of the patch and the latter control the mass density distribution

of the lipids within the patch. The total potential energy corresponding to these latter forces can be written as

$$E_p = \int_\Omega dn_1 v_1 + dn_2 v_2 = \int_\Omega d^2r \left[\bar{\rho}\phi \frac{v_1}{\mu_1} + \bar{\rho}(1-\phi)\frac{v_2}{\mu_2} \right] , \tag{12.3}$$

where $d^2r = dx\,dy$, and μ_α denotes the mass of one lipid of the species α. Introducing $v = v_2/\mu_2$ and $u = v_1/\mu_1 - v_2/\mu_2$, this potential energy can be rewritten as:

$$E_p = \int_\Omega d^2r \left[\bar{\rho} v + \bar{\rho}\phi u \right] . \tag{12.4}$$

At equilibrium, the lipid density $\bar{\rho}$, the composition ϕ and the shape h of the monolayer are controlled by the external actions represented by $u(x,y)$, $v(x,y)$ and $\boldsymbol{w}(x,y)$.

Let us study a small deformation of the monolayer patch at equilibrium: $\Omega \to \Omega + \delta\Omega$, $h \to h + \delta h$, $\bar{\rho} \to \bar{\rho} + \delta\bar{\rho}$ and $\phi \to \phi + \delta\phi$. Each element of the patch, initially at position (x,y), undergoes a displacement $\delta\boldsymbol{a}(x,y)$, with $\delta a_z = \delta h + h_k \delta a_k$ [113]. The variation of the effective Hamiltonian of the monolayer patch during the deformation reads

$$\delta F = \int_\Omega d^2r \left[\frac{\partial \bar{f}}{\partial \bar{\rho}}\delta\bar{\rho} + \frac{\partial \bar{f}}{\partial \phi}\delta\phi + \frac{\partial \bar{f}}{\partial h_i}\delta h_i + \frac{\partial \bar{f}}{\partial h_{ij}}\delta h_{ij} \right] + \int_{\delta\Omega} d^2r\, \bar{f}, \tag{12.5}$$

We now perform two integrations by parts, and we use the relation

$$\int_{\delta\Omega} d^2r = \int_{\mathcal{B}} ds\, m_i\, \delta a_i \,, \tag{12.6}$$

where $\mathcal{B}$ denotes the boundary of Ω. Assuming that the translation of the monolayer edges is performed at a fixed orientation of its normal, so that $\delta h_j = -h_{jk}\delta a_k$ along the boundary [113], we obtain

$$\begin{aligned} \delta F &= \int_\Omega d^2r \left[\frac{\partial \bar{f}}{\partial \bar{\rho}}\delta\bar{\rho} + \frac{\partial \bar{f}}{\partial \phi}\delta\phi + \frac{\delta F}{\delta h}\delta h \right] \\ &+ \int_{\mathcal{B}} ds\, m_i \left\{ \bar{f}\delta a_i + \left[\frac{\partial \bar{f}}{\partial h_i} - \partial_j \frac{\partial \bar{f}}{\partial h_{ij}} \right] \delta a_z \right. \\ &+ \left. \left[\left(\partial_j \frac{\partial \bar{f}}{\partial h_{ij}} - \frac{\partial \bar{f}}{\partial h_i} \right) h_k - \frac{\partial \bar{f}}{\partial h_{ij}} h_{jk} \right] \delta a_k \right\}, \end{aligned} \tag{12.7}$$

where

$$\frac{\delta F}{\delta h} = \partial_k \partial_j \frac{\partial \bar{f}}{\partial h_{jk}} - \partial_j \frac{\partial \bar{f}}{\partial h_j} \,. \tag{12.8}$$

The potential energy variation during the deformation is

$$\delta E_p = \int_\Omega d^2r \left[(v + u\phi)\, \delta\bar{\rho} + u\bar{\rho}\, \delta\phi \right] + \int_{\mathcal{B}} ds\, m_i\, \delta a_i \left[v\bar{\rho} + u\bar{\rho}\phi \right] . \tag{12.9}$$

The total variation $\delta F + \delta E_p$ of the energy of the system must be balanced by the work δW done by the surface force density $\boldsymbol{w}$ and by the boundary forces exerted by the rest of the membrane on our patch. Since the translation of the monolayer edges is performed at a fixed orientation of its normal, the torques produce no work. We may write

$$\delta W = \int_\Omega d^2r \left[w_k \delta a_k + w_z \delta a_z\right] + \int_{\mathcal{B}} ds\, m_i \left[\Sigma_{ki}\delta a_k + \Sigma_{zi}\delta a_z\right] . \tag{12.10}$$

As the monolayer patch is considered as a closed system, the total mass of each lipid species in the patch is constant during our deformation:

$$\int_\Omega d^2r\, \bar{\rho} = M \;\text{ and }\; \int_\Omega d^2r\, \bar{\rho}\phi = M_1, \tag{12.11}$$

where M and M_1 are constants. Let us introduce two constant Lagrange multipliers λ and μ to implement these two global constraints. The relation $\delta F + \delta E_p - \delta W + \lambda\delta M + \mu\delta M_1 = 0$ must hold for any infinitesimal deformation of the monolayer patch. The identification of bulk terms in this relation yields

$$w_z = \frac{\delta F}{\delta h} \text{ and } w_k = -h_k w_z\,, \tag{12.12}$$

$$\frac{\partial \bar{f}}{\partial \bar{\rho}} = -(v+\lambda) - (u+\mu)\phi\,, \tag{12.13}$$

$$\frac{\partial \bar{f}}{\partial \phi} = -(u+\mu)\bar{\rho}\,. \tag{12.14}$$

By identifying the boundary terms and using Eq. (12.13), we obtain the components of the membrane stress tensor:

$$\Sigma_{ij} = \left(\bar{f} - \bar{\rho}\frac{\partial \bar{f}}{\partial \bar{\rho}}\right)\delta_{ij} - \left(\frac{\partial \bar{f}}{\partial h_j} - \partial_k \frac{\partial \bar{f}}{\partial h_{kj}}\right) h_i - \frac{\partial \bar{f}}{\partial h_{kj}} h_{ki}, \tag{12.15}$$

$$\Sigma_{zj} = \frac{\partial \bar{f}}{\partial h_j} - \partial_k \frac{\partial \bar{f}}{\partial h_{kj}}, \tag{12.16}$$

which generalizes the result of Ref. [113] to the case where there are inhomogeneities in ρ and ϕ. Note that the fraction of each lipid species does not appear explicitly in this result. Therefore, Eqs. (12.15)–(12.16) hold both for one-component monolayers and for two-component monolayers. Note also that $\boldsymbol{\Sigma}$ does not depend directly on the external actions, which confirms its intrinsic nature.

Comparing our result with Ref. [113] shows that taking into account lipid density variations only changes the isotropic term of the stress tensor, which now reads $\bar{f} - \bar{\rho}\,\partial\bar{f}/\partial\bar{\rho}$. This term is reminiscent of minus the pressure of a two-dimensional homogeneous fluid binary mixture with area A described by an effective Hamiltonian $F(T, A, N_1, N_2) = Af(T, \rho, \phi)$:

$$-P = \left.\frac{\partial F}{\partial A}\right|_{T,N_1,N_2} = f - \rho \left.\frac{\partial f}{\partial \rho}\right|_{T,\phi} . \tag{12.17}$$

While the last expression can be used locally in a non-homogeneous fluid mixture, the case of the membrane is more complex since its effective Hamiltonian depends on the curvature. The "surface pressure" in a membrane is sometimes defined as $\rho\,\partial g/\partial\rho - g$ where g is the part of the membrane Hamiltonian density f that depends only on ρ [252] or, equivalently, what remains of f for a planar membrane [232]. Interestingly, we find that the isotropic part of the membrane stress tensor does not identify to minus this surface pressure, since it is the complete, curvature-dependent projected Hamiltonian density $\bar{f}$ that appears in $\bar{f} - \bar{\rho}\,\partial\bar{f}/\partial\bar{\rho}$.

The divergence of the stress tensor gives the force per unit area, $\boldsymbol{p}$, exerted by the rest of the monolayer on the patch. By direct differentiation, we obtain:

$$p_z = \partial_j \Sigma_{zj} = -\frac{\delta F}{\delta h}, \tag{12.18}$$

$$p_i = \partial_j \Sigma_{ij} = \frac{\delta F}{\delta h} h_i - \bar{\rho}\,\partial_i \frac{\partial \bar{f}}{\partial \bar{\rho}} + \frac{\partial \bar{f}}{\partial \phi}\partial_i \phi, \tag{12.19}$$

where we have used $\partial_i f = (\partial\bar{f}/\partial\bar{\rho})\partial_i\bar{\rho} + (\partial\bar{f}/\partial\phi)\partial_i\phi + (\partial\bar{f}/\partial h_j)h_{ij} + (\partial\bar{f}/\partial h_{jk})h_{ijk}$. At equilibrium, we can use Eqs. (12.12)–(12.14) to express $\boldsymbol{p}$, which yields

$$p_z = -w_z, \tag{12.20}$$

$$p_i = -w_i + \bar{\rho}\partial_i v + \bar{\rho}\phi\partial_i u\,. \tag{12.21}$$

These relations constitute the balance of surface force densities for the monolayer at equilibrium. In particular, $\boldsymbol{p}$ vanishes at equilibrium when the membrane is submitted to no external actions (i.e. $\boldsymbol{w} = \boldsymbol{0}$ and $u = v = 0$).

12.3 Monolayer model

12.3.1 Hamiltonian density in terms of local variables

a. One-component monolayer

Let us derive the elastic effective Hamiltonian of a monolayer in a bilayer from basic principles, first for a one-component monolayer. We will recover and extend the model of Ref. [224], which corresponds to a local version of the ADE model.

We assume that the Hamiltonian density f per unit area of the monolayer depends only on the mass density ρ and on the local principal curvatures c_1 and c_2 of this monolayer. As explained at the beginning of the previous Section, the gradients of the curvature and of the density are neglected in our description. Note that, unlike $\bar{f}$ and $\bar{\rho}$, f and ρ are the effective Hamiltonian and the mass per actual unit area of the monolayer, and not per projected unit area. We use for both monolayers the density and the principal curvatures defined on the same surface $\mathcal{S}$ of the bilayer, so that the curvatures are common to the two monolayers.

We will consider the physically relevant regime of curvature radii much larger than the membrane thickness. We will also restrict ourselves to small variations of the density around a reference density ρ_0. Note that it can be convenient to take

ρ_0 different from the equilibrium density $\rho_{\rm eq}$ of a plane monolayer with fixed total mass, for instance to study a monolayer under tension. Let us define

$$r = \frac{\rho - \rho_0}{\rho_0} = \mathcal{O}(\epsilon), \tag{12.22}$$

$$H = (c_1 + c_2)\, e = \mathcal{O}(\epsilon), \tag{12.23}$$

$$K = c_1 c_2\, e^2 = \mathcal{O}\big(\epsilon^2\big), \tag{12.24}$$

where e is a small length in the nanometer range that allows to define the dimensionless total curvature H and the dimensionless Gaussian curvature K, while ϵ is a small dimensionless parameter used to control the order of our expansions. Since we typically expect $10^{-4} \leq |r| \leq 10^{-2}$ and $10^{-4} \leq |c_i\, e| \leq 10^{-2}$, it is sensible to assume that r and H are first-order quantities while K is a second-order quantity. The Hamiltonian density f is a function of the three dimensionless small variables r, H and K.

To study small deformations, we write a second-order expansion of f:

$$f(r, H, K) = \sigma_0 + A_1\, H + A_2\, (r - H)^2 + A_3\, H^2 + A_4\, K + \mathcal{O}\big(\epsilon^3\big). \tag{12.25}$$

Three comments are due here:
i) We have not included any term linear in r in this expansion. Indeed, the total mass of the monolayer, i.e. the integral of $\rho = \rho_0(1 + r)$, is assumed to be constant, so including a term linear in r is equivalent to redefining the constant term σ_0.
ii) The freedom associated with the choice of e allows to set the coefficient of $-rH$ equal to twice that of r^2.
iii) All the coefficients in Eq. (12.25) depend on the reference density ρ_0. We will come back in the following on the constitutive relation $\sigma_0(\rho_0)$.

Defining the constants κ, $\bar{\kappa}$, c_0 and k through

$$A_1 = -\frac{\kappa c_0}{2e}, \quad A_2 = \frac{1}{2}k, \quad A_3 = \frac{\kappa}{4e^2}, \quad A_4 = \frac{\bar{\kappa}}{2e^2}, \tag{12.26}$$

and setting $c = c_1 + c_2$, we obtain the following expression, which generalizes those of Refs. [224, 232]:

$$f = \sigma_0 + \frac{k}{2}\,(r - ec)^2 - \frac{\kappa c_0}{2}c + \frac{\kappa}{4}c^2 + \frac{\bar{\kappa}}{2}c_1 c_2 + \mathcal{O}\big(\epsilon^3\big). \tag{12.27}$$

Note that all the above terms have the same order of magnitude. Indeed, since typically $k \approx 10^{-1}\,\mathrm{J/m^2}$, $\kappa \approx \bar{\kappa} \approx 10^{-19}\,\mathrm{J}$, $e \approx 1\,\mathrm{nm}$ and $c_0^{-1} \approx 50\,\mathrm{nm}$ (see, e.g., Refs. [5, 27, 35]), we have $A_2 \approx A_3 \approx A_4 \approx 100\, A_1$. The advantage of the procedure we have employed is that we control precisely the order of the expansion.

In Eq. (12.27), e can be interpreted as the distance between the surface $\mathcal{S}$ where c_1, c_2 and r are defined and the neutral surface of the monolayer [27, 229]. As a matter of fact, the density on a surface parallel to $\mathcal{S}$ can be expressed as a function of the distance ℓ between $\mathcal{S}$ and this surface as $r(\ell) = r \pm \ell c + \mathcal{O}(\ell c)^2$, where the sign depends on the orientation. We choose the minus sign here, keeping in mind that the second monolayer then has the plus sign (see Fig. 12.2). Let us now consider

the surface such that $\ell = e$. If f is written as a function of $r(e) \equiv r_n$ and of the curvatures, it features no coupling between these variables. This corresponds to the definition of the neutral surface [27], which means that e is the distance between $\mathcal{S}$ and the neutral surface of the monolayer. On this surface, the density which minimizes f for any given membrane shape is ρ_0 (at first order in ϵ).

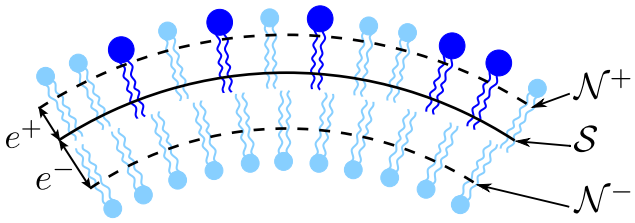

Figure 12.2: Schematic drawing of a lipid bilayer. The principal curvatures c_1, c_2 and the scaled densities $r^\pm$ of both monolayers are defined on $\mathcal{S}$. The distances between $\mathcal{S}$ and the neutral surfaces $\mathcal{N}^\pm$ of monolayers $\pm$ are denoted $e^\pm$. If the orientation convention is chosen in such a way that $c < 0$ on the drawing, the densities on $\mathcal{N}^\pm$ are $r_n^\pm = r^\pm \pm e^\pm c + \mathcal{O}(\epsilon^2)$. In this example, monolayer $+$ is constituted of two different lipid species.

Let us examine the case of a plane monolayer with fixed total mass. Its equilibrium density $\rho_{\text{eq}} = \rho_0 (1 + r_{\text{eq}})$ can be obtained by minimizing its effective Hamiltonian per unit mass

$$\frac{f}{\rho} = \frac{\sigma_0}{\rho_0}(1 - r) + \frac{k + 2\sigma_0}{2\rho_0} r^2 + \mathcal{O}(\epsilon^3) \tag{12.28}$$

with respect to r. We obtain the raw result $r_{\text{eq}} = \sigma_0/(k + 2\sigma_0)$. For our description to be consistent, r_{eq} must be first-order[1]. Hence, $\sigma_0/k = \mathcal{O}(\epsilon)$, which yields

$$r_{\text{eq}} = \frac{\sigma_0}{k}\,, \tag{12.29}$$

at first order. Hence

$$\sigma_0(\rho_0) = k\,\frac{\rho_{\text{eq}} - \rho_0}{\rho_{\text{eq}}} + \mathcal{O}\left(\frac{\rho_{\text{eq}} - \rho_0}{\rho_{\text{eq}}}\right)^2. \tag{12.30}$$

In particular, σ_0 vanishes when $\rho_0 = \rho_{\text{eq}}$.

b. Two-component monolayer

Let us now consider the case of a two-component monolayer. The mass fraction ϕ of one lipid species must be taken into accout in our monolayer model. In order to study small variations of ϕ around a reference value ϕ_0, we introduce a fourth small variable

$$\psi = \frac{\phi - \phi_0}{\phi_0} = \mathcal{O}(\epsilon)\,. \tag{12.31}$$

[1] In other words, we assume that our reference density ρ_0 is sufficiently close to ρ_{eq} for the second-order expansion of f to be valid at ρ_{eq}.

The expansion of f can now be written as:

$$\begin{aligned} f &= \sigma_0 + \sigma_1\psi + \frac{\sigma_2}{2}\psi^2 + \frac{k}{2}\left(r - ec\right)^2 - \frac{\kappa}{2}\left(c_0 + \tilde{c}_0\psi\right)c \\ &+ \frac{\kappa}{4}c^2 + \frac{\bar{\kappa}}{2}c_1c_2 + \mathcal{O}\left(\epsilon^3\right) , \end{aligned} \tag{12.32}$$

where all the coefficients depend on ϕ_0 as well as on ρ_0. It is not necessary to include a term in $r\psi$ in this expansion. As a matter of fact, the conservation of the total mass of each lipid species in the monolayer entails that the integral of $\rho\phi$ is a constant as well as the one of ρ, so a linear term in $r\psi$ would be redundant with the one in ψ.

The equilibrium density ρ_{eq} for a flat monolayer with a fixed total mass and a uniform lipid composition $\phi = \phi_0$ has the same expression Eq. (12.29) as in the case of a single-component monolayer, but its value depends on ϕ_0 since σ_0 and k do.

Expanding f in terms of small variables relies on the assumption that f is analytical. However, in the case where ϕ is very small, the effective Hamiltonian contains a non-analytic part, arising from the entropy of mixing (see, e.g., Ref. [233]), which reads per unit surface $\tilde{\sigma}(1+r)\phi\ln\phi$, with $\tilde{\sigma} = k_{\mathrm{B}}T\rho_0/\mu_1$, where μ_1 is the mass of one lipid of the species with mass fraction ϕ. In order to include this term, let us write f as:

$$\begin{aligned} f &= \sigma_0 + \sigma_1\psi + \frac{\sigma_2}{2}\psi^2 + [\![\tilde{\sigma}\left(1+r\right)\phi\ln\phi]\!] + \frac{k}{2}\left(r - ec\right)^2 \\ &- \frac{\kappa}{2}\left(c_0 + \tilde{c}_0\psi\right)c + \frac{\kappa}{4}c^2 + \frac{\bar{\kappa}}{2}c_1c_2 + \mathcal{O}\left(\epsilon^3\right) , \end{aligned} \tag{12.33}$$

where the term between double square brackets must be taken into account only if ϕ is very small, in which case ψ stands for ϕ and not for $(\phi - \phi_0)/\phi_0$. In the following, the double square brackets will always be used with this meaning.

12.3.2 Consistency with the ADE model

The area-difference elasticity (ADE) model [39–41] can be deduced from this model by considering a membrane made of two one-component monolayers (denoted $+$ and $-$ as on Fig. 12.2) with fixed total masses $M^{\pm}$, and by eliminating the densities by minimization [39]. Choosing $\rho_0^{\pm} = \rho_{\mathrm{eq}}^{\pm}$, which implies $\sigma_0^{\pm} = 0$, we have

$$f^{\pm} = \frac{k^{\pm}}{2}\left(r^{\pm} \pm e^{\pm}c\right)^2 \pm \frac{\kappa^{\pm}c_0^{\pm}}{2}c + \frac{\kappa^{\pm}}{4}c^2 + \frac{\bar{\kappa}^{\pm}}{2}c_1c_2 \,. \tag{12.34}$$

Since c_1 and c_2 are defined on the same surface $\mathcal{S}$ of the bilayer, and since a single orientation convention is adopted for both monolayers, the curvatures are common to the two monolayers. Here e^+ (resp. e^-) is the (positive) distance between $\mathcal{S}$ and the neutral surface of bilayer $+$ (resp. $-$). The $\pm$ sign in front of $c_0^{\pm}$ ensures that two identical monolayers forming a bilayer would share the same value of c_0. Note that the Hamiltonian density f defined in the previous Section corresponds to f^-.

Let us minimize with respect to $r^\pm$ the effective Hamiltonian of each monolayer with fixed total mass $M^\pm$ and total area A (defined on $\mathcal{S}$, like $r^\pm$ and c_1 and c_2). To take into account the constraints associated with the total masses, we introduce two Lagrange multipliers $\lambda^\pm$. We thus minimize $f^\pm - \lambda^\pm \rho_0^\pm (1 + r^\pm)$ with respect to $r^\pm$, which gives

$$r^\pm = \frac{\lambda^\pm \rho_0^\pm}{k^\pm} \mp e^\pm c\,. \tag{12.35}$$

Using the constraint $\int_A dA\, \rho_0^\pm (1 + r^\pm) = M^\pm$ yields

$$\frac{\lambda^\pm \rho_0^\pm}{k^\pm} = \frac{M^\pm}{\rho_0^\pm A} - 1 \pm \frac{e^\pm}{A} \int_A dA\, c\,. \tag{12.36}$$

Let us define the relaxed area $A_0^\pm$ of a monolayer as the area (defined on $\mathcal{S}$) that it would spontaneously adopt in the absence of any constraint:

$$A_0^\pm = M^\pm / \rho_0^\pm\,, \tag{12.37}$$

and its actual area $A^\pm$ measured on the neutral surface of the monolayer, which verifies:

$$\frac{A^\pm}{A} = 1 \mp \frac{e^\pm}{A} \int_A dA\, c + \mathcal{O}\big(\epsilon^2\big)\ . \tag{12.38}$$

We may then rewrite Eq. (12.36) as $\lambda^\pm \rho_0^\pm / k^\pm = (A_0^\pm - A^\pm)/A$, so that Eq. (12.35) becomes

$$r^\pm \pm e^\pm c = \frac{A_0^\pm - A^\pm}{A}\,. \tag{12.39}$$

Thus, after this partial minimization with respect to $r^\pm$, the monolayer Hamiltonian density can be written as

$$f^\pm = \frac{k^\pm}{2} \left(\frac{A^\pm - A_0^\pm}{A} \right)^2 \pm \frac{\kappa^\pm c_0^\pm}{2} c + \frac{\kappa^\pm}{4} c^2 + \frac{\bar\kappa^\pm}{2} c_1 c_2\,. \tag{12.40}$$

The total effective Hamiltonian F^b of the bilayer is obtained by integrating $f^+ + f^-$ over $\mathcal{S}$. Defining the bilayer elastic constants and spontaneous curvature as

$$\kappa^b = \frac{\kappa^+ + \kappa^-}{2}, \quad \bar\kappa^b = \frac{\bar\kappa^+ + \bar\kappa^-}{2}, \quad c_0^b = \frac{\kappa^- c_0^- - \kappa^+ c_0^+}{\kappa^+ + \kappa^-}, \tag{12.41}$$

we obtain

$$F^b = \frac{k^+}{2A} \left(A^+ - A_0^+\right)^2 + \frac{k^-}{2A} \left(A^- - A_0^-\right)^2 + \int_A dA \left[\frac{\kappa^b}{2} c^2 - \kappa^b c_0^b\, c + \bar\kappa^b\, c_1 c_2 \right]. \tag{12.42}$$

If the position of $\mathcal{S}$ in the bilayer, which was arbitrary until now, is chosen in such a way that

$$e^- k^- = e^+ k^+\,, \tag{12.43}$$

F^b can be written as

$$F^b = \frac{k^b}{A} \left(A - A_0\right)^2 + \frac{K^b}{4A} \left(\Delta A - \Delta A_0\right)^2 + \int_A dA \left[\frac{\kappa^b}{2} c^2 - \kappa^b c_0^b\, c + \bar\kappa^b\, c_1 c_2 \right], \tag{12.44}$$

with $\Delta A = A^- - A^+$, $\Delta A_0 = A_0^- - A_0^+$, and

$$k^b = \frac{k^+ + k^-}{2}, \quad K^b = \frac{2k^+k^-}{k^+ + k^-}, \quad A_0 = \frac{k^+A_0^+ + k^-A_0^-}{k^+ + k^-}. \tag{12.45}$$

Eq. (12.43) expresses that $\mathcal{S}$ is the neutral surface of the bilayer [253]. Thus, e^+ (resp. e^-) is the distance between the neutral surface of the monolayer + (resp. −) and the neutral surface of the bilayer.

The total effective Hamiltonian F^b of the bilayer Eq. (12.44), corresponds to the ADE model [39, 40] (see Sec. 1.3.3, in particular Eq. (1.14)). Hence, our model, which accounts for density heterogeneities in each monolayer, can be viewed as a local version of the ADE model.

12.4 Projected stress tensor

12.4.1 Stress tensor of a monolayer

In order to obtain the projected stress tensor of our monolayer, we need to determine the projected energy density $\bar{f}(\bar{r}, \psi, h_i, h_{ij})$ associated with $f(r, \psi, c_1, c_2)$. We now assume that the monolayer exhibits only small deviations from the reference plane (x, y). Then, if $h_i = \mathcal{O}(\epsilon)$ and $e\, h_{ij} = \mathcal{O}(\epsilon)$, Eqs. (12.23)–(12.24) are satisfied because $e\,(c_1 + c_2) = e\,c = e\,\nabla^2 h + \mathcal{O}(\epsilon^3)$ and $e^2\, c_1 c_2 = e^2\, \det(h_{ij}) + \mathcal{O}(\epsilon^4)$.

The projected Hamiltonian density $\bar{f}$ and the projected mass density $\bar{\rho}$ are given by

$$\bar{f} = f\sqrt{1 + (\boldsymbol{\nabla} h)^2} = f + \frac{\sigma_0}{2}\,(\boldsymbol{\nabla} h)^2 + \mathcal{O}\big(\epsilon^3\big)\,, \tag{12.46}$$

$$\bar{\rho} = \rho\sqrt{1 + (\boldsymbol{\nabla} h)^2} = \rho + \frac{\rho_0}{2}\,(\boldsymbol{\nabla} h)^2 + \mathcal{O}\big(\epsilon^3\big)\,, \tag{12.47}$$

Hence, defining the scaled projected density as

$$\bar{r} = \frac{\bar{\rho} - \rho_0}{\rho_0} = r + \frac{1}{2}\,(\boldsymbol{\nabla} h)^2 + \mathcal{O}\big(\epsilon^3\big)\,, \tag{12.48}$$

we obtain from Eq. (12.33)

$$\begin{aligned} \bar{f} &= \sigma_0 + \sigma_1\psi + \frac{\sigma_2}{2}\psi^2 + \frac{\sigma_0}{2}\,(\boldsymbol{\nabla} h)^2 + \frac{k}{2}\left(\bar{r} - e\nabla^2 h\right)^2 \\ &+ \frac{\kappa}{4}\left(\nabla^2 h\right)^2 - \frac{\kappa}{2}\,(c_0 + \tilde{c}_0\psi)\,\nabla^2 h + \frac{\bar{\kappa}}{2}\det(h_{ij}) \\ &+ [\![\tilde{\sigma}\,(1 + \bar{r})\,\phi\ln\phi]\!] + \mathcal{O}\big(\epsilon^3\big)\ . \end{aligned} \tag{12.49}$$

We can now calculate the components of the projected stress tensor from Eqs. (12.15) and (12.16), noting that $\bar{\rho}\,\partial\bar{f}/\partial\bar{\rho} = (1 + \bar{r})\,\partial\bar{f}/\partial\bar{r}$. We will restrict ourselves to the first order in ϵ here, but the tangential components of the stress tensor are

calculated at second order in Appendix B, Sec. 12.9. We obtain

$$\Sigma_{ij} = \left[\sigma_0 + \sigma_1\psi - k\left(\bar{r} - e\nabla^2 h\right) - \frac{\kappa c_0}{2}\nabla^2 h\right]\delta_{ij} + \frac{\kappa c_0}{2}h_{ij} + \mathcal{O}\left(\epsilon^2\right), \quad (12.50)$$

$$\Sigma_{zj} = \sigma_0 h_j + ke\,\partial_j\left(\bar{r} - e\nabla^2 h\right) - \frac{\kappa}{2}\partial_j\nabla^2 h + \frac{\kappa\tilde{c}_0}{2}\partial_j\psi + \mathcal{O}\left(\epsilon^2\right). \quad (12.51)$$

Note that the non-analytic term coming from the entropy of mixing, which we have put between double square brackets in Eq. (12.49), does not contribute to the stress tensor. This is because this term is proportional to $\bar{\rho}$, so it disappears when one computes $\bar{f} - \bar{\rho}\,\partial\bar{f}/\partial\bar{\rho}$. The expression of the stress tensor is thus the same whether ϕ is small or whether it is close to a finite value ϕ_0.

For $h = 0$, $\bar{r} = 0$ and $\psi = 0$, Eq. (12.50) gives $\Sigma_{ij} = \sigma_0\,\delta_{ij}$. Hence σ_0 can be interpreted as the tension of a flat membrane with uniform density ρ_0 and uniform lipid composition ϕ_0. It is consistent with the fact that σ_0 vanishes for $\rho_0 = \rho_{\rm eq}$. Besides, Eq. (12.30) may now be interpreted as a Hookean law for the tension of a flat membrane with no inhomogeneities [254].

12.4.2 Comparison with the stress tensor associated with the Helfrich model

Let us compare our results with those coming from the Helfrich model, in which the tension σ is a phenomenological parameter arising either from the Lagrange multiplier implementing the area constraint, or from the chemical potential of a lipid reservoir, as stressed in Sec. 1.3.2-b.. For a monolayer with elastic constants $\frac{1}{2}\kappa$ and $\frac{1}{2}\bar{\kappa}$, tension σ and spontaneous curvature c_0, the Helfrich Hamiltonian density is

$$f = \sigma + \frac{\kappa}{4}c^2 - \frac{\kappa c_0}{2}c + \frac{\bar{\kappa}}{2}c_1 c_2\,, \quad (12.52)$$

so that its projected version reads at second order in ϵ:

$$\bar{f} = \sigma + \frac{\sigma}{2}\left(\boldsymbol{\nabla} h\right)^2 + \frac{\kappa}{4}\left(\nabla^2 h\right)^2 - \frac{\kappa c_0}{2}\nabla^2 h + \frac{\bar{\kappa}}{2}\det(h_{ij}). \quad (12.53)$$

The corresponding stress tensor takes the form [113]:

$$\Sigma^{\rm H}_{ij} = \left(\sigma - \frac{\kappa c_0}{2}\nabla^2 h\right)\delta_{ij} + \frac{\kappa c_0}{2}h_{ij} + \mathcal{O}\left(\epsilon^2\right), \quad (12.54)$$

$$\Sigma^{\rm H}_{zj} = \sigma h_j - \frac{\kappa}{2}\partial_j\nabla^2 h + \mathcal{O}\left(\epsilon^2\right). \quad (12.55)$$

Comparing Eqs. (12.54)–(12.55) with Eqs. (12.50)–(12.51), we find that we may write

$$\Sigma_{ij} = \Sigma^{\rm H}_{ij} + \mathcal{O}\left(\epsilon^2\right), \quad (12.56)$$

$$\Sigma_{zj} = \Sigma^{\rm H}_{zj} - e\,\partial_j\sigma + \left(\frac{\kappa\tilde{c}_0}{2} + e\sigma_1\right)\partial_j\psi + \mathcal{O}\left(\epsilon^2\right), \quad (12.57)$$

if we define

$$\sigma = \sigma_0 + \sigma_1\psi - k\left(\bar{r} - e\nabla^2 h\right) + \mathcal{O}\left(\epsilon^2\right). \tag{12.58}$$

Thus, if the scaled lipid composition ψ and the scaled density on the monolayer neutral surface $\bar{r}_n = \bar{r} - e\nabla^2 h + \mathcal{O}(\epsilon^2)$ are both homogeneous, σ is a constant. The stress tensor then has the same form in our model as in the Helfrich model. But contrary to the Helfrich tension, our σ, which may be viewed as a *dynamical surface tension*, can feature inhomogenities. In the inhomogeneous case, new terms appear in Σ_{zj}. Hence, our stress tensor extends the one associated with the Helfrich model [113] to the case where the lipid density and composition are not homogeneous.

12.4.3 Stress tensor in the ADE model

For a one-component monolayer, the components of the stress tensor at first order in ϵ in Eqs. (12.50)–(12.51) are explicitly given by

$$\Sigma_{xx} = \sigma_0 - k\left[\bar{r} - e\left(h_{xx} + h_{yy}\right)\right] - \frac{\kappa c_0}{2} h_{yy}\,, \tag{12.59}$$

$$\Sigma_{xy} = \frac{\kappa c_0}{2} h_{xy}\,, \tag{12.60}$$

$$\Sigma_{zx} = \sigma_0 h_x + ke\,\bar{r}_x - \frac{\tilde{\kappa}}{2}\left(h_{xxx} + h_{xyy}\right), \tag{12.61}$$

where $\bar{r}_i \equiv \partial_i \bar{r}$ and $\tilde{\kappa} = \kappa + 2ke^2$. The three other components of the stress tensor follow from exchanging x and y.

Even when the membrane exhibits large-scale deformations, it is possible to express the stress tensor at a given point M in the local tangent frame (X, Y) diagonalizing the curvature tensor. Calling X (resp. Y) the principal direction associated with the principal curvature c_1 (resp. c_2), we have $h_X = h_Y = h_{XY} = 0$, $h_{XX} = c_1$ and $h_{YY} = c_2$ at point M. Hence $\bar{r} = r$ and $c = \nabla^2 h = c_1 + c_2$. The components of the projected stress tensor read at first order:

$$\Sigma_{XX} = \sigma_0 - k\left(r - ec\right) - \frac{\kappa c_0}{2}\, c_2, \tag{12.62}$$

$$\Sigma_{YY} = \sigma_0 - k\left(r - ec\right) - \frac{\kappa c_0}{2}\, c_1, \tag{12.63}$$

$$\Sigma_{XY} = \Sigma_{YX} = 0\,, \tag{12.64}$$

$$\Sigma_{ZX} = -\frac{\kappa}{2}\partial_X c\,. \tag{12.65}$$

The tangential stress tensor is thus diagonal.

Choosing $\rho_0 = \rho_{\text{eq}}$ and using Eq. (12.39), which comes from partial minimization of the monolayer effective Hamiltonian with respect to $r^{\pm}$, we obtain at first order for each monolayer

$$\Sigma^{\pm}_{XX} = k^{\pm}\,\frac{A^{\pm} - A_0^{\pm}}{A} \pm \frac{\kappa^{\pm} c_0^{\pm}}{2}\, c_2\,, \tag{12.66}$$

$$\Sigma^{\pm}_{YY} = k^{\pm}\,\frac{A^{\pm} - A_0^{\pm}}{A} \pm \frac{\kappa^{\pm} c_0^{\pm}}{2}\, c_1\,. \tag{12.67}$$

Summing the contributions from the two monolayers, we obtain the stress tensor of a bilayer in the ADE model, still at first order:

$$\Sigma^b_{XX} = 2k^b \frac{A - A_0}{A} - \kappa^b c^b_0 \, c_2 \,, \tag{12.68}$$

$$\Sigma^b_{YY} = 2k^b \frac{A - A_0}{A} - \kappa^b c^b_0 \, c_1 \,, \tag{12.69}$$

$$\Sigma^b_{ZX} = -\kappa^b \partial_X c \,. \tag{12.70}$$

where k^b, A_0, κ^b and c^b_0 are defined in Sec. 12.3.2.

In the Helfrich model, the stress tensor of a bilayer with elastic constant κ^b and spontaneous curvature c^b_0 can be written in the principal tangent frame from Eqs. (12.54) and (12.55). It reads at first order in ϵ:

$$\Sigma^{\mathrm{H}}_{XX} = \sigma - \kappa^b c^b_0 \, c_2 \,, \tag{12.71}$$

$$\Sigma^{\mathrm{H}}_{YY} = \sigma - \kappa^b c^b_0 \, c_1 \,, \tag{12.72}$$

$$\Sigma^{\mathrm{H}}_{XY} = \Sigma^{\mathrm{H}}_{YX} = 0 \,, \tag{12.73}$$

$$\Sigma^{\mathrm{H}}_{ZX} = -\kappa^b \partial_X c \,. \tag{12.74}$$

Thus, the stress tensor in the ADE model has the same form as the one in the Helfrich model, with $\sigma = 2k^b \left(A - A_0\right)/A$. In light of the previous Section, this equivalence is not surprising since in the ADE model, $\phi = 0$, and $\bar{r}_n$ is homogeneous as shown by Eq. (12.39).

12.5 Force density in a monolayer

12.5.1 Calculation from the projected stress tensor

Now that we have obtained the stress tensor for our monolayer model, we can calculate the corresponding force per unit area $\boldsymbol{p}$ by taking the divergence of Eqs. (12.50) and (12.51): $p_i = \partial_j \Sigma_{ij}$ and $p_z = \partial_j \Sigma_{zj}$. This force exerted per unit area of the monolayer by the rest of the monolayer plays an important part in a dynamical description of a membrane. Indeed, its tangential component is involved in the generalized Stokes equation describing the two-dimensional flow in the monolayer, while its normal component is involved in the normal force balance of the membrane (see Ref. [224] and Chapter 9).

We obtain at first order in ϵ:

$$p_i = -k \, \partial_i \left(\bar{r} - e \, \nabla^2 h\right) + \sigma_1 \partial_i \psi \,, \tag{12.75}$$

$$p_z = \sigma_0 \nabla^2 h - \frac{\tilde{\kappa}}{2} \nabla^4 h + ke \, \nabla^2 \bar{r} + \frac{\kappa \tilde{c}_0}{2} \nabla^2 \psi \,. \tag{12.76}$$

Both of these results give back those of Ref. [224] in the particular case of a bilayer constituted of two identical one-component monolayers, if the reference density is $\rho_0 = \rho_{\mathrm{eq}}$. We have thus justified the expression of these force densities from the membrane stress tensor and generalized them.

This force density can also be derived from the general expressions Eqs. (12.18) and (12.19). Note that Eq. (12.18) indicates that $p_z = -\delta F/\delta h$, which is indeed the force taken into account in Eq. (3) of Ref. [224]. Besides, applying Eq. (12.19) to the Hamiltonian density Eq. (12.49) with $\phi = 0$ shows that, in this specific case, $p_i = -\partial_i(\delta F/\delta \bar{r}) + \mathcal{O}(\epsilon^2)$. This justifies the "gradient of the surface pressure" term $-\boldsymbol{\nabla}(\delta F/\delta r)$ used in Eq. (4) of Ref. [224].

12.5.2 Direct covariant calculation

a. Definitions and notations

In this Section, we will not restrict ourselves to membranes undergoing small deformations around the flat shape. In general, a membrane can be considered, in a coarse-grained description, as a two-dimensional surface embedded in the three-dimensional space. The position of a fluid element in the membrane can be described by a three-dimensional vector $\boldsymbol{R}(u^1, u^2)$, where u^1 and u^2 are two parameters labelling each fluid element. Mathematically, these parameters are internal coordinates in the two-dimensional surface, and physically they correspond to Lagrangian coordinates.

We are now going to introduce some basic definitions and notations used to describe the shape of a surface in differential geometry [26, 232, 252]. At each point $\boldsymbol{R}$ of the surface, it is possible to define two vectors tangent to the surface through

$$\boldsymbol{t}_\alpha = \frac{\partial \boldsymbol{R}}{\partial u^\alpha} \equiv \partial_\alpha \boldsymbol{R}\,, \tag{12.77}$$

where $\alpha \in \{1, 2\}$. These two vectors are supposed to be linearly independent. Thus,

$$\boldsymbol{n} = \frac{\boldsymbol{t}_1 \times \boldsymbol{t}_2}{|\boldsymbol{t}_1 \times \boldsymbol{t}_2|} \tag{12.78}$$

is a unit normal to the surface at point $\boldsymbol{R}$. The metric tensor of the surface can be expressed as

$$a_{\alpha\beta} = \boldsymbol{t}_\alpha \cdot \boldsymbol{t}_\beta\,, \tag{12.79}$$

so that the area element of the surface reads

$$dA = \sqrt{a}\, d^2u\,, \tag{12.80}$$

where a is the determinant of $a_{\alpha\beta}$, and $d^2u = du^1 du^2$. The inverse metric tensor $a^{\alpha\beta}$ is defined by the relation

$$a^{\alpha\beta} a_{\beta\gamma} = \delta^\alpha_\gamma\,, \tag{12.81}$$

where δ^α_γ is the Kronecker symbol. In the last relation, as well as in the following, the Einstein summation convention is used. We may now define the contravariant tangent vectors as

$$\boldsymbol{t}^\alpha = a^{\alpha\beta} \boldsymbol{t}_\beta\,. \tag{12.82}$$

A complete description of a surface is given by its metric tensor (or first fundamental form) and its curvature tensor (or second fundamental form)

$$b_{\alpha\beta} = \boldsymbol{n} \cdot \partial_\alpha \boldsymbol{t}_\beta = \boldsymbol{n} \cdot \partial_\alpha \partial_\beta \boldsymbol{R} \,. \tag{12.83}$$

The principal curvatures c_1 and c_2 of the surface are the eigenvalues of $b^\alpha_\beta = a^{\alpha\gamma} b_{\gamma\beta}$, which enables to express the total curvature and the Gaussian curvature from the curvature tensor:

$$c = c_1 + c_2 = b^\alpha_\alpha \,, \tag{12.84}$$

$$c_1 c_2 = \det b^\alpha_\beta \,. \tag{12.85}$$

b. Force density in a monolayer

The surface density of internal forces $\boldsymbol{q}$ in a two-component monolayer with effective Hamiltonian $F = \int dA\, f$ can be expressed as the functional derivative

$$\boldsymbol{q}(u^1, u^2) = -\frac{1}{\sqrt{a}} \left. \frac{\delta F}{\delta \boldsymbol{R}(u^1, u^2)} \right|_{\rho\sqrt{a},\, \rho\phi\sqrt{a}} \,, \tag{12.86}$$

where, as in the previous Sections, ρ is the total mass density of lipids, and ϕ the mass fraction of one lipid species [232, 252, 255]. This expression is a consequence of the principle of virtual work: for a small deformation $\delta\boldsymbol{R}$ of the membrane at equilibrium, the variation of the membrane effective Hamiltonian reads

$$\delta F = -\int dA\; \boldsymbol{q} \cdot \delta \boldsymbol{R} = -\int d^2u\; \sqrt{a}\; \boldsymbol{q} \cdot \delta \boldsymbol{R} \,. \tag{12.87}$$

For the underlying force balance on each fluid element to be valid, the virtual deformation $\delta\boldsymbol{R}$ must be performed at constant total mass $dm = \rho\, dA = \rho\sqrt{a}\; d^2u$ and composition in each fluid element. Hence, the functional derivative in Eq. (12.86) must be taken at constant $\rho\sqrt{a}$ and $\rho\phi\sqrt{a}$.

Let us calculate the force density corresponding to Eq. (12.86) for a monolayer with Hamiltonian density

$$\begin{aligned} f &= \sigma_0 + \sigma_1 \psi + \frac{\sigma_2}{2}\psi^2 + [\![\tilde{\sigma}\,(1+r)\,\phi \ln \phi]\!] + \frac{k}{2}\,(r - ec)^2 \\ &- \frac{\kappa}{2}\,(c_0 + \tilde{c}_0 \psi)\, c + \frac{\kappa}{4} c^2 + \frac{\bar{\kappa}}{2} c_1 c_2 . \end{aligned} \tag{12.88}$$

This Hamiltonian density corresponds to Eq. (12.33) truncated at second order in ϵ. The two constraints on the deformation $\delta\boldsymbol{R}$, $\delta(\rho\sqrt{a}) = 0$ and $\delta(\rho\phi\sqrt{a}) = 0$, are equivalent to

$$\sqrt{a}\,\delta r + (1+r)\delta\sqrt{a} = 0 \tag{12.89}$$

$$\sqrt{a}\,\delta\psi = 0 \,, \tag{12.90}$$

where we have used the fact that $1+r>0$. To enforce these two independent local constraints, we use two local Lagrange multipliers, λ and μ. The principle of virtual work Eq. (12.87) then reads

$$\delta F - \int d^2u \left\{ \lambda \left[\sqrt{a}\,\delta r + (1+r)\delta\sqrt{a} \right] + \mu\,\sqrt{a}\,\delta\psi \right\} = \delta W\,, \tag{12.91}$$

where

$$\delta W = -\int dA\; \boldsymbol{q}\cdot\delta\boldsymbol{R}\,. \tag{12.92}$$

We assume that the topology of the membrane is not affected by the virtual deformation. The Gauss-Bonnet theorem then yields $\delta\left(\int dA\; c_1c_2\right)=0$. The transformation of the left-hand side of Eq. (12.91) can be performed along the same lines as in Ref. [256]. These calculations, which are presented in Appendix A, Sec. 12.8, yield:

$$\boldsymbol{q}\cdot\boldsymbol{t}_\alpha = -k\,(1+r)\,\partial_\alpha\,(r-ec) + \left(\sigma_1+\sigma_2\psi-\frac{\kappa\tilde{c}_0}{2}c\right)\partial_\alpha\psi\,, \tag{12.93}$$

$$\begin{aligned}\boldsymbol{q}\cdot\boldsymbol{n} = {} & \left(\sigma_0+\sigma_1\psi+\frac{\sigma_2}{2}\psi^2-\frac{k}{2}r^2-kr\right)c-\frac{\tilde{\kappa}}{4}c^3 \\ & +\left[\tilde{\kappa}c-\kappa\left(c_0+\tilde{c}_0\psi\right)-2ke\;r\right]c_1c_2 \\ & +ke\,(1+r)\,c^2+ke\,\Delta r-\frac{\tilde{\kappa}}{2}\Delta c+\frac{\kappa\tilde{c}_0}{2}\Delta\psi\,,\end{aligned} \tag{12.94}$$

where Δ is a shorthand for the Laplace-Beltrami operator $(1/\sqrt{a})\partial_\alpha(a^{\alpha\beta}\sqrt{a}\partial_\beta)$. The force density $\boldsymbol{q}$ can be expressed from its tangential component Eq. (12.93) and normal component Eq. (12.94) as

$$\boldsymbol{q} = (\boldsymbol{q}\cdot\boldsymbol{t}_\alpha)\boldsymbol{t}^\alpha + (\boldsymbol{q}\cdot\boldsymbol{n})\boldsymbol{n}\,. \tag{12.95}$$

We have thus obtained the general expression of the force density in a two-component monolayer with Hamiltonian density in Eq. (12.88). This expression gives back the one in Ref. [232] in the particular case of a one-component monolayer with $c_0=0$.

Note that, in this Section, we have used the Hamiltonian density truncated at second order, Eq. (12.88), as if it were exact. The force density $\boldsymbol{q}$ expressed in Eqs. (12.93)–(12.95) is the one corresponding to this model, and it contains second and third-order terms. This approach is consistent with the one of Refs. [232, 252, 256]. However, in the present Chapter, we have constructed the Hamiltonian density as a general expansion around a reference state, controlling the order in ϵ of this expansion. In our approach, if the Hamiltonian density f is kept at second order, the force density can be known only at first order.

12.5.3 Comparison between the two results

In this Chapter, except in Sec. 12.5.2, we have described membranes in the Monge gauge, i.e., by their height with respect to a reference plane. Such a description is very convenient to study the membrane small deformations around the flat shape.

In the Monge gauge, the position of a fluid element in the membrane is given by $\boldsymbol{R}(x,y) = (x,\, y,\, h(x,y))$, where x and y are Cartesian coordinates in the reference plane and $z = h(x,y)$ describes the height of the membrane with respect to the reference plane. The coordinates (x,y) of a fluid element characterize its position in the membrane: they are Eulerian coordinates.

In Sec. 12.5.2, we have found the force density $\boldsymbol{q}$ in a monolayer, whatever its shape. In our derivation of $\boldsymbol{q}$, the parameters (u^1, u^2) describing the surface were Lagrangian coordinates, labelling each fluid element. However, as the force density is a physical quantity, it does not depend on the parametrization of the surface [252]. Thus, the expression we have found for $\boldsymbol{q}$ is valid (for each given membrane shape) in the Monge gauge.

We may now compare the force density obtained in Sec. 12.5.2 with the one obtained from the projected stress tensor in Sec. 12.5.1. For this, we will write explicitly in the Monge gauge the general result obtained in Sec. 12.5.2. With $u^1 = x$ and $u^2 = y$, the tangent vectors read in the Monge gauge $\boldsymbol{t}_1 = (1,\, 0,\, \partial_x h)$ and $\boldsymbol{t}_2 = (0,\, 1,\, \partial_y h)$. It is then straightforward to find the expression of $\boldsymbol{n}$, $a_{\alpha\beta}$ and $a^{\alpha\beta}$ in the Monge gauge (see, e.g., Ref. [252]). Using these explicit expressions, and keeping only first order terms in ϵ, Eqs. (12.93) and (12.94) can be written as:

$$q_i = -k\,\partial_i\left(\bar{r} - e\,\nabla^2 h\right) + \sigma_1 \partial_i \psi + \mathcal{O}\left(\epsilon^2\right), \tag{12.96}$$

$$q_z = \sigma_0 \nabla^2 h - \frac{\tilde{\kappa}}{2}\nabla^4 h + ke\,\nabla^2 \bar{r} + \frac{\kappa \tilde{c}_0}{2}\nabla^2 \psi + \mathcal{O}\left(\epsilon^2\right), \tag{12.97}$$

where $i \in \{x, y\}$. We notice that, at this order, Eq. (12.96) is identical to Eq. (12.75) and Eq. (12.97) is identical to Eq. (12.76). Note that $\boldsymbol{q}$ is a force density per actual unit area of the monolayer while $\boldsymbol{p}$ is a force density per projected unit area. However, this difference is irrelevant at first order.

We have just shown that the force density obtained from the divergence of the projected stress tensor is consistent with the one calculated directly by using the principle of virtual work in covariant formalism. The projected stress tensor thus allows to calculate easily both the normal and the tangential components of the force density in a membrane in the Monge gauge, without having to resort to a covariant formulation.

12.6 Applications

The force density in a membrane with lipid density and composition inhomogeneities can be used to understand qualitatively and quantitatively the dynamics of a membrane submitted to a local perturbation. We are going to illustrate this force density on simple examples related to the local injection of a reagent close to a membrane (see Fig. 12.3), which modifies locally the properties of the membrane. The full dynamics of this situation has been studied in the previous Chapters, starting with the force density we now focus on.

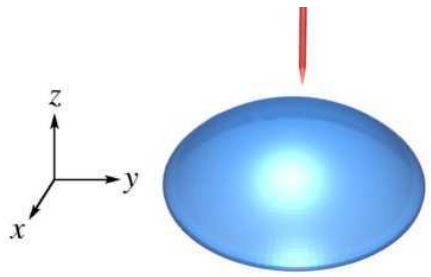

Figure 12.3: Local injection of a reagent from a micropipette close to a vesicle. The lipids in the external monolayer of the vesicle will be affected. The injection is sufficiently local for us to focus on a small, nearly-plane zone of the membrane.

12.6.1 Forces arising from a modification of composition

Let us consider initially a one-component flat membrane at equilibrium with uniform lipid density. Let us assume that, at time $t = 0$, some lipids in the external monolayer of this membrane (monolayer +, as on Fig. 12.2), are suddenly chemically modified due to a microinjection of a reagent close to the membrane (see Fig. 12.3). Then there is a fraction $\phi(x, y)$, assumed to be small, of modified lipids in this monolayer. The force density in the external monolayer at time $t = 0^+$, just after the injection, when the shape and the density have not changed yet, is given by:

$$\boldsymbol{p}^+ \;=\; \sigma_1 \boldsymbol{\nabla}\phi + \frac{\kappa \tilde{c}_0}{2} \nabla^2 \phi \; \boldsymbol{e}_z \,, \tag{12.98}$$

where $\boldsymbol{e}_z$ is a unit vector in the z direction. This force density corresponds to Eqs. (12.75) and (12.76) in the case of a flat "+" monolayer with uniform density. Hence, modifying locally the lipids of a monolayer will generically induce a deformation of the membrane. The internal monolayer is not affected by the chemical modification, so the force density remains zero in it.

Let us take the position of the micropipette injecting the reagent as the origin of our (x, y) frame. Then, ϕ is a decreasing function of the radial coordinate r. Let us study the case where ϕ is a Gaussian:

$$\phi(r) = \phi_0 \, \exp\left(-\frac{r^2}{2\,R^2}\right) \,. \tag{12.99}$$

This can represent the field of modified lipids resulting from a diffusion of the reagent in the solution surrounding the vesicle before it hits the membrane. It is straightforward to calculate the corresponding force density. Its normal and radial components, nondimensionalized by their maximal values, are plotted as a function of r/R in Fig. 12.4.

The constants σ_1 and $\tilde{c}_0$ that appear in the force density arise from the ϕ-dependence of the effective Hamiltonian per unit area of a monolayer (see Eq. 12.33). Physically, they describe the change in the equilibrium density and the spontaneous curvature of the membrane due to a generic modification of the lipids (see Chapter 9,

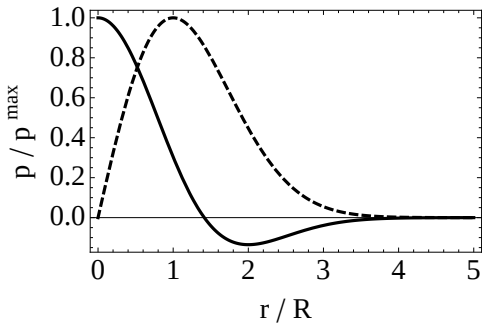

Figure 12.4: Nondimensionalized force density in the external monolayer of a membrane just after a local chemical modification, with Gaussian ϕ. Plain line: normal component $p_z/p_z^{\max}$. Dashed line: radial component $p_r/p_r^{\max}$.

especially Sec. 9.2.3). Their signs, and thus, those of the force density components, depend on the nature of the modification. In the case where $\sigma_1 < 0$ and $\tilde{c}_0 < 0$, which corresponds to modified lipids favoring a smaller density and a larger curvature (in absolute value), the lipids in front of the pipette are submitted to a normal force going towards the exterior of the vesicle, which will yield a local deformation of the membrane in this direction. Meanwhile, a radial force drives the lipids of the external monolayer to flow in the membrane towards larger values of r, due to the fact that the modified lipids favor a smaller density.

This situation describes well the onset of the deformation studied in the previous Chapters, which is induced by microinjecting a reagent close to a membrane.

12.6.2 Forces arising from a local deformation at uniform density

Apart from composition, another important effect captured by our study is the coupling between the membrane shape and the density. To shed light onto this effect, let us consider a locally deformed membrane with uniform density (on the bilayer midsurface). This can correspond to a membrane which has deformed very rapidly from a flat shape, before the density adjusts to the new deformed shape. Indeed, the symmetric density (i.e., the sum of the densities in the two monolayers) is not coupled to the deformation, while the antisymmetric density is [219, 224, 228, 231]. Thus, intermonolayer friction is involved when the density adjusts to the deformation. The associated timescale can be quite large, e.g., a few seconds for deformations on length scales of order 20 μm, so there is indeed a lapse when a deformed membrane with non-adjusted density exists in the experiments described in Chapter 10.

To isolate the effect of the shape and density, we will focus on a one-component membrane here (note that the external monolayer is a two-component one in the experiments described in Chapter 10). Let us take $\rho_0 = \rho_{\text{eq}}$ as our reference density in both (identical) monolayers. Then, Eq. (12.30) ensures that $\sigma_0 = 0$. The force

density in monolayers "±" caused by the deformation is given by:

$$\boldsymbol{p}^{\pm} \;=\; \mp ke\,\boldsymbol{\nabla}(\nabla^2 h) - \frac{\tilde{\kappa}}{2}\nabla^4 h\,\boldsymbol{e}_z\,. \tag{12.100}$$

This force density corresponds to Eqs. (12.75) and (12.76) in the case of one-component monolayers with uniform density.

Let us consider for instance a Gaussian-shaped deformation towards the exterior, centered on the origin:

$$h(r) = h_0\,\exp\left(-\frac{r^2}{2\,R^2}\right)\,. \tag{12.101}$$

The normal and radial components of the corresponding force density, nondimensionalized by the absolute value of their maxima, are plotted as a function of r/R in Fig. 12.5.

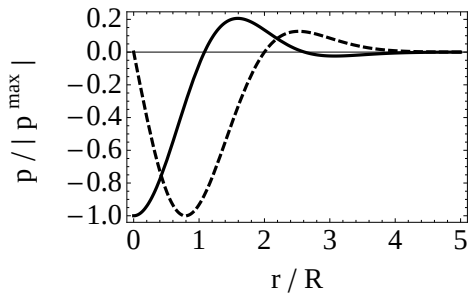

Figure 12.5: Nondimensionalized force density in monolayer "+" just after a local deformation, with Gaussian h. Plain line: normal component $p_z/|p_z^{\max}|$. Dashed line: radial component $p_r/|p_r^{\max}|$. In monolayer "−", p_z is identical and p_r is opposite.

Since $ke > 0$ and $\tilde{\kappa} > 0$, at small r, the lipids are submitted to a normal force going towards the interior of the vesicle: this will lead to a relaxation of the deformation. This is due to the fact that the membrane considered here is symmetric, so its equilibrium shape is flat. Meanwhile, a radial force drives the lipids of the external monolayer to flow in the membrane, for the density to adjust to the shape (see Fig. 12.6). Indeed, in a curved membrane at equilibrium, the density is uniform on the neutral surface of each monolayer, and not on the membrane midsurface. The radial forces are opposite in the external and in the internal monolayer, because the orientations of these monolayers are opposite while they share the same curvature. Hence, for the density to adjust to the deformed shape, it is necessary that the lipids in one monolayer slide with respect to the ones in the other monolayer, which involves intermonolayer friction (see Chapters 10 and 11).

The force densities in the membrane are the basis of a hydrodynamic description of the membrane (for a review, see Ref. [257]). Our work enables to take into account lipid density and composition inhomogeneities in such dynamical studies. In the previous Chapters, we have used the force densities derived here to describe the dynamics of a membrane local deformation induced by a local injection of a basic solution close to a giant unilamellar vesicle.

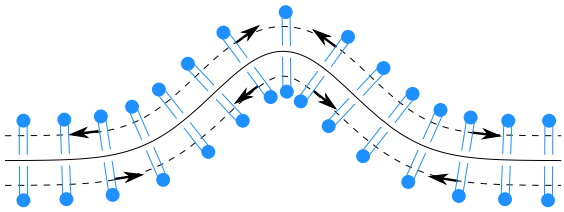

Figure 12.6: Membrane with Gaussian h, that has just deformed from a flat shape. The density has not adjusted to the new deformed shape yet. The lipids are thus at equal distance on the midlayer (plain line). The equilibrium density for this deformed shape would correspond to lipids at equal distance on the neutral surface of each monolayer (dashed lines). The arrows indicate the direction of the tangential force density in the membrane, consistent with Fig. 12.5.

12.7 Conclusion

We have derived a general formula expressing the projected stress tensor in a monolayer as a function of the monolayer Hamiltonian density, taking into account inhomogeneities in the lipid density and composition. This general formula has been applied to a generic monolayer model constructed from basic principles. Our model is a local version of the ADE model, and we have found in particular the stress tensor associated with the ADE model.

In the Monge gauge, the projected stress tensor provides a convenient way of deriving the force density in a monolayer, which is the basis of a hydrodynamic description of a membrane (see Chapter 9). The result is consistent with a direct calculation of the force density from the principle of virtual work in covariant formalism. We have shown an example of application to the calculation of force density in a locally perturbed membrane. These force density constitute the basis of the dynamical study presented in the previous Chapters.

Moreover, the stress tensor contains more information than the force density, since it provides the actual force exerted by a piece of membrane along its edge. Indeed, the stress tensor associated with the Helfrich model [101, 113] has already been used to study various situations, such as the boundary conditions on a membrane with a free exposed edge [258], the adhesion of a fluid membrane [259, 260], the surface tension of fluctuating membranes [36, 38] and the force exerted by a fluctuating membrane tubule [37]. The stress tensor is also a useful tool in the study of membrane-mediated interactions [99, 100, 114]. Since the stress tensor studied in the present Chapter generalizes the one associated with the Helfrich model to monolayers with density and composition inhomogeneities, it may enable to extend such applications.

12.8 Appendix A: Covariant calculation of the force density

In this Section, we are going to present the main steps of our covariant calculation of the force density in a monolayer, which leads to Eqs. (12.93)–(12.94). This calculation follows the same lines as the one in Ref. [256].

As the Gaussian curvature term contained in the total monolayer effective Hamiltonian

$$F = \int dA\, f = \int d^2u\, \sqrt{a}\, f \tag{12.102}$$

does not vary during the virtual deformation $\delta\boldsymbol{R}$, we may replace the Hamiltonian density Eq. (12.88) by

$$\tilde{f} = f - \frac{\bar{\kappa}}{2} c_1 c_2 \tag{12.103}$$

in our calculations. The variation of the membrane effective Hamiltonian during the deformation then reads

$$\delta F = \int d^2u\, \tilde{f}\, \delta\sqrt{a} + \int d^2u\, \sqrt{a}\, \delta\tilde{f}\,, \tag{12.104}$$

with

$$\begin{aligned} \delta\tilde{f} &= \left[\sigma_1 + \sigma_2\psi - \frac{\kappa\tilde{c}_0}{2}c + [\![\tilde{\sigma}\,(1+r)\,(1+\ln\phi)]\!]\right]\delta\psi \\ &+ \left[k(r-ec) + [\![\tilde{\sigma}\phi\ln\phi]\!]\right]\delta r + I_1\delta c\,, \end{aligned} \tag{12.105}$$

where we have defined

$$I_1 = \frac{\kappa}{2}\left(c - c_0 - \tilde{c}_0\psi\right) - ek\left(r - ec\right)\,. \tag{12.106}$$

The principle of virtual work Eq. (12.87) may now be written as

$$\begin{aligned} \delta W &= \int dA \Bigg\{ I_1\delta c + \left[k(r-ec) + [\![\tilde{\sigma}\phi\ln\phi]\!] - \lambda\right]\delta r \\ &+ \left[\sigma_1 + \sigma_2\psi - \frac{\kappa\tilde{c}_0}{2}c + [\![\tilde{\sigma}\,(1+r)\,(1+\ln\phi)]\!] - \mu\right]\delta\psi \Bigg\} \\ &+ \int d^2u \left[\tilde{f} - \lambda\,(1+r)\right]\delta\sqrt{a}\,, \end{aligned} \tag{12.107}$$

where δW is given by Eq. (12.92). The variations δc and $\delta\sqrt{a}$ only come from the variation $\delta\boldsymbol{R}$ of the *shape* of the monolayer. The coupling between $\delta\boldsymbol{R}$ and δr and $\delta\psi$, which comes from the constraints Eqs. (12.89)–(12.90), has been accounted for by introducing the Lagrange multipliers λ and μ. Hence, $\delta\boldsymbol{R}$, δr and $\delta\psi$ should now be considered as independent variations, and the terms in δr and $\delta\psi$ must vanish for Eq. (12.107) to be valid for any virtual deformation, yielding

$$\lambda = k(r-ec) + [\![\tilde{\sigma}\phi\ln\phi]\!]\,, \tag{12.108}$$

$$\mu = \sigma_1 + \sigma_2\psi - \frac{\kappa\tilde{c}_0}{2}c + [\![\tilde{\sigma}\,(1+r)\,(1+\ln\phi)]\!]\,. \tag{12.109}$$

We thus obtain

$$\delta W = \int d^2u \left(\sqrt{a}\, I_1 \delta c + I_2 \delta\sqrt{a}\right) , \tag{12.110}$$

where we have defined

$$I_2 = \sigma_0 + \sigma_1\psi + \frac{\sigma_2}{2}\psi^2 - \frac{\kappa}{2}\left(c_0 + \tilde{c}_0\psi\right)c + \frac{\kappa}{4}c^2 + \frac{k}{2}\left(ec - r\right)\left(r + ec + 2\right) . \tag{12.111}$$

Note that the contribution of the term between double square brackets has vanished, as in our calculation of $\boldsymbol{\Sigma}$.

Thanks to the relations

$$\delta\sqrt{a} = \sqrt{a}\, \boldsymbol{t}^\alpha \cdot \delta\boldsymbol{t}_\alpha , \tag{12.112}$$

$$\delta c = a^{\alpha\beta}\left(\partial_\alpha \boldsymbol{n}\right)\cdot\delta\boldsymbol{t}_\beta - \boldsymbol{t}^\alpha \cdot \delta\left(\partial_\alpha \boldsymbol{n}\right) , \tag{12.113}$$

$$\delta\boldsymbol{n} = -\left(\boldsymbol{n}\cdot\delta\boldsymbol{t}_\beta\right)\boldsymbol{t}^\beta , \tag{12.114}$$

δW can be expressed only in terms of $\delta\boldsymbol{t}_\alpha$. Performing two integrations by parts and using the relations [26]

$$\boldsymbol{t}_{\alpha|\beta} = b_{\alpha\beta}\boldsymbol{n} , \tag{12.115}$$

$$\boldsymbol{n}_{|\alpha} = \partial_\alpha \boldsymbol{n} = -b_{\alpha\beta}\boldsymbol{t}^\beta , \tag{12.116}$$

where $g_{|\alpha}$ denotes the covariant derivative (associated with the metric $a_{\alpha\beta}$) with respect to u^α of a function g defined on the surface [26], we obtain

$$\delta W = -\int dA \left[\left(a^{\alpha\beta}I_1 - b^{\alpha\beta}I_2\right)\boldsymbol{t}_\alpha + a^{\alpha\beta}\left(\partial_\alpha I_2\right)\boldsymbol{n}\right]_{|\beta}\cdot\delta\boldsymbol{R} . \tag{12.117}$$

Identifying Eq. (12.117) with Eq. (12.92) for any infinitesimal virtual deformation $\delta\boldsymbol{R}$, we obtain the sought force density:

$$\boldsymbol{q} = \left[\left(a^{\alpha\beta}I_1 - b^{\alpha\beta}I_2\right)\boldsymbol{t}_\alpha + a^{\alpha\beta}\left(\partial_\alpha I_2\right)\boldsymbol{n}\right]_{|\beta} . \tag{12.118}$$

Performing the covariant derivative with respect to u^β in Eq. (12.118), using Eqs. (12.115)–(12.116) and the relations [26]

$$b^\alpha_{\beta|\alpha} = \partial_\beta c , \tag{12.119}$$

$$b^{\alpha\beta}b_{\beta\alpha} = c^2 - c_1c_2 , \tag{12.120}$$

and taking the scalar product of $\boldsymbol{q}$ with $\boldsymbol{t}_\alpha$ (resp. $\boldsymbol{n}$) finally leads to Eq. (12.93) (resp. Eq. (12.94)).

12.9 Appendix B: Tangential stress tensor at second order

For the Helfrich model, the tangential components of the stress tensor can be obtained at second order from the effective Hamiltonian at second order[113]. On the contrary, here, because of the term $\partial\bar{f}/\partial\bar{r}$, one cannot obtain Σ_{ij} at order ϵ^2 without taking into account in $\bar{f}$ the terms of order ϵ^3 which depend on $\bar{r}$.

When such third order terms are included, f becomes

$$\begin{aligned} f &= \sigma_0 + \sigma_1\psi + \frac{\sigma_2}{2}\psi^2 + [\![\tilde{\sigma}\,(1+r)\,\phi\ln\phi]\!] \\ &+ \frac{k}{2}\,(r-ec)^2 - \frac{\kappa}{2}\,(c_0+\tilde{c}_0\psi)\,c + \frac{\kappa}{4}c^2 + \frac{\bar{\kappa}}{2}c_1c_2 \\ &+ \frac{\sigma_1'}{2}r^2\psi + \frac{\sigma_2'}{2}r\psi^2 + \frac{k'}{3}r^3 + \frac{\kappa c_0'}{2}r^2c - \frac{\kappa\tilde{c}_0'}{2}\psi rc \\ &+ \frac{\kappa'}{4}rc^2 + \frac{\bar{\kappa}'}{2}rc_1c_2 + \mathcal{O}'\!\left(\epsilon^4\right), \end{aligned} \tag{12.121}$$

where $\mathcal{O}'(\epsilon^4)$ stands for terms of order ϵ^4, *or terms of order* ϵ^3 *independent of* r. Indeed, the latter may be discarded because they will not contribute to the stress tensor at order ϵ^2. The new terms in f may be considered as originating from a density-dependence of the constitutive constants k, κ, $\bar{\kappa}$, c_0, $\tilde{c}_0$, σ_1 and σ_2.

Using the relations

$$\bar{f} = f\sqrt{1+(\boldsymbol{\nabla}h)^2} = f + \frac{\sigma_0}{2}\,(\boldsymbol{\nabla}h)^2 + \mathcal{O}'\!\left(\epsilon^4\right), \tag{12.122}$$

$$c = \nabla^2 h + \mathcal{O}'\!\left(\epsilon^4\right), \tag{12.123}$$

$$c_1c_2 = \det(h_{ij}) + \mathcal{O}'\!\left(\epsilon^4\right), \tag{12.124}$$

$$\bar{r} = r + \frac{1}{2}\,(\boldsymbol{\nabla}h)^2 + \mathcal{O}'\!\left(\epsilon^4\right), \tag{12.125}$$

we obtain

$$\begin{aligned} \bar{f} &= \sigma_0 + \frac{\sigma_0}{2}\,(\boldsymbol{\nabla}h)^2 + \sigma_1\,\psi + \frac{\sigma_2}{2}\,\psi^2 + [\![\tilde{\sigma}\,(1+\bar{r})\,\phi\ln\phi]\!] \\ &+ \frac{k}{2}\left(\bar{r} - e\nabla^2 h\right)^2 - \frac{\kappa}{2}\,(c_0+\tilde{c}_0\psi)\,\nabla^2 h + \frac{\kappa}{4}\left(\nabla^2 h\right)^2 \\ &+ \frac{\bar{\kappa}}{2}\det(h_{ij}) + \left[\frac{\kappa'}{4}\left(\nabla^2 h\right)^2 + \frac{\bar{\kappa}'}{2}\det\left(h_{ij}\right)\right. \\ &- \left.\frac{k}{2}\,(\boldsymbol{\nabla}h)^2 + \frac{\sigma_2'}{2}\,\psi^2 - \frac{\kappa\tilde{c}_0'}{2}\,\psi\nabla^2 h\right]\bar{r} \\ &+ \left(\frac{\sigma_1'}{2}\,\psi - \frac{\kappa c_0'}{2}\,\nabla^2 h\right)\bar{r}^2 + \frac{k'}{3}\,\bar{r}^3 + \mathcal{O}'\!\left(\epsilon^4\right). \end{aligned} \tag{12.126}$$

Eqs. (12.15) and (12.126) yield

$$\begin{aligned}
\Sigma_{ij} &= \Bigg\{\sigma_0 + \sigma_1\,\psi + \frac{\sigma_2 - \sigma_2'}{2}\,\psi^2 + \frac{\sigma_0 + k}{2}\,(\boldsymbol{\nabla} h)^2 \\
&\quad - (k + \sigma_1'\psi)\,\bar{r} - (k + 2k')\,\frac{\bar{r}^2}{2} + \frac{\tilde{\kappa} - \kappa'}{4}\left(\nabla^2 h\right)^2 \\
&\quad + \left[ke - \frac{\kappa}{2}\,(c_0 + \tilde{c}_0\psi) + \kappa c_0'\,\bar{r} + \frac{\kappa\tilde{c}_0'}{2}\,\psi\right]\nabla^2 h \\
&\quad - \frac{\bar{\kappa}'}{2}\det\left(h_{ij}\right)\Bigg\}\delta_{ij} - \sigma_0\,h_i h_j + \frac{\kappa}{2}\,(c_0 + \tilde{c}_0\psi)\,h_{ij} \\
&- \frac{\tilde{\kappa}}{2}\left(h_{ij}\nabla^2 h - h_i\partial_j\nabla^2 h\right) + ke\,(h_{ij}\bar{r} - h_i\partial_j\bar{r}) \\
&- \frac{\kappa\tilde{c}_0}{2}\,h_i\partial_j\psi + \mathcal{O}\left(\epsilon^3\right). \qquad (12.127)
\end{aligned}$$

where $\tilde{\kappa} = \kappa + 2ke^2$ as before. The non-analytic term present in $\bar{f}$ at small ϕ does not contribute to the stress tensor, for the same reason as before.

In the principal tangent frame, the tangential components of the stress tensor at second order are given by

$$\begin{aligned}
\Sigma_{XX} &= \sigma_0 + \sigma_1\,\psi + \frac{\sigma_2 - \sigma_2'}{2}\,\psi^2 - (k + \sigma_1'\psi)\,r \\
&\quad - (k + 2k')\,\frac{r^2}{2} + \left(ke + \kappa c_0'\,r + \frac{\kappa\tilde{c}_0'}{2}\,\psi\right)c \\
&\quad - \frac{\kappa}{2}\,(c_0 + \tilde{c}_0\psi)\,c_2 + ke\;rc_1 \\
&\quad - \frac{\tilde{\kappa} + \kappa'}{4}\,c_1^2 + \frac{\tilde{\kappa} - \kappa'}{4}\,c_2^2 - \frac{\kappa' + \bar{\kappa}'}{2}\,c_1 c_2, \qquad (12.128) \\
\Sigma_{XY} &= \Sigma_{YX} = 0\,. \qquad (12.129)
\end{aligned}$$

Σ_{YY} can be obtained by exchanging c_1 and c_2 in Σ_{XX}. This tangential stress tensor thus remains diagonal at second order in the principal tangent frame, like the one associated with the Helfrich model [113].

Conclusion

Lipid bilayers, which form the basis of biological membranes, are self-assembled structures. This gives them many original physical properties. Lipid bilayers deform easily under the action of thermal fluctuations at ambient temperature: they belong to the field of soft matter. In addition, however strange it may seem at first sight, they are both fluid and elastic. Lipid molecules, which are not covalently linked together, are free to rearrange within a monolayer: at physiological temperature, each of the two monolayers of the membrane forms a two-dimensional fluid. At the same time, the bilayer resists bending and stretching. Indeed, the hydrophobic interactions that induce the self-assembly of the bilayer in water give a preferred shape to the membrane, which is flat in the up-down symmetric case, and they also yield an effective preferred area per lipid molecule. Thanks to this specific structure, lipid bilayers can deform quite easily while being robust. This is very important because during cell life, biological membranes keep deforming dynamically.

While a pure homogeneous lipid bilayer membrane already features very rich physical properties, a biological membrane is in fact a much more complex system. Indeed, it is a heterogeneous structure, composed of different lipid species and containing various inclusions. Among these inclusions, membrane proteins are especially important, both because they are numerous and because they have key biological functions in cells. These inclusions interact with the membrane and with each other through the membrane, which can have important consequences on their behavior. In addition, a biological membrane is surrounded by a heterogeneous and constantly changing environment, which can influence and perturb it.

In this thesis, we investigated some aspects of the statistics and dynamics of complex biological membranes. We started from the physics of the pure lipid bilayer membrane, to study some generic effects of the presence of one or two inclusions, or of a local chemical change of the environment. In other words, we dealt with cases that involve a small amount of complexity.

In Part I, we focused on the Casimir-like interaction between two membrane inclusions. This interaction is a generic, long-range, membrane-mediated force arising from the fact that inclusions constrain the thermal fluctuations of the shape of the membrane. We calculated the fluctuations of the Casimir-like force between two point-like inclusions, showing that the Casimir-like force is dominated by its fluctuations, and studying the dependence of these fluctuations on the distance between the two inclusions. This work led us to investigate a more general issue: in order to study the Casimir-like force beyond its thermal equilibrium value, for

instance its fluctuations or its out-of-equilibrium behavior, it is necessary to define precisely the force exerted on an inclusion by the correlated fluid it is immersed in, in a microstate of this fluid. We examined the respective origins of two different definitions of this force, which are currently used in the literature, their domains of application, and the differences they yield. Finally, returning to membranes, we studied Casimir-like interactions between rod-shaped membrane inclusions, which can model semiflexible polymers. We calculated the Casimir-like force for four different types of rigid rods, and we investigated the effect of a finite out-of-plane bending rigidity of the rods. In this geometry, the Casimir-like force is much stronger than in the case of point-like inclusions, and it can yield effective attraction and bending of the rods toward each other.

In Part II, we examined membrane elasticity at the nanoscale, which plays an important part in local membrane deformations in the vicinity of proteins. We put forward the importance of a term that was previously neglected in the models dealing with membrane elasticity at the nanoscale and especially with local thickness heterogeneities. We reanalyzed recent numerical data, as well as experimental data, and we found some clues for the actual presence of this term. Studying these local membrane thickness deformations is interesting in order to understand how the membrane and the proteins within it can influence each other. The local thickness deformations induced in membranes by proteins yield short-range membrane-mediated interactions between such proteins, and can also affect protein function.

In Part III, we presented a theoretical description of local chemical perturbations of the environment of a lipid bilayer membrane. In particular, our aim was to describe as closely as possible microinjection experiments conducted on model membranes. We revisited membrane linear dynamics from first principles, accounting for density and composition heterogeneities in the membrane. As in Part II, local heterogeneities of lipid density played a key part in our study. However, in Part III, our focus was on micron-scale heterogeneities. We confronted our theoretical predictions to experimental results regarding the dynamical deformation of a membrane submitted to a local pH increase, obtaining good agreement. Finally, we investigated in more detail the dynamical response of a membrane to a continuous reagent concentration increase. We showed that the study of dynamical local perturbations yields more information than the standard study of static and global perturbations of the membrane environment. Understanding the response of the membrane to local chemical modifications of its environment is crucial because chemical heterogeneities are ubiquitous and strongly related to many biological processes. In particular, local pH heterogeneities are tightly coupled to cell motility or ATP synthesis in mitochondria.

Some perspectives

It would be useful to investigate the fluctuations of Casimir-like force in the case of critical binary mixtures. Indeed, since Casimir-like forces are studied experimentally in this case [66], this would be a good opportunity to compare the theoretical predictions regarding fluctuations to experimental results. Regarding membranes,

a natural extension of our work on point-like inclusions would be to study the fluctuations of the Casimir-like force in the case of extended inclusions. Indeed, we would expect a dependence of the signal-to-noise ratio on the size of the inclusions.

As far as membrane elasticity at the nanoscale is concerned, our model could be applied to the study of membrane-mediated interactions between proteins that induce local membrane thickness deformations. Indeed, these interactions have recently been measured more precisely both experimentally and in numerical simulations, and the agreement between numerical data and the predictions of standard theoretical models does not seem to be satisfactory [183]. One can wonder whether our additional term would improve this agreement.

Our theoretical description of local membrane modifications, which focuses on the case of a chemical equilibrium with a reagent, could be adapted to irreversible modifications of the lipids. Diffusion of the modified lipids within the membrane would then play an important part in the relaxation of the perturbation. Another interesting and biologically relevant situation corresponds to a change of the flip-flop rate of some lipids due to the chemical modification. Extending our description to this case is actually quite straightforward: only the mass conservation equations in each monolayer have to be modified, in order to account for lipid exchange between the two monolayers. For instance, if the flip-flop rate of some lipids in the external monolayer of a vesicle is increased by the local microinjection of a reagent, the membrane should keep deforming even when the stationary reagent profile has been reached in the fluid above the membrane, as more and more lipids flip. More generally, the study of membrane deformations in response to local chemical modifications opens the way to investigating whether, or under what conditions, passive chemotaxis could occur.

Publications

- A.-F. Bitbol, P. G. Dommersnes and J.-B. Fournier, *Fluctuations of the Casimir-like force between two membrane inclusions*, Physical Review E 81, 050903(R) (2010) [114].
  DOI: 10.1103/PhysRevE.81.050903 – Preprint: ArXiv:1004.5218

- A.-F. Bitbol, L. Peliti and J.-B. Fournier, *Membrane stress tensor in the presence of lipid density and composition inhomogeneities*, European Physical Journal E 34, 53 (2011) [187].
  DOI: 10.1140/epje/i2011-11053-4 – Preprint: ArXiv:1010.3857

- A.-F. Bitbol and J.-B. Fournier, *Forces exerted by a correlated fluid on embedded inclusions*, Physical Review E 83, 061107 (2011) [130].
  DOI: 10.1103/PhysRevE.83.061107 – Preprint: ArXiv:1102.1377

- A.-F. Bitbol, J.-B. Fournier, M. I. Angelova and N. Puff, *Dynamical membrane curvature instability controlled by intermonolayer friction*, Journal of Physics: Condensed Matter 23, 284102 (2011) [231].
  DOI: 10.1088/0953-8984/23/28/284102 – Preprint: ArXiv:1107.1854

- A.-F. Bitbol, K. Sin Ronia and J.-B. Fournier, *Universal amplitudes of the Casimir-like interactions between four types of rods in fluid membranes*, EuroPhysics Letters 96, 40013 (2011) [151].
  DOI: 10.1209/0295-5075/96/40013 – Preprint: ArXiv:1111.2525

- A.-F. Bitbol, N. Puff, Y. Sakuma, M. Imai, J.-B. Fournier and M. I. Angelova, *Lipid membrane deformation in response to a local pH modification: theory and experiments*, Soft Matter 8, 6073–6082 (2012) [243].
  DOI: 10.1039/c2sm25519g – Preprint: ArXiv:1205.1142

- A.-F. Bitbol, D. Constantin and J.-B. Fournier, *Bilayer elasticity at the nanoscale: the need for new terms*, PLoS ONE 7(11), e48306 (2012) [186].
  DOI: 10.1371/journal.pone.0048306 – Preprint: ArXiv:1211.2192

- A.-F. Bitbol and J.-B. Fournier, *Membrane properties revealed by spatiotemporal response to a local inhomogeneity*, Biochimica et Biophysica Acta: Biomembranes, in press (2012) [248].
  DOI: 10.1016/j.bbamem.2012.11.024 – Preprint: ArXiv:1212.0162

Bibliography

[1] G. Karp. *Cell and molecular biology: concepts and experiments, 6th edition.* John Wiley & Sons, 2010.

[2] M. Eigen and P. Schuster. *The hypercycle, a principle of natural self-organization.* Springer-Verlag, 1979.

[3] H. R. Maturana and F. J. Varela. *Autopoiesis and cognition: the realization of the living (Boston studies in the philosophy of science, Vol. 42).* D. Reidel publishing company, Kluwer, 1980.

[4] B. Alberts, A. Johnson, J. Lewis, M. Raff, K. Roberts, and P. Walter. *Molecular biology of the cell, 6th edition.* Garland Science, New York, 2008.

[5] O. G. Mouritsen. *Life – as a matter of fat: the emerging science of lipidomics.* Springer, Berlin, 2005.

[6] P. L. Luisi. Autopoiesis: a review and a reappraisal. *Naturwissenschaften*, 90:49–59, 2003.

[7] J. R. Baker. The cell-theory: A restatement, history, and critique – Part III: the cell as a morphological unit. *Quarterly Journal of Microscopical Science*, 93:157–190, 1952.

[8] J. D. Robertson. Membrane structure. *Journal of Cell Biology*, 91:189–194, 1981.

[9] M. Edidin. Lipids on the frontier: a century of cell-membrane bilayers. *Nature Reviews Molecular Cell Biology*, 4:414–418, 2003.

[10] W. Stoeckenius and D. M. Engelman. Current models for the structure of biological membranes. *Journal of Cell Biology*, 42:613–646, 1969.

[11] J. N. Israelachvili. *Intermolecular and surface forces, Second edition.* Academic Press, 1992.

[12] D. Chandler. Interfaces and the driving force of hydrophobic assembly. *Nature*, 437:640–647, 2005.

[13] P.-A. Monnard and D. W. Deamer. Membrane self-assembly processes: steps toward the first cellular life. *The Anatomical Record*, 268:196–207, 2002.

[14] A. D. Bangham, M. M. Standish, and G. Weissmann. The action of steroids and streptolysin S on the permeability of phospholipid structures to cations. *Journal of Molecular Biology*, 13:253–259, 1965.

[15] C. Billerit, I. Wegrzyn, G. D. M. Jeffries, P. Dommersnes, O. Orwar, and A. Jesorka. Heat-induced formation of single giant unilamellar vesicles. *Soft Matter*, 7:9751, 2011.

[16] P. Walde, K. Cosentino, H. Engel, and P. Stano. Giant vesicles: preparations and applications. *ChemBioChem*, 11:848–865, 2010.

[17] J. P. Reeves and R. M. Dowben. Formation and properties of thin-walled phospholipid vesicles. *Journal of Cellular Physiology*, 73:49–60, 1969.

[18] M. I. Angelova and D. S. Dimitrov. Liposome electroformation. *Faraday Discussions of the Chemical Society*, 81:303–311, 1986.

[19] S. Pautot, B. J. Frisken, J.-X. Cheng, X. S. Xie, and D. A. Weitz. Spontaneous formation of lipid structures at oil/water/lipid interfaces. *Langmuir*, 19:10281–10287, 2003.

[20] P. G. de Gennes. *Soft matter.* Nobel Lecture, 1991.

[21] L. D. Frye and M. Edidin. The rapid intermixing of cell surface antigens after formation of mouse-human heterokaryons. *Journal of Cell Science*, 7:319–335, 1970.

[22] J.-B. Fournier. Microscopic membrane elasticity and interactions among membrane inclusions: interplay between the shape, dilation, tilt and tilt-difference modes. *European Physical Journal B*, 11:261–272, 1999.

[23] M. C. Watson, E. S. Penev, P. M. Welch, and F. L. H. Brown. Thermal fluctuations in shape, thickness, and molecular orientation in lipid bilayers. *Journal of Chemical Physics*, 135:244701, 2011.

[24] W. Helfrich. Elastic properties of lipid bilayers – Theory and possible experiments. *Zeitschrift für Naturforschung C – Journal of Biosciences*, 28:693–703, 1973.

[25] P. B. Canham. The minimum energy of bending as a possible explanation of the biconcave shape of the human red blood cell. *Journal of Theoretical Biology*, 26:61–76, 1970.

[26] R. Aris. *Vectors, tensors, and the basic equations of fluid dynamics.* Dover, New York, 1989.

[27] S. A. Safran. *Statistical thermodynamics of surfaces, interfaces and membranes.* Addison-Wesley, 1994.

[28] S. Buchin. *Lectures on differential geometry.* World Scientific, Singapore, 1980.

[29] J.-B. Fournier. *Theoretical description of complex matter*. Course given in the Theoretical Physics of Complex Systems Master's degree program, University Paris Diderot (unpublished).

[30] R. M. Servuss, W. Harbich, and W. Helfrich. Measurement of the curvature-elastic modulus of egg lecithin bilayers. *Biochimica et Biophysica Acta – Biomembranes*, 436:900–903, 1976.

[31] J. Pécréaux, H.-G. Döbereiner, J. Prost, J.-F. Joanny, and P. Bassereau. Refined contour analysis of giant unilamellar vesicles. *European Physical Journal E*, 13:277–290, 2004.

[32] L. Peliti and S. Leibler. Effect of thermal fluctuations on systems with small surface tension. *Physical Review Letters*, 54:1690–1693, 1985.

[33] C. Barbetta. *Forces and fluctuations in planar, spherical and tubular membranes*. PhD thesis, University Paris Diderot, 2010. Available online on the TEL (Thèses En Ligne) repository: http://tel.archives-ouvertes.fr.

[34] W. Rawicz, K. C. Olbrich, T. McIntosh, D. Needham, and E. Evans. Effect of chain length and unsaturation on elasticity of lipid bilayers. *Biophysical Journal*, 79:328–339, 2000.

[35] E. Evans and W. Rawicz. Entropy-driven tension and bending elasticity in condensed-fluid membranes. *Physical Review Letters*, 64:2094–2097, 1990.

[36] J.-B. Fournier and C. Barbetta. Direct calculation from the stress tensor of the lateral surface tension of fluctuating fluid membranes. *Physical Review Letters*, 100:078103, 2008.

[37] C. Barbetta and J.-B. Fournier. On the fluctuations of the force exerted by a lipid nanotubule. *European Physical Journal E*, 29:183–189, 2009.

[38] C. Barbetta, A. Imparato, and J.-B. Fournier. On the surface tension of fluctuating quasi-spherical vesicles. *European Physical Journal E*, 31:333–342, 2010.

[39] L. Miao, U. Seifert, M. Wortis, and H.-G. Döbereiner. Budding transitions of fluid-bilayer vesicles: The effect of area-difference elasticity. *Physical Review E*, 49(6):5389–5407, 1994.

[40] S. Svetina, M. Brumen, and B. Žekš. Lipid bilayer elasticity and the bilayer couple interpretation of red-cell shape transformations and lysis. *Studia Biophysica*, 110:177–184, 1985.

[41] U. Seifert, L. Miao, H.-G. Döbereiner, and M. Wortis. Budding transition for bilayer fluid vesicles with area-difference elasticity. In R. Lipowsky, D. Richter, and K. Kremer, editors, *The Structure and Conformation of Amphiphilic Membranes – Springer Proceedings in Physics, Vol. 66*, pages 93–96. Springer, Berlin, 1992.

[42] H.-G. Döbereiner, E. Evans, M. Kraus, U. Seifert, and M. Wortis. Mapping vesicle shapes into the phase diagram: A comparison of experiment and theory. *Physical Review E*, 55:4458–4474, 1997.

[43] H.-G. Döbereiner. Properties of giant vesicles. *Current Opinion in Colloid and Interface Science*, 5:256–263, 2000.

[44] U. Seifert. Fluid vesicles. In *Lecture Notes: 'Physics meets Biology. From Soft Matter to Cell Biology', 35th Spring School, Institute of Solid State Research, Forschungszentrum Jülich*, 2004.

[45] P. W. Milonni. *The Quantum Vacuum – An Introduction to Quantum Electrodynamics*. Academic Press, 1994.

[46] F. London. On the theory and system of molecular forces. *Zeitschrift für Physik*, 63(3):245–279, 1930.

[47] H. Hinne. *Quantum chemistry classic scientific papers*. World Scientific, 1999.

[48] S. K. Lamoreaux. Casimir forces: Still surprising after 60 years. *Physics Today*, 60(5):40–45, 2007.

[49] H. C. Hamaker. The London–van der Waals attraction between spherical particles. *Physica*, 4(10):1058–1072, 1937.

[50] E. J. W. Verwey and J. T. G. Overbeek. Long distance forces acting between colloidal particles. *Transactions of the Faraday Society*, 42(B):117–131, 1946.

[51] E. J. W. Verwey. Theory of the Stability of Lyophobic Colloids. *Journal of Physical Chemistry*, 51(3):631–636, 1947.

[52] H. B. G. Casimir and D. Polder. The Influence of Retardation on the London–van der Waals Forces. *Physical Review*, 73(4):360–372, 1948.

[53] H. B. G. Casimir. Sur les forces van der Waals–London. *Journal de chimie physique et de physico-chimie biologique*, 46(7-8):407–410, 1949.

[54] E. A. Power and T. Thirunamachandran. Casimir-Polder potential as an interaction between induced dipoles. *Physical Review A*, 48(6):4761–4763, 1993.

[55] H. B. G. Casimir. On the attraction between two perfectly conducting plates. *Proceedings of the Koninklijke Nederlandse Akademie van Wetenschappen*, 51(7):793–796, 1948.

[56] E. M. Lifshitz. The theory of molecular attractive forces between solids. *Soviet Physics Journal of Experimental and Theoretical Physics*, 2(1):73–83, 1956.

[57] W. Broer, G. Palasantzas, J. Knoester, and V. B. Svetovoy. Roughness correction to the Casimir force at short separations: contact distance and extreme value statistics. *Physical Review B*, 85:155410, 2012.

[58] S. K. Lamoreaux. Demonstration of the Casimir force in the 0.6 to 6 μm range. *Physical Review Letters*, 78(1):5–8, 1997.

[59] U. Mohideen and A. Roy. Precision measurement of the Casimir force from 0.1 to 0.9 μm. *Physical Review Letters*, 81(21):4549–4552, 1998.

[60] P. Ball. Feel the force (News feature). *Nature*, 447:772, 2007.

[61] A. Lambrecht. The Casimir effect: a force from nothing. *Physics World*, 15(9):29, 2002.

[62] M. Kardar and R. Golestanian. The "friction" of vacuum, and other fluctuation-induced forces. *Review of Modern Physics*, 71(4):1233–1245, 1999.

[63] A. Gambassi. The Casimir effect: from quantum to critical fluctuations. *Journal of Physics: Conference Series*, 161:012037, 2009.

[64] M. E. Fisher and P. G. de Gennes. Wall phenomena in a critical binary mixture. *Comptes rendus hebdomadaires des séances de l'académie des sciences – Série B*, 287(8):207–209, 1978.

[65] M. Krech. *The Casimir Effect in Critical Systems*. World Scientific, 1994.

[66] C. Hertlein, L. Helden, A. Gambassi, S. Dietrich, and C. Bechinger. Direct measurement of critical Casimir forces. *Nature*, 451(7175):172–175, 2008.

[67] O. Vasilyev, A. Gambassi, A. Maciolek, and S. Dietrich. Monte Carlo simulation results for critical Casimir forces. *Europhysics Letters*, 80:60009, 2007.

[68] A. Ajdari, L. Peliti, and J. Prost. Fluctuation-induced long-range forces in liquid crystals. *Physical Review Letters*, 66(11):1481, 1991.

[69] P. Ziherl, R. Podgornik, and S. Zumer. Pseudo-Casimir structural force drives spinodal dewetting in nematic liquid crystals. *Physical Review Letters*, 84(6):1228–1231, 2000.

[70] M. Goulian, R. Bruinsma, and P. Pincus. Long-range forces in heterogeneous fluid membranes. *Europhysics Letters*, 22(2):145–150, 1993. Erratum: *Europhysics Letters* 23(2):155, 1993. Comment: Ref. [80]. A factor 2 in the Casimir force was corrected in Ref. [84].

[71] J. M. Park and T. C. Lubensky. Interactions between membrane inclusions on fluctuating membranes. *Journal de Physique I*, 6(9):1217–1235, 1996.

[72] P. G. Dommersnes and J.-B. Fournier. N-body study of anisotropic membrane inclusions: Membrane mediated interactions and ordered aggregation. *European Physical Journal B*, 12(1):9–12, 1999.

[73] P. G. Dommersnes and J.-B. Fournier. Casimir and mean-field interactions between membrane inclusions subject to external torques. *Europhysics Letters*, 46(2):256–261, 1999.

[74] D. S. Dean and M. Manghi. Fluctuation-induced interactions between domains in membranes. *Physical Review E*, 74(2):021916, 2006.

[75] E. Noruzifar and M. Oettel. Anisotropies in thermal Casimir interactions: Ellipsoidal colloids trapped at a fluid interface. *Physical Review E*, 79(5):051401, 2009.

[76] H. Li and M. Kardar. Fluctuation-induced forces between manifolds immersed in correlated fluids. *Physical Review A*, 46(10):6490–6500, 1992.

[77] A. Maciolek, A. Gambassi, and S. Dietrich. Critical Casimir effect in superfluid wetting films. *Physical Review E*, 76(3):031124, 2007.

[78] J. Goldstone, A. Salam, and S. Weinberg. Broken Symmetries. *Physical Review*, 127:965, 1962.

[79] M. Kardar. *Statistical physics of fields*. Cambridge University Press, 2007.

[80] J.-B. Fournier and P. G. Dommersnes. Comment on "Long-range forces in heterogeneous fluid membranes". *Europhysics Letters*, 39(6):681–682, 1997.

[81] R. R. Netz. Inclusions in fluctuating membranes: exact results. *Journal de Physique I – France*, 7:833–852, 1997.

[82] I. Koltover, J. O. Rädler, and C. R. Safinya. Membrane mediated attraction and ordered aggregation of colloidal particles bound to giant phospholipid vesicles. *Physical Review Letters*, 82:1991–1994, 1999.

[83] T. R. Weikl. Fluctuation-induced aggregation of rigid membrane inclusions. *Europhysics Letters*, 54:547–553, 2001.

[84] R. Golestanian, M. Goulian, and M. Kardar. Fluctuation-induced interactions between rods on a membrane. *Physical Review E*, 54(6):6725–6734, 1996.

[85] R. Golestanian, M. Goulian, and M. Kardar. Fluctuation-induced interactions between rods on membranes and interfaces. *Europhysics Letters*, 33(3):241–245, 1996.

[86] R. Golestanian. Reduced persistence length and fluctuation-induced interactions of directed semiflexible polymers on fluctuating surfaces. *Europhysics Letters*, 36:557, 1996.

[87] R. Podgornik. Orientational ordering of polymers on a fluctuating flexible surface. *Physical Review E*, 52:5170–5177, 1995.

[88] P. Gosselin, H. Mohrbach, and M. M. Müller. Interface-mediated interactions: Entropic forces of curved membranes. *Physical Review E*, 83:051921, 2011.

[89] W. Helfrich and T.R. Weikl. Two direct methods to calculate fluctuation forces between rigid objects embedded in fluid membranes. *European Physical Journal E*, 5:423–439, 2001.

[90] C. Yolcu, I. Z. Rothstein, and M. Deserno. Effective field theory approach to Casimir interactions on soft matter surfaces. *Europhysics Letters*, 96:20003, 2011.

[91] B. M. Axilrod and E. Teller. Interaction of the van der Waals type between three atoms. *Journal of Chemical Physics*, 11(6):299–300, 1943.

[92] H.-K. Lin, R. Zandi, U. Mohideen, and L. P Pryadko. Fluctuation-induced forces between inclusions in a fluid membrane under tension. *Physical Review Letters*, 107:228104, 2011.

[93] S. J. Rahi, T. Emig, N. Graham, R. L. Jaffe, and Kardar M. Scattering theory approach to electrodynamic Casimir forces. *Physical Review D*, 80:085021, 2009.

[94] B. V. Derjaguin. Analysis of friction and adhesion – IV. The theory of the adhesion of small particles. *Kolloid Zeitschrift*, 69:155, 1934.

[95] P. G. Dommersnes and J.-B. Fournier. The many-body problem for anisotropic membrane inclusions and the self-assembly of "saddle" defects into an "egg carton". *Biophysical Journal*, 83:2898–2905, 2002.

[96] N. Destainville. Cluster phases of membrane proteins. *Physical Review E*, 77:011905, 1998.

[97] P. G. Dommersnes, J.-B. Fournier, and Galatola P. Long-range elastic forces between membrane inclusions in spherical vesicles. *Europhysics Letters*, 42:233–238, 1998.

[98] T. R. Weikl, M. M. Kozlov, and W. Helfrich. Interaction of conical membrane inclusions: Effect of lateral tension. *Physical Review E*, 57:6988–6995, 1998.

[99] M. M. Müller, M. Deserno, and J. Guven. Interface-mediated interactions between particles: A geometrical approach. *Physical Review E*, 72:061407, 2005.

[100] M. M. Müller, M. Deserno, and J. Guven. Geometry of surface-mediated interactions. *Europhysics Letters*, 69:482–488, 2005.

[101] R. Capovilla and J. Guven. Stresses in lipid membranes. *Journal of Physics A*, 35(30):6233–6247, 2002.

[102] T. R. Weikl. Indirect interactions of membrane-adsorbed cylinders. *European Physical Journal E*, 12:265–273, 2003.

[103] B. J. Reynwar, G. Illya, V. A. Harmandaris, M. M. Mueller, K. Kremer, and M. Deserno. Aggregation and vesiculation of membrane proteins by curvature-mediated interactions. *Nature*, 447:461–464, 2007.

[104] B. J. Reynwar and M. Deserno. Membrane-mediated interactions between circular particles in the strongly curved regime. *Soft Matter*, 7:8567, 2011.

[105] S. Semrau, T. Idema, T. Schmidt, and C. Storm. Membrane-mediated interactions measured using membrane domains. *Biophysical Journal*, 96:4906–4915, 2009.

[106] L. S. Brown and G. J. Maclay. Vacuum stress between conducting plates – an image solution. *Physical Review*, 184(5):1272, 1969.

[107] G. Barton. On the fluctuations of the Casimir force. *Journal of Physics A*, 24(5):991–1005, 1991.

[108] M. T. Jaekel and S. Reynaud. Fluctuations and dissipation for a mirror in vacuum. *Quantum Optics*, 4(1):39–53, 1992.

[109] D. Robaschik and E. Wieczorek. Fluctuations of the Casimir pressure at finite temperature. *Physical Review D*, 52(4):2341–2354, 1995.

[110] R. Messina and R. Passante. Fluctuations of the Casimir-Polder force between an atom and a conducting wall. *Physical Review A*, 76(3):032107, 2007.

[111] D. Bartolo, A. Ajdari, J.-B. Fournier, and R. Golestanian. Fluctuations of fluctuation-induced Casimir-like forces. *Physical Review Letters*, 89(23):230601, 2002.

[112] D. Dantchev and M. Krech. Critical Casimir force and its fluctuations in lattice spin models: Exact and Monte Carlo results. *Physical Review E*, 69(4, Part 2):046119, 2004.

[113] J.-B. Fournier. On the stress and torque tensors in fluid membranes. *Soft Matter*, 3(7):883–888, 2007.

[114] A.-F. Bitbol, P. G. Dommersnes, and J.-B. Fournier. Fluctuations of the Casimir-like force between two membrane inclusions. *Physical Review E*, 81:050903(R), 2010.

[115] P. D. Blood and G. A. Voth. Direct observation of Bin/amphiphysin/Rvs (BAR) domain-induced membrane curvature by means of molecular dynamics simulations. *Proceedings of the National Academy of Sciences of the United States of America*, 103(41):15068–15072, 2006.

[116] E. Gottwein, J. Bodem, B. Muller, A. Schmechel, H. Zentgraf, and H. G. Krausslich. The Mason-Pfizer monkey virus PPPY and PSAP motifs both contribute to virus release. *Journal of Virology*, 77(17):9474–9485, 2003.

[117] H. T. McMahon and J. L. Gallop. Membrane curvature and mechanisms of dynamic cell membrane remodelling. *Nature*, 438:590–596, 2005.

[118] J. Zimmerberg and M. M. Kozlov. How proteins produce cellular membrane curvature. *Nature Reviews – Molecular Cell Biology*, 7:9–19, 2006.

[119] P. M. Chaikin and T. C. Lubensky. *Principles of condensed matter physics*. Cambridge University Press, 1995.

[120] M. Le Bellac. *Quantum and Statistical Field Theory*. Clarendon Press, Oxford, 1992.

[121] D. Bartolo, A. Ajdari, and J.-B. Fournier. Effective interactions between inclusions in complex fluids driven out of equilibrium. *Physical Review E*, 67:061112, 2003.

[122] A. Najafi and R. Golestanian. Forces induced by nonequilibrium fluctuations: The Soret-Casimir effect. *Europhysics Letters*, 68(6):776, 2004.

[123] A. Gambassi and S. Dietrich. Critical Dynamics in Thin Films. *Journal of Statistical Physics*, 123(5):929, 2006.

[124] A. Gambassi. Relaxation phenomena at criticality. *European Physical Journal B*, 64:379, 2008.

[125] P. Rodriguez-Lopez, R. Brito, and R. Soto. Dynamical approach to the Casimir effect. *Physical Review E*, 83:031102, 2011.

[126] D. S. Dean and A. Gopinathan. The non-equilibrium behavior of pseudo-Casimir forces. *Journal of Statistical Mechanics*, page L08001, 2009.

[127] D. S. Dean and A. Gopinathan. Out-of-equilibrium behavior of Casimir-type fluctuation-induced forces for classical fields. *Physical Review E*, 81:041126, 2010.

[128] V. Démery and D. S. Dean. Drag forces in classical fields. *Physical Review Letters*, 104:080601, 2010.

[129] V. Démery and D. S. Dean. Drag forces on inclusions in classical fields with dissipative dynamics. *European Physical Journal E*, 32:377, 2010.

[130] A.-F. Bitbol and J.-B. Fournier. Forces exerted by a correlated fluid on embedded inclusions. *Physical Review E*, 83:061107, 2011.

[131] G. K. Batchelor. *An Introduction to Fluid Dynamics*. Cambridge University Press, 1967.

[132] R. Brito, U. Marini Bettolo Marconi, and R. Soto. Generalized Casimir forces in nonequilibrium systems. *Physical Review E*, 76:011113, 2007.

[133] P. R. Buenzli and R. Soto. Violation of the action-reaction principle and self-forces induced by nonequilibrium fluctuations. *Physical Review E*, 78:020102(R), 2008.

[134] B. Podolsky and C. Kikuchi. A generalized electrodynamics. *Physical Review*, 65(7-8):228, 1944.

[135] K. O. Tielheim. Note on classical fields of higher order. *Proceedings of the Physical Society*, 91:798, 1967.

[136] L. S. Schulman. *Techniques and Applications of Path Integration*. Dover, 2005.

[137] P. W. Milonni, R. J. Cook, and M. E. Goggin. Radiation pressure from the vacuum – Physical interpretation of the Casimir force. *Physical Review A*, 38(3):1621–1623, 1988.

[138] P. S. Niemela, M. S. Miettinen, L. Monticelli, H. Hammaren, P. Bjelkmar, T. Murtola, E. Lindahl, and I. Vattulainen. Membrane proteins diffuse as dynamic complexes with lipids. *Journal of the American Chemical Society*, 132:7574–7575, 2010.

[139] L. Bocquet and J.-L. Barrat. Flow boundary conditions from nano- to micro-scales. *Soft Matter*, 3:685–693, 2007.

[140] K. Sekimoto. *Stochastic Energetics*. Springer-Verlag, 2010.

[141] M. Burgess. *Classical Covariant Fields*. Cambridge University Press, 2002.

[142] P. Di Francesco, P. Mathieu, and D. Sénéchal. *Conformal Field Theory*. Springer-Verlag, 1997.

[143] S. Kondrat, L. Harnau, and S. Dietrich. Critical Casimir interaction of ellipsoidal colloids with a planar wall. *Journal of Chemical Physics*, 131:204902, 2009.

[144] M. E. Gurtin. *An Introduction to Continuum Mechanics*. Academic Press, 1981.

[145] L. Limozin, M. Bärmann, and E. Sackmann. On the organization of self-assembled actin networks in giant vesicles. *European Physical Journal E*, 10:319, 2003.

[146] M. Hase and K. Yoshikawa. Structural transition of actin filament in a cell-sized water droplet with a phospholipid membrane. *Journal of Chemical Physics*, 124:104903, 2006.

[147] M. Osawa, D. E. Anderson, and H. P. Erickson. Reconstitution of contractile FtsZ rings in liposomes. *Science*, 320:792, 2008.

[148] M. Bokvist, F. Lindström, A. Watts, and G. Gröbner. Two types of Alzheimer's beta-amyloid (1–40) peptide membrane interactions: Aggregation preventing transmembrane anchoring versus accelerated surface fibril formation. *Journal of Molecular Biology*, 335:1039, 2004.

[149] T. L. Williams, B. R. G. Johnson, B. Urbanc, A. T. A. Jenkins, S. D. A. Connell, and L. C. Serpell. Aβ42 oligomers, but not fibrils, simultaneously bind to and cause damage to ganglioside-containing lipid membranes. *Biochemical Journal*, 439:67–77, 2011.

[150] D. Constantin, P. Davidson, and C. Chanéac. Lyotropic lamellar phase doped with a nematic phase of magnetic nanorods. *Langmuir*, 26:4586, 2010.

[151] A.-F. Bitbol, K. Sin Ronia, and J.-B. Fournier. Universal amplitudes of the Casimir-like interactions between four types of rods in fluid membranes. *Europhysics Letters*, 96:40013, 2011.

[152] M. Goulian, R. Bruinsma, and P. Pincus. Long-range forces in heterogeneous fluid membranes. *Europhysics Letters*, 22(2):145–150, 1993.

[153] R. Büscher and T. Emig. Nonperturbative approach to Casimir interactions in periodic geometries. *Physical Review A*, 69:062101, 2004.

[154] K. Sin Ronia and J.-B. Fournier. *In preparation.*

[155] E. Elizalde. *Ten Physical Applications of Spectral Zeta Functions.* Springer, Berlin, 1995.

[156] H. Lehle and M. Oettel. Importance of boundary conditions for fluctuation-induced forces between colloids at interfaces. *Physical Review E*, 75:011602, 2007.

[157] P. C. Jost, O. H. Griffiths, R. A. Capaldi, and G. Vanderkooi. Evidence for boundary lipid in membranes. *Proceedings of the National Academy of Sciences of the United States of America*, 70:480–484, 1973.

[158] S. Marčelja. Lipid-mediated protein interaction in membranes. *Biochimica et Biophysica Acta – Biomembranes*, 455:1–7, 1976.

[159] H. Schröder. Aggregation of proteins in membranes. An example of fluctuation induced interactions in liquid crystals. *Journal of Chemical Physics*, 67:1617, 1977.

[160] J. C. Owicki, M. W. Springgate, and H. McConnell. Theoretical study of protein-lipid interactions in bilayer membranes. *Proceedings of the National Academy of Sciences of the United States of America*, 75:1616–1619, 1978.

[161] J. A. Killian. Hydrophobic mismatch between proteins and lipids in membranes. *Biochimica et Biophysica Acta – Biomembranes*, 1376:401–416, 1998.

[162] L. E. Cybulski, M. Martín, M. C. Mansilla, A. Fernández, and D. de Mendoza. Membrane thickness cue for cold sensing in a bacterium. *Current Biology*, 20:1539–1544, 2010.

[163] J. Ballering, L. E. Cybulski, D. de Mendoza, and J. A. Killian. A systematic approach towards elucidation of the mode of action of a bacterial thermosensor. *Biophysical Journal*, 102:493a–494a, 2012.

[164] L. E. Cybulski, D. de Mendoza, J. Ballering, and J. A. Killian. How does thermosensor DesK measure membrane thickness? Tryptophan fluorescence and mutagenesis analysis. *Biophysical Journal*, 102:494a, 2012.

[165] C. Scharnagl, M. Moerch, and D. Langosch. How backbone flexibility of transmembrane helices can determine peptide/lipid interactions in a mixed bilayer: a molecular dynamics study. *Biophysical Journal*, 102:623a–624a, 2012.

[166] H. W. Florey. *Penicillin.* Nobel Lecture, 1945.

[167] D. A. Kelkar and A. Chattopadhyay. The gramicidin ion channel: A model membrane protein. *Biochimica et Biophysica Acta – Biomembranes*, 1768:2011–2025, 2007.

[168] J. A. Lundbaek, R. E. Koeppe II, and O. S. Andersen. Amphiphile regulation of ion channel function by changes in the bilayer spring constant. *Proceedings of the National Academy of Sciences of the United States of America*, 107:15427–15430, 2010.

[169] A. M. O'Connell, R. E. Koeppe II, and O. S. Andersen. Kinetics of gramicidin channel formation in lipid bilayers: transmembrane monomer association. *Science*, 250:1256–1259, 1990.

[170] M. Goulian, O. N. Mesquita, D. K. Fygenson, C. Nielsen, O. S. Andersen, and A. Libchaber. Gramicidin channel kinetics under tension. *Biophysical Journal*, 74:328–337, 1998.

[171] J. R. Elliott, D. Needham, J. P. Dilger, and D. A. Haydon. The effects of bilayer thickness and tension on gramicidin single-channel lifetime. *Biochimica et Biophysica Acta – Biomembranes*, 735:95–103, 1983.

[172] H. W. Huang. Deformation free energy of bilayer membrane and its effect on gramicidin channel lifetime. *Biophysical Journal*, 50:1061–1070, 1986.

[173] H. A. Kolb and E. Bamberg. Influence of membrane thickness and ion concentration on the properties of the gramicidin A channel: autocorrelation, spectral power density, relaxation and single-channel studies. *Biochimica et Biophysica Acta – Biomembranes*, 464:127–141, 1977.

[174] P. Helfrich and E. Jakobsson. Calculation of deformation energies and conformations in lipid membranes containing gramicidin channels. *Biophysical Journal*, 57:1075–1084, 1990.

[175] N. Dan, P. Pincus, and S. A. Safran. Membrane-induced interactions between inclusions. *Langmuir*, 9:2768–2771, 1993.

[176] H. Aranda-Espinoza, A. Berman, N. Dan, P. Pincus, and S. Safran. Interaction between inclusions embedded in membranes. *Biophysical Journal*, 71:648, 1996.

[177] J. C. Owicki and H. McConnell. Theory of protein-lipid and protein-protein interactions in bilayer membranes. *Proceedings of the National Academy of Sciences of the United States of America*, 76:4750–4754, 1979.

[178] O. G. Mouritsen and M. Bloom. Mattress model of lipid-protein interactions in membranes. *Biophysical Journal*, 46:141–153, 1984.

[179] P. G. de Gennes. *The Physics of Liquid Crystals*. Clarendon Press, Oxford, 1974.

[180] G. Brannigan and F. L. H. Brown. A consistent model for thermal fluctuations and protein-induced deformations in lipid bilayers. *Biophysical Journal*, 90(5):1501–1520, 2006.

[181] G. Brannigan and F. L. H. Brown. Contributions of gaussian curvature and nonconstant lipid volume to protein deformation of lipid bilayers. *Biophysical Journal*, 92(3):864–876, 2007.

[182] E. Lindahl and O. Edholm. Mesoscopic undulations and thickness fluctuations in lipid bilayers from molecular dynamics simulations. *Biophysical Journal*, 79(1):426–433, 2000.

[183] B. West, F. L. H. Brown, and F. Schmid. Membrane-protein interactions in a generic coarse-grained model for lipid bilayers. *Biophysical Journal*, 96(1):101–115, 2009.

[184] S. J. Marrink and A. E. Mark. Effect of undulations on surface tension in simulated bilayers. *Journal of Physical Chemistry B*, 105(26):6122–6127, 2001.

[185] K. I. Lee, T. Kim, R. W. Pastor, O. S. Andersen, and W. Im. Assessment of membrane deformation continuum elastic models based on molecular simulations of gramicidin A. *Biophysical Journal*, 102:296a, 2012.

[186] A.-F. Bitbol, D. Constantin, and J.-B. Fournier. Bilayer elasticity at the nanoscale: the need for new terms. *PLoS ONE*, 7(11):e48306, 2012.

[187] A.-F. Bitbol, L. Peliti, and J.-B. Fournier. Membrane stress tensor in the presence of lipid density and composition inhomogeneities. *European Physical Journal E*, 34:53, 2011.

[188] C. Nielsen, M. Goulian, and O. S. Andersen. Energetics of inclusion-induced bilayer deformations. *Biophysical Journal*, 74:1966–1983, 1998. Erratum: *Biophysical Journal* 76: 2317 (1999).

[189] K. A. Sharp, A. Nicholls, R. F. Fine, and B. Honig. Reconciling the magnitude of the microscopic and macroscopic hydrophobic effects. *Science*, 252:106–109, 1991.

[190] S. May and A. Ben-Shaul. Molecular theory of lipid-protein interaction and the L_α-$H_{||}$ transition. *Biophysical Journal*, 76:751–767, 1999.

[191] S. B. Hladky and D. W. R. Gruen. Thickness fluctuations in black lipid membranes. *Biophysical Journal*, 38:251–258, 1982.

[192] J. A. Lundbaek and O. S. Andersen. Spring constants for channel-induced lipid bilayer deformations estimates using gramicidin channels. *Biophysical Journal*, 76(2):889–895, 1999.

[193] T.-C. Hwang, R. E. Koeppe II, and O. S. Andersen. Genistein can modulate channel function by a phosphorylation-independent mechanism: importance of hydrophobic mismatch and bilayer mechanics. *Biochemistry*, 42(46):13646–13658, 2003.

[194] H. Chung and M. Caffrey. The curvature elastic-energy function of the lipid-water cubic mesophase. *Nature*, 368:224–226, 1994.

[195] H. Chung and M. Caffrey. The neutral area surface of the cubic mesophase: location and properties. *Biophysical Journal*, 66:377–381, 1994.

[196] R. H. Templer. On the area neutral surface of inverse bicontinuous cubic phases of lyotropic liquid crystals. *Langmuir*, 11:334–340, 1995.

[197] R. H. Templer, D. C. Turner, P. Harper, and J. M. Seddon. Corrections to some models of the curvature elastic energy of inverse bicontinuous cubic phases. *Journal de Physique II France*, 5:1053–1065, 1995.

[198] H. Vacklin, B. J. Khoo, K. H. Madan, J. M. Seddon, and R. H. Templer. The bending elasticity of 1-monoolein upon relief of packing stress. *Langmuir*, 16:4741–4748, 2000.

[199] J. A. Szule, N. L. Fuller, and R. P. Rand. The effects of acyl chain length and saturation of diacylglycerols and phosphatidylcholines on membrane monolayer curvature. *Biophysical Journal*, 83:977–984, 2002.

[200] S. Leikin, M. M. Kozlov, N. L. Fuller, and R. P. Rand. Measured effects of diacylglycerol on structural and elastic properties of phospholipid membranes. *Biophysical Journal*, 71:2623–2632, 1996.

[201] T. K. Rostovtseva, P. A. Gurnev, D. Jacobs, M. Weinrich, and S. M. Bezrukov. Interaction of novel anticancer drug erastin with lipid bilayers probed by gramicidin A. *Biophysical Journal*, 102:85a, 2012.

[202] D. Constantin. Membrane-mediated repulsion between gramicidin pores. *Biochimica et Biophysica Acta – Biomembranes*, 1788:1782–1789, 2009.

[203] J. Adler. Chemotaxis in bacteria. *Science*, 153(3737):708–716, 1966.

[204] A. S. Cans, R. Wittenberg, R. Karlsson, L. Sombers, O. Karlsson, O. Orwar, and E. Ewing. Artificial cells: Unique insights into exocytosis using liposomes and lipid nanotubes. *Proceedings of the National Academy of Sciences of the United States of America*, 100(2):400–404, 2003.

[205] P. Streicher, P. Nassoy, M. Bärmann, A. Dif, V. Marci-Artzner, F. Brochard-Wyart, J. Spatz, and P. Bassereau. Integrin reconstituted in GUVs: A biomimetic system to study initial steps of cell spreading. *Biochimica et Biophysica Acta – Biomembranes*, 1788(10):2291–2300, 2009.

[206] F. Campelo and A. Hernández-Machado. Polymer-induced tubulation in lipid vesicles. *Physical Review Letters*, 100:158103, 2008.

[207] T. Baumgart, S. T. Hess, and W. W. Webb. Imaging coexisting fluid domains in biomembrane models coupling curvature and line tension. *Nature*, 425:821–824, 2003.

[208] M. Yanagisawa, M. Imai, T. Masui, S. Komura, and T. Ohta. Growth Dynamics of Domains in Ternary Fluid Vesicles. *Biophysical Journal*, 92(1):115–125, 2007.

[209] S. L. Veatch and S. L. Keller. Organization in Lipid Membranes Containing Cholesterol. *Physical Review Letters*, 89:268101, 2002.

[210] R. Wick, M. I. Angelova, P. Walde, and P. L. Luisi. Microinjection into giant vesicles and light microscopy investigation of enzyme mediated vesicle transformations. *Chemistry & Biology*, 3:105–111, 1996.

[211] M. I. Angelova, N. Hristova, and I. Tsoneva. DNA-induced endocytosis upon local microinjection to giant unilamellar cationic vesicles. *European Biophysics Journal*, 28:142–150, 1999.

[212] N. Borghi, O. Rossier, and F. Brochard-Wyart. Hydrodynamic extrusion of tubes from giant vesicles. *Europhysics Letters*, 64(6):837–843, 2003.

[213] N. Khalifat, N. Puff, S. Bonneau, J. B. Fournier, and M. I. Angelova. Membrane deformation under local pH gradient: mimicking mitochondrial cristae dynamics. *Biophysical Journal*, 95(10):4924–4933, 2008.

[214] C. Martin, S. F. Pedersen, A. Schwab, and C. Stock. Intracellular pH gradients in migrating cells. *American Journal of Physiology – Cell Physiology*, 300:C490–C495, 2011.

[215] L. Stüwe, M. Müller, A. Fabian, J. Waning, S. Mally, J. Noël, A. Schwab, and C. Stock. pH dependence of melanoma cell migration: protons extruded by NHE1 dominate protons of the bulk solution. *Journal of Physiology*, 585:351–360, 2007.

[216] K. M. Davies, M. Strauss, B. Daum, J. H. Kief, H. D. Osiewacz, A. Rycovska, V. Zickermann, and W. Kühlbrandt. Macromolecular organization of ATP synthase and complex I in whole mitochondria. *Proceedings of the National Academy of Sciences of the United States of America*, 108(34):14121–14126, 2011.

[217] C. A. Mannella, M. Marko, and K. Buttle. Reconsidering mitochondrial structure: new views of an old organelle. *Trends in Biochemical Sciences*, 22:37–38, 1997.

[218] C. A. Mannella. Structure and dynamics of the mitochondrial inner membrane cristae. *Biochimica et Biophysica Acta – Molecular Cell Research*, 1763:542–548, 2006.

[219] J.-B. Fournier, N. Khalifat, N. Puff, and M. I. Angelova. Chemically triggered ejection of membrane tubules controlled by intermonolayer friction. *Physical Review Letters*, 102:018102, 2009.

[220] J. B. Lee, P. G. Petrov, and H. G. Döbereiner. Curvature of zwitterionic membranes in transverse pH gradients. *Langmuir*, 15:8543–8546, 1999.

[221] H.-G. Döbereiner, O. Selchow, and R. Lipowsky. Spontaneous curvature of fluid vesicles induced by trans-bilayer sugar asymmetry. *European Biophysics Journal*, 28:174–178, 1999.

[222] P. G. Petrov, J. B. Lee, and H. G. Döbereiner. Coupling chemical reactions to membrane curvature: a photochemical morphology switch. *Europhysics Letters*, 48:435–441, 1999.

[223] F. Brochard and J.-F. Lennon. Frequency spectrum of flicker phenomenon in erythrocytes. *Journal de Physique*, 36:1035–1047, 1975.

[224] U. Seifert and S. A. Langer. Viscous modes of fluid bilayer membranes. *Europhysics Letters*, 23:71–76, 1993.

[225] E. Evans, A. Yeung, R. Waugh, and J. Song. Dynamic coupling and nonlocal curvature elasticity in bilayer membranes. In R. Lipowsky, D. Richter, and K. Kremer, editors, *The Structure and Conformation of Amphiphilic Membranes – Springer Proceedings in Physics, Vol. 66*, pages 148–153. Springer, Berlin, 1992.

[226] E. Evans and E. Sackmann. Translational and rotational drag coefficients for a disk moving in a liquid membrane associated with a rigid substrate. *Journal of Fluid Mechanics*, 194:553–561, 1988.

[227] R. Merkel, E. Sackmann, and E. Evans. Molecular friction and epitactic coupling between monolayers in supported bilayers. *Journal de Physique, France*, 50:1535–1555, 1989.

[228] E. Evans and A. Yeung. Hidden dynamics in rapid changes of bilayer shape. *Chemistry and Physics of Lipids*, 73:39–56, 1994.

[229] A. G. Petrov and I. Bivas. Elastic and flexoelectric aspects of out-of-plane fluctuations in biological and model membranes. *Progress in Surface Science*, 16:389–512, 1984.

[230] P. Sens. Dynamics of nonequilibrium membrane bud formation. *Physical Review Letters*, 93(10):108103, 2004.

[231] A.-F. Bitbol, J.-B. Fournier, M. I. Angelova, and N. Puff. Dynamical membrane curvature instability controlled by intermonolayer friction. *Journal of Physics: Condensed Matter*, 23:284102, 2011.

[232] L. Miao, M. A. Lomholt, and J. Kleis. Dynamics of shape fluctuations of quasi-spherical vesicles revisited. *European Physical Journal E*, 9:143–160, 2002.

[233] M. Doi. *Introduction to polymer physics*. Oxford Science Publications, 1995.

[234] I. Tsafrir, D. Sagi, T. Arzi, M.-A. Guedeau-Boudeville, V. Frette, D. Kandel, and J. Stavans. Pearling Instabilities of Membrane Tubes with Anchored Polymers. *Physical Review Letters*, 86(6):1138–1141, 2001.

[235] I. Tsafrir, Y. Caspi, M.-A. Guedeau-Boudeville, T. Arzi, and J. Stavans. Budding and tubulation in highly oblate vesicles by anchored amphiphilic molecules. *Physical Review Letters*, 91:138102, 2003.

[236] G. Staneva, M. Seigneuret, K. Koumanov, G. Trugnan, and M. I. Angelova. Detergents induce raft-like domains budding and fission from giant unilamellar heterogeneous vesicles – A direct microscopy observation. *Chemistry and Physics of Lipids*, 136(1):55–66, 2005.

[237] N. Khalifat, J.-B. Fournier, M. I. Angelova, and N. Puff. Lipid packing variations induced by pH in cardiolipin-containing bilayers: The driving force for the cristae-like shape instability. *Biochimica et Biophysica Acta – Biomembranes*, 1808:2724–2733, 2011.

[238] T. Pott and P. Méléard. The dynamics of vesicle thermal fluctuations is controlled by intermonolayer friction. *Europhysics Letters*, 59:87, 2002.

[239] S. A. Shkulipa, W. K. den Otter, and W. J. Briels. Thermal undulations of lipid bilayers relax by intermonolayer friction at submicrometer length scales. *Physical Review Letters*, 96:178302, 2006.

[240] M. Eigen. Proton transfer acid-base catalysis and enzymatic hydrolysis – I. Elementary processes. *Angewandte Chemie (International Edition)*, 3(1):1, 1964.

[241] A. Alastuey, M. Magro, and P. Pujol. *Physique et outils mathématiques – méthodes et exemples*. EDP Sciences et CNRS Editions, 2008.

[242] N. Khalifat, N. Puff, M. Dliaa, and M. I. Angelova. Amyloid-beta and the failure to form mitochondrial cristae: a biomimetic study involving artificial membranes. *Journal of Alzheimer's Disease*, 28:33–48, 2012.

[243] A.-F. Bitbol, N. Puff, Y. Sakuma, M. Imai, J.-B. Fournier, and M. I. Angelova. Lipid membrane deformation in response to a local pH modification: theory and experiments. *Soft Matter*, 8:6073–6082, 2012.

[244] R. C. MacDonald, R. I. MacDonald, B. P. Menco, K. Takeshita, N. K. Subbarao, and L. R. Hu. Small-volume extrusion apparatus for preparation of large, unilamellar vesicles. *Biochimica et Biophysica Acta – Biomembranes*, 1061:293–303, 1991.

[245] F. C. Tsui, D. M. Ojcius, and W. L. Hubbell. The intrinsic pKa values for phosphatidylserine and phosphatidylethanolamine in phosphatidylcholine host bilayers. *Biophysical Journal*, 49:459–458, 1986.

[246] E. L. Cussler. *Diffusion – Mass transfer in fluid systems*. Cambridge University Press, 2009.

[247] J. C. Crocker and D. G. Grier. Methods of digital video microscopy for colloidal studies. *Journal of Colloid and Interface Science*, 179:298–310, 1995.

[248] A.-F. Bitbol and J.-B. Fournier. Membrane properties revealed by spatiotemporal response to a local inhomogeneity. *Biochimica et Biophysica Acta – Biomembranes*, in press, 2012.

[249] D. Kabaso, R. Shlomovitz, T. Auth, V. L. Lew, and N. S. Gov. Curling and local shape changes of red blood cell membranes driven by cytoskeletal reorganization. *Biophysical Journal*, 99:808–816, 2010.

[250] G. Napoli and L. Vergori. Equilibrium of nematic vesicles. *Journal of Physics A: Mathematical and Theoretical*, 43:445207, 2010.

[251] M. M. Müller and M. Deserno. Balancing torques in membrane-mediated interactions: Exact results and numerical illustrations. *Physical Review E*, 76:011921, 2007.

[252] W. Cai and T. C. Lubensky. Hydrodynamics and dynamic fluctuations of fluid membranes. *Physical Review E*, 52:4251–4266, 1995.

[253] E. A. Evans. Bending resistance and chemically-induced moments in membrane bilayers. *Biophysical Journal*, 14:923–931, 1974.

[254] S. A. Shkulipa, W. K. den Otter, and W. J. Briels. Simulations of the dynamics of thermal undulations in lipid bilayers in the tensionless state and under stress. *Journal of Chemical Physics*, 125:234905, 2006.

[255] M. A. Lomholt, P. L. Hansen, and L. Miao. A general theory of non-equilibrium dynamics of lipid-protein fluid membranes. *European Physical Journal E*, 16:439–461, 2005.

[256] J. T. Jenkins. Static equilibrium configurations of a model red blood cell. *Journal of Mathematical Biology*, 4:149–169, 1977.

[257] T. R. Powers. Dynamics of filaments and membranes in a viscous fluid. *Review of Modern Physics*, 82:1607–1631, 2010.

[258] R. Capovilla, J. Guven, and J. A. Santiago. Lipid membranes with an edge. *Physical Review E*, 66:021607, 2002.

[259] R. Capovilla and J. Guven. Geometry of lipid vesicle adhesion. *Physical Review E*, 66:041604, 2002.

[260] M. Deserno, M. M. Müller, and J. Guven. Contact lines for fluid surface adhesion. *Physical Review E*, 76:011605, 2007.